PROCEEDINGS

of the International Conference on

"Microwave and THz Technologies, Photonics and Wireless Communications"

MAY 4-6, 2016

Yerevan, Armenia

PROCEEDINGS
of the International Conference on

"Microwave and THz Technologies, Photonics and Wireless Communications"

IRPhE' 2016

May 4-6, Yerevan, Armenia

Organized by
Institute of Radiophysics and Electronics NAS RA

Industrial partner

Keysight LLC (Russia)

IRPhE' 2016 Main Topics:
- **Microwave devices, antennas, propagations and remote sensing**
- **THz technique, spectroscopy and applications**
- **Photonics**
- **Wireless communications**
- **Alternative semiconductor and dielectric materials, electronic devices**
- **Exhibition: Keysight Technologies & National Instruments**

Conference Chairs:
Radik Martirosyan, (President NAS RA)
ArsenHakhoumian, (Ass. Member NAS RA, IRPhE)

Program Committee:
Prof. Radik Martirosyan, (President NAS Armenia)
Prof. Arsen Hakhoumian, (IRPhE, Armenia)
Prof. Boris Kutuza, (IRE RAS, Russia)
Prof. Kiejin Lee (Sogang University, South Korea)
Prof. Robert Minasian (Sidney University, Australia)
Prof. Stepan Petrosyan (IRPhE, Armenia)
Prof. Garik Markaryan, (Lancaster University, UK)
Prof. Yuri Avetisyan (YSU, Armenia)
Prof. Khachik Nerkararyan (YSU, Armenia)

Organizing Committee:
Chairman: Prof. Radik Martirosyan, (President NAS RA)
Co-chairman: Prof. Arsen Hakhoumian, (IRPhE, RA)
Prof. Hrant Matevosyan   (IRPhE, NAS RA)
Dr. Ashkhen Yesayan, (IRPhE, RA)
Dr. Emil Asmaryan, (IRPhE, RA)
Dr. Tigran Zakaryan, (IRPhE, RA)
Prof. Garik Markaryan, (Lancaster University, UK)
Dr. Hapet Barsegyan, (Integra, USA)

Preface

The International Conference "Microwave and THz Technologies, Photonics and Wireless Communications" (IRPhE'2016) was held in Yerevan, Armenia, from May 4 to May 6, 2014. The IRPhE' 2016 Conference was an open forum for the presentation and discussion of current research achievements in Microwave and THz technologies, wireless communications, photonics and its applications.

This year IRPhE' 2016 Conference was dedicated to the 80th anniversary of Academician Radik M. Martirosyan, the current President of National Academy of Sciences of RA.

Content

Photonics &Wireless Communications

THz Technique, Spectroscopy and Applications

Alternative Semiconductor Materials, Electronic Devices

Microwave Devices, Antennas, Propagations and Remote Sensing

Conditions of single-frequency radiation from fiber laser with FBG mirrors: numerical analysis by the method of single expression

H.V. Baghdasaryan[1], T.M. Knyazyan[1], T.T. Hovhannisyan[1], M. Marciniak[2]

[1] *National Polytechnic University of Armenia, 105 Terian str., 0009 Yerevan, Armenia*
[2] *National Institute of Telecommunications, 1 Szachowa Street, 04-894 Warsaw, Poland*
[2] *Kielce University of Technology, al. Tysiaclecia Painstwa Polskiego 7, 25-314 Kielce, Poland*

In the current paper DBR (distributed Bragg reflector) fiber laser consisting of a piece of an amplifying fiber terminated by two fiber Bragg gratings (FBGs) serving as resonant mirrors is considered. The method of single expression (MSE) is used for self-consisting numerical simulation of plane wave interaction with the DBR fiber laser structure to determine correctly the length of the amplifying fiber for single longitudinal-mode lasing. In the modelling, initially, transmission spectra of DBR fiber laser have been analysed at different lengths of the fiber between FBGs at absence of loss or gain. Full transmission at the Bragg wavelength of FBGs is obtained for the row of increasing lengths of the fiber between FBGs. By inclusion of gain in the amplifying fiber of these resonant lengths a stable single longitudinal-mode radiation at the resonant Bragg wavelength is obtained.

I. INTRODUCTION

Single longitudinal-mode (SLM) lasers are under high demand in optical communication, interferometric sensing, coherent light detection and ranging, laser spectroscopy, etc. [1]. While relevant semiconductor SLM lasers are long time in use, an advanced fiber SLM lasers are still at the stage of investigation as prospective devices. They have an advantage to be inherently in-fiber devices permitting realization of all-fiber construction. Though contemporary fiber lasers are successfully substituting bulky semiconductor and solid-state lasers in different applications, however there is still strong requirement in robust and cheep SLM fiber lasers [1].

SLM fiber lasers operate with only one longitudinal-mode permitting emission of quasi-monochromatic radiation of a very narrow linewidth and low noise. Appropriate structures are distributed feedback (DFB) fiber lasers and distributed Bragg reflector (DBR) fiber lasers.

DFB fiber lasers are structures where periodical modulation of permittivity is imprinted within a piece of fiber (called fiber Bragg grating (FBG)) while possessing a gain [2]. These lasers possess a robust single longitudinal-mode operation, but they are complex in preparation since require high doping concentration in active fiber to achieve enough gain for overcoming losses in the cavity and maintaining the lasing action. Inherent restrictions of FBG lengths bring to the output power limitation as well.

Their counterparts are DBR fiber lasers which are free from the length restriction of an amplifying fiber, that permit to use active fibers with modest and low dopant concentration [1, 3]. DBR fiber lasers consist of an amplifying fiber between two FBGs at it ends, serving as resonant mirrors (Fig.1).
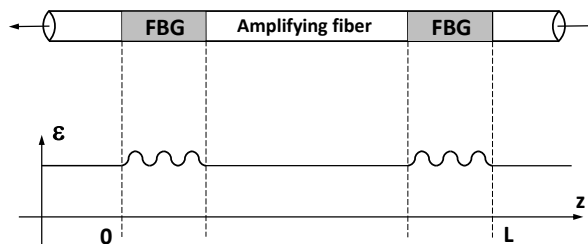
Fig. 1. Schematic of DBR fiber laser.

DBR fiber laser is comparatively easy to build, but there is a disadvantage of non-stable single longitudinal-mode operation, that is observed as a mode hopping. Mode hopping is the phenomenon of sudden jumps of radiating frequency. To reach the single-frequency lasing, the length of an active medium (amplifying fiber) should be determined correctly by taking into account field penetration in FBG mirrors, which are inseparable parts of the lasing structure. Previously relevant analytical analysis has been done in

[3]. However, there no well-defined conditions of single-frequency radiation have been presented. In this connection precise wavelength-scale electromagnetic analysis is pertinent.

In the presented work the conditions of single longitudinal-mode radiation from DBR fiber laser are obtained via correct numerical simulation by the method of single expression (MSE) [4 - 6]. Here the backbone of the MSE for wave normal incidence on a modulated structure is presented. From Maxwell's equations in 1D case the following Helmholtz equation can be obtained for linearly polarized complex electric field component $\dot{E}_x(z)$:

$$\frac{d^2\dot{E}_x(z)}{dz^2} + k_0^2\widetilde{\varepsilon}(z)\dot{E}_x(z) = 0, \tag{1}$$

where $k_0 = \omega/c$ is the free space propagation constant, $\widetilde{\varepsilon}(z) = \varepsilon'(z) + j\varepsilon''(z)$ is the complex permittivity of a medium. The essence of the MSE is presentation of a general solution of Helmholtz equation for electric field component $\dot{E}_x(z)$ in the special form of a single expression:

$$\dot{E}_x(z) = U(z)\cdot\exp(-jS(z)) \tag{2}$$

instead of the traditional presentation as a sum of counter-propagating waves. Here U(z) and S(z) are real quantities describing the resulting electric field amplitude and phase, respectively. Time dependence $\exp(j\omega t)$ is assumed but suppressed throughout the analysis. Solution in the form (2) prevails upon the traditional approach of counter-propagating waves and is more general because it is not relied on the superposition principle. This form of solution describes all possible distributions in space of electric field amplitude, corresponding to standing, propagating or evanescent waves in a medium of negative permittivity. It means that no preliminary assumptions concerning the Helmholtz equation's solution in different media are needed in the MSE. This gives advantages in investigation of wave interaction with any longitudinally non-uniform linear and intensity dependent non-linear media with the same ease and exactness.

II. Numerical Simulations of Optical Characteristics of DBR Fiber Laser

In the current work the structure of DBR fiber laser consisting of two uniform sinusoidally modulated FBGs with the length of L_{FBG} separated by an amplifying fiber of the length L_{Spacer} is considered (Fig. 2a). A permittivity profile of each uniform FBG is represented in Fig. 2b.

a)   b)
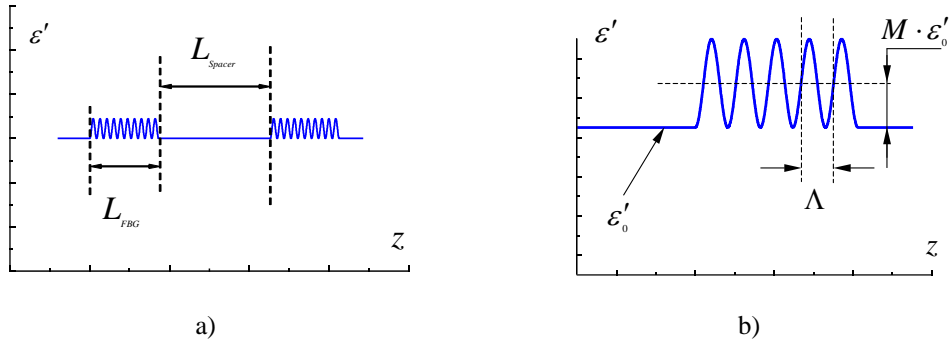
Fig. 2. Typical permittivity profile of DBR fiber laser a), permittivity profile of a uniform FBG with modulation period Λ and modulation amplitude $M\cdot\varepsilon_0'$ b).

The permittivity variation in FBG is assumed above the permittivity of fiber ε_0' on the value $M\cdot\varepsilon_0'$. In this case modulation of permittivity in FBG is described as:

$$\varepsilon'_{FBG}(z) = \varepsilon_0'\cdot(1 + M + M\cdot\cos(2\pi\frac{z}{\Lambda})), \tag{3}$$

where $\Lambda = \dfrac{\lambda_{0Br}}{2\sqrt{\varepsilon_0' + M\cdot\varepsilon_0'}}$ is the period of permittivity modulation, λ_{0Br} is the central wavelength, called Bragg wavelength, where the maximal reflectance of FBG is observed. For certainty we considered

4

the FBG with modulation coefficient $M = 0.1$, $\varepsilon_0' = 2.25$, $\varepsilon_0'' = 0$, number of periods in FBG $N = 30$, Bragg wavelength $\lambda_{0Br} = 1300$ nm. At this value of Bragg wavelength the modulation period is $\Lambda = 433.33$ nm and the length of FBG is $L_{FBG} = 12395.01$ nm.

Consideration of spectral characteristics of DBR fiber laser's structure is pertinent to start from the analysis of its transmittance dependence on the distance between FBGs (so called spacer) at the Bragg wavelength $\lambda_{0Br} = 1300$ nm at the absence of loss or gain in the structure (for "cold" resonator) (Fig. 3).
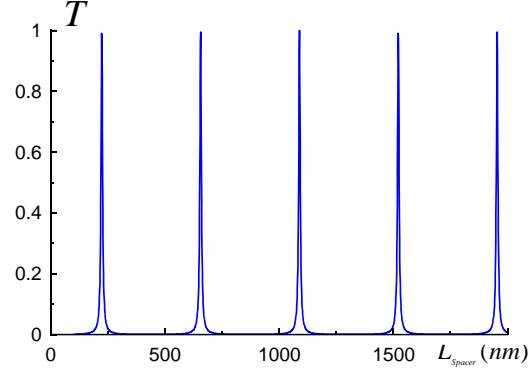
Fig. 3. Transmittance of FBG-spacer-FBG structure on the length of the spacer at $\lambda_0 = \lambda_{0Br} = 1300$ nm.

As it follows from the numerical analysis by the MSE resonant full transmissions are observed at the specific lengths of the spacer L_{Spacer}:

$$L_{Spacer} = \frac{\lambda_{0Br}}{3.9\sqrt{\varepsilon_{Spacer}}} + \frac{\lambda_{0Br}}{2\sqrt{\varepsilon_{Spacer}}} \cdot m, \quad m = 0,1,2,3.... \qquad (4)$$

These lengths of the spacer are resonant meaning, that at these lengths the single-frequency radiation is possible since full transmission of the structure is favourable for light amplification. This assertion is confirmed by the numerical simulations presented below.

Numerical modelling has been done for different resonant lengths of the spacer (4), initially for the "cold" resonator (without amplification in the spacer). For certainty at the resonant spacer length $L_{FBG} < L_{spacer} < 2L_{FBG}$ three narrow transmission peaks within the low transmission band are observed (Fig. 4a).

a)

b)
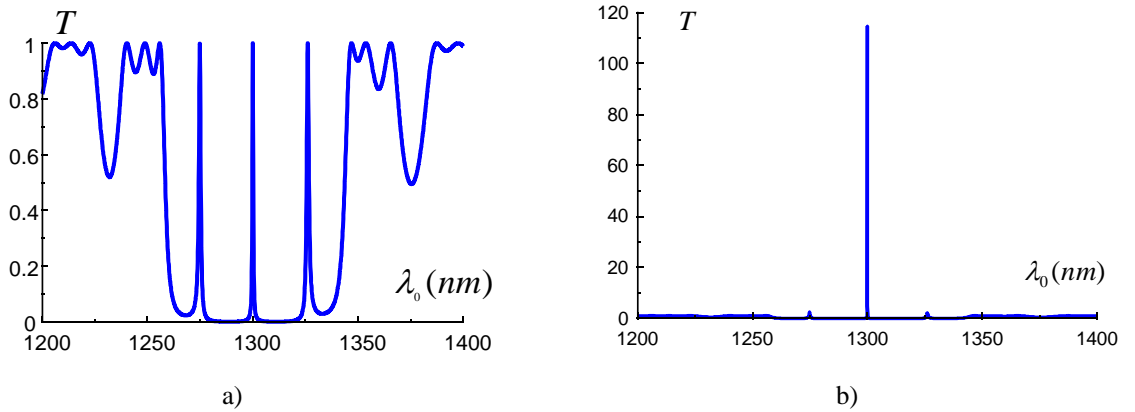
Fig. 4. Transmission spectra of FBG-spacer-FBG structure of the resonant spacer length $L_{FBG} < L_{spacer} < 2L_{FBG}$ without amplification in the spacer ($\varepsilon_{spacer}'' = 0$) a), and at amplification in the spacer ($\varepsilon_{spacer}'' = 0.001$) b). $L_{FBG} = 12395$ nm, $L_{spacer} = 15389$ nm.

It is worth to note, that the low transmission band of FBG-spacer-FBG structure coincides with the

relevant width of forbidden band-gap of single FBG. By inclusion of amplification in the spacer an essential increase of the transmittance above unity takes place only for the central peak at the Bragg wavelength $\lambda_0 = \lambda_{0Br} = 1300$ nm (Fig. 4b).

By further increase of the spacer's length additional peaks are observed within the same low transmission band and at some value of amplification again only one peak is observed at the resonant length of the spacer satisfying the condition (4) at $\lambda_0 = \lambda_{0Br} = 1300$ nm. At this wavelength high value, essentially greater than unity for the reflectance and transmittance are obtained at the modest value of amplification that is a clear indication of laser radiation from the structure [7].

III. CONCLUSIONS

For single longitudinal-mode lasing of DBR fiber laser the length of an amplifying fiber is determined correctly via wavelength-scale electromagnetic modelling by the MSE. As it follows from numerical simulation, at the increase of the length of the spacer an increase of the number of peaks in low transmission band is observed. By inclusion of amplification in the spacer only one radiating peak is survived at $\lambda_0 = \lambda_{0Br}$ for the resonant lengths of the spacer by satisfying the condition (4).

Thus, by the proper choice of the length of the amplifying fiber spacer it is possible to have a stable single longitudinal-mode radiation from the structure of DBR fiber laser.

ACKNOWLEDGEMENTS

IV. REFERENCES

[1]   W. Shi., "Single-frequency fiber lasers using rare-earth-doped silica" SPIE Newsroom. DOI: 10.1117/2.1201506.005740, 25 June 2015.
[2]   B. Yin et al., "Single-Frequency and Single-Polarization DFB Fiber Laser Based on Tapered FBG and Self-Injection Locking", IEEE Photonics Journal, vol. 7, No. 3, June 2015.
[3]   Y.O. Barmenkov et.al., "Effective length of short Fabry-Perot cavity formed by uniform fiber Bragg gratings", Optics Express, vol. 14, No. 14, pp. 6394 – 6399, 10 July 2006.
[4]   H.V. Baghdasaryan, "Method of backward calculation, in the book: Photonic Devices for Telecommunications: how to model and measure", Editor G. Guekos, Springer-Verlag, pp.56-65, 1999.
[5]   H.V. Baghdasaryan, T.M. Knyazyan, "Modelling of strongly nonlinear sinusoidal Bragg gratings by the Method of Single Expression" Optical and Quantum Electronics, vol. 32 (6/8), pp. 869-883, 2000.
[6]   H.V. Baghdasaryan, "Basics of the Method of Single Expression: New Approach for Solving Boundary Problems in Classical Electrodynamics", Monograph: Chartaraget, Yerevan, 164 pages, 2013.
[7]   A.Yariv, P. Yeh, "Photonics/Optical Electronics in Modern Communication", Oxford University Press. Sixth Edition. 2007. Page 239.

Slot Nano-Antenna Integrated with Plasmonic Waveguide

H. Haroyan

Yerevan State University, Yerevan, Armenia

Plasmonic slot nano-antenna coupled with plasmonic waveguide is considered. Different types (monopole, C-shape) of plasmonic slot-nanoantenas are investigated, as well as numerical investigations of 3D structures based on finite element method (FEM) are realized. The conditions of maximal efficiency coupling between antenna and waveguide are clarified. In order to obtain maximal radiation the optimal sizes of slot antennas have been estimated. The radiation patterns of different antennas configurations are obtained based on numerical calculations. The possibility of slot antenna far-field pattern radiation shape tuning by varying orientation of slot relative to SPP propagation direction in waveguide is demonstrated.

I. INTRODUCTION

Optical antennas, analogues of microwave antennas, are a new concept in physical optics which enable technology for manipulating optical radiation at subwavelength scales [1,2]. Traditionally, in the field of optics and photonics light is commonly controlled by using elements such as mirrors, lenses, fibers and diffractive elements. Such type of manipulation relies on the wave nature of electromagnetic field and does not provide an ability to control the light on the subwavelength scales. On the other hand, in the radiowave and microwave regime, using antennas of various designs to control electromagnetic fields on the subwavelength dimensions is a well-established technique. From this point of view, the optical analogues of radiofrequency (RF) antennas can overcome the challenges of light subwavelength control and help surpass the diffraction limit, making it possible to manipulate, control, and visualize optical fields on nanometer scale.

Good approach to confine electromagnetic energy has been to take advantage of surface Plasmon polaritons (SPP). The SPP is quasi-two-dimensional electromagnetic excitations, propagating along a dielectric–metal interface and having the field components decaying exponentially into both neighboring media [3,4] offering the possibility of realizing subwavelength confinement.

The objective of optical antenna design is equivalent to that of classical antenna design: to optimize the energy transfer between a localized source or receiver and the free-radiation field [5]. So the optical antenna could be defined as a device to efficiently convert free-propagating optical radiation to localized energy, and vice versa [6]. Theory of optical antennas is generally developed in the analogy of their RF counterparts. But it should be noted that it is not the directly extension of RF antenna theory on the optical counterparts, due to the crucial differences in their physical properties and scaling behavior. Most of these dissimilarities appear because metals are not perfect conductors at optical frequencies.

As the slot-type antenna can be combined with any plasmonic components made on a metallic plane easily, we expect that the slot nano-antenna will be integrated further with other plasmonic devices and play an important role in plasmonic integrated nano-circuits in the future. Various types of optical antennas (gap antennas, Yagi-Uda antenna, bowtie, etc.) have been designed, and their scattering and directivity features are investigated [7,8]. Recently the theory for optical wired antennas was developed in [9], according it an additional electrical field is appears in the wire due to imperfect conductivity of metal. Based on Babinet's principle by applying $E \leftrightarrow H$, $Z \rightarrow -1/Z$ interchanges (see ref. [10]) radiated field distributions we can find a solution for slot antenna as well.

By summarizing above mentioned features of considered structure the main advantages of plasmonic slot nano-antennas can be stated as follows:

- Slot antenna has high potential for integration and combination with other plasmonic components.
- High signal to noise ratio due to metal layer blocking of incident light.
- Vertical radiation of lateral SPP modes.
- Slot antenna can act as "plasmonic via" in nanophotonic circuits composed of several layers.

In this paper different types (monopole, dipole, C-shape) of plasmonic slot-nanoantenas integrated with plasmonic waveguides are investigated, as well as numerical investigation of 3D structures based on finite element method (FEM) is realized.

Let's consider the structure of plasmonic slot antenna integrated with waveguide (see Figure 1). To realize the plasmonic waveguide the metal-dielectric-metal triple layer structure is taken. As a dielectric sandwiched between two metal layers the air is considered with dielectric permittivity: $\varepsilon_{air}=1$. As the metal material silver is used with $\varepsilon_m=-23.06+0.394i$ dielectric permittivity at the wavelength $\lambda=700$ nm. For SPP excitation method the well-known Kretschmann method is applied.
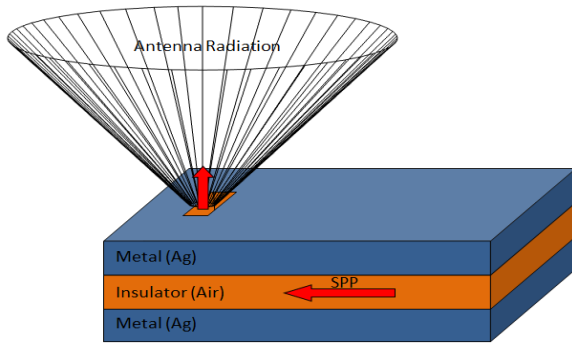
Figure 1. Schematic view of slot nano- antenna radiation coupled with plasmonic waveguide.
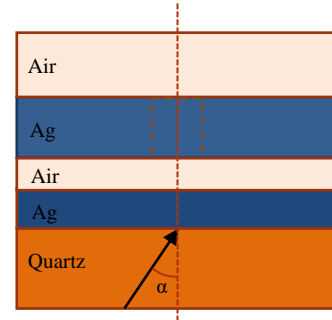
Figure 2. Shematic view of strucuture layers.

For effective SPP excitation a quartz substrate is used with dielectric permittivity: $\varepsilon_d=2.5$. It is worth to mention that SPP excitation and further propagation in metal-dielectric-metal plane waveguide is quite sensitive to the incident angle α of electromagnetic field onto the bottom metal layer (see Figure 2). To find the optimal incident angle from point of view SPP excitation the 3D simulation model has been built. As the measure of SPP excitation the reflectance from metal layer has been chosen. The smaller reflectance, the higher penetration rate into the metal layer and hence the more effective SPP excitation. To achieve the effective SPP excitation the thicknesses of bottom metal layer has been taken about $\lambda/10$.
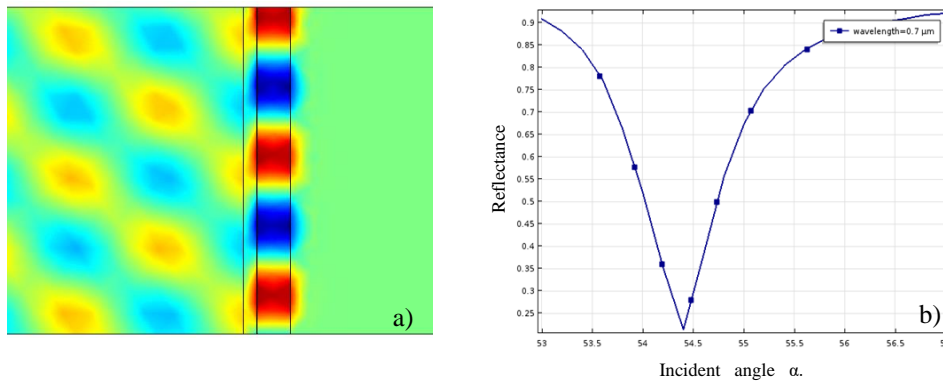
Figure 3. a) Electric field pattern at the optimal incident angle then SPP is excited between two metal layers. b) Reflectance vs. incident angle α.

As we can see from Figure 3.b) the optimal incident angle is $\alpha=54.4^o$ which brings to the effective SPP excitation and propagation mode formation in planar SPP waveguide (see Figure 3.a).

III.   SIMULATION RESULTS AND DISCUSSIONS

After SPP excitation in waveguide the monopole slot antenna has been milled in the second- upper metal layer. In order to clarify the orientation of slot relative to SPP propagation direction in waveguide the second stage of modeling has been carried out.

The results of simulations are presented in Figure 4. From Figure 4 follows that maximal coupling between slot antenna and waveguide is realized then θ=90°, which means that for effective coupling slot should be milled in perpendicular direction of SPP propagation.
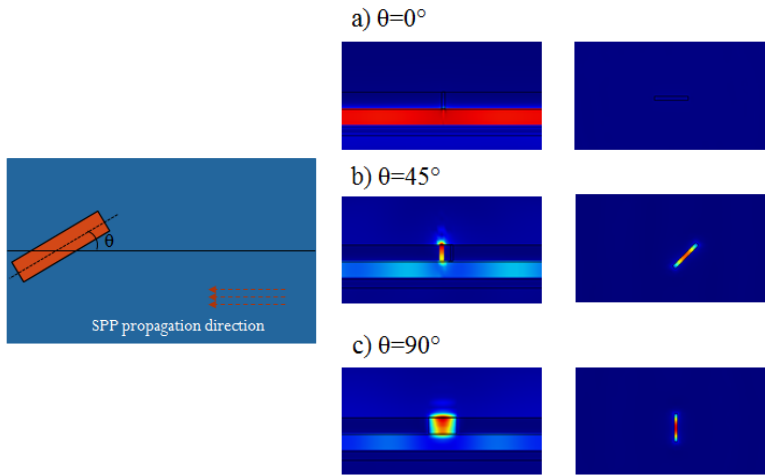
Figure 4. Electric field view for different slot orientation a) θ=0°, b) θ=45°, c) θ=90°, and schematic top view of structure.

From RF antenna theory, it is well known the relation between working wavelengths and antenna sizes. One example is the half-wave dipole antenna which length is equal to a half-wavelength at the frequency of operation. The half-wave dipole antenna has a resonance at the wavelength equal to double length of dipole, hence the impedance matching condition is the best at this wavelength. Keeping in mind this fact, by the same way we investigate the radiation efficiency dependence on slot length for slot nano-antenna. The simulation results for different wavelengths (λ=700,800 and 1000 nm) show that radiation efficiency has a resonant like behavior regarding to gap length (see Figure 5.a)). It is important to mention that maximum of radiation efficiency corresponds to the gap size equal to the quarter of working wavelength: $d_x= λ/4$. This result is in good agreement with conventional RF antenna theory. The same results have been obtained for dipole slot antenna, but here $d_x = λ/4$ is only one length of dipole hence the overall size of dipole slot is equal to half of the operating wavelength.
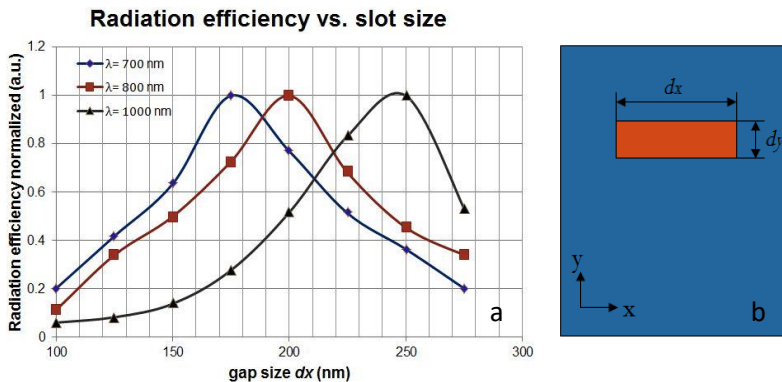
Figure 5. a) Radiation efficiency vs. slot size. b) Schematic top view of slot monopole antenna.

Finally, far-field radiation patterns for plasmonic slot antennas have been obtained. The obtained results for far-field pattern again well corresponds to their RF counterparts. It should be noted that far-field pattern shape depends on slot orientation. In the non perpendicular case of slot and SPP propagation direction we can see pronounced side lobe, moreover this side lobe arises in direction strictly corresponding to the angle between slot and SPP propagation direction (see Figure 6). This fact opens up possibility of radiation pattern shape tuning by varying orientation of slot relative to SPP propagation direction in waveguide.

From the point of view of obtaining the circular polarization it is interesting to consider C-shape slot antenna. The numerical investigations show that the far-field radiation pattern strongly depends on the size d of the gap between edges of C-shape (see Figure 7). Here the internal r and external R radii of C-shape have been chosen according to the following relation: L=2π(R+r)/2≈λ. This condition is also well known from RF antenna theory, which corresponds to the maximum radiation efficiency. In our case R=120 nm, r=100nm at λ=700 nm.

a) θ=90°

b) θ=+45°

c) θ=-45°

Figure 6. Electric field distribution near the monopole slot antenna and far-field pattern for slot's different orientations a) θ=90°, b) θ=+45°, c) θ=45°.

a) Annual slot antenna d=0 nm

b) C-shape slot antenna d=50 nm

c) C-shape slot antenna d=150 nm
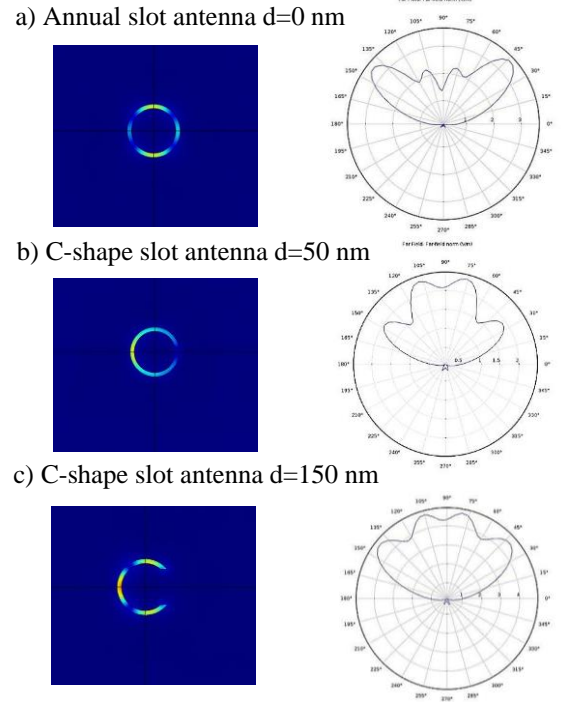
Figure 7. Electric field distribution near the C shape slot antenna and far-field pattern for slot's different shapes a) d=0 nm, b) d=50 nm, c) d=150 nm.

From Figure 7 follows that the larger the gap size d between C-shape edges the smother the top of the far-field radiation pattern. As it is expected in the case of annual slot (d=0), the radiation in perpendicular direction is minimal (see Figure 7. a)).

IV. CONCLUSION

By summarizing, we can conclude what in this work different types of plasmonic slot nano-antennas have been investigated. The advantages of slot type plasmonic antennas have been pointed out. Optimal conditions for efficiently coupling of antenna and waveguide have been clarified. In order to obtain maximal radiation efficiency the optimal sizes of slot antennas have been estimated. Far-field radiation patterns of various types (monopole and C-shape) of plasmonic slot nano-antennas have been presented. The possibility of slot antenna far-field pattern radiation shape tuning by varying orientation of slot relative to SPP propagation direction in waveguide has been shown.

V. REFERENCES

[1]. P. Bharadwaj, B. Deutsch, L.Novotny,"Optical Antennas", Adv. Opt. Photon 1, pp. 438-483, 2009.
[2]. T. H. Taminiau, F.D.Stefani, N. F. van Hulst, "Enhanced directional excitation and emission of single emitters by a nano-optical Yagi-Uda antenna"Opt. Express 16, pp. 10858-10866, 2008.
[3]. H. Raether, Surface Plasmons, Springer, 1998.
[4]. W. Barnes, A.Dereux, T. Ebbesen, review article Surface plasmon subwavelength optics", Nature, 424, pp.824-830, 2003.
[5]. L. Novotny and N. van Hulst, "Antennas for light", Nature Photonics, vol. 5, pp.83-90, 2011.
[6]. B. Hecht et. all, Elsevier, p. 275, 2007.
[7]. J. Alda, J. Rico-Garcia, J. Lopes-Alonso, G. Boreman,"Optical antennas for nano-photonic applications", Nanotechnology vol. 16, pp.S230-S234, 2005.
[8]. F. Gonzalez, and G. Boreman, Infrared Phys. Technol., vol. 146, , p.418, 2004.
[9]. J. Dorfmuller, R. Vogelgesang, W. Khunsin, et al." Plasmonic nanowire antennas: experiment, simulation, and theory", Nano Lett. 10, pp. 3596-3603, 2010.
[10]. S. Orfandis, "Electromagnetic Waves and Antennas", NJ 2008.

Detecting of complex modulated optical signals
and optical modulation analysis
for gigabit and terabit transmission lines

V. Morarenko

Keysight Technologies, Moscow, Russia

In on/off keying (OOK), we are able to detect the signal simply with a photodiode, which converts the optical power into an electrical current I_{Photo}. However, the result only contains the amplitude (Fig. 1). I_{Photo} does not provide any information on the angular frequency ω_s and the phase φ_s. Thus, the QPSK signal in the time domain on the right side cannot be directly mapped to the IQ diagram on the left without ambiguity.
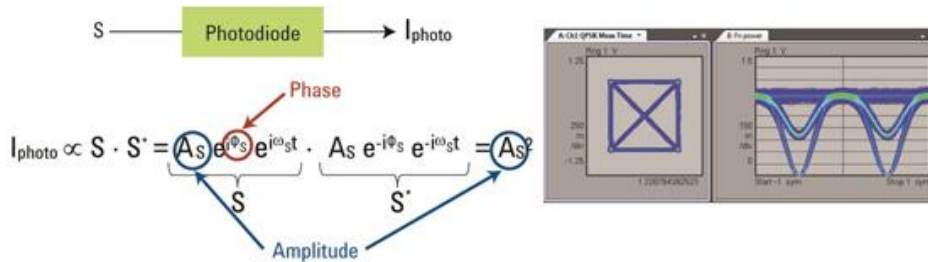
Fig. 1. In direct detection, the photo current I_{Photo} only provides information on the light amplitude.

The key to solve both problems lies in measuring not the absolute phase but the phase relative to a known reference signal. The ideally monochromatic laser that produces the reference signal R is often referred to as the "local oscillator". Also we can suppress all other phase-independent terms with a balanced receiver. Here, the signal to be detected S and the reference signal R are summed on one branch and subtracted on the second branch of a 2x2 optical combiner (which could be a fiber optical or free-space optical coupler). Each of the resulting signals is detected by one photodiode. The difference between the two photocurrents is then used.

To recover both amplitude and phase, a coherent receiver should provide the in-phase (I) component and the quadrature (Q) component as two separate output signals. For this purpose, we need a second balanced detector. A single local oscillator provides the reference signal for both of them but the phase must be shifted by $\pi/2$ to obtain the Q part. Figure 2 gives, for the case of a QPSK signal, an idea of the whole setup, which is called an "IQ demodulator".
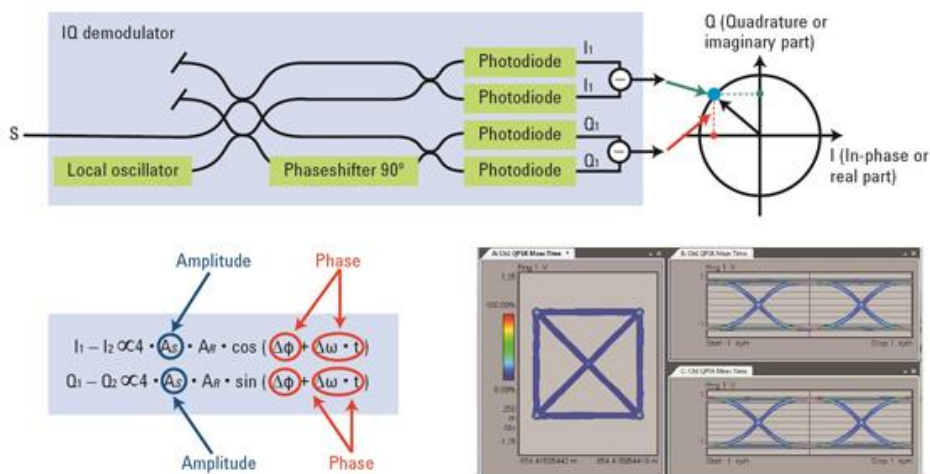
Fig. 2. IQ demodulator providing two independent measurements that both contain information
on amplitude and phase.

For dual polarization, we have to further develop the demodulator concept. The basic principle stays the same: after a polarization splitter, we now have two IQ demodulators, one for the *x*-polarization and the other one for the *y*-polarization. Only one local oscillator provides the reference signals for all branches.

Then, with **real-time sampling,** we can reconstruct the complete signal in all domains and without limitations regarding the modulation format. Neither do we face any limitations regarding signal length in heterodyne time-domain detection. PMD and CD can be compensated during signal processing. In this case, only the signal processing is the throughput limiting factor. At the same time, we have to be aware that we need four-channel high-speed equipment for this approach, such as a high-performance real-time digitizer with very low jitter and noise and a high effective number of bits (ENOB) over the whole frequency range.

SOLUTION

Unlike the high-speed optical networks of the past, where modulating an optical wave's amplitude on and off at high-rates was sufficient, today's optical links are following the wireless industry's lead to high order modulation formats. Complex modulation formats extend beyond on-off keying by encoding communication symbols with both amplitude and phase information. The Keysight's N4391A optical modulation analyzer (Fig. 3) is optimized for analysis of these kinds of new optical modulation formats. It supports transmission rates of 40/100 G and beyond. The N4391A is the ideal instrument for advanced research on higher than 112 Gbit/s transmission speeds. For example, if two N4391A are combined together, it will be possible to achieve a 126 GHz frequency span and analyze terabit signals.

Characterization of the signal quality of a vector modulated signal right at the transmitter output or along the link is the core application of this kind of instrument. Most important analysis and measurement tools are:

- Optical constellation diagram
- Error vector magnitude (EVM)
- Phase error
- BER, BER(EVM)
- CD, 1st order PMD compensation and measurement
- Quadrature error
- IQ imbalance
- IQ offset
- Frequency offset
- Symbol rate detection and tracking
- Laser line width
- Polarization of analyzed symbols
- Support of more than 30 modulation formats
- Adaptive equalization
- Custom OFDM and APSK demodulator available
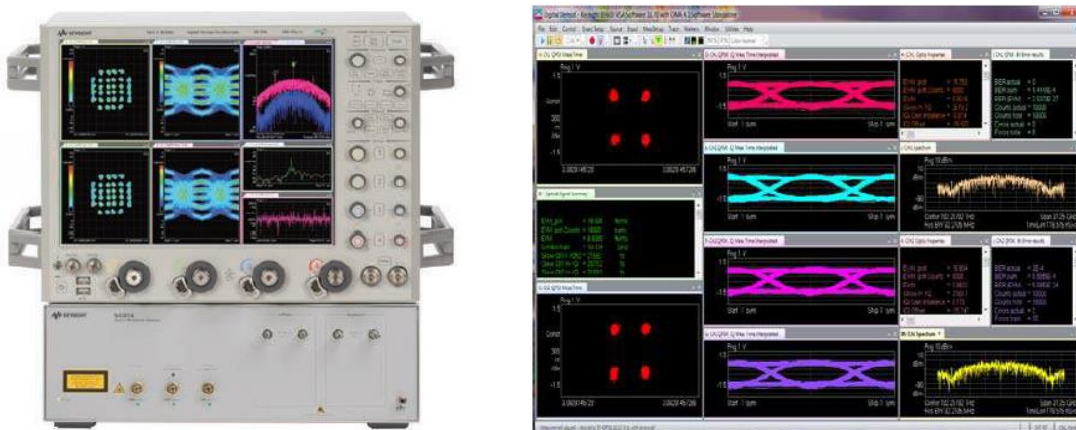
Fig. 3. The N4391A and its default screen layout

REFERENCES

1. S. Michel. How to detect complex modulated optical signals. Lightwave magazine. April, 2014.
2. Block diagram from "OIF Implementation Agreement for Integrated Dual Polarization Intradyne Coherent Receivers."
3. Lightwave Catalog Volume 2: Optical-Electrical / Polarization / Complex Modulation. Keysight Technologies, Inc. 2015. Published in USA.

Defining a Channel Sounding Measurement System
for Characterization of 5G Air Interfaces

Maksim Sokovishin

Keysight Technologies, Moscow, Russia

With its aggressive performance goals, the emerging 5G standard will almost certainly incorporate a combination of millimeter-wave (mmWave) frequencies, ultra-broad bandwidths and massive multiple-input/multiple-output (MIMO) methods. Although each of these adds difficulty to the design of transmitters and receivers, the most significant unknowns are in the over-the-air radio channels between user equipment (UE) and base station (BS). To fully characterize the channel (see figure 1), it is necessary to create mathematical models of channel performance and use them to define new air interface standards for 5G.
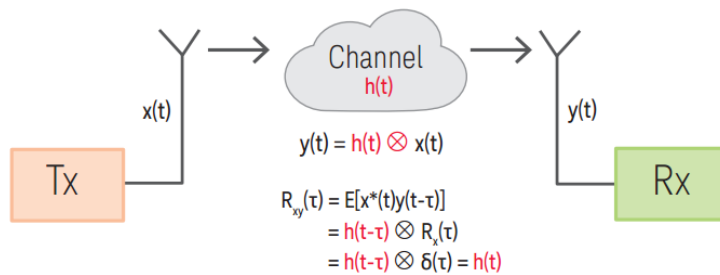
Fig. 1. Approximate mathematical model of the RF radio channel

Drawing from the preceding comparisons, Keysight's preferred approach uses wideband correlation as the baseband sounding technique and switched-transmit/parallel-receive for assessing MIMO data capture. could increase the total measurement speed with minimal cross-channel interference. Figure 2 illustrates the basic architecture. On the left, the transmitter side includes a single-channel wideband signal generator and mmWave switch. On the right, the receiver side provides parallel signal acquisition with a wideband multi-channel receiver that can be implemented using high-performance digitizers or wideband vector signal analyzers.
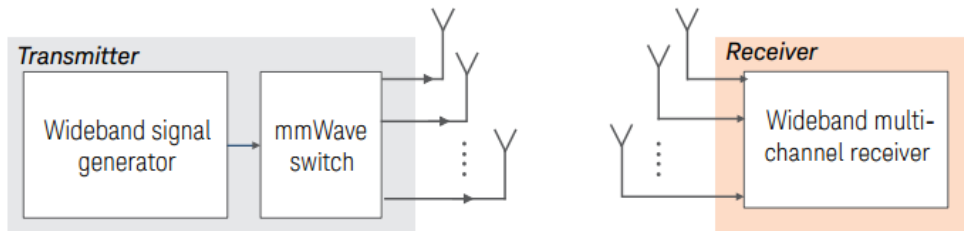
Fig. 2. The basic implementation of the switched-transmit/parallel-receive architecture

To achieve precise results, system synchronization and calibration are required. The channel sounding system must be capable of measuring and characterizing its own phase and amplitude impairments and compensating for the following issues: inter-channel phase errors, antenna errors in amplitude and phase, I/Q mismatch errors, spectral flatness errors.

The various channel parameter estimation algorithms can be categorized to 3 types: beamforming based, subspace based, maximum likelihood (ML) based algorithms. The beamforming based algorithms are simple with poor estimation performance. The subspace-based algorithms have good performance, but the maximum number of paths the algorithm can estimate is less than the number of receiving antennas, thus these algorithms cannot work well for more complex channel scenarios. The ML based algorithm (e.g. SAGE) is well accepted and widely used due to its high estimation precision and its capability of joint parameter estimator for multiple channel parameters, what's more, the maximum estimating path number is not limited by the number of antenna array elements. In general the setup based on the metrology grade equipment is shown on figure 3.
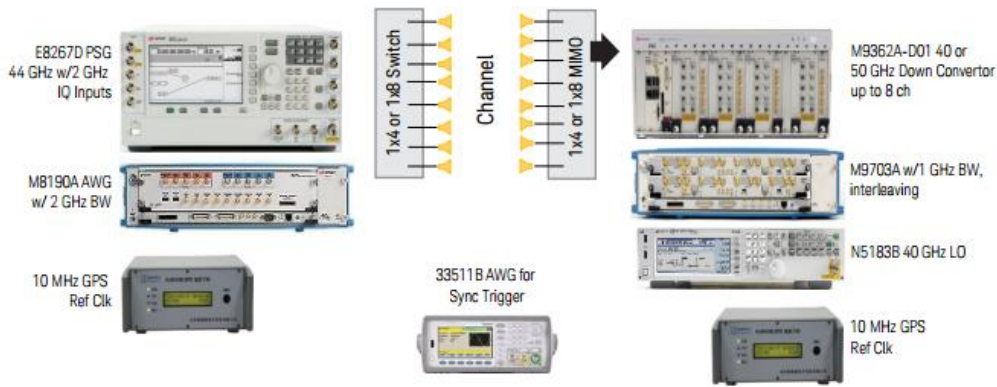
Fig. 3. Keysight 5G channel sounding reference solution
(the transmitter subsystem is on the left and the receiver subsystem is on the right)

By implementing real-time correlation processing in the digitizer's (M9703A) embedded FPGA, the resulting data compression enables storage into onboard memory. The captured CIR signals can be transferred in real time through the PCIe bus. Figure 4 shows an example screen from the SystemVue 5G verification library that is used to specify instrument configuration for CIR data capture and post processing of channel parameter estimations. Using those tools and the pictured system produced the channel parameter estimation results could be extracted and then processed with the SystemVue or separately.
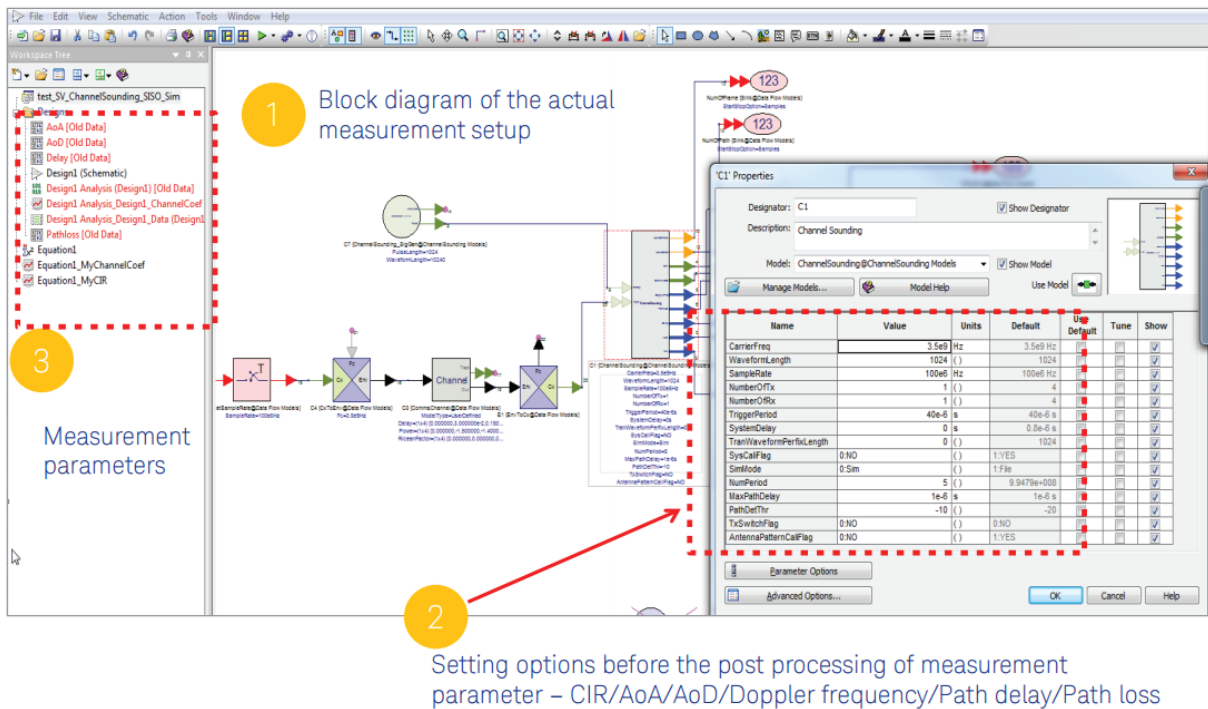
Fig. 4. Extraction of path loss, path delay profile, AoD, and AoA in SystemVue

Keysight's reference solution uses wideband correlation as the baseband sounding technique and switched-transmit/parallel-receive for MIMO data capture. This provides three important advantages: fast measurement speed, MIMO sounding capability and fully characterized high-level measurement performance.

References

1. Mark Pierpoint, Gabriel M. Rebeiz. Paving The Way For 5G Realization and mmWave Communication Systems. Microwave Journal. April, 2016.
2. Sangkyo Shin. The Communication System Architect's Guide to 5G Physical Layer Modeling. Keysight White Paper. December, 2015.

National Instruments technologies in 5G research and prototyping

Suren Eyramjyan

National Instruments AM LLC., Hovsep Emin 123, 0051, Yerevan, Armenia

National Instruments (NI) is collaborating with top researchers focused on wireless research, specifically 5G wireless communications. The graphical system design approach combines LabVIEW Communications System Design software with the software defined radio (SDR) platform to help researchers innovate faster. Using this approach, engineers can reduce the time from theory to results by testing their designs in a real-world environment. The company provides appropriate platform solutions for all modern vectors for 5G research, including Massive MIMO systems, mmWave band utilization, Physical Layer Enhancement (or New Waveforms) and Dense Wireless Networks.

I. Introduction

At NI we've identified 4 key vectors for 5G research – candidate technologies in need of prototyping to evaluate their viability in future wireless standards:
Massive MIMO and beamforming, mmWave, Phisical Layer (PHY) Enhancements (or New Waveforms), and Dense Wireless Networks (fig. 1.). At the original paper, we are going to introduce the research and prototyping works where NI technologies' used as main platform in each vector separately.
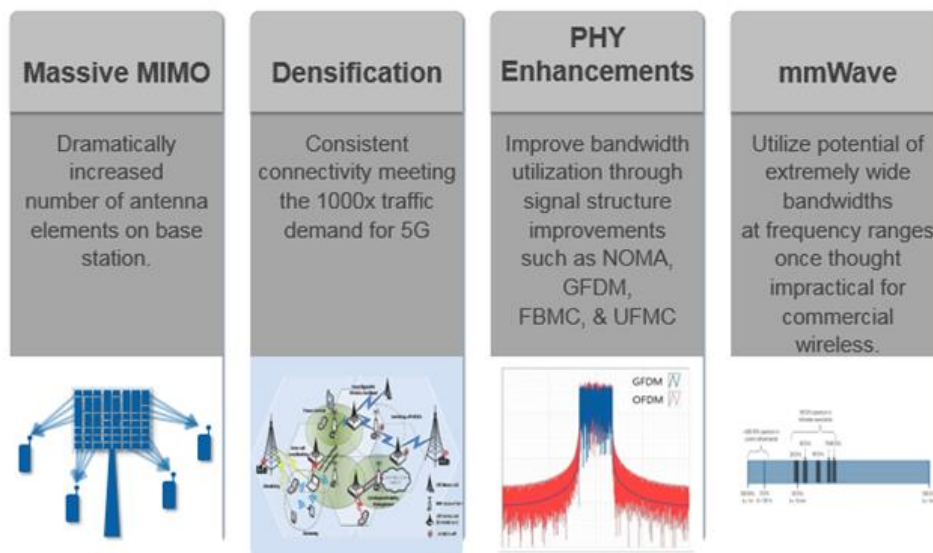
Fig. 1. The 5G research vectors

II. NI technologies for 5G Research in each vector

a) Massive MIMO

Massive MIMO is an exciting area of 5G wireless research. For next-generation wireless data networks, it promises significant gains that offer the ability to accommodate more users at higher data rates with better reliability while consuming less power. Using the NI Massive MIMO Software Architecture, researchers can build Massive MIMO testbeds to rapidly prototype large-scale antenna systems using award-winning LabVIEW

system design software and state-of-the-art NI USRP™ RIO software defined radios (SDRs). With a simplified design flow for creating FPGA-based logic and streamlined deployment for high-performance processing, researchers in this field can meet the demands of prototyping these highly complex systems with a unified hardware and software design flow [1].

Outlined below is a complete Massive MIMO prototyping system. It includes the hardware and software needed to build the world's most versatile, flexible, and scalable Massive MIMO testbed capable of real-time, two-way communication over bands and bandwidths of interest to the research community. With NI software defined radios (SDRs) and LabVIEW system design software, the modular nature of the MIMO system allows for scaling from only a few antennas to a 128-antenna Massive MIMO system (fig. 2.). With the flexible hardware, it can be redeployed in other configurations as wireless research needs evolve over time, such as as distributed nodes in an ad-hoc network, or as multi-cell coordinated networks [1].

Fig. 2. One of the World's First Real-Time Massive MIMO Testbeds - Created at Lund University Using the Massive MIMO prototyping system [2]

b) Physical Layers Enhancement

The proliferation of smart devices has led to a wireless spectrum shortage, which means researchers are seeking new ways to alleviate the bandwidth crunch and increase network data capacity. Market analysts predict that spectrum demand in the U.S. will outstrip capacity by 2017 [3].

Through the RF/Communications Lead User program, NI works with leading research institutions around the world to address network capacity concerns [3].

One of these institutions was a TU Dresden. TU Dresden joined the RF/Communications Lead User program in 2011 and demonstrated a fully functional generalized frequency division multiplexing (GFDM) [4, 5] prototype at NIWeek 2013 in Austin, Texas. Many of their ideas are rapidly prototyped on the USRP platform, such as GFDM as a upgrade to OFDM and postdistortion techniques to mitigate the effects of dirty power amplifiers, as a first proof of concept and then moved to PXI for higher performance real-time processing that is needed for live demonstration and algorithm validation (fig. 3).
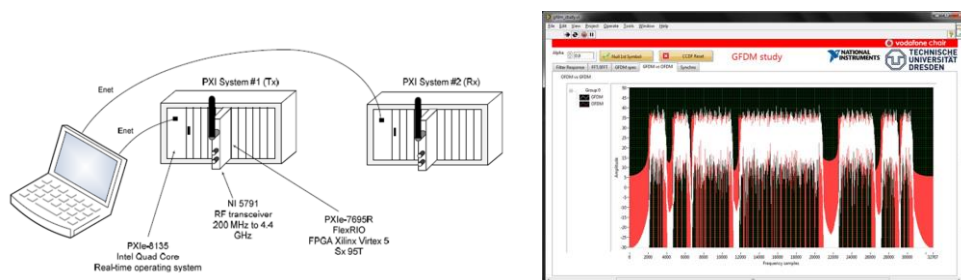
Fig. 3. GFDM Testbed and Software interface with GFDMand OFDM Waveforms

c) mmWave

Service operators around the world have paid billions of dollars for spectrum to service their customers. The exorbitant auction prices for spectrum below 6 GHz highlights the strength of the competitive market forces but also the scarcity of this precious resource. As stated above, enhanced data rates and increased capacity are constrained by spectrum according to Shannon. More spectrum yields higher data rates, which enable service operators to accommodate more users while also delivering a consistent mobile broadband data experience. In contrast, mmWave spectrum is plentiful and lightly licensed, meaning it is accessible to service operators around the world. The challenges impacting mmWave adoption lie primarily in the unanswered technical questions regarding this unexplored and largely uninvestigated spectrum [6].

The mmWave Transceiver System is an SDR platform for building mmWave applications including system prototyping. It gives users access to a flexible hardware platform and application software that enables real-time over the air mmWave communications research. The software is open to the user and can be modified as research needs change so designed can be iterated and optimized to meet specific goals or objectives [6].

The NI mmWave platform were used by researchers and scientists to do mmWave band channel sounding [7] as well as achieve data rates up to 14Gbps [8]. In fig. 4 demonstrated the baseband prototype system for mmWave investigation.

Fig. 4. Baseband prototype system for mmWave investigation with 1GHz real-time bandwidth

d) Dense Wireless Networks

Next-generation wireless networks (5G) cope with significant traffic increase because of high-quality video transmission and cloud-based applications. This creates the need for a revolutionary change in architecture rather than a series of local and incremental technology updates. A dense heterogeneous deployment of small cells such as pico/femto cells in addition to high-power macro cells is a potential solution. In this area, a significant amount of research relies on simulations at PHY, MAC, and higher layers, but it is still necessary to validate the algorithms for next-generation systems in a real-time testbed. The ever-increasing complexity in all layers of current and future generations of cellular wireless systems, however, has made an end-to-end demonstration of the network limited to industrial research labs or large academic institutions. As a solution to tame the dense deployment of wireless networks, we propose an NI PXI platform based on NI LabVIEW software in which an LTE-like SISO OFDM PHY layer is integrated with an open-source protocol stack to prototype PHY/MAC cross layer algorithms within a CROWD (Connectivity management for eneRgy Optimised Wireless Dense networks) software-defined networking (SDN) framework [9].

Figure 5 shows the general overview of the testbed architecture. The functions of the MAC and higher layer

protocols (including CROWD Local Controller) run on a Linux computer. The protocol stack communicates with the PHY layer running on the NI PXI system over Ethernet using an L1-L2 API that is based on a small cell forum API [11]. We have implemented the complex high-throughput baseband signal processing for an "LTE-like" OFDM transceiver for the eNB and UE in LabVIEW FPGA using several NI FlexRIO FPGA modules because of the high-throughput requirements. We use the NI 5791 adapter module for NI FlexRIO as the RF transceiver. This module has continuous frequency coverage from 200 MHz to 4.4 GHz and 100 MHz of instantaneous bandwidth on both TX and RX chains. It features a single-stage, direct conversion architecture, which povides high bandwidth in the small form factor of an NI FlexRIO adapter module.
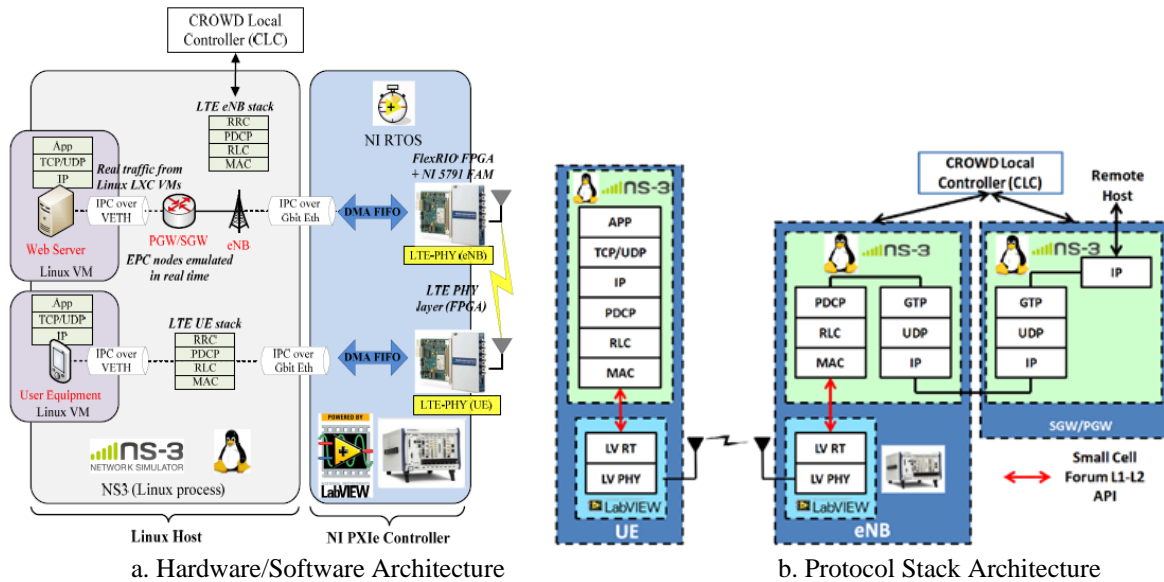
a. Hardware/Software Architecture   b. Protocol Stack Architecture
Fig. 5. General overview of the testbed architecture

III. REFERENCES

[1] http://www.ni.com/white-paper/52382/en/
[2] Larsson, E.; Edfors, O.; Tufvesson, F.; Marzetta, T., "Massive MIMO for next generation wireless systems," in Communications Magazine, IEEE , vol.52, no.2, pp.186-195, February 2014.
[3] http://www.ni.com/newsroom/release/national-instruments-lead-user-program-paving-the-way-for-5g-wireless/en/
[4] N. Michailow, M. Matthé, I. Gaspar, A. Caldevilla, L. Mendes,A. Festag and G. Fettweis, "Generalized Frequency Division Multiplexing for 5th Generation Cellular Networks," IEEE Transactions on Communications, vol. 62, no. 9, pp. 3045–3061, 2014.
[5] http://www.microwavejournal.com/ext/resources/whitepapers/2012/december2012/TU-Dresden-uses-NI-Platform-for-5G-Research.pdf
[6] http://www.ni.com/white-paper/53095/en/
[7] http://wireless.engineering.nyu.edu/ThePulse/04/NYU-WIRELESS-at-NI-Week.php
[8] http://www.ni.com/white-paper/53096/en/
[9] http://www.ni.com/white-paper/52339/en/

Spectral Efficiency Improvement in Nonlinear Wireless Systems

H. Haroyan[1], G. Harutyunyan[2], T. Harutyunyan[1], S. Sargsyan[1,2]

[1] *Yerevan State University*, *Yerevan, Armenia*
[2] *"Antel Design" LLC, Yerevan, Armenia*

The improvement possibility of spectral efficiency (SE) in nonlinear wireless systems using time-frequency packing (TF-packing) technique is demonstrated. The new, not so much complicated calculation method of achievable spectral efficiency (ASE) based on bit error rate (BER) estimation is proposed. Calculation accuracy and working bounds of proposed method are clarified. It is shown that the ASE reaches its maximum value then time packing factor (TPF) is about 0.7. The calculated ASE for 16APSK modulation is about 5.5, which surpasses the maximum achievable value for orthogonal signaling by 1.5. For 32APSK modulation, the ASE at TPF≈0.7 exceeds the orthogonal signaling at least by 0.5.

I. Introduction

Nowadays the improvement of spectral efficiency (SE) in wireless systems is one of the most important problems. Traditional method, allowing to improve SE, is the increasing of modulation order. On the other hand, the higher the modulation order, the sensitive the modulated signal against nonlinearities. Another approach to increase the system effectiveness are techniques, allowing to improve the SE. Different methods to improve the system SE exist, examples of these methods are Faster-than-Nyquist (FTN) technique [1-3], Time-Frequency (TF) packing technique and so on. The improvement of SE can be also reached by using simpler methods such as reducing the roll-off factor of transmitter shaping filter and/or increasing the signal baud rate [4]. However, the using of above-mentioned simpler techniques increases the inter-symbol interference (ISI). To moderate the impacts of increased ISI, the more complicated receiver systems shall be used, including sophisticated equalizers. TF packing techniques promise to provide increased SEs lower-order modulation formats applied to broadband forward link and broadcasting of satellite systems. Improving the SE without increasing the constellation order can be considerably convenient since it is well known that low-order constellations are more robust to channel impairments such as time-varying phase noise and non-linearity.

The improved SE in transmitter side does not yet means the overall improvement of system performance, the receiver side should also be considered. Hence the new parameter of spectrum efficiency should be used- the achievable spectral efficiency (ASE) where the receiver side is also involved. The special interest of this study is to estimate the ASE level for considered techniques (e.g. TF packing) in comparison with the ASE level that is achieved by using high order modulations for the stipulated satellite channel conditions. The common method of calculating ASE as achievable information rate (AIR) per bandwidth is complicated from the engineering point of view, since the AIR shall include a complex Gaussian probability density function. Instead, a new less complicated calculation method of ASE based on bit error rate (BER) estimation is proposed. In addition, the ASE working bounds and calculation accuracy are clarified. To achieve the enhancement of SE, the equalizer is designed and applied on the receiver side. Based on numerical calculations of proposed method, ASE improvement is demonstrated for different nonlinearity scenarios of wireless systems, particularly in the DVS-S2(X) satellite systems, using time-frequency packing (TF-packing) technique.

II. TF Packing for Linear Modulations

Let's consider the forward link of a satellite system, where synchronous users employ the same linear modulation (such as MPSK, MQAM), shaping pulse $p(t)$, which is regularly shifted in the time and frequency domains, of multiples of T seconds and F Hz respectively. A perfect synchronization among the data streams (downlink assumption) is assumed, and that the transmitted symbols $\{x_{n,l}\}$ belong to a given zero-mean M-th order complex constellation and are independent and uniformly distributed (i.u.d.). Under these assumptions, the transmitted baseband signal will have the following form [5]-[6]:

$$x(t) = \sqrt{E_S TF} \sum_{n=-\infty}^{\infty} \sum_{l=-\infty}^{\infty} x_{n,l} p(t - nT) e^{j2\pi lFt} . \tag{1}$$

In (1) E_S is the symbol energy, $x_{n,l}$ is the symbol transmitted by l-th user during k-th symbol interval. Pulse shapes can have different forms (root-raised cosine (RRC), rectangular (REC) or Gaussian). In DVB-S2(X) standard, the base pulse is an RRC-shaped pulse with roll-off factor α.

The received signal is corrupted by the additive white Gaussian noise (AWGN) channel and can be expressed as

$$r(t) = x(t) + w(t) , \tag{2}$$

where $w(t)$ is a circularly symmetric 0-mean white Gaussian noise process with power spectral density N_0. At the receiver, it is assumed that a filter matched to the time-frequency shifted replicas of the base pulse is employed, together with symbol-by-symbol detection algorithm. This is the optimal choice in the maximum a posteriori (MAP) detection algorithm only if the signals $\{ p(t - nT) e^{j2\pi kFt} \}_{n,k}$ are mutually orthogonal.

As it is shown in [6], the detected symbols can be represented as a sum of three terms, one of which will represent the transmitted symbol and the other two - the background noise and the interference due to the adjacent signals as a zero-mean Gaussian process with power spectral density (PSD) equal to N_I (so-called auxiliary channel) correspondingly. Hence, two different impairments experienced by the receiver can be pointed out.

It should be noted that such approximation is valid only when symbol-by-symbol detector is used in the receiver side. However, if advanced detector (including equalizer) is considered in the receiver side, the use of the auxiliary channel model is not justified, therefore in this work ISI importation has been carried out directly in time-packing block which is described in section IV more detailed.

III.   ASE CALCULATION METHOD BASED ON BER ESTIMATION

This section is dedicated to analyzing and description of a new method of ASE improvement, based on BER estimation. As the main evaluation criteria, ASE has been chosen [5]-[6].

As it is well known, a common method to calculate ASE is by defining achievable information rate (AIR). According to [5], ASE can be defined as

$$\eta_{AIR} = (1 / FT) I(x_{0,0}; y_{0,0}) \ \ [bit / (s \cdot Hz)] , \tag{3}$$

where I is the AIR. First, it is worth to mention that in equation (3) the auxiliary channel model is used which is not expedient in the case of advanced detector with using equalizers. On the other hand, the expression (3) is rather complicated and, from engineering point of view, a simple expression for ASE that is defined in terms of provided link quality is more practical. As a link quality parameter, the BER can be used. Below are the rationales of using BER for ASE bounds estimation.

The average mutual information represents the average uncertainty that leads to the thought that both AIR and BER are interrelated quantities since BER also directly depends on the outcome uncertainty. Furthermore, in the presence of nonlinear HPA working in near to saturation mode (quasi-pure and only pure nonlinear regions) the changing of the input power level for fixed modulation type brings not only to changing of the BER performance, but also influences the information spectra due to nonlinearity. This spectral spreading (in the case of increasing input power level) brings to the ASE reduction, at the same time resulting to BER performance decreasing. Hence, a relation exists between ASE and BER.

Based on analyzing of boundary values of ASE, it can be obtained a relationship between ASE and BER. It is obvious that the maximum value of ASE can be obtained if BER tends to zero and vice versa, if BER tends to its maximum value, ASE gets its minimum value. In (3) AIR can be substituted by BER obtaining a relationship between them, which can be done by analyzing AIR vs. signal-to-noise ratio (SNR) (or E_S / N_0) and BER vs. SNR (or E_S / N_0) and then solving this parametric equation. Based on assumptions given above, the following expression for ASE was obtained:

$$\eta_{BER} = \frac{1}{FT} \log_2 \left[M \cdot \left(1 - \frac{M-1}{M} \cdot BER \right) \right] \ [bit / (s \cdot Hz)] . \tag{4}$$

To derive (4) also in a graphical way, the following steps have been realized: First of all, AIR vs. E_S / N_0 and BER vs. E_S / N_0 for a given scenario have been obtained. Then, solving a parametric equation, AIR vs. BER can be received, which will allow to get a relationship between ASE vs. AIR and ASE vs. BER equations.

To find out the working range of the proposed equation, a comparative analysis was performed between ASE vs. AIR and ASE vs. BER equations for different scenarios. The graphical representation of these comparisons is presented in Figure 1 for 16APSK modulation.

These analysis show that using (3) and (4) the values of ASE coincide quite well for larger E_S / N_0 values (for example $E_S / N_0 > 14$ dB for 16APSK and $E_S / N_0 > 7$ dB for QPSK). This result is predictable as for smaller E_S / N_0 values calculation accuracy of BER abruptly decreases, which in its order brings to reduction of ASE vs. BER accuracy.
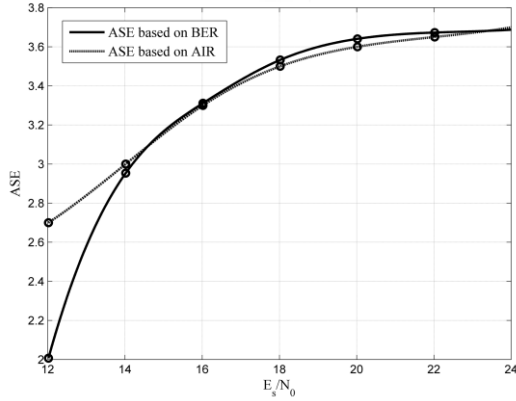
Fig. 1. ASE vs. E_S / N_0 for 16APSK Modulation.   Fig. 2. BER vs. TPF for 16APSK Modulation and IBO = -7 dB
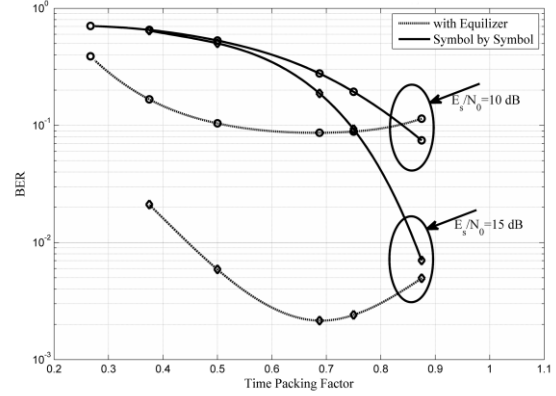
Thus, given analysis allows clarifying the working range of proposed equation (4) from E_S / N_0 point of view. It is worth to mention that the range of E_S / N_0 starting which ASE vs. BER expression returns results near to the ones of ASE vs. AIR, commonly used in the literature, is not out of range of E_S / N_0 of DVB-S2(X) standard, especially taking into account that in this work coding is not considered which is available in DVB-S2(X) standard.

IV. NUMERIC CALCULATION, MODELING AND DISCUSSION

Based on the obtained results numerical calculations were performed using MATLAB/Simulink model. The model consists of the transmitter, which includes also the time-packing block, uplink and downlink channels, non-linear power amplifier and a receiver, which can involve also an equalizer. The role of the equalizer is to minimize the noise, caused by time-packing block. It can be noticed (see Figure 2) that the best BER performance can be received when time-packing factor (TPF) is equal to 0.7 and begins to deteriorate either increasing or decreasing the TPF. This means that when TPF tends to 1, ISI is absent and equalizer can't largely improve BER and moreover, slightly deteriorates it. For the TPF values smaller than 0.7, ISI begins to increase and equalizer is not able to entirely compensate ISI, which affects the BER performance.

It is worth to compare BER values in the presence of detectors, which include equalizer as well as symbol-by-symbol detectors. Figure 2 represents BER vs. TPF for 16APSK modulation in the case of IBO, equal to -7 dB. The dependence is shown for two fixed E_S / N_0 values ($E_S / N_0 = 10$ dB and $E_S / N_0 = 15$ dB).

As it can be seen from Figure 2, symbol-by-symbol detector cannot cope with ISI, arisen from time-packing and BER abruptly deteriorates in the transition region from TPF=0.7 to TPF=0.8. This transition is as abrupt as E_S / N_0 is larger. Unlike symbol-by-symbol detector, the designed equalizer algorithm of which is not very complex struggles pretty well against ISI, which brings to hope of receiving improved ASE.

Given dependence allows also to determine better TPF region from the BER point of view. As it can be seen from Figure 2, the best BER lies within the range of TPF=0.6 and TPF=0.8. This analysis allows specify the TPF region during the process of receiving further results.

It can be seen that ASE can be improved for particular values of TPF. For comparison, 16APSK modulation was selected and time-packing was applied. Besides, the controlled ISI was applied, which was compensated by the equalizer to give a possibility to control ASE. Obtained in such way values of ASE were

then compared with the ASE values received by 32APSK modulation and for the same IBO values of power amplifier when time-packing was not applied. From Figure 3 follows that the ASE for 16APSK modulation is about 5.5 that exceeds the level, maximum achievable for orthogonal signaling even if 32APSK is used by 1.5. This result shows that the ASE of nonlinear system can be improved without increasing the order of modulation by applying TF packing technique, of course by using more complicated receiver.

It is worth to mention that as it can be seen from Figure 4 when the time-packing is applied without the use of equalizer then it is not possible to receive any ASE improvement.
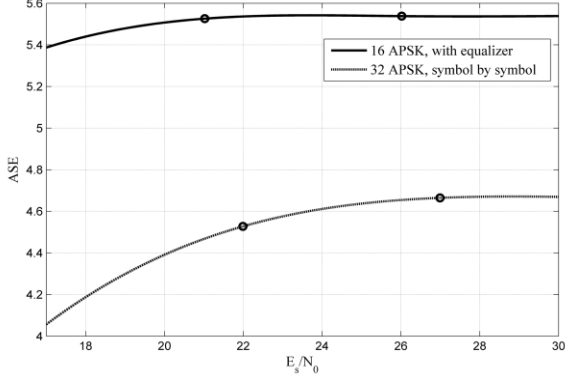
Fig. 3. ASE vs. E_S / N_0 for 16APSK modulation with equalizer and 32 APSK modulation with symbol by symbol receiver., TPF = 0.7, IBO = -3dB.
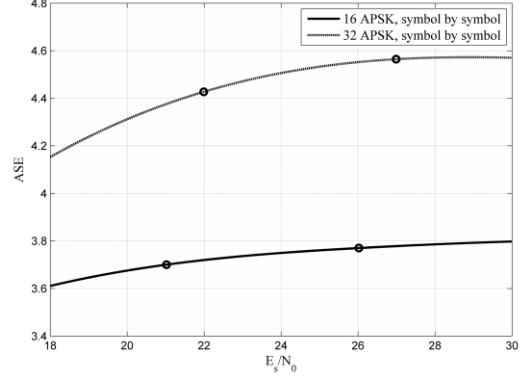
Fig. 4. ASE vs. E_S / N_0 for 16APSK and 32 APSK modulations with symbol by symbol receivers., TPF = 0.7, IBO = -3dB.

V.   CONCLUSION

By summarizing, we can conclude what in this work the possibility of using TF packing for improving SE in nonlinear satellite systems was discussed. The common method of calculating ASE as AIR per bandwidth is complicated from the engineering point of view, since the AIR shall include a complex Gaussian probability density function. Instead, a new less complicated calculation method of ASE based on BER estimation was proposed. In addition, the ASE working bounds and calculation accuracy were clarified. The results allow concluding that SE improvement using time-packing is achievable in expense of complicating the receiver scheme, adding equalizer to it. It is interesting that this improvement is available also in the nonlinear working regions of power amplifier. The obtained results show that the ASE reaches its maximum value at TPF≈0.7. As example, the ASE for 16APSK modulation is about 5.5 that exceeds the level, maximum achievable for orthogonal signaling by 1.5. For 32APSK modulation, the ASE at TPF≈0.7 exceeds the orthogonal signaling at least by 0.5. It is also worth to mention that SE improvement is harder to achieve with increase of nonlinearity of the system, which is predictable, since the nonlinearity negatively affects the behavior of the overall system and, particularly, the operation of equalizer.

VI.   REFERENCES

[1] J. E. Mazo, "Faster-than-Nyquist signaling," Bell System Tech. J., 54, p. 1450, 1975.
[2] J. E. Mazo, H. J. Landau, "On the minimum distance problem for faster-than-Nyquist signaling," IEEE Trans. Inform. Theory, p. 1420, 1988.
[3] A. Liveris, C. N. Georghiades, "Faster-than-Nyquist signaling," IEEE Trans. Commun., 47, p. 1502, 2003.
[4] S. Cioni, G. Colavolpe, C. Ernst, A. Ginesi, "Bandwidth optimization for satellite digital broadcasting," in Proc. 31st AIAA International Communication Satellite Systems Conference, DOI: 10.2514/6, 2013, p. 5658.
[5] A. Barbieri, D. Fertonani, G. Colavolpe, "Time-frequency packing for linear modulations: spectral efficiency and practical detection schemes," IEEE Transactions on Communications, vol. 57, No. 10, pp. 2951-2959, 2009.
[6] A. Modenini, G. Colavolpe, N. Alagha, "How to significantly improve the spectral efficiency of linear modulations through time-frequency packing and advanced processing," in Proc. IEEE Intern. Conf. Commun, 2012, pp. 3260-3264.

Green Communication for GSM Network

K. Nikoghosyan, G. Yeghoyan

Redinet CJSC , Azatutyan str. 24/7-24/8, 0014 Yerevan, Armenia

Power consumption is currently one of the major challenges faced by mobile operators. Recent explosive growth of smartphones market adoption and the consequent mobile internet traffic requirements have prompted waves of research and standard development activities to meet the expected future demands in an energy-efficient manner. Wireless access networks will be a major component of the communication infrastructure required by other "green" solutions for the efficient management of energy including remote monitoring, control and smart administration. In this paper we present the important issue to enhance the energy consumption efficiency of cellular network without compromising coverage and users perceived Quality of Service (QoS). The reason is twofold. First, mobile operators need to reduce their operational energy bill due to recent dramatic increase in energy costs. Second, there is a request of environmental protection to reduce CO_2 emissions. Today's mobile network have a strong potential for power saving. Most of consumed energy on the mobile networks (about 70%) is related to Radio Access Network (RAN) defining relation among power consumption, carried traffic and the coverage area. Therefore, power consumption in the RAN (BTS sites) is an important factor in the cellular network. Today's running cellular networks have been designed to maximize coverage area, traffic while energy consumption efficiency has not yet played a prime goal.

Mobile operator 1 in country 1 (M1) is based on traditional solution: one core network and separate RANs for 2G and 3G, Mobile operator 2 in country 2 (M2) operates a significantly smaller network built on modern technologies like Software Defined Radio Base Stations (SDR BTS).
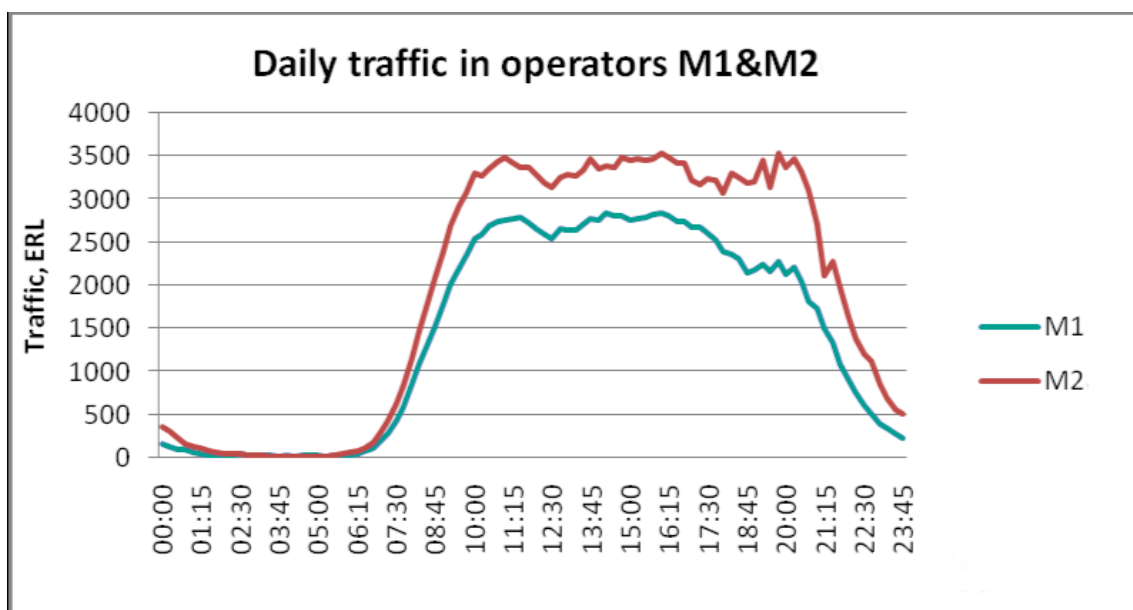
Fig. 1 – Comparing traffic of M1 and M2 network
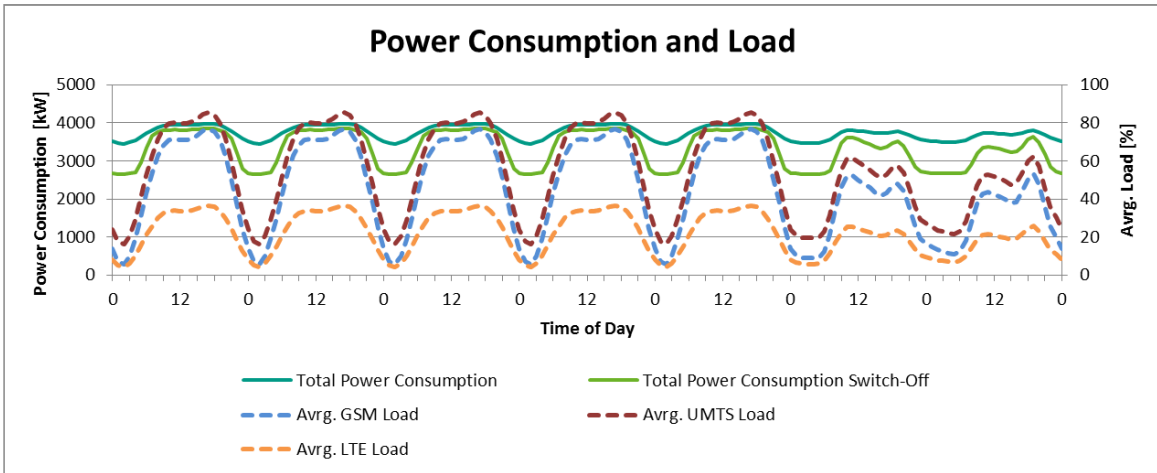
Fig. 2 – Modeled Load and Power Consumption profile for M1, generated by BCD
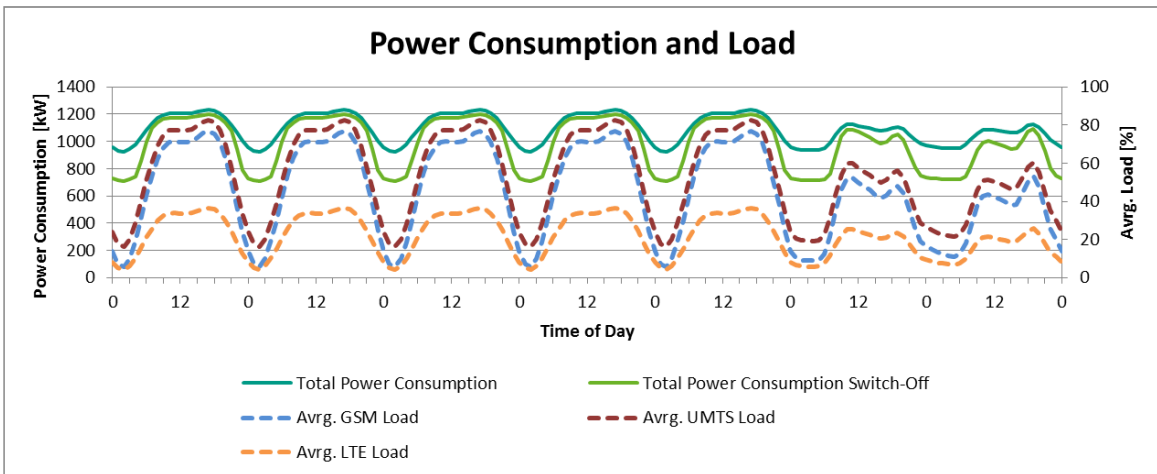
Fig. 3 – Modeled Load and Power Consumption profile for M2, generated by BCD

The investigation shows correlation between the type of equipment used by an operator (old vs modern) and the energy consumption level, as the base stations deployed by M2 network consume 40% less energy.

Since about 65% of energy of cellular network is consumed by the BTS macrocells sites we consider three following components for power reduction:

- BTSs includes scheduler which operate according to the traffic load dynamically. BTS may turned on and off (soft sleep mode) according to the dynamic of traffic load.
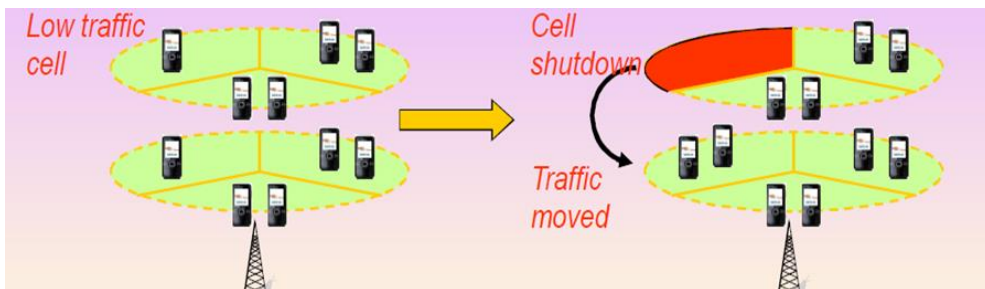
Fig. 4 – Soft Sleep Mode

- Cell zooming scalability as a function of traffic load, channel condition and required data rate.
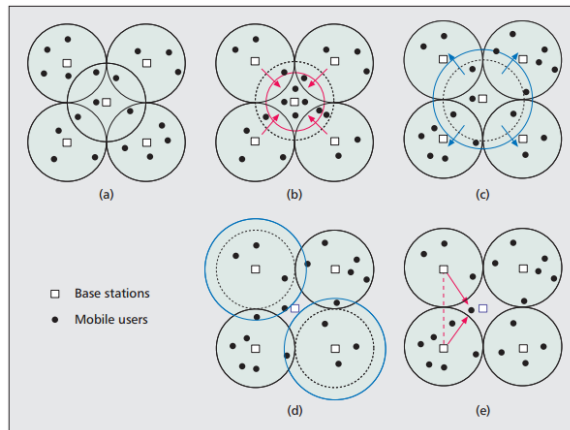
Fig. 5 - Cell zooming operations in cellular networks: a) Cells with original size; b) Central cell zooms in when load increases; c) Central cell zooms out when load decreases; d) Central cell sleeps and neighboring cells zoom out; e) Central cell sleeps and neighboring cells transmit cooperatively.
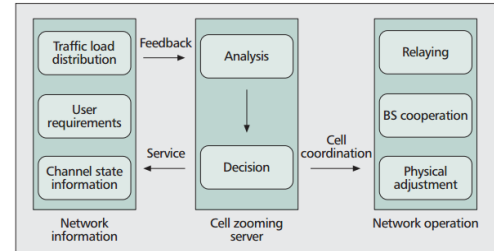
Fig. 6 – Cell zooming operational framework

- About half of energy in the Remote Radio Unit (RRU) consumes in the Power Amplifier (PA) while power consumption in 3G CDMA networks changes linearly as a function of bandwidth and signal quality which requires a high quality PA.

A significant amount of energy today is wasted by not having appropriate BTS site soft sleep mechanism in place. Regular approach, i.e. maximum load scenario is a rather rare case in typical network deployment. Most of the time the network infrastructure is operated with semi load efficiency leading to a significant waste of energy. It is essential to have optimal loads sizing, accurate data on BTS load pattern as well as potential renewable energy sources (basically PV solar and Wind) especially in rural area. We study these relations and algorithms to approach green communications in this paper. This study is based on the number of BTS, their configuration and topologies have been deployed in Orange Armenia GSM Network.

REFERENCES

[1] Dr.Andreas Eisenblätter, Rafał Pisz, Szymon Stefański "GreenNets White Paper - Power consumption and CO2 footprint reduction in mobile networks by advanced automated network management approaches" pp. 5-7, http://www.greennets.eu/download/361/.

[2] Chethana R Murthy, Dr. Kavitha "IRACST – International Journal of Computer Networks and Wireless Communications (IJCNWC), ISSN: 2250-3501", vol.2, no.2, pp. 232-236, 2012.

[3] Yuli Song, Dongxiao Li, and Zhansheng Wu, "Discussion on smart power saving technology of BTS", Designing Techniques of Posts and Telecommunications, vol. 31, no. 3, pp. 70-73, 2010.

[4] Zhisheng Niu, Yiqun Wu, Jie Gong, and Zexi Yang, Tsinghua University, Cell Zooming for Cost-Efficient Green Cellular Networks - http://network.ee.tsinghua.edu.cn/papers/NiuCommag10.pdf.

[5] Eunsung Oh, Krishnamachari, B, Xin Liu, Zhisheng Niu, "Toward Dynamic Energy-Efficient Operation of Cellular Network Infrastructure", Communications Magazine, IEEE, vol. 49, no. 6, pp. 56-61, 2011.

Renewable Hybrid Off-Grid Power Solution for GSM Network

G. Yeghoyan, K. Nikoghosyan

Redinet CJSC , Azatutyan str. 24/7-24/8, 0014 Yerevan, Armenia

This paper gives an overview of existing power network of BTS sites of Orange Armenia and present technical and economical assessment for proper selection of technologies on Hybrid efficient power system as a backup DC power supply in the urban and rural areas. Using renewable sources to power GSM base station sites is far better than the conventional diesel system especially in rural areas where there is no utility power. The proposed system reduces both the cost and the amount of CO_2 emitted from the entire setup. Renewable energy is derived from resources such as wind, rain, sunlight, tides, waves and geothermal heat.

Typical GSM network can be viewed as composed by three different sections:

- Mobile Switching Center (MSC)

- Base Transceiver Station (BTS)

- Mobile Terminals, normally limited to the hand-held devices.

The key elements are the BTSs because their contribution is the most relevant for the total energy consumption. The power consumption per function within the BTS site can be differentiated as follows: more than 60% of the power is consumed by the radio equipment and amplifiers, 11% is consumed by the DC power system and 25% by the cooling equipment (air conditioning unit). Therefore it is very important to consider BTS energy savings strategies applied both to the radio equipment, i.e. radio "standby" mode and to the cooling, i.e. passive cooling (free cooling) and advanced climate control. Hybrid Off-Grid systems are particularly well-suited for applications in rural remote areas, where electric utility service does not exist or unstable grid power supply. In comparison with the costs of High Voltage Line (HVL) extension or the high costs of fuel delivery to remote locations and site maintenance costs, hybrids can offer several benefits to telecommunication operators particularly: Decreased fuel consumption by 30–90%, decreased grid energy consumption by 30%, Save massive BTS outages (around 70%) due to Genset failures, environment friendly, extended maintenance and replacement intervals (diesel Genset typically accounts for 30% of the total OPEX of a BTS site). The Renewable Hybrid BTS site consist of Solar Photovoltaic Panels which converts the Sun light into electrical energy and charge the 48V Battery bank during the day time. An efficient MPPT solar charge controller is used to maximize the power output from the PV modules to charge the battery bank. Control logic developed to utilize the different energy resources in efficient techniques and keep the battery fully charged by providing priority to solar charging and using Utility power or Diesel Generator power in the absence of solar power.
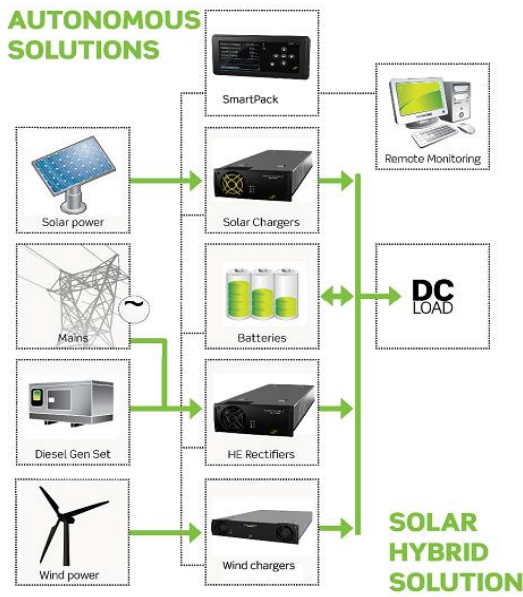
- Several energy sources can be utilized for feeding the DC load and charging the batteries; AC from mains or generator, and renewable source as wind and solar.

- The hybrid site controller logs energy produced by the various sources.

- The energy logs, key parameters and status are sent to the MultiSite Monitor server

Fig. 1 – Hybrid Site
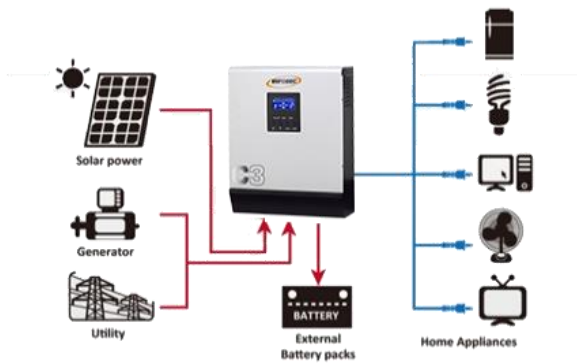
Fig. 2 - Operation Diagram Using the C3 MPPT with photovoltaic input and mains or power generator
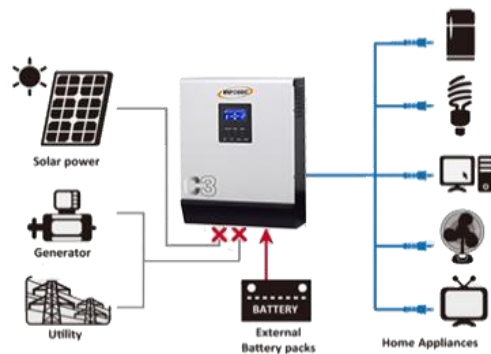
Fig. 3 - Using the C3 MPPT in battery mode

This system does not depend on a single power source. Multiple power sources are used. This study is based on the Eltek's high efficiency Hybrid Solution have been deployed in Orange Armenia GSM Network. The Benefits of Eltek's Hybrid Power Solution are as follows:

- Up to 75% OPEX reduction

- More than 96% rectifiers/solar chargers efficiency

- Reduced CO2 emissions

- Reduced service maintenance

- Fully integrated of all energy sources: Grid, Solar, Wind, Diesel Genset

References

[1] Eltek Company , "High Efficiency Hybrid Excellence" presentation, http://www.eltek.com/wip4/download_doc_647.epl?id=7769.

[2] D. U. Ike, A. U. Adoghe, A. Abdulkareem ,"Analysis of Telecom Base Stations Powered By Solar Energy", International Journal of Scientific & Technology Research, vol. 3, no 4, April 2014.

[3] A. V. Anayochukwu et al. , "Potentials of Optimized Hybrid System in Powering Off-Grid Macro Base Transmitter Station Site", International Journal of Renewable Energy Research, vol.3, no.4, pp 862-869, 2013.

[4] A.N. Celik, "The system performance of autonomous photovoltaic-wind hybrid energy systems using synthetically generated weather data", Renewable Energy, vol. 27, pp. 107-121, 2002.

Progressive THz Spectrometric Technologies Applied for
Non-Invasive Evaluation of Bio-Medical Tissues

Seizi Nishizawa[1]*, Eugene H. Morita [2]†, Takeshi Nagashima[3],
Katsuko S. Furukawa[4], and Takashi Ushida[5]

[1] *FIR-FU, University of Fukui, 3-9-1 Bunkyo, Fukui 910-8507 Japan*
[2] *Faculty of Agriculture, Ehime University, 10-13 Dohgo, Matsuyama, Ehime 790-8577 Japan*
[3] *Faculty of Science and Engineering, Setsunan University, 17-8 Ikeda Nakamachi, Neyagawa, Osaka 572-8508 Japan*
[4]*Department of Bioengineering, Faculty of Engineering, Univ. of Tokyo, 7-3-1 Hongo, Bunkyo, Tokyo113-8654 Japan*
[5]*Division of Regenerative Medical Engineering, Center for Disease Biology and Integrative Medicine, School of Medicine, University of Tokyo, 7-3-1 Hongo, Bunkyo, Tokyo 113-8654 Japan*

----

*Present address: D-305 Incubation Office Tama, Tokyo SME Support Center, 3-6-1Azum, Akishima,Tokyo196-0033Japan
†Present address:Faculty of Science Dept. of Chemistry, Josai University, 1-1, Keyakidai, Sakato, Saitama 350-0295 Japan

The terahertz time-domain spectroscopy (THz-TDS) has recently been carried out with a wide expansion of intrinsic measurements valid for quality control of industrial products of dielectric functional materials, bio-molecules, and crystalline morphology of pharmaceutical reagents. After describing an overview of the newly developed advanced sampling technologies of the biomedical THz-TDS applications, we will describe some details of the latest results of non-invasive evaluation of bio-medical tissues. The bound water ratio obtained through THz-TDS analysis that elucidates extracellular matrix (ECM)-water interactions could potentially be a valid parameter for evaluating the degree of cartilage tissue formation.

I. INTRODUCTION

The generation of coherent terahertz (THz) radiation through the femtosecond pulse laser irradiation on a photoconductive antenna has been effectively utilized for the promising new far-infrared spectrometric technique of the terahertz time-domain spectroscopy (THz-TDS)[1-4]. The THz-TDS technique has the advantage of higher signal-to-noise-ratio, and makes it possible to measure not only the transmission intensities $T(\omega)$ but also the intrinsic phase shifts $\Delta\varphi(\omega)$, which makes direct estimation of the complex dielectric constant $\varepsilon^*(\omega)$[2]. The intrinsic phase shifts $\Delta\varphi(\omega)$ also provide analytical estimations of the dispersion relations for various elementary excitations[3]. The THz-TDS technique has recently been carried out with a wide expansion of intrinsic measurements valid for quality control of industrial products of dielectric functional materials, bio-molecules, and crystalline morphology of pharmaceutical reagents[2-4]. Here, after the description of an overview of the newly developed advanced sampling technologies of the biomedical THz-TDS applications, we describe some details of the latest results of non-invasive evaluation of bio-medical tissues expected critical contribution in the regenerative medicine to be one of the promising clinical therapies. The bound water ratio obtained through THz-TDS analysis that elucidates extracellular
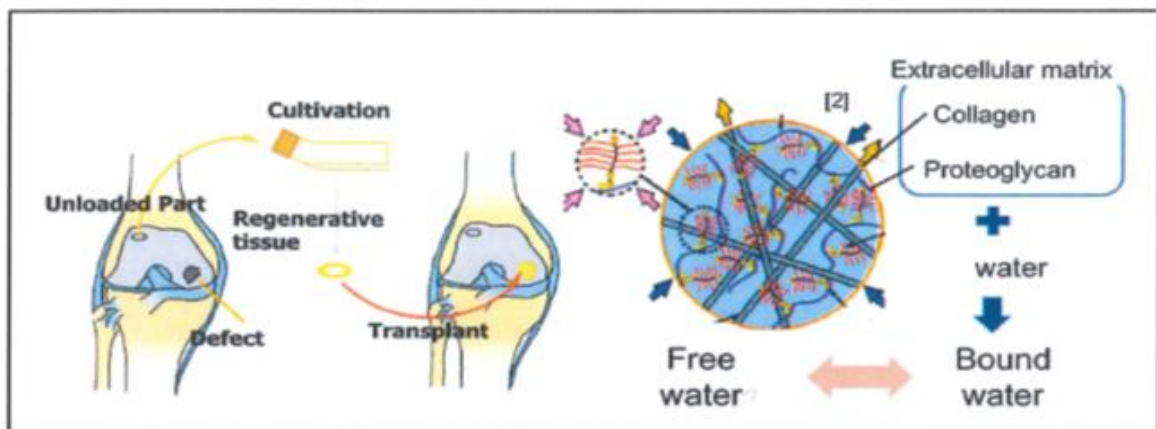
Fig.1 Schematics for organizational structure of the articular cartilage

matrix (ECM) water interactions could potentially be a valid parameter for evaluating the degree of cartilage tissue formation in the process of synthesizing processing an artificial human cartilage

II. WIDEBAND THZ-TDS INSTRUMENTS

Compact THz-TDS instrument has been newly developed with the advantages of high SNR in Far-infrared region below 170cm^{-1} and applied for versatile measurements (transmission, reflection, liquid, gas, ATR, mapping, temperature dependence and etc.) [2]. For the THz-TDS FTIR. An absorption spectrum on air was measuredandcompared with the water vapour absorption spectra offered from the Jet Propulsion Laboratory (JPL). As shown already in the profceedings of the Internaitonal Conference on «Microwave and THz Technologies and Wireless Communications»(2014) at Yerevan [5], the wavenumbers of the absorption lines agree with the absorption data of JPL and also the spectral resolution is less than 0.02[cm^{-1}] which was confirmed by the water vapor absorption line at 57.22 [cm^{-1}] measured at less than 60 Pa. The spectral converage depends on the femtosecondlaser. The THz raidation source spectra measred by the laser (Femtolasers Productions GmbH: Integral Pro) which pulse duration is less than 10 femtosecond. The THz radiation is observed from about 1 [cm^{-1}] to 230 [cm^{-1}]. Almost all compact type femtosecond lasers are possible to set on the instrument.

Between 230 and 340[cm^{-1}], the THz radiation is absorbed by the GaAs phonon absorption bands of the photoconductive antennas. It is expected that the high frequency limit of THz radiation will become higher than 440 [cm^{-1}] by avoiding the absorption of the GaAs substrates. The recent progress in the research application for the far-infrared measurements on new functional materials. A new instrument of Thz-TDS has been developed with the advanced optical configuration which consists of a composite THz-TDS optics and a high throughput Michelson (Martin-Puplett configuration) interferometer. A photographic view of the optical fconfiguration is shown in Fig.2. The instrument is for use in the qualitative analyses of optelectric constants of materials in which the spectrum wavenumber coverage is expanded to the NIR reigon.
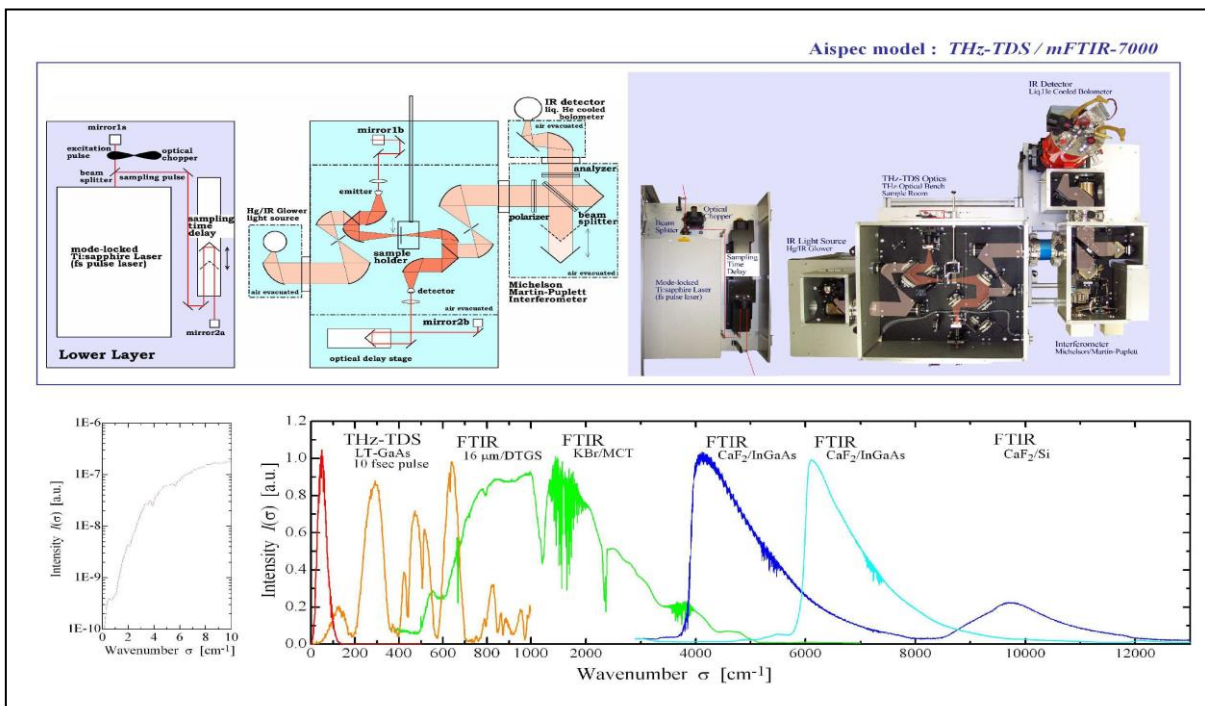
Fig. 2 Advanced optics of the composite THz-TDS combined with a high throughput Michelson (Martin- Puplett configuration) interferometer (FTIR) (upper) and expansion of the spectrum wavenumber coverage to the NIR region (lower). [2,3]
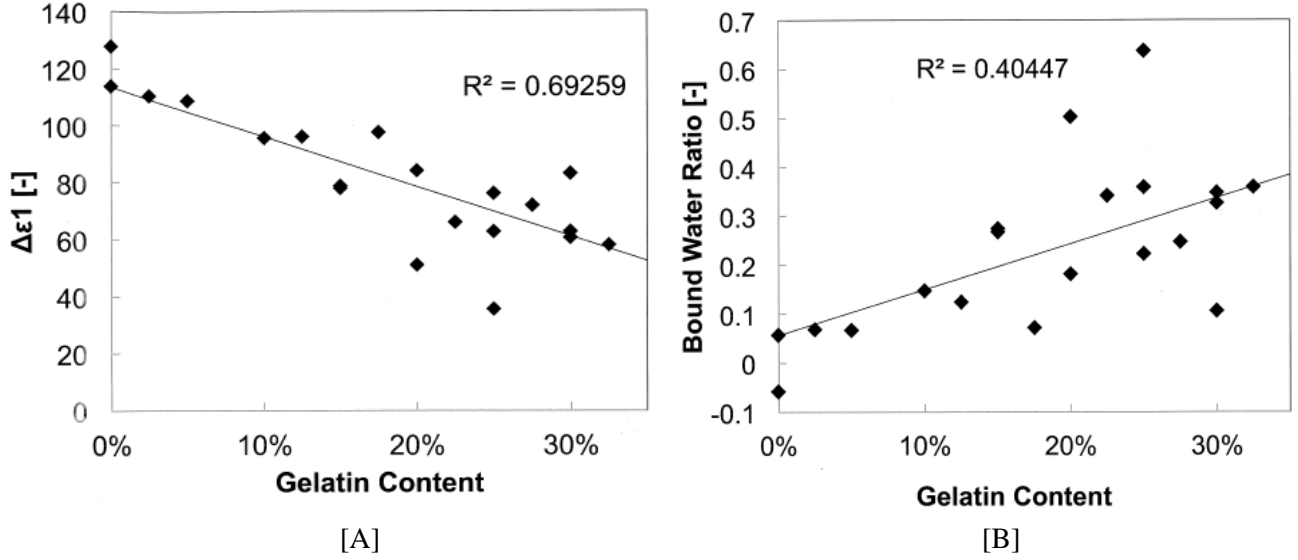
Fig. 3 Dependence of dielectric relaxation strength on gelatin-gel concentration [A], and on bound water ratio [B] [6]

III. MEASUREMENT RESULTS AND DISCUSSION

The regenerative medicine is thought to be one of the promising clinical therapies. Many basic and clinical researches are undergoing for realizing the regenerative medicine. In vitro regenerated tissues should be quantitatively evaluated before their implantation. However, we could adopt neither destructive nor invasive methods for that purpose, because the tissues are regenerated in vitro not in a mass-production manner but a tailor-made manner. Therefore, it is indispensable to develop non-invasive methods for evaluating the in propose to adopt terahertz time domain spectroscopy (THz-TDS) for evaluating regenerated cartilages.

Articular cartilage composed of 70% water and almost 30% extracellular matrix ECM, which contain biopolymers such as collagen and proteoglycan. Mow et al. (1988)[7] reported that some water hydrated to ECM (called bound water) which is contribute to almost 50% stiffness of cartilage tissue. Hence, we assumed that the change in bound water (which is strongly attracted to ECM) ratio within tissue reflected change in mechanical properties of tissue.

We added gelatin powder (Gelatin from porcine skin, SIGMA-ALDRICH) without further purification to 90°C water, prepared 0-32.5% gelatin gel samples, and pressed each sample while hot to 90μm thickness. For cartilage tissue samples, we took samples from bovine knee joints, sliced into 60μm thickness with a microtome, and then sorted them into three groups along depth: superficial (20%), middle (50%) and deep (39%) layers. We measured each sample with THz-TDS [6] (IRS-2700Npro, Aispec) under dry air purge and obtained the complex dielectric constant $\varepsilon^*(\omega)$ for a range of 0.5-2.5 THz.

The complex dielectric constant can be decomposed into four peak components as written in Eq. (1)[8],

$$\tilde{\varepsilon}(\omega) = \frac{\Delta\varepsilon_1}{1 + i\omega\tau_1} + \frac{\Delta\varepsilon_2}{1 + i\omega\tau_2} + \frac{A_s}{\omega_s^2 - \omega^2 + i\omega\gamma_s} + \varepsilon_\infty \qquad (1)$$

,

where slow relaxation strength $\Delta\varepsilon$, is proportional to the amount of free water molecules.

For gelatin gel, we calculated bound water ratio f_{bound} by considering relaxation strength of the sample, $\Delta\varepsilon_1$ as the contribution of free water. Sample, relaxation strength of water $\Delta\varepsilon_{1\text{ water}}$ and water content in volume σ_{water} as written in Eq. (2).

$$f_{Bound} = 1 - \frac{\Delta\varepsilon_{1,Sample}}{\sigma_{Water}\Delta\varepsilon_{1,Water}} \qquad (2)$$

Fig. 3 [A] shows that the relationship between gelatin content and slow dielectric relaxation strength $\Delta\varepsilon_1$.

31

Gelatin gel with higher concentration showed lower relaxation strength. Fig.3 [B] shows the relationship between gelatin content and bound water ratio. Gelatin gel with higher concentration showed higher bound water ratio, which accords with former studies. Fig.4 shows the result of THz measurement and protein assay. The deeper layer contained more proteoglycan, which accords with former studies, and showed weaker dielectric relaxation. Fig.5 shows the result of mechanical test that the deeper layer showed more viscosity, which also accords with former studies. It also indicates that dielectric relaxation decrease in accordance with higher viscosity. The decrease of dielectric relaxation can be regarded as the increase of bound water. Hence, it is suggested that THz-TDS can detect water status and cartilage chemical and mechanical properties.
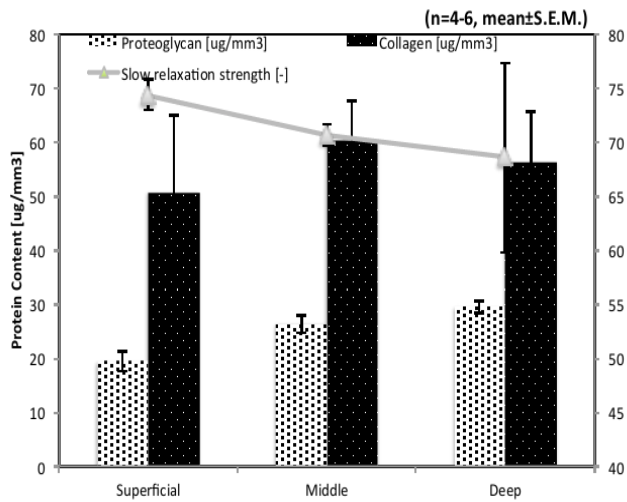
Fig.4 The dependence of dielectric relaxation strengh on proteoglycan content [6]
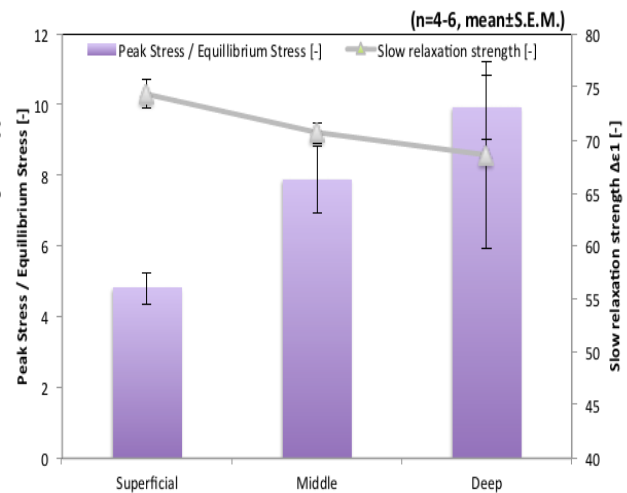
Fig.5 The dependence of dynamical viscosity on dielectric relaxation strengh [6]

IV. CONCLUSION

The bound water ratio obtained through THz-TDS analysis which may elucidate ECM-water interactions could potentially be a valid parameter when evaluating the degree of cartilage tissue formation, and therefore could be useful for the development of non-invasive evaluation methods of tissue-engineered cartilage.

V. REFERENCES

[1] K. Sakai, ed., "Terahertz Optoelectronics", pp203-265, Springer-Verlag Berlin Heidelberg, 2005.
[2] S. Nishizawa, T. Iwamoto, K. Shirawachi, and M.W. Takeda, M. Tani and K. Sakai, Special Review issues, Proc. 1999, IEEE, 7th Inter. Conf. on Terahertz Electronics, (1999) 308; S. Nishizawa, N. Tsumura, H. Kitahara, M.W. Takeda and N. Kojima, Special Review issues, Phys. Med. Bio. vol.47, p.3771, 2002.
[3] S. Kojima, N. Tsumura, M. Takeda, and S. Nishizawa, "Far- Infrared Phonon-Polariton Dispersion Probed by Terahertz Time-Domain Spectroscopy" Phys. Rev. B vol. 67, p.035102, 2002; Kojima, S., Takeda, M.W., and Nishizawa, S., J. Molecular Structure pp.651-653 vol. 285, (2003)
[4] M. Tasumi, ed., "Introduction to Experimental Infrared Spectroscopy", pp269-286, John Wiley, West Sussex (2014);
[5] S. Nishizawa, T. Nagashima and M.W. Takeda, Proc. Of the International Conference on Microwave And THz Technologies and Wireless Communications", Yerevan, Armenia, (2014)1; 2012)5.
[6] I. Moritomo, A. Kamada, T. Ota, S. Nishizawa, K. Furukawa and T. Ushida, " Non-Destructive Evaluation of Tissue Engineered Cartilage by Thz-TDS " to be published in the near future.
[7] Mow, V. C. et al. International Journal of Solids and Structures, vol.35, no. 34, pp.4945-4962, 1998.
[8] Yada, H. et al. Chemical Physics Letters, vol. 464, no.4, pp.166-170, 2008.

Waveguide Transitions With Various Crossections for the Terahertz Range

M.Ts Ayvazyan

National Polytechnic University of Armenia, Teryan 105, 0009 Yerevan. Armenia

Abstract - It is proposed that, in the terahertz wavelength range, waveguides of the class "hollow dielectric channel" be used as a guiding system. When constructing circuits for various purposes it is necessary to use various waveguide junctions with the cross-sectional dimensions of the inlet and outlet. In this wave of higher types emerge in the case of multi-wavelength waveguides. In such devices, the working mode conversion to the higher wave types should be minimal. Application of Velden Zakson method allows to calculate the level of transformation of the operating mode to higher wave types and basic dimensions of the proposed conversions.

Keywords - *terahertz range, a waveguides of a class "hollow dielectric channel", losses, self-filtration, working mode, higher types of waves, crossection.*

I. INTRODUCTION

In the terahertz range it is most actual challenge to choosing waveguide system from which you can create functional elements for various purposes. In a review article [1] refers performed the work of the individual devices based on open quasi-optical lines. Due of the number of features (an open line, dimensions, weight) the use of quasi-lines is limited, as a rule, for the measuring circuits. The main technical specifications of complete sets of waveguide functional elements 120-180 GHz band prepared on the basis of wave guides by class "the hollow dielectric channel" given in [2,3 and 4]. In this paper, it is proposed to use the method of cross-sections and the method Pheld- Zakson for the calculation the losses in the transitions between the waveguides with different cross-sections [5,6]. We consider the waveguide transition metal-dielectric waveguides (MDW) with round and square cross-sections, as well as the excitation of these waveguides.

II. EXCITATION METAL DIELECTRIC WAVEGUIDE WITH A SQUARECROSS-SECTION

The general principle of constructing high performance waveguide exciters is as follows: need to smoothly change the shape and dimensions of the waveguide of the primary so, as to have a certain sectional amplitude and phase distribution of the field component needed to the distribution of the working wave field. For elimination the additional conversion to parasitic modes horn is performed symmetrical to the axis and sufficiently long (≥ 50 wavelength), or with a complex shape forming, which is determined by known methods [5].

If in this section butt the excited waveguide and continue it, the losses of excitation will be minimal. When both direct docking the waveguides the field of metallic waveguide excites the amount of waves of DC-wave waveguide. If we neglect the damping of these waves, the power P_i of $i-$th wave is calculated by a formula obtained by Pheld - Zakson [5,6].

$$P_i = \frac{\left| \iint\limits_{S_1} \left[\vec{E}_0 \, \vec{H}_i \right] \vec{\ell} \, dS \right|^2}{\left| \iint\limits_{S} \left[\vec{E}_i \, \vec{H}_i \right] \vec{\ell} \, dS \right|} , \qquad (1)$$

where S_1 – the effective sectional area of the excitation waveguide, the S – cross-section of the DC-waveguide l – a unit vector directed along the axis oZ, $\vec{E}_0$ and $\vec{H}_0$ – the fields components of the exciting wave, $\vec{E}_i$ and $\vec{H}_i$ – the field components of the excited wave.

The power of the falling wave is calculated as the real part of the flow of the Poynting vector through S_1:

$$P_O = \text{Re} \int_{S_1} \left[\vec{E}_0 \vec{H}_0^* \right] \vec{l} \, d S , \qquad (2)$$

The efficiency of excitation η is equal:

$$\eta = \frac{P_i}{P_O}, \qquad (3)$$

The dependence of the field components of the coordinates of « y » - for working type of waves in the metal waveguide and DC-waveguides is the same, the maximum excitation efficiency is obtained dimensions $b \neq b_1$ (see Figure 1.). As for the coordinate "x", the corresponding dependence of the field component abutting waveguides are different and the maximum efficiency of the LM_{11} wave excitation is possible when $\alpha \neq \alpha_1$ [6].

In this case, the joint between the waveguides should realize the optimal jump and then a rectangular distribution of the wave field TE_{10} how would fit in cosine distribution of the LM_{11} wave.

Having done the necessary changes we can get the final excitation efficiency

$$\eta = \frac{8}{\pi^2 m^2} \frac{\left[\sin \dfrac{\pi n a_1}{2a} \right]^2}{\dfrac{a_1}{a}} \delta_{mn} , \qquad (4)$$

where $\delta_{mn} = 1$ when $n = 1$, m - odd,

$\delta_{mn} = 0$ when $n \neq 1$, or m - an even.
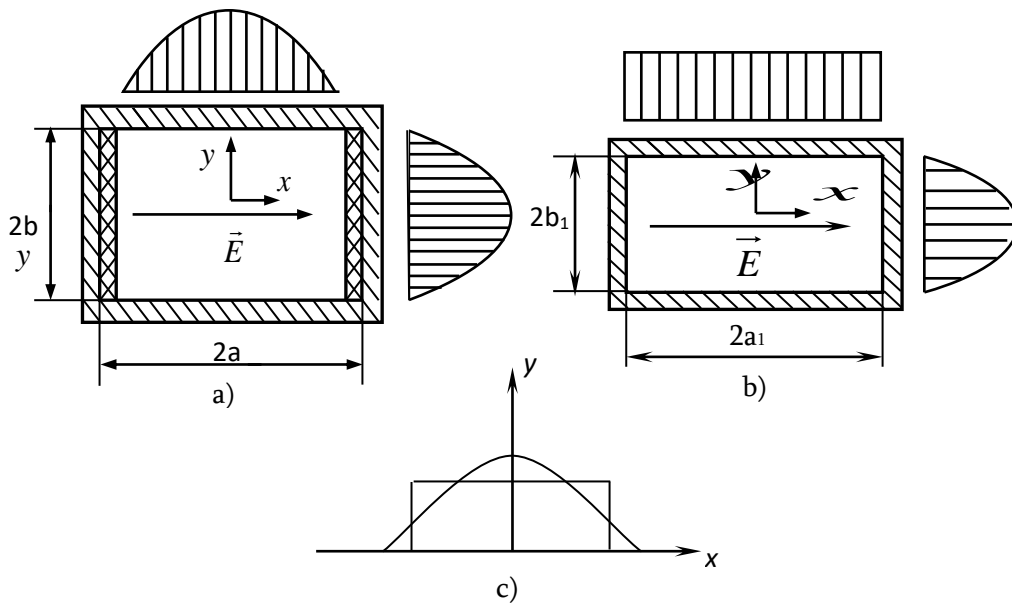
Fig. 1. The distribution of the fields a) rectangular WDM, b) rectangular metal waveguide,
c) the principle of excitation.

As follows from (4), the efficiency of excitation does not depend on the frequency, and, LM_{m1} wave excited ($m-$ odd). The resulting expression allows haw to calculate the efficiency of excitation the $i-$th wave. Note, that to obtain higher efficiency, it is necessary to increase the number of channels at the exit of the horn.

III. EXCITATION OF METAL DIELECTRIC WAVEGUIDE OF CIRCULAR CROSS SECTION

Along with rectangular waveguides widely applied DC-waveguides of circular cross section [2]. In microwave circuits based on these waveguides as the working mode is chosen the least damped hybrid wave EH_{11} which have in a cross-section linearly polarized field. The transverse component of the field of the wave (in leading order of $1/ka$) is written in the form

$$
\begin{aligned}
\mathrm{E}_r &= BJ_0(\alpha, r)\cos\varphi e^{-jhz} \\
\mathrm{E}_\varphi &= -BJ_0(\alpha, r)\sin\varphi e^{-jhz} \\
H_\varphi &= E_r, \qquad H_r = E_\varphi
\end{aligned}
\tag{5}
$$

where $J_0(\alpha, r)-$ the zero-order Bessel, $B-$ amplitude coefficient, r, φ and $z-$ cylindrical coordinates, $\alpha -$ cross wave number which determined from the dispersion equation. The simplest way to is excited EH_{11} wave to use the TE_{10} wave with using the optimal jumps. The analytical expression for the calculation of the efficiency of excitation of circular metal dielectric waveguide is obtained from (2) and has the following form:

$$
\eta = \frac{2}{b_1} \frac{\left(I_1 + \dfrac{\mathrm{A}_2}{\mathrm{A}_1} I_2\right)}{\left[a_2\left(\dfrac{\mathrm{A}_2^2}{\mathrm{A}_1^2} - 1\right) + a_1\right]I_3},
\tag{6}
$$

where

$$
I_1 = \int\limits_{a_2}^{a_1}\int\limits_0^{b_1} J_0\left(\mu_{m1}\sqrt{\frac{\chi^2}{a^2} + \frac{y^2}{a^2}}\right)\cos\frac{\pi}{2b_1}\, y\, d\chi dy
$$

$$
I_2 = \int\limits_0^{a_2}\int\limits_0^{b_1} J_0\left(\mu_{m1}\sqrt{\frac{\chi^2}{a^2} + \frac{y^2}{a^2}}\right)\cos\frac{\pi}{2b_1}\, y\, d\chi dy,
$$

$$
I_3 = \int\limits_0^{a}\int\limits_0^{a} J_0^2\left(\mu_{m1}\sqrt{\frac{\chi^2}{a^2} + \frac{y^2}{a^2}}\right) d\chi dy,
$$

$$
\tag{7}
$$

through the a designated radius of the excited waveguide.

IV. THE TRANSITION FROM THE METAL DIELECTRIC WAVEGUIDE WITH SQUARE CROSS-SECTION TO CIRCULAR WAVEGUIDE

The rotary joints usually are prepared on the basis of circular waveguides. Other functional elements of waveguide paths, to preserve the stability of the polarization are performed based on the metal-dielectric waveguide of square cross section [2]. Numerical investigations by Pheld – Zakson method (Formula 1) showed that the lowest conversion loss provides the best jump. Conditions of optimal jump can be written as

$$2a = 0.9D, \tag{8}$$

where $2a$ is the transverse dimension of the square metal-dielectric waveguide, D − the diameter of the circular metal-dielectric waveguide. Estimated value of the loss on the conversion for the jump with the metal-dielectric waveguide cross-sectional 10x10 mm dimensions of 10x10 mm to a circular metal-dielectric waveguide was 0.05 dB, the measured loss at a frequency 150 GHz do not exceed 0.1 dB.

V. SMOOTH TRANSITIONS

When designing a waveguide transitions main task is to choose the length and form of transition. In [5] theoretically justified the possibility of creating a smooth transition at length with small level of losses on the transformation on the working wavelength in the higher types of waves. In this article, calculated transition length and its form for the MDW at a wavelength 1 mm. Dimensions are jointed waveguides in the narrow part of 10 mm, and a wide portion - 20 mm. Following the notation of [5], we obtain a $a(0) = 5$ mm, and $a(L) = 10$ mm. The length of the smoothed, optimal transition L calculated by the formula (17.22) given in [5]. In this case, the transition length is 186 mm.

Profile of transition is calculated by a parametric formula

$$a(\zeta) = \sqrt{a(0)a(L)}e^{-\frac{1}{2}\ln q*\cos \pi\zeta}, \tag{9}$$

where $\zeta = z/L$, $q = a(L)/a(0)$, z − is the longitudinal coordinate of the transition that takes values from 0 to L. Calculated values of the transition profile listed in the table.

Table

$a(\zeta)$, мм	5	5.01	5.27	5.69	6.28	6.99	7.79	8.59	9.28	9.85	10
L, мм	0	18.6	37.2	55.8	74.4	93.0	111.6	130.2	148.8	167.4	186

Profile of optimal transition built on the calculation results of table is shown in Fig. 2. As can be seen from the figure, the dimensions of the smooth transition from the entrance and exit with the same size input and output portions of the wave guides. This makes possible to realize the transitions between waveguides of different cross sections without discontinuities, which in turn minimizes the conversion losses of the working mode to higher wave types. Thus, the calculated losses in conversion is 0.15 dB.
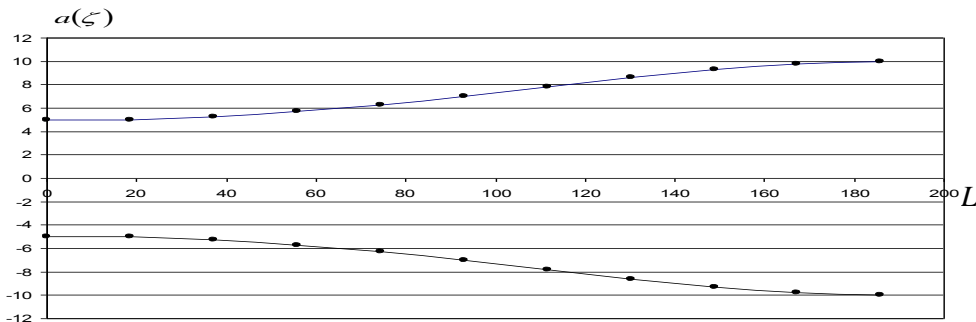
Fig. 2. Profile of optimal transition $\lambda = 1mm$, $a(0) = 5mm$, $a(L) = 10mm$ $\lambda mi = 1\ mm$,

VI. CONCLUSION

The results obtained allow to realize transitions for metal dielectric waveguide with different cross sections. This provides a low level of losses on the conversion.The proposed transition can be widely used in devices for various applications, working in the terahertz range.

VII. REFERENCES

[1] S. Afshar, T. Monro, D.Abbott et al. "Terahertz dielectric waveguides," Advances in Optics and Photonics, vol. 5, pp.169–215, 2013.

[2] V.K. Kiselev, A.A. Kostenko, G.I. Khlopov, M.S. Yanovsky, "Quasi-optical antenna-feeder systems," ed. Khlopov G.I., IPP "Contrast", 2013, 408 p.

[3] G.A. Sharov, "Waveguide devices for centimeter and millimeter waves," M: Goryachay liniya - Telecom, 2016, p. 639 (in Russian).

[4] R.S. Avakyan, K.R. Aghababyn, M.Ts. Ayvazyan, Yu.N. Kazantsev, R.M. Martirossian, "Complete set of waveguide elements for 120-180 GHz band," 16-th International Conference on Infrared and Millimeter Waves. Lausanne, 1991, pp. 642-643.

[5] B.Z. Katsenelenbaum, "The theory of irregular waveguides with slowly varying parameters," M .: Publishing House of the USSR Academy of Sciences, 1961, p.216 (in Russian).

[6] L.A. Vaynshteyn, Electromagnetic waves. - M .: AST, 1988, p. 440.

[7] Yu.N. Kazantsev, "Electromagnetic waves in dielectric rectangular channels," Radio engineering and Electronics, Radiotekhnika i Elektronika, vol. 23, no. 10, pp. 2060-2068, 1978. (in Russian. Translated in Radio Engineering and Electronic Physics).

[8] Meriakry V.V., Matveev R.F., Vaganov R.B. Multi-wavelength waveguides with random irregularities. Moscow: Sovetskoe Radio Publ., 162 p., 1972. (in Russian).

[9] Yu.N. Kazantsev, O.A. Kharlashkin, "Rectangular waveguides of class "hollow dielectric channel" Radiotekhnika i Elektronika, vol. 23, no 10, pp. 2060-2068, 1978, (in Russian. Translated in Radio Engineering and Electronic Physics).

[10] R.A. Valitov, S.F. Dyubko, A.V. Sokolov, "Sub-Millimeter Wave Engineering, Moscow" Sovetskoe Radio Publ., 477 p., 1969. (in Russian).

What is the Primary Target of the Action Millimeter Waves on Biological Objects?

V. Kalantaryan[1], R. Martirosyan[1], Yu. Babayan[2], H. Badalyan[3], S.Yayloyan[4]

[1]*Yerevan State University, dept.Microwave Radiophysics and Telecommunication, A.Manoogian str.1, 0025 Yerevan, Armenia*

[2]*National University of architecture and construction of Armenia, Teryan str.97, 0025 Yerevan,Armenia*

[3]*Yerevan State University, dept.General physics, A.Manoogian str.1, 0025 Yerevan, Armenia*

[4] *Institute of Radiophysics and Electronics, Alikhanian Brothers str. 1, 0203 Ashtarak, Armenia*

vkalantaryan@ysu.am

It has been experimentally shown that the low-intensity millimeter waves (MMWs) do not act directly on DNA molecules, and the influence takes place through a mediated influence of the MMWs on the water, stimulating structural change of the water shell surrounding the DNA. Thereby, it may conclude that the primary targets of the influence of the low intensity (non-thermal) nonionizing millimeter waves on the DNA water solutions are the water molecules.

I. INTRODUCTION

The assumption that changes in the DNA melting parameters under the influence of low intensity non-ionizing millimeter waves (MMWs) stipulated by the structure of water, is based on the fact that the resonant absorption frequencies of DNA are in the region of 2 to 9 GHz [1]. Hence, we assume that at a frequency of 64.5 GHz the changes in the values of temperature melting T_m and melting interval ΔT can not be due to the resonance absorption of DNA, i.e. the radiation not directly influences on the DNA. Consequently, the increase in the thermostability of DNA during the irradiation by MMWs with a frequency 64.5 GHz can be caused by their mediated influence through the water.

II. EXPERIMENTAL RESULTS AND DISCUSSION

DNA-samples were prepared in the irradiated only water-salt solution (buffer) for the confirmation of the mentioned fact. As a source of millimeter wave radiation the generators of coherent Extremely High Frequency oscillations G4-141 and G4-142 (Russian made) were used, operating in a range of frequencies of 38.5÷78.8 GHz. The exposure to millimeter waves was conducted in the far-field zone of cone-shaped antenna at a distance of 400 mm from the radiating plane of the antenna in the mode of continuous generation with incident power density (IPD) at the location of the object about 10 µW/cm**2**. The calculated value for the specific absorption rate (SAR) is approximately equal to 0.2 W/kg. Melting curves obtained for them do not practically differ from the curves obtained by irradiation of DNA solutions within the experimental error. Therefore, it can be assumed that the observed changes in the parameters of DNA-denaturation are caused just by changes in the structure of water arising due to exposure. This is also indicated by the results on the measurement of the density of aqueous salt solutions of DNA in the case of irradiating by MM-waves. For a control the densities of bidistilled water and water-salt solution were also measured before and after irradiation. The studies have shown that in the case of irradiation by pure water with a frequency of 64.5 GHz, its density does not practically change, while the density of the buffer and the DNA-solution increases. This indicates that the structural state of pure water does not change due to irradiation, since under these medium conditions the water molecules form a most stable, from a thermodynamic point of view, structure, and an increase in ordering after exposure becomes thermodynamically non-profit. Therefore, the density of water under these conditions should not be changed. In contrast, in the case of irradiation of the buffer and the DNA-solution by non-ionizing millimeter electromagnetic waves the dehydration of DNA and being present in solution ions of Na^+ occurs. Moreover,

most probably, the water molecules are involved in the formation of additional bonds with the salt ions or with functional and atomic groups of macromolecules, which leads to an increase in size of the ions or macromolecules, and the latter is the cause of density increase. The results of measurements of the density buffer and the DNA-solution are summarized in Table 1.

Table 1. Magnitude of solution density (g/cm³) before and after exposure of MM-radiation at 64.5 GHz.

Time of irradiation, min	Buffer	Buffer + DNA
0	0.999201 ± 0.000005	0.999232 ± 0.000004
30	0.999220 ± 0.000005	0.999242 ± 0.000005
60	0.999241 ± 0.000004	0.999269 ± 0.000004
90	0.999253 ± 0.000004	0.999291 ± 0.000005

As it can be seen from the table, there is almost the same dynamics of changing of the buffer and the DNA-solution densities. And the obtained data are in a good agreement with the results of DNA-melting. The dependence of the density of the DNA-solution on the temperature has been also studied, in the case of irradiation by duration of 90 and 120 min, to detect changes in the structure of water by irradiation, depending on temperature. It is found that with increasing temperature the density of the irradiated and non-irradiated DNA is reduced, but there is a significant difference between the solution of the irradiated and non-irradiated DNA.

As it can be seen from the Figure 1, the dependence of ρ on T (ρ is the difference between the solution densities for irradiated and non-irradiated DNA) increases slightly in the range of temperature 20<T<40°C, and in the range of 40<T<70°C it is observed a sharp decrease in ρ. With further increase of temperature (T>70°C) ρ sharply increases and as a result a minimum at a temperature of about 70°C on the curve is observed, that corresponds to the melting point of DNA. As it follows from the spectrophotometric melting curves, denaturation of DNA occurs in the interval of temperature changes 60<T<85°C. Therefore, this dependence may be caused by the fact that the dehydration of the irradiated DNA with increasing temperature inecreases to a greater extent than in the case of non-irradiated DNA, and at T=70°C, when a half of DNA is in a melted state, the increasing of dehydration degree of the irradiated DNA is the maximal. The further increase in temperature leads to a sharp increase of ρ. It is assumed that during irradiation some part of the "free" water molecules,
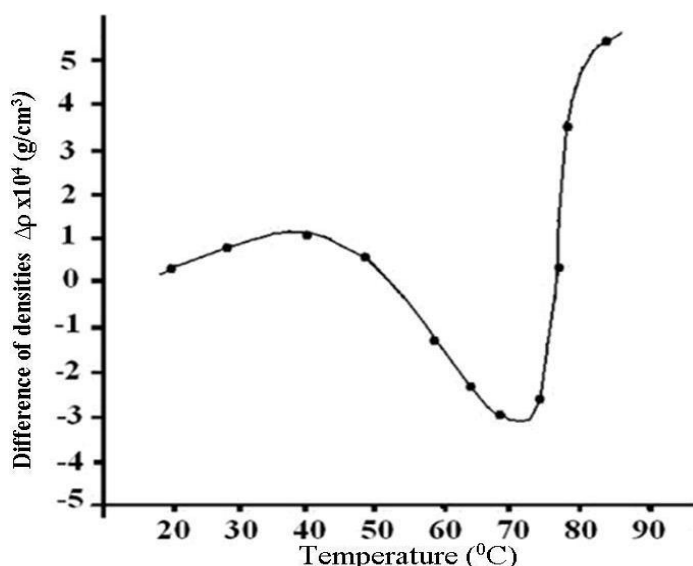
Fig. 1. Curve of dependence of $\Delta\rho$ difference of density of solutions irradiated for 90 min and non-irradiated DNA on temperature

which were involved in the hydrate structure of DNA, is released after exposure, leading to a sharp decrease in the density of the water-DNA system, while an analogous phenomenon does not occur in the case of non-irradiated DNA, and the density of the latter undergoes minor changes. Further, with an increase in temperature there is an increase of the lability both of macromolecule and hexagonal structures of water, so that in all likelihood these structures are involved in the hydration shell of macromolecule, and the density of this system increases.

III. CONCLUSION

  It is experimentally shown that millimeter range low intensity electromagnetic fields do not directly act on DNA molecules, and the influence takes place through a mediated influence of the EMFs on the water, bringing to a structure change of the water cover surrounding the DNA. We have also studied the change in the degree of dehydration of the irradiated and non-irradiated DNA on temperature in the range from 20 to 90^0C. It is shown that the increasing of dehydration degree of the irradiated DNA is the maximal at 70^0C when a half of DNA is in a melted state (melting point of DNA).

REFERENCES

[1]. B.N.Rodionov, "Energo-informational effect of low-energetic electromagnetic radiations on biological objects", New Medical Technologies Report, vol.6, no.(3-4), pp.24-29, 1999.

[2]. V.Kalantaryan, R.Martirosyan at al, "Effect on tumoral cells of low intensity electromagnetic waves", Progress In Electromagnetics Research Letters, vol. 20, pp. 97-105, 2011.

Dielectric Anisotropy of Human Bone
in Spectral Range 0.2 to 2.5 THz

A.S. Nikoghosyan[1], R.M. Martirosyan[1], T. He[2], J. Shen[2]

[1]*Yerevan State University, 1 Alex Manoogian, 0025 Yerevan, Armenia*

[2]*Capital Normal University, Key Laboratory for Terahertz Spectroscopy and Imaging, Beijing, 100048 China*

Terahertz time domain spectroscopy (THz-TDS) was applied to study anisotropic properties of a human jawbone in transmission geometry. The fiber femtosecond laser (Fx-100, IMRA) with a pulse width of 113 fs, a central wavelength of 800 nm and an average power of 120 mW was used as a laser source for pumping and detecting terahertz pulses. The polarization of the THz pulse is linear. The experimental results indicate that the refractive indices $n(\omega)$ and the absorption coefficients $\alpha(\omega)$ of a human jawbone change with the alteration of the direction of the linear polarization vector of the electric field of THz pulse relative to the axis of the plate of the human jawbone.

I. INTRODUCTION

A bone material is composed of an organic matrix of collagen fibers and mineral hydroxyapatite ($Ca_5(PO_4)_3OH$), nanoparticles. An average tooth dentin contains 70% hydroxyapatite crystals, 20% collagen (e.g., proteins), and 10% water. The organic constituents provide flexibility, whereas the mineral provides strength. Due to the specific arrangement of mineral platelets and collagen fibrils with respect to the main axis in case of a long bone, signals relative to vibrational units of both mineral and collagen can result highly anisotropic. Up to now, very few studies have been conducted concerning the study of the human bones [1, 2] and its anisotropy by THz radiation [3].

Many biological tissues are structurally anisotropic. Tissue birefringence results from the linear anisotropy of fibrous structures, which forms the extracellular media. The refractive index of a medium is higher along the length of fibres than along their cross section [3]. A tissue structure is a system composed of parallel cylinders that create a uniaxial birefringent medium with the optic c- axis parallel to the fibrils (ciliders) axes (Fig.1a). A structure of parallel dielectric cylinders immersed in isotropic homogeneous ground substance behaves as a positive uniaxial birefringent medium. The hidroxyapatite can be found in space between cylinders - collagen fibrils periodically separated by a tiny gap from 1 nm to 40 nm (Fig.1b).

In this paper we report the results obtained from a study of dielectric anisotropic properties of a human jawbone in transmission geometry using THz time-domain spectroscopy (THz -TDS).

.

$$\Delta n_{oe} = (n_e - n_o) > 0$$

(a)   (b)

1nm & 40 nm gaps
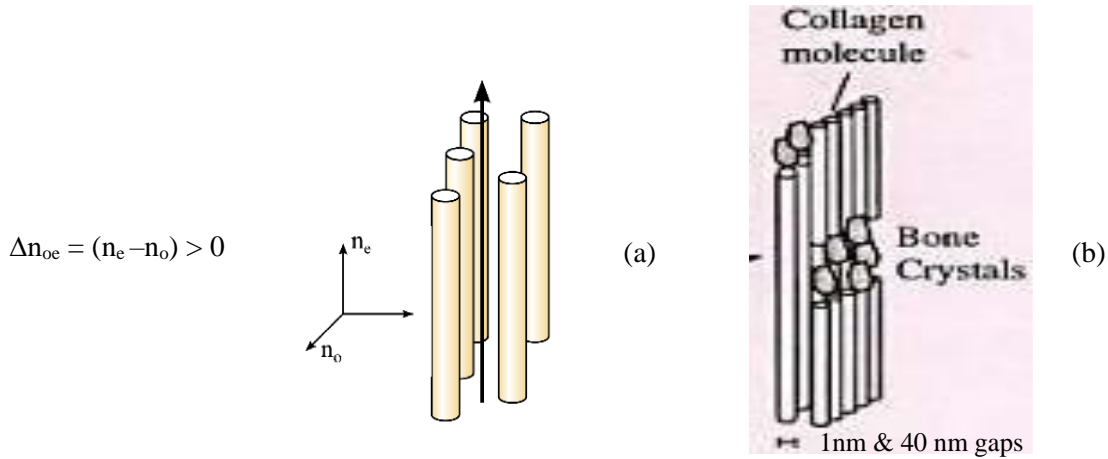
Fig.1. System of long dielectric cylinders with diameters ranging from 20 to 400 nm (a). The hidroxyapatite can be found in space between cylinders - collagen fibrils periodically separated by a tiny gap from 1 nm to 40 nm (b).

II. EXPERIMENTAL TECHNIQUE

A schematic arrangement of the THz-TDS system, demonstrating the principal configuration used to obtain THz spectral data, is shown in Fig.2. The fiber femtosecond laser (Fx-100, IMRA) with a pulse duration of 112 fs, a central wavelength of 800 nm and an average power of 120 mW was used as a laser source for pumping and detecting terahertz pulses. The laser output, in the form of high repetition frequency - 75 MHz, is divided into two optical paths - the pump and probe beams. The pump beam is focused into a gap between biased electrodes deposited upon the surface of gallium arsenide. The pumping pulses have photon energy (1.43 eV) above the direct band-gap of the GaAs thas inducing conductivity changes. Electron–hole pairs are created by each laser pulse in a semiconductor, which, when accelerated by the bias field, act as a transient current source. The transient current radiates a sub-picosecond, single-cycle coherent THz electric pulse, Fig.3a. The THz pulse from photoconductive antenna (PCA) is emitted in a dipole like pattern. The resulting radiation is polarized along the direction of the bias field. The polarization ratio is usually better than 10:1.
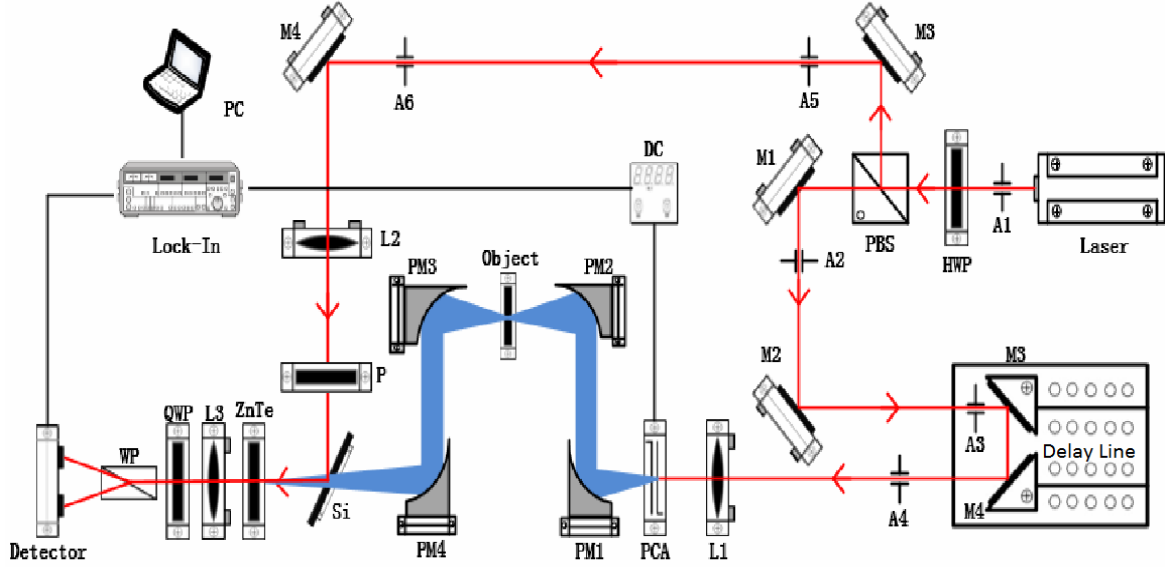
Fig.2. Schematic diagram demonstrating the principles of a THz-TDS experiment

The THz pulse after PCA is collected and directed to the object using parabolic mirrors (PM). The THz radiation transmitted through the object is then directed by two PM towards a detector. A small fraction of the pump optical beam - probe beam, was used for coherent detection of transmitted radiation from the object (jawbone) using a dynamic free-space electro-optic cell. This consists of electro-optic crystal – ZnTe with a (110) crystal orientation, a quarter-wave plate providing optical bias, and the Wollaston prism (WP) as the analyzer. Thus, the whole system represents a version of a coherent pump-probe spectroscopic setup [4].

The electro-optic sampling method is widely applied for the coherent detection of THz pulse due to its short response time, high sensitivity and wide bandwidth. For the EO sampling, the phase-matching condition (Fig.3a,b) requires the group velocity of probe pulse equal to the phase velocity of THz pulse. The phase mismatch is defined as [5]

$$\Delta k = \frac{f_{THz}}{c}(n_{THz}(f_{Thz}) - n_g(f_{probe}))$$

The amplitude of detection response is proportional to the thickness of crystal ZnTe at the phase-matching condition, but a thicker crystal results in the reduction of bandwidth of THz pulse. The compromise should be made between the detection response and bandwidth. We used a ZnTe crystal of 1 mm thickness, ipso facto to provide the coherent detection of THz pulse in spectral range from 0.2 THz to 2.7 THz.

Using interferometric control over the optical delay between the pump and probe pulses, the time domain dependence of THz electric field is recorded. The balanced electro-optic detection method provides an

excellent signal to noise ratio >1500 (to a noise-limited frequency of 3 THz) by the use of phase sensitive amplification with a lock-in amplifier. Two spectra, THz field and phase, are processed via a fast Fourier transform from originally obtained time-domain dependence. Although the spectrum of bone [2] in THz region was reported, the response of the jawbone tissue to polarized light is still unknown.

THz time-domain transmission spectroscopic properties of the jawbone is presented in Fig. 3 and Fig. 4.
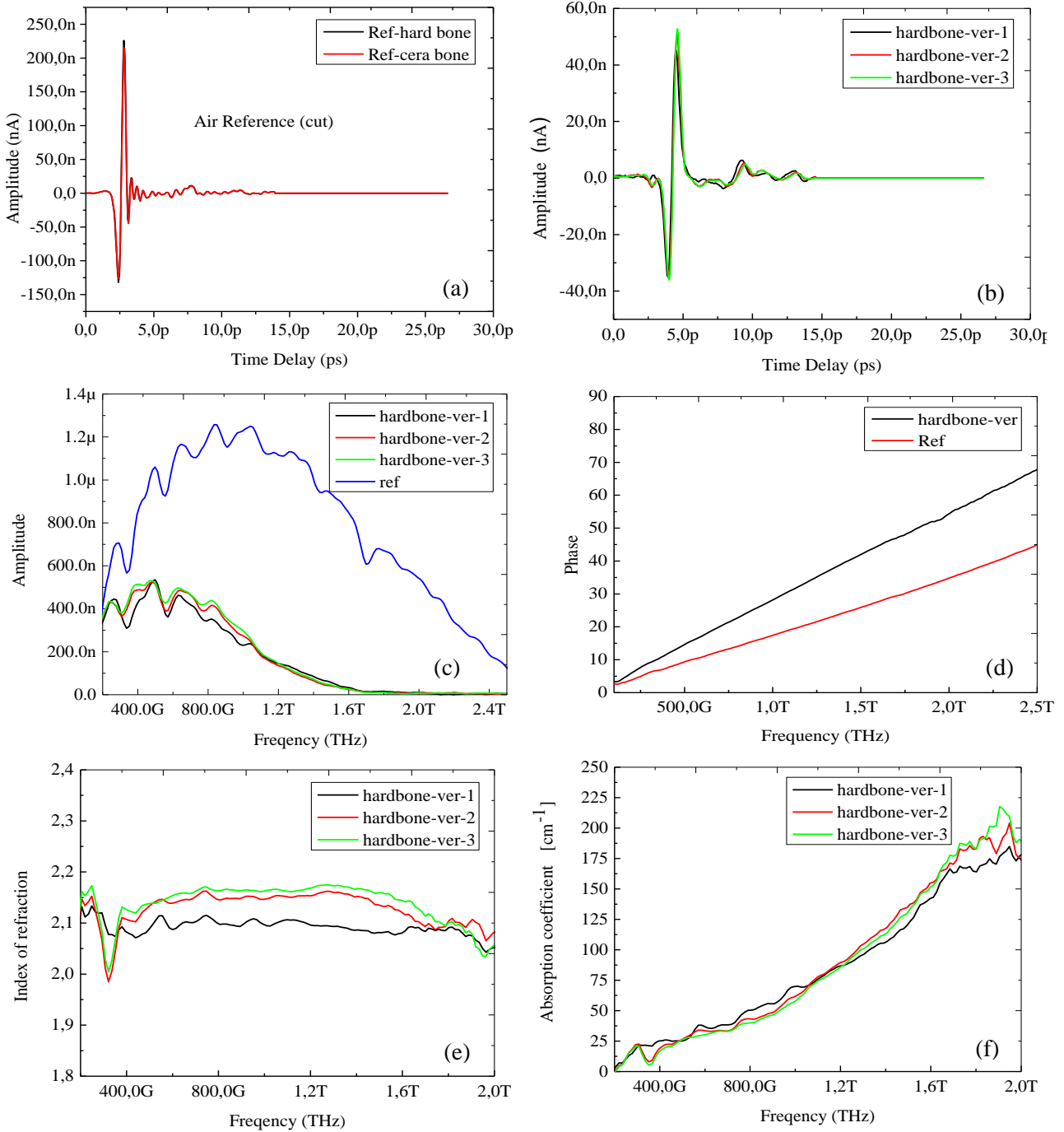
Fig.3. Temporal waveforms of THz pulses transmitted through (a) the air and (b) jawbone, THz amplitude spectra of the fields after a FFT (c); phase-frequency response (d); refractive index (e) and absorption coefficient human jawbone (f). The THz pulse polarization is parallel to the bone axis.

.

Temporary forms of the reference pulse $E_1(t)$ (Fig. 3a), transmitted through free space - the air, and then the pulse $E_2(t)$ passed through the jawbone of thicknesses d = 0.44 mm (Fig. 3b) were measured. To

demonstrate the reproducibility of the experiment on Fig. 3 (b, c, e, f) the curves of three consecutive measurements are given.

The index of refraction **n(ω)** and absorption coefficient **α(ω)** for different directions of the laser polarization are depicted in Fig.4c and Fig.4d.
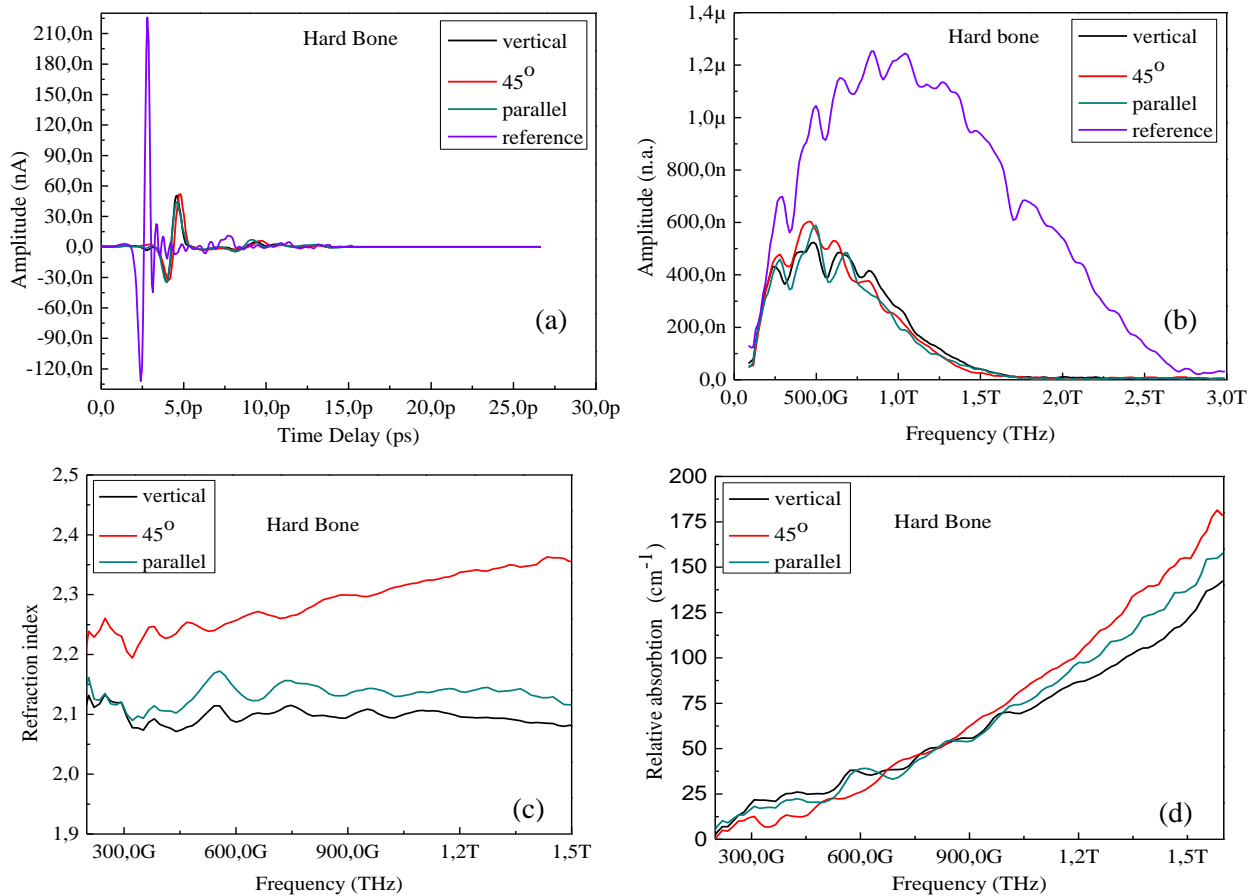
Fig.4. The index of refraction n(ω) and absorption coefficient α(ω) for different directions of the laser polarization (vertical, 45°, and parallel to the bone axis), in the spectral range of 0.2-2.5 THz.

III. CONCLUSIONS

Dielectric anisotropy of a human jawbone has been studied using THz time-domain transmission spectroscopy in the wide frequency range 0.2–2.5 THz. The refractive index n(ω) and absorption coefficient α(ω) for different directions of the THz pulse polarization were measured. The difference n(ω) and α(ω) in different directions at any frequency can be associated with the structural anisotropy of a bone that is, both with different dimensions of the bone particles and a specific tissue structure. This is the first representation of the frequency-dependent refractive index n(ω) and absorption coefficient α(ω) of jawbone.

IV. REFERENCES

[1] R. A. Magal,. N. Reznikov, R. Shahar, S. Weiner, "Three-dimensional structure of minipig fibrolamellar bone: Adaptation to axial loading", J. Struct. Biol., vol.186, pp. 253–264, 2014.

[2] E. Berry, A. J. Fitzgerald, N. N. Zinov'ev, G. C. Walker, S. Homer-Vanniasinkam, C. D. Sudworth, R. E. Miles, J. M. Chamberlain, M.A. Smith, "Optical properties of tissue measured using terahertz pulsed imaging", Proceedings of SPIE: Medical Imaging 2003: Physics of Medical Imaging, 5030. pp. 459-470.

[3] V. V.Tuchin, "Tissue Optics and Photonics: Biological Tissue Structures", J. of Biomedical Photonics & Eng, vol. 1, no.1, pp. 3-21, March 2015.

[4] A. S. Nikoghosyan, H. Ting, S. Jingling, R. M. Martirosyan, M. Yu.Tunyan, A. V. Papikyan, A. A. Papikyan, "Optical properties of human jawbone and human bone sabstitute CERABONE® in the terahertz range", Journal of Contemporary Physics (Armenia Ac. Sci.), vol. 51, no. 3, pp. 256-264, 2016.

[5] A. Yariv, Inroduction to Optical Electronics. Moscow, "Высшая школа", 1983.

Terahertz Pulses Generation via Optical Rectification in LiNbO₃ Crystal by Step-Wise Phase Mask

G. K. Abgaryan, Yu. H. Avetisyan, A. H. Makaryan, V. R. Tadevosyan

Microwave Radiophysics and Telecommunications Dept., Yerevan State University, Alex Manoogian 1, 0025 Yerevan, Armenia.

Generation of the broadband terahertz (THz) radiation via optical rectification of femtosecond laser pulses in the single-domain lithium niobate crystal equipped with the step-wise mask (SWM) was investigated. It was shown that by using SWM is possible to achieve phase matching for the spectral components of the terahertz pulse in the wide frequency range, thus ensuring efficient conversion of laser radiation in the terahertz range.

The efficiency of the THz radiation, depending on the parameters of SWM was investigated. The radiation pattern of THz generation and the temporal characteristics of THz pulses for different numbers of the step of SWM were analyzed. It was shown that with increasing number of SWM steps, the magnitude of THz field strongly grows and shrinking at the same time the radiation pattern.

I. INTRODUCTION

The electromagnetic waves of terahertz range ($\sim 0.1 \div 10$ THz) occupy an intermediate region between the microwave and infrared frequency ranges and are of considerable interest for various applications in the fields of the high-speed communications, molecular spectroscopy, medical diagnostics, in the security systems, for visualization of objects, and etc. [1, 2]. Despite the big breakthrough of the last decades in the field of terahertz radiation sources, this area remains one of the technically poorly secured part of spectrum. This encourages many researchers to seek new methods to create the highly effective and affordable terahertz sources with the necessary parameters for the variety of applications. For many applications there is a need for the broadband THz pulses. In particular, the ultrabroadband terahertz video pulses are ideal for the time-domain spectroscopy technique [3, 4].

The difference frequency generation and the optical rectification of femtosecond laser pulses are the widely used methods for generating the terahertz radiation [4, 5]. It was shown in [6–8] that using the wide-aperture beams in the transverse direction of periodically polarized lithium niobate crystal one may obtain the quasi-monochromatic generation of terahertz radiation with the center frequency determined by the spatial period Λ of periodically polarized lithium niobate crystal (PPLN). The periodically inverted domain structure of the PPLN crystal is used to produce the constructive interference of terahertz waves radiated from the separate regions of the PPLN. However, the oscillation frequency in this case is predetermined by the spatial period of the PPLN domain structure and therefore it cannot be changed after the sample preparation.

To overcome this disadvantage in the generation of narrow-band terahertz radiation, the single-domain lithium niobate crystal with the variety of the phase masks (PM) recently has been used. With the shadow or binary PM located in front of the single-domain nonlinear LiNbO₃ crystal, the virtual quasi-periodic structure is formed that provides the phase matching for the specific frequency of terahertz radiation. The frequency of the radiation can be tuned by change of the spatial period Λ of PM.

However shadow or binary PM cannot be used for generation broadband THz pulses. To overcome this problem in [8] was presented a new method for efficient THz-pulses generation by OR in the single-domain lithium niobate crystal. It's based on using the step-wise mask (SWM) (Fig. 1), which provide quasi-linear time delay of femtosecond laser pulses along cross-section of the optical beam, thus forming a tilted amplitude front of beam.

II. BROADBAND PHASE MATCHING BY USING SWM

In the case of SWM, in contrast to the diffraction grating, the formed laser beam until the nonlinear crystal extend not in the air, but in mask, wherein wavelength of the radiation is less than in the air. This reduces the beam distortion associated with diffraction scattering.

Every crystal layer (along direction of the laser beam propagation) radiates THz-pulses at the Cherenkov angle. Due to using of step-wise mask it is possible to have a structure where these THz-pulses reach exit surface of the crystal simultaneously [8].
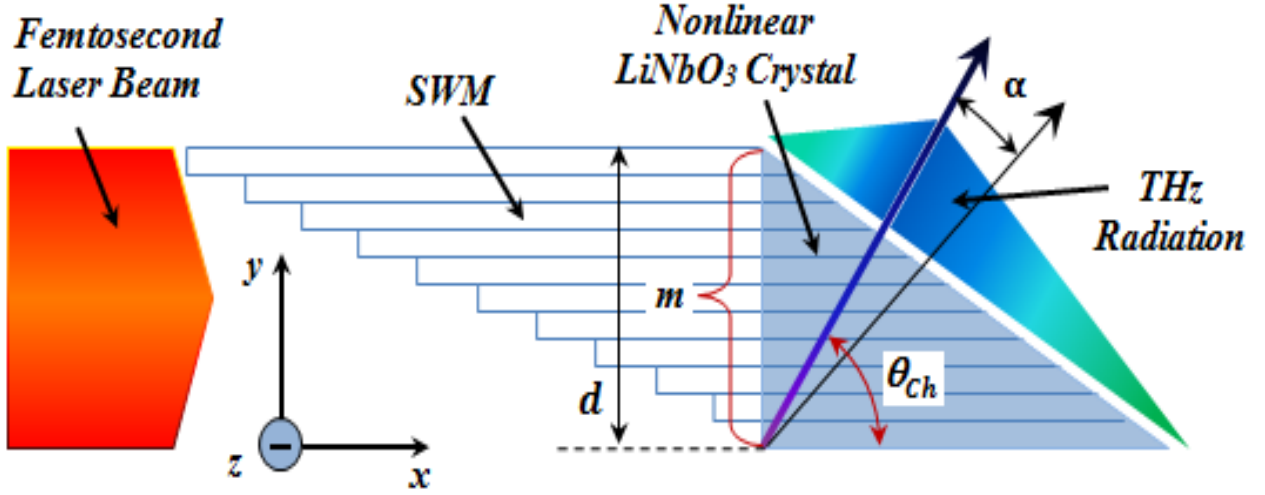
Fig.1. The schematic representation of the LiNbO₃ crystal with the SWM for the efficient generation of broadband terahertz pulses.

Taking into account the losses of terahertz radiation in the nonlinear crystal, there is no sense to use the laser beams with the transverse dimensions greater than $1/\beta$ (β is the absorption coefficient). Therefore, it is reasonable to restrict also the lateral dimension d of the nonlinear crystal ($d_{max} = 1/\beta$). Using as the SWM material the crystalline quartz with $d = 1$ mm size, we obtain for the mask length $l = 8$ mm. To avoid the diffraction distortions caused by the exciting laser pulses, the mask layers may be separated from each other by the thin mirror coatings.

In present work the dependence of angular distribution of the spectral components and the temporal form of THz pulses on the step size of SWM were investigated.

III. THE SPECTRAL AND TEMPORAL PARAMETERS OF THZ PULSES GENERATED BY USING SWM

The spectral composition and angular distribution of the THz radiation are strongly dependent on the size of SWM steps and on the dimensions of nonlinear crystal.

The expressions for the angular distribution of spectral components and a temporary form of terahertz radiation have the following form [9]:

$$S(\alpha, f, m) = S_0(f)\left(\sum_{k=1}^{p} \frac{k \cdot q}{p} \cos\left[k\varphi(f,\alpha) \right] + \sum_{k=p+1}^{m} (m-k)\cos\left[k\varphi(f,\alpha) \right] \right) \qquad (1)$$

$$E(\alpha, t, m) = \int_{\Delta f} S_0(f)\left(\sum_{k=1}^{p} \frac{k \cdot q}{p} \cos\left[k\varphi(f,\alpha) \right] + \sum_{k=p+1}^{m} (m-k)\cos\left[k\varphi(f,\alpha) \right] \right)\cos(2\pi f \cdot t)df \quad , \qquad (2)$$

where

$$\varphi(f,\alpha) = \left(\frac{2\pi d \cdot \sin(\alpha)}{c \cdot m \cdot \cos\theta_{ch}} \right) f \quad , \qquad (3)$$

$\theta_{ch} = \arccos\left(n_{op}/n_{THz}\right)$ - is the Cherenkov angle for THz radiation, $S_0(f)$ -is the spectrum of the THz pulse emitted from the elementary cell of nonlinear crystal and Δf - is the THz band, for which the phase matching condition performed ($f_{max}\left[\text{THz}\right] = 3m/100d\left[\text{mm}\right]$).

From (1) and (2) follows that the main part of terahertz wave is emitted perpendicular to the output surface of the nonlinear crystal ($\alpha = 0$).

The SWM parameters should be chosen based on the following considerations. To ensure the propagation of laser beam in the SWM without diffraction, the size of mask step should be essentially larger than the wavelength of laser radiation. However, to ensure the constructive interference for all radiated terahertz pulses from the different layers of the crystal, the step size of the SWM cannot be chosen greater than the half-wavelength of terahertz radiation [7].

The angular dependence of the magnitude of THz radiation for different values of the number of SWM step m in the wave zone when the transverse dimension of the phase mask is $d = 1$ mm is shown in Fig. 2a. Here is assumed that the spectrum $S_0(f)$ has a Gaussian shape centered at 0.5 THz ($(S(f) = S_0 \cdot \exp\left(f - 0.5\right)^2)$.

In Fig. 2b the dependence of the temporal shape of THz pulse emitted perpendicular to the output surface of the nonlinear crystal ($\alpha = 0$) on the value m is presented.
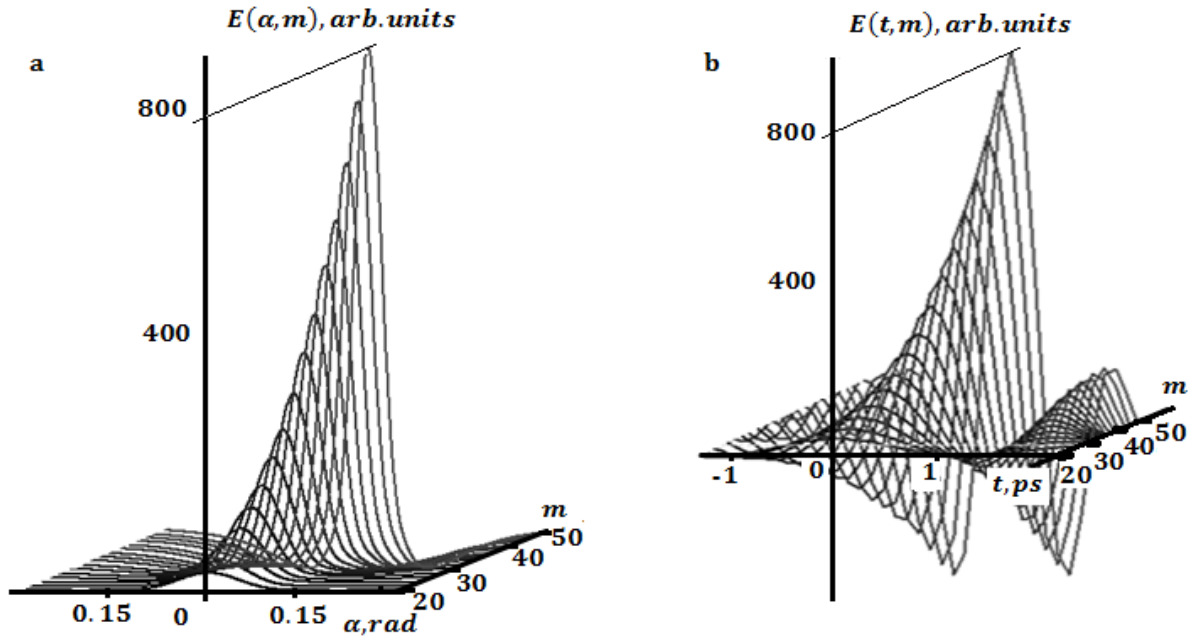
Fig. 2. (a) Angular dependence of the magnitude of THz radiation for different values of m. (b) Dependence of the temporal shape of THz pulse on m at $\alpha = 0$.

Fig. 2 shows that with the increase in the number of steps of SWM, the magnitude of THz field strongly grows and shrinking at the same time the radiation pattern. This is due to the fact that with the increase in the number of steps at a constant transverse dimension of SWM d the steps dimensions decrease, thereby providing the phase matching in a wide band of THz spectrum. This also leads to shortening of the pulse duration.

The increase of the peak value of the THz field depending on the steps number, at the transverse dimension of SWM $d = 1$ mm, is given in Fig. 3a.

Increasing of the transverse dimension of SWM d at a constant number m of steps leads to the increase in the size of a single step, which reduces the maximum frequency f_{max} for which the phase matching can be provided. For example, for SWM with size $d = 1$ mm with different numbers of steps m = 20, 30, 40. 50, phase matching can be provided respectively till the frequencies 0.6 THz, 0.9 THz, 1.2THz and 1.5 THz.
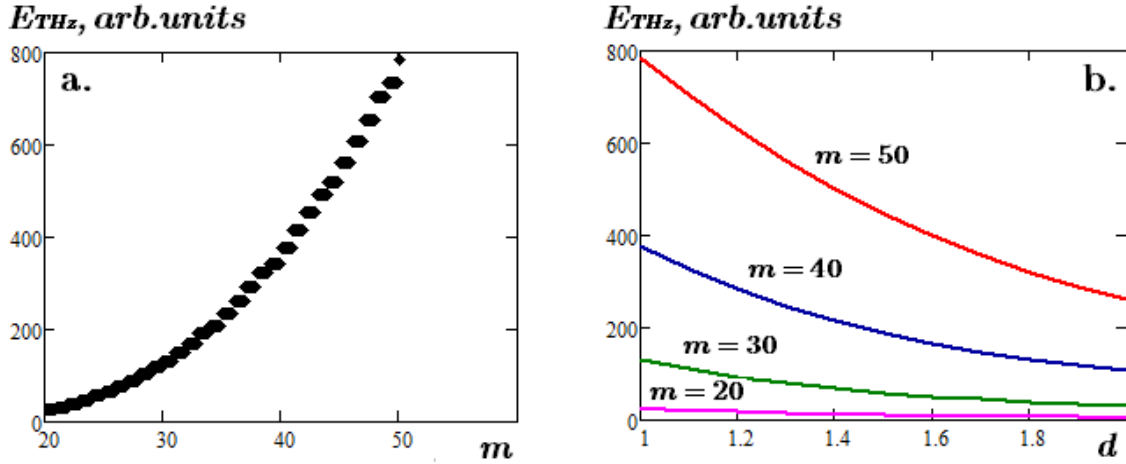
Fig. 3. Dependence of the peak value of the THz field (a) on the number *m* of SWM step, (b) on the size of the input face of the nonlinear crystal, for different values of *m*.

For **d** =2 mm the maximum phase matching frequency reduced accordingly twice 0.3 THz, 0.45 THz, 0.6THz and 0.75 THz. Thus at the increasing of the transverse dimension of SWM the spectrum of THz pulse is depleted, and despite the fact that the power of the laser pulse is increased by increasing the size of the beam, THz radiation decreases still (Fig. 3b).

IV. CONCLUSION

The generation of broadband terahertz radiation via optical rectification of femtosecond laser pulses in the single-domain lithium niobate crystal equipped with the SWM is investigated. It is shown that by using SWM is possible to achieve phase matching for the spectral components of the terahertz pulse in the wide frequency range, thus ensuring efficient conversion of laser radiation to the terahertz range.

The angular distribution of THz field and the temporal form of THz pulses in the far-field region were investigated. It is shown that the different temporal forms of THz pulses can be obtained by changing number of steps of the SWM.

V. REFERENCES

[1] J. Federici and L. Moeller, "Review of terahertz and subterahertz wireless communications", J. Appl. Phys., vol.107, no.11, p.111101, 2010.
[2] S. Yoshida, K. Suizu, E. Kato, Y. Nakagomi, Y. Ogawa, and K. Kawase, "A high-sensitivity terahertz sensing method using a metallic mesh with unique transmission properties", J. Mol. Spectrosc., vol.256, no.1, pp.146–151, 2009.
[3] G. Kh. Kitaeva, "Terahertz generation by means of optical lasers", Laser Phys. Lett., vol.5, no.8, pp.559–576, 2008.
[4] M. Tonouchi, "Cutting-edge terahertz technology", Nat. Photonics 1(2), pp.97–105, 2007.
[5] Y.-S. Lee, Principles of Terahertz Science and Technology (Springer, 2009).
[6] C. Zhang, Yu. Avetisyan, A. Glosser, I. Kawayama, H. Murakami, M. Tonouchi, "Bandwidth tunable THz wave generation in large-area periodically poled lithium niobate", Optics Express, vol.20, no.8, pp.5784-5790, 2012.
[7] C. Zhang, Yu. Avetisyan, G. Abgaryan, I. Kawayama, H. Murakami, M. Tonouchi , "Tunable narrowband terahertz generation in lithium niobate crystals using a binary phase mask", Optics Letters, vol. 38, no. 6, pp. 953-955, 2013.
[8] G.K. Abgaryan, Yu.H. Avetisyan, A.H. Makaryan, V.R. Tadevosyan, "Broadband THz Generation in Lithium Niobate Crystal by Step-Wise Phase Mask", Proc. of int. conf. on "Microwave and THz Technologies and Applications", pp. 13-16, 2015.
[9] G. K. Abgaryan, Yu. H. Avetisyan, A. H. Makaryan, V. R. Tadevosyan, "Investigation of parameters of terahertz pulses generated in single-domain LiNbO$_3$ crystal by step-wise phase mask", J. of Contemporary Physics , vol. 51, no. 1, pp 35-40, 2016.

Optical Properties of Human Jawbone and CERABONE® in the Terahertz Range

A.S. Nikoghosyan[1], T. He[2], J.Shen[2], R.M. Martirosyan[1], M.Yu.Tunyan[3], A.V. Papikyan[3], A.A. Papikyan[3]

[1]*Yerevan State University, 1 A. Manoogian, 0025 Yerevan, Armenia,*
[2]*Capital Normal University, Key Laboratory for Terahertz Spectroscopy and Imaging*, Beijing, 100048 *China*
[3]*Yerevan State Medical University, 2 Koryun St, 0025 Yerevan, Armenia*
nika@ysu.am

The refractive indices n(ω) and absorption coefficients α(ω) of the human jawbone and bone substitute Cerabone® were determined in vitro by the terahertz time-domain spectroscopy in a wide frequency range from 0.2 to 2.5 THz. It is shown that the refractive index of the human jawbone changes between the values of 2.24 and 2.36, and Cerabone® between 2.4 and 2. 65. Depending on frequency the absorption coefficient of the human jawbone increases from 1.7 cm^{-1} to 178.5 cm^{-1}, showing several resonance absorption lines after 1.6 THz. The absorption coefficient of Cerabone® increases from zero to 80 cm^{-1}, and the resonance absorption occurs at 1.7 THz. The obtained results allowed us to determine the proximity of the physical properties of the Cerabone® with the natural bone matrix.

I. INTRODUCTION

Recent advances in medical research are aimed at solving the problems associated with increasing the duration and quality of human life. The developed technologies contribute to the creation of materials for artificial organs and tissues. Currently, the treatment, repair and replacement of various parts of the human body including skin, muscle, blood vessels, nerves, bone apply a variety of materials – metals, polymers, ceramics.

In action on the human body implants are classified as: 1) toxic (when the surrounding tissues mortify at the contact), these are most metals; 2) bio-inert (nontoxic but biologically inactive) - based ceramics Al_2O_3, ZrO_2; 3) bioactive (nontoxic, biologically active, fused with the bone tissue) - the type of biopolymer composites based on calcium phosphate. The widely applied bioactive materials are bio-glass and materials based on hydroxyapatite (HAP) [1]. The chemical formula for dense and porous ceramic hydroxyapatite is HAP- $Ca_{10}(PO_4)_6(OH)_2$ (Fig.1a). Bio-ceramic hydroxyapatite is completely absorbed by a living organism. A few years after implantation of hydroxyapatite, it should be completely dissolved and be replaced by a new bone, that is, the prosthesis should be replaced by the newly formed bone tissue. This is the case of the ideal type of artificial implant, since the problems of strength and biocompatibility do not arise at all. However, the negative effect of the implant is that the "resorption" - in the blood, lymph and tissue fluids pass large amounts of calcium (Ca) and phosphorus (P), and it is unknown how the Ca and P may affect the human body as a whole.

Cerabone® natural bovine bone grafting material (Fig.1b) of the German production is produced from bovine bone mineral phase, which has maximum similarity to human bone (chemical composition, porosity, and surface morphology). During the manufacturing process based on the high-temperature heating, all the organic components, proteins are removed, eliminating the potential for immunological reactions. Basic properties of Cerabone® are as follows: (a) slowly dissolves and quickly integrates with the bone; (b) shows a three-dimensional long-term stability of the implant; (c) does not lead to inflammatory reactions; (g) exhibits the optimal cell adhesion and the absorption of blood; (b) safe and sterile; (b) easy to handle.

The improvement of artificial materials will lead to the emergence of new alternatives and thus will contribute to the improvement of existing methods for treating many diseases. Artificial bone should correspond as precisely as possible the replaced part of the skeleton with the chemical and physical properties. Unfortunately, the level of modern technology does not allow to create a material that is entirely consistent with the natural bone matrix.

The most widespread practical use of terahertz (THz) waves (frequency range from 0.1 to 30 THz) is found in THz time-domain spectroscopy and in the THz imaging [2, 3]. It is known that the time of

vibrational motion of biological molecules have the order of picoseconds, and therefore, the frequency of vibrations is in the terahertz frequency range. Intermolecular interactions are usually weaker than the intramolecular and only THz spectroscopy in the time domain is sensitive to resolve their spectrum in the THz range. THz wave is of non-invasive (since the photon energy of terahertz waves at several orders of magnitude is smaller than the photon energy of the X-ray wavelength) and non-contacting nature, which can penetrate into the non-conductive materials and to provide additional spectroscopic data for the accurate diagnosis and analysis of the material.

In the present work we used the method of the THz time domain spectroscopy (TDS), to research the proximity of the physical properties of the Cerabone® (bone transplantation material) with the natural bone matrix - the human jawbone - in the frequency range 0.2–2.5 THz.
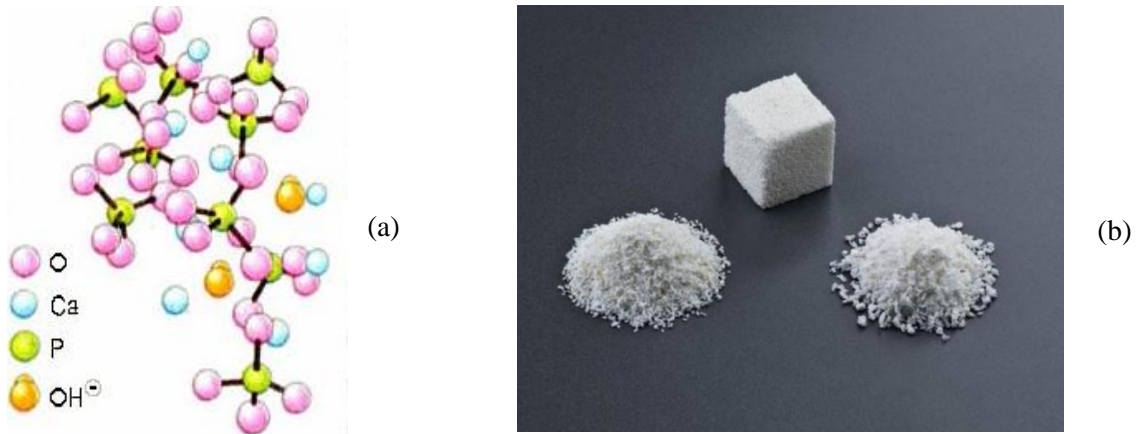
Fig.1. Detail of the crystal lattice the bioactive material – hydroxyapatite $Ca_{10}(PO_4)_6(OH)_2$ (a), and photo Cerabone®(b).

II. EXPERIMENTAL RESEARCH OF CERABONE® AND HUMAN JAWBONE BY THz SPECTROSCOPY METHOD

THz spectroscopy method in the time domain allows to register the temporary form of the THz pulse after its interaction with the sample, and to determine the complex spectrum of the material using the fast Fourier transform. However, to determine the physical properties of the sample, the absorption coefficient α (ω) and the refractive index $n(\omega)$ over the entire spectral THz frequency range, it is necessary to conduct two measurements. Temporary forms of the reference pulse $E_1(t)$, transmitted through free space - the air, and then the pulse $E_2(t)$ passed through the test materials (Fig. 2, Fig.3) were measured.

To measure optical properties of Cerabone® and human jawbone a THz time-domain spectrometer was applied. The fiber femtosecond laser (Fx-100, IMRA) with a pulse width of 113 fs, with a central wavelength of 800 nm and a repetition rate of 75 MHz and a power of 120 mW was used as a laser source for pumping and detecting terahertz pulses. Radiation from the fiber femtosecond laser was divided into two parts by a polarizing beam splitter: the pump and probe beams. The pump beam after the delay line was focused on GaAs photoconductive antenna. Antenna was used as a source of subpicosecond pulses of THz radiation. THz radiation, using parabolic mirrors, was collected and focused on the test material. THz radiation passed through the test material was directed to the ZnTe crystal. The coherent detection of temporal shape of the electric field of THz pulses was performed using cell, which consisted of electro-optical ZnTe crystal orientation (110), 1 mm thick, $\lambda/4$ plate and a polarizer, a Wollaston prism, separating the s- and p-polarization. The detector was controlled with a probing beam, the response of which was proportional to the amplitude and sign of the electric field of the THz pulse. Amplitude $\left| \dot{T}(\omega, \dot{n}) \right| = \left| \dfrac{\dot{E}_2(\omega)}{\dot{E}_1(\omega)} \right|$ and phase $\Phi(\omega) = \Phi_2(\omega) - \Phi_1(\omega)$ of complex transfer function of the sample $\dot{T}(\omega)$ obtained experimentally from the

relationship of Fourier transform of the measured terahertz fields $E_1(t)$ and $E_2(t)$ and $\Phi_2(\omega)$, $\Phi_1(\omega)$ [4]. The refractive index and the absolute absorption coefficient of the substance in a frequency range from 0.2 to 2.5 THz are obtained from the expressions

$$n(\omega) \cong 1 + \frac{c}{\omega d}\Phi(\omega), \qquad \alpha(\omega) = -\frac{2}{d}\ln\left[\left|\dot{T}(\omega)\right|\frac{\left[1+\dot{n}(\omega)\right]^2}{4\dot{n}(\omega)}\right]$$

The temporal waveforms of THz pulses are shown in Fig. 2 (a) as the references. The Fig. 2 (b) and Fig. 3 (a) are the THz pulses passing through the jawbone and Cerebone, respectively. The THz waveform in frequency is shown in Fig. 2(c) and Fig. 3(b). The absolute absorption and the refractive index of the jawbone and the Cerebone are obtained and shown in Fig. 2(d,e) and 3(c.d), respectinvely.

51
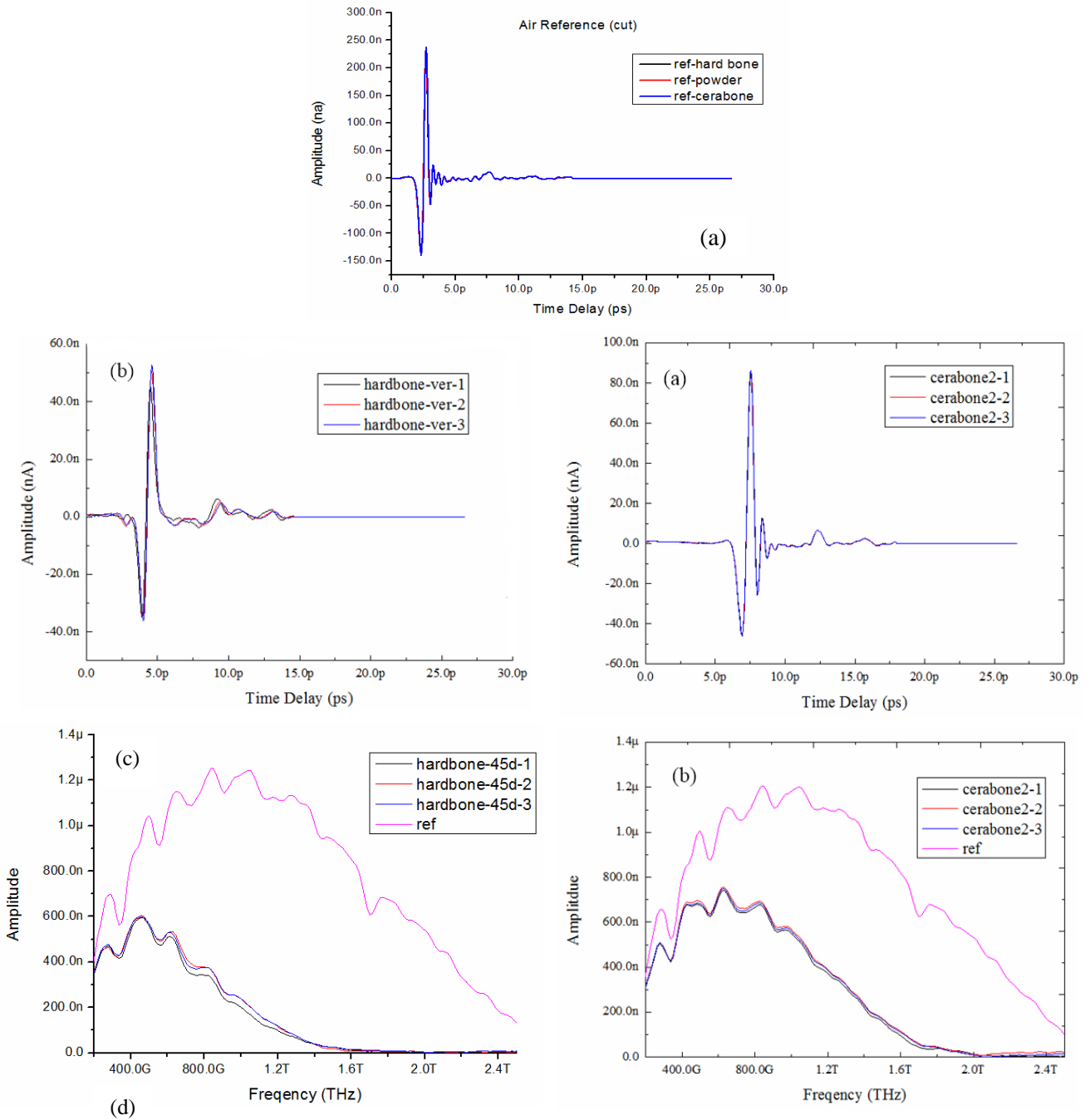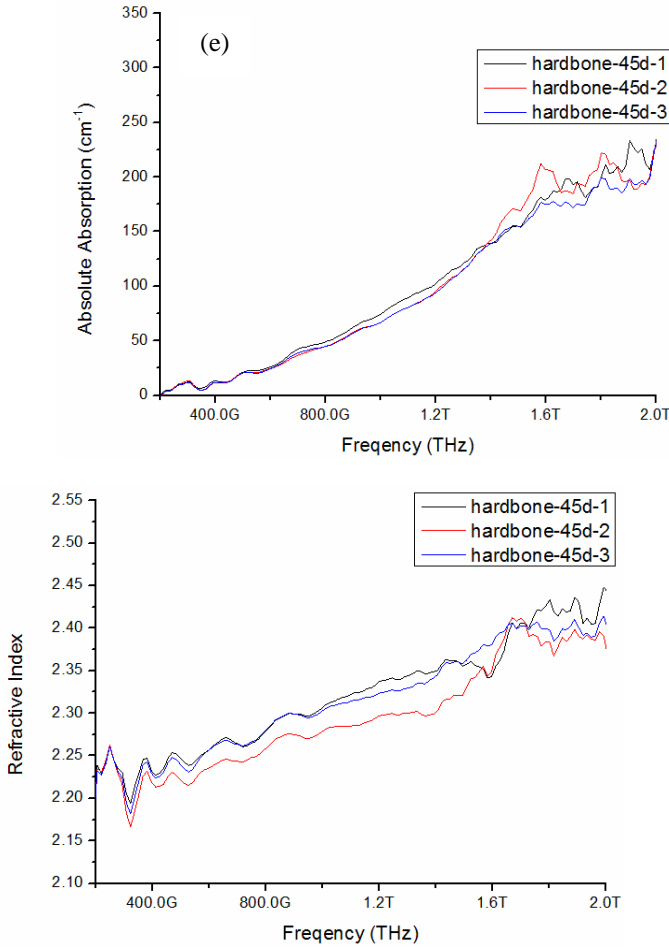
Fig.2. Temporal waveforms of THz pulses transmitted through (a) the air and (b) jawbone, and its amplitude spectra after a FFT (c); absorption coefficient (d) and refractive index human jawbone (e).
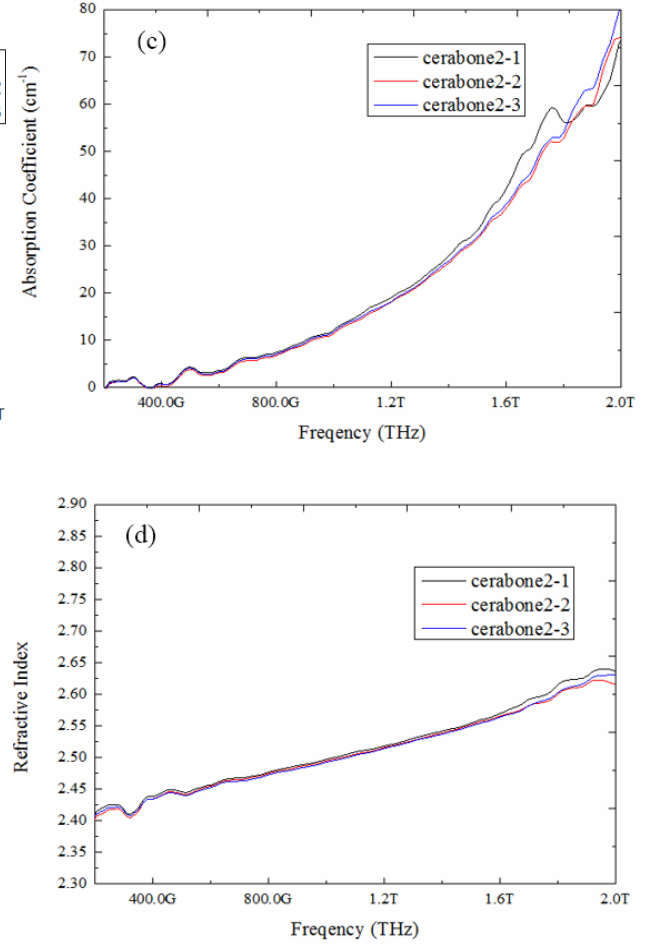
Fig.3. Temporal waveform of the THz pulse transmitted through Cerabone® (a), and its spectrum after a Fast Fourier Transform (b), the absorption coefficient (c) and refractive index Cerabone® (d).

III. CONCLUSION

It is shown that the refractive index of the human jawbone changes in a wide frequency range from 0.2 to 2.5 THz between the values of 2.24 and 2.36, and Cerabone® between 2.4 and 2.65. The absorption coefficient of the human jawbone depending on frequency increases from 1.7 cm^{-1} to 210 cm^{-1} showing several resonance absorption lines after 1.6 THz. The absorption coefficient of Cerabone® increases to 80 cm^{-1}, and the resonance absorption occurs at 1.7 THz. This is the first representation of the frequency-dependent refractive index and absorption coefficient of jawbone and Cerabone®.

IV. REFERENCES

[1] H. Aoki, Y. Shin, M. Akao, T. Tsuji, T. Togawa, Y. Ukegawa, R. Kikuchi. In: Biological and biomechanical performances of biomaterials, P. Cristel, et al. (Ed.), Amsterdam, Elsvier, pp.1–3, 1966.

[2] A.J. Fitzgerald, E. Berry, N.N. Zinov'ev, S. Homer-Vanniasinkam, R.E. Miles, J.M. Chamberlain, M.A. Smith. J. Biol. Phys., vol 29, p.123, 2003.

[3] N.N. Zinov'ev, A.S. Nikoghosyan, J.M. Chamberlain. Proceedings of SPIE, vol. pp. 6257, 62570P1- 62570P8, 2006.

[4] A.S. Nikoghosyan, H. Ting, S. Jingling, R.M. Martirosyan, M.Yu.Tunyan, A.V. Papikyan, A.A. Papikyan, "Optical properties of human jawbone and human bone sabstitute CERABONE® in the terahertz range", Journal Of Contemporary Physics (Armenia Ac. Sci.), vol. 51, no. 3, pp. 256-264, 2016.

Terahertz Waves Propagation in a LiNbO₃ Wedge Antenna

A.S. Nikoghosyan, Sh. Kh. Arakelyan

Yerevan State University, Alex Manoogian str. 1, 0025 Yerevan, Armenia

The terahertz (THz) wave propagation in LiNbO₃ wedge crystal was investigated. In order to study the THz wave propagation in the crystal, located within a free space, a simulation by the finite-element method was performed. The THz pulses were generated via optical rectification of femtosecond pulses of a Ti: Sapphire laser in the nonlinear optical wedge crystal. In order to analyze experimental results - the propagation of the most intense spectral lines of the THz pulse (in the range of 270 GHz - 1016 GHz) was modeled by means of COMSOL Multiphysics software.

I. INTRODUCTION

Terahertz waves have been found in a wide range of applications in science and engineering such as in the fields of time domain spectroscopy, medical diagnosis, imaging of concealed items, security, biological sensing, defense**,** space science, space instrumentation, etc. Terahertz waves offer a lot of benefits for radar applications, such as line-of-sight propagation and a higher imaging resolution. It is known that by reducing the cross-section of the dielectric antenna, a high resolution image can be obtained without changing the frequency of operation.

Recently, in most near-field microwave-imaging systems sharp metallic tips [1] or rectangular waveguides (aperture based method) are used as probes. The spatial resolution of the images is inversely proportional to the waveguide's cross-section area and the size of the tip. A probe using a metallic aperture was demonstrated in the Ref [2] for obtaining a resolution of 7 μm (λ/86). In Ref [3] the waveguide (made out of a low loss dielectric material) with pyramidal sharpened tip has been proposed to reach a resolution of about 20 μm (λ/200). The dielectric antenna is a promising technique which unlike the tip method, demonstrates a greater power efficiency. Another similar tip method with a resolution of 150 nm (λ/1000) is presented in Ref [4, 5], and a resolution of 10 nm is presented in [6]. In all these works, the THz radiation was supplied to the probes. A substantial part of the THz radiation was lost as a result of its coupling with the input surface of the probe. In order to avoid this kind of losses of the THz radiation in Ref [6-10] generation of THz radiation has been experimentally investigated in nonlinear wedge crystal. The wedge shape allows to concentrate the THz field in a nonlinear crystal, reduce the undesirable effects of the diffraction, as well as to get most part of the energy at the exit of the crystal. In the case of a laser-driven THz rectangular LiNbO₃ nonlinear crystal antenna, about 46% of the THz radiation reflects from the exit surface of the crystal due to the crystal's high reflection factor [11].

The finite-element method was employed to model and simulate the THz wave propagation (of the most intense spectral lines of THz pulse) in a LiNbO₃ wedge antenna in order to analyze experimental results [9]; and to visualize how the form of the crystal influences on the THz radiation both inside and outside the crystal in the near-field zone.

II. THZ WAVES PROPAGATION IN A LINBO₃ WEDGE ANTENNA

The THz pulses were generated via optical rectification of femtosecond pulses of a Ti: Sapphire laser, a central wavelength λ=800 nm, in a wedge crystal, Fig.1. A schematic diagram of the experimental setup, demonstrating the principles of THz pulse generation and detection, to obtain THz spectral data is shown in Fig.2. The linear tapered broad band dielectric antenna, has been fabricated from LiNbO₃ nonlinear crystal. The optical field strength **E** and nonlinear polarization **P** vectors, as well as the optical axis of the crystal, were parallel to the height of the wedge crystal. In this case, the linearly polarized THz radiation is generated due to the largest second-order nonlinear tensor element d_{33} ($P_z = d_{33} E_z E_z^*$).
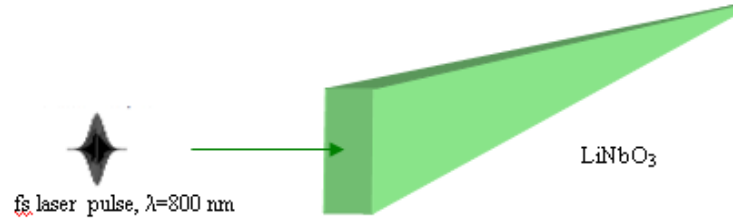
Fig.1. Laser-driven LiNbO3 wedge THz broadband antenna
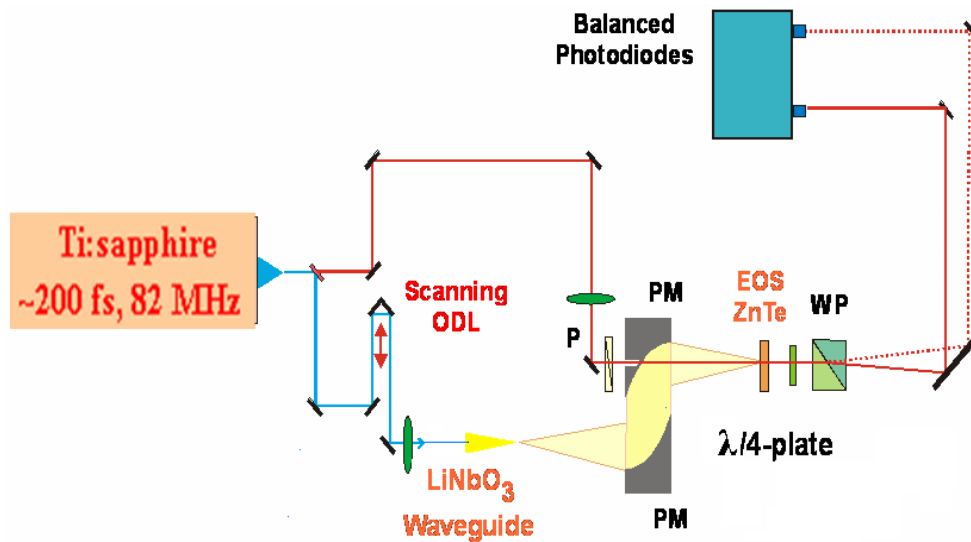
Fig.2. Schematic diagram demonstrating the principles of THz pulse generation and detection

The propagation of THz waves in $LiNbO_3$ crystal with frequencies equal to the most intense spectral lines in THz pulse spectra [9] (at: 270 GHz, 290 GHz, 330 GHz, 409 GHz, 451 GHz, 500 GHz, 644 GHz, 760 GHz, 802 GHz, 1000 GHz and 1016 GHz) were investigated.

To simulate the THz wave propagation in the $LiNbO_3$ wedged crystal located within a free space, the software 'COMSOL Multiphysics' was used. A domain of simulation is a 3D space. In order to provide good convergence for the solution the mesh has been built from tetrahedral cells the maximum size of which has been taken to be $\lambda/10$ Fig.3(a). All elements of the system with the physical parameters and boundary conditions are described by a set the partial differential equations. To solve correctly the equation system which describes the distribution of the THz wave field, the largest size of the cell should not be greater then one third of the wave length. In our case it was 3 times smaller to get more accuracy. The following values were input into the program: the real and the imaginary parts of the dielectric function and the power for the given THz extraordinary wave. The values of n and α calculated through the formula given in [11].

It is shown that the mode structure and phase velocity of the THz radiation are changing during its propagation through the wedge crystal, Fig.3, Fig.4, as the THz field passes from the single mode Ex_{11} to multimode regime and vice versa. The THz field has been focused. The full energy of the THz radiation propagating along straight lines parallel to the Z-axis of the wedge crystal is distributed between both – external (outside of the plate) and internal fields. The red color in Fig.3 and Fig.4 indicates positive values and blue indicates negative values of the THz electric field.

The distribution of THz electric field E_z component for the wedge crystal lengths of 2.5 mm and 12 mm respectively, is shown in Fig.4. The cross-sectional area of the crystal was 0.27×1 mm^2. As the length of the wedge increases, the beam-width decreases, namely, the directional diagram becomes sharper and the relative gain of the antenna increases.
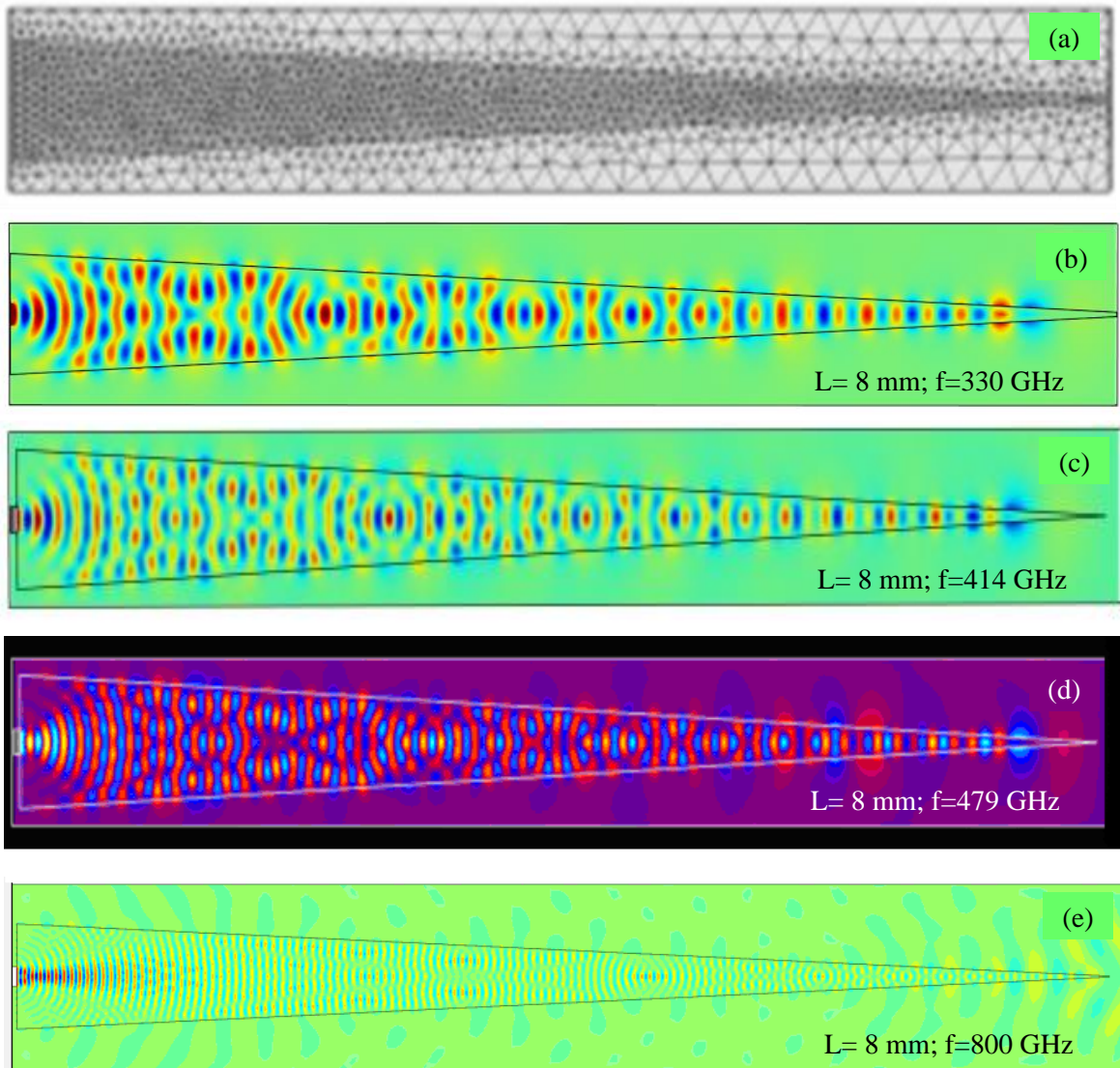
Fig.3. The spatial distribution of the E_x (z) components of the THz electric field during propagation along the *z* axis at frequency of 330 GHz, 414 GHz, 479 GHz, 800 GHz: (a) lateral view in (xz) plane, L = 8 mm.
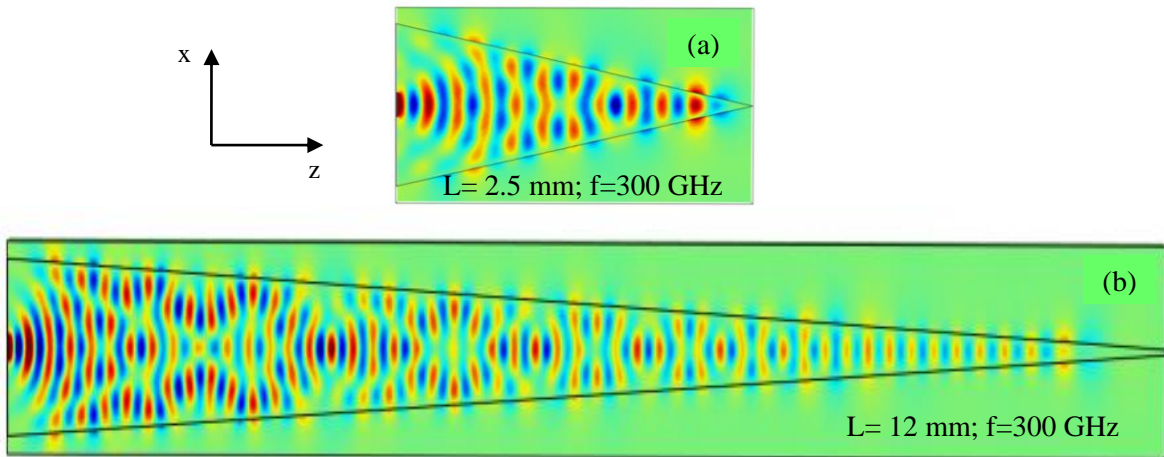
Fig.4. The spatial distribution E_x(z)-component of the THz electric field at 300 GHz frequency, axb = 0.27 x 0.8 mm^2, L = 2.5mm and L = 12 mm.

III CONCLUSION

The relatively infrequent use of dielectric antennas is due to the lack of analysis tools. Maxwell's equations have an analytical solution only for a rectangular shape crystal. This inhibited the development and application of arbitrarily shaped dielectric antennas. Only recently the simulation of electromagnetic fields in arbitrarily shaped dielectric antennas has become available.

The finite-element method was employed to model and simulate the THz wave propagation in a wedge antenna in order to analyze the experimental results [9]. Excitation of THz radiation in the wedge antenna (made from nonlinear optical crystal $LiNbO_3$) by an optical laser pulse permits the solution of problems connected with coupling of electromagnetic waves at the input and output of the crystal – mode matching and single mode propagation

Numerical simulation results showed changes in the mode structure of the THz radiation along the length of the crystal, the concentration of the THz field inside the crystal (Fig.3, Fig.4) and the radiation structure from the crystal-air interface. THz energy concentration by dielectric wedge antenna improves the spatial resolution and increases the signal/noise ratio (SNR) for the THz imaging and spectroscopy. The wedge THz antenna may be applied in other areas, in particular, in ultra-high-speed electronic integrated circuit

IV REFERENCES

[1] N. van der Valk and P. Planken, "Electro-optic detection of subwavelength terahertz spot sizes in the near field of a metal tip," Applied Physics Letters, vol. 81, no. 9, pp. 1558 - 60, 2002.

[2] 0. Mitrofanov, M. Lee, J. Hsu, I. Brener, R. Harel, J. Federici, J. Wynn, L. Pfeiffer, and K. West, "Collection-mode near-field imaging with 0.5-thz pulses," IEEE Journal of Selected Topics in Quantum Electronics, vol. 7, no. 4, pp. 600 -607, 2001.

[3] N. Klein, P. Lahl, U. Poppe, F. Kadlec, and P. Kuzel, "A metal-dielectric antenna for terahertz near-field imaging," Journal of Applied Physics, vol. 98, no. 1, pp. 014910-1 - 014910-5, 2005.

[4] K. Wang, A. Barkan, and D. Mittleman, "Sub-wavelength resolution using apertureless terahertz near-field microscopy," in Conference on Lasers and Electro-Optics (CLEO), Baltimore, USA, 2003.
K. Wang and D. M. Mittleman, Ni. C. J. van der Valk and P. C. M. Planken, "Antenna effects in terahertz apertureless near-field optical microscopy", Applied Physics Letters, vol. 85, no. 14, pp.2715- 2717, 2004.

[5] H.-T. Chen, R. Kersting, and G. C. Cho, "Terahertz imaging with nanometer resolution," Applied Physics Letters, vol. 83, pp. 3009 - 3011, 2003.

[6] R. Hillenbrand and F. Keilmann, "Material-specific mapping of metal semiconductor dielectric nanosystems at 10 nm resolution by backscattering near-field optical microscopy," Applied Physics Letters, vol. 80, pp. 25–7, 2002.

[7] A.S. Nikoghosyan, "USP Generation in the Millimeter and Centimeter Band in a Waveguide Partially Filled with a Nonlinear Crystal ", Quant. Electronika, vol. 15, N5, pp. 969-971, 1988.

[8] A.S. Nikoghosyan, P.M. Martirosyan., A.A. Hakhoumian,, J.M. Chamberlain, R.A. Dudley, N.N. Zinov'ev, "Generation of THz Radiation in Waveguides Partially Loaded with Nonlinear Crystal," Inter. Journal Electromagnetic Waves and Electronic System. vol. 11, N4, pp. 47-55, 2006.

[9] A.S. Nikoghosyan "Laser-Driven LiNbO3 Crystal Wedge THz Antenna" Inter. Conference IRMMW-THz 2013 at Mainz, Germany, September 5-10, Tu-P.54, 2013.

[10] A.S. Nikoghosyan, "Laser Driven Terahertz Dielectric Wedge Antenna Placed in Free Space or in Hollow Metallic Waveguide". Inter. Conference IRMMW-THz 2010 at Rome, Italy, September 5-10, Tu-P.54, 2010.

[11] N.N. Zinov`ev, A.S. Nikoghosyan, J.M. Chamberlain. Terahertz Radiation from a Nonlinear Slab Traversed by an Optical Pulse. Physical Review Letters, vol. 98, pp. 044801-1 044801-4, 2007.

Ferromagnetic Detector of Infrared Radiation

D. Bagdasaryan[1], A. Hakhoumian[2], R. Martirosian[1,2], H. Julfayan[2],
A. Makaryan[1], F. Nazari[1], V. Tadevosyan[1]

[1] *Microwave Radiophysics and Telecommunications Dept., Yerevan State University,*
[2] *Institute of Radiophysics and Electronics, Armenian National Academy of Sciences.*

The detection of laser radiation in the magnetized ferromagnetic yttrium iron garnet (YIG) at room temperature was experimentally obtained. A magnetic sensor (a coil inductor wound around YIG sample) was used to register changes in the magnetic moment of the magnetized YIG sample. The bias magnetization of the ferromagnetic sample required for detection was carried out using an inductive coil wrapped on the horseshoe-shaped ferrite docked to the sample. The dependence of the detection efficiency on the magnetizing current was investigated.

It is shown, that in providing a good decoupling between current source and the magnetic bias coil, such a system can be successfully used for the registration and conversion of short laser pulses in infrared region.

I. INTRODUCTION

In recent decades it was actively investigated different magneto-optical and opto-magnetic phenomena in the ferromagnetic mediums, particularly magnetic moment inversion under the influence of ultra-short laser pulses [1-3]. In [4] and [5] works were studied the inverse Faraday and Voigt (Cotton-Mouton) effects. In the other works [6-8] the detection of visible and infrared linearly polarized laser radiation in the magnetized transparent ferromagnetic at room temperature was experimentally obtained. It was shown that the amplitude and sign of detected signal strictly depend on external magnetic field, the polarization of laser radiation and the magnetization curve of ferromagnetic medium. These phenomena cannot be explained by the inverse Faraday and Voigt effects.

The detection of electromagnetic radiation in microwave range in ferromagnetic medium was studied well [9-10]. It has resonance behavior and fully explains by ferromagnetic resonance theory. However, the mechanisms of interaction of laser radiation in the infrared and visible regions are still the subject of discussions and debates.

In the works [6-8] it was shown that in soft ferromagnetic medium at the absence of magnetic bias field the detection of electromagnetic wave does not occur for any shape of magnetization curve of ferromagnetic sample. The detected signal arises only in the magnetized sample due to the changes of magnetic moment under the influence of electromagnetic radiation.

Upon the application of a magnetizing external magnetic field, the detected signal is still zero as long as the magnetization curve remains linear. Detected signal initially increases with increasing of the external magnetic field, reaches a maximum in the range, where the magnetization curve has the maximum nonlinearity. Near of turning point of the magnetization curve the signal reaches to zero. With the increasing of the external magnetic field the detected signal changes polarity and again begins to increase to the next maximum. At full saturation, the reorientation of the magnetic moment hardly occurs under the action of laser radiation, which leads to a drop in the amplitude of the detected signal.

In [6-8], where the ferromagnetic samples (YIG 0.4 mm thick single-crystal ferrite NM2000 5 mm thick) with the magnetic sensors were used, the optimal value of the external magnetic field is in the range of 20-100G. Furthermore, in the detecting process changes in the magnetic moment occurs along the applied magnetic field. This makes it possible magnetize the sample not only by external electromagnet or a permanent magnet, but also by an induction coil wound around magnetic sensor.

In present work the detection of laser radiation was experimentally obtained, at the magnetic biasing of the ferromagnetic sample using an inductive coil wrapped on a horseshoe-shaped ferrite docked to the sample.

II. EXPERIMENTAL INVESTIGATION OF FERROMAGNETIC DETECTOR

Block diagram of the experimental setup is shown in the Fig. 1. A neodymium pulse laser with $\lambda = 1.06$ µm wavelength as a radiation source was used (the pulse power ~1 MW, repetition rate ~10 Hz). The radiationwas linearly polarized. The absorption coefficient of the monocrystalline YIG sample, applied in our experiments was $\gamma \approx 15 \text{cm}^{-1}$.

A coil inductor wound around ferromagnetic sample was used as a magnetic sensor to register changes in the magnetic moment of the magnetized YIG sample. A change in the magnetic moment of the YIG crystal leads to the change in the magnetic flux, which induces a voltage in the inductor coil.

In [6-8] for the magnetic bias to the desired value for the nonlinear interaction of the external electromagnets have been used. Here an induction coil wound around the horseshoe-shaped ferrite for magnetizing of ferromagnetic sample we used (see Fig. 1).
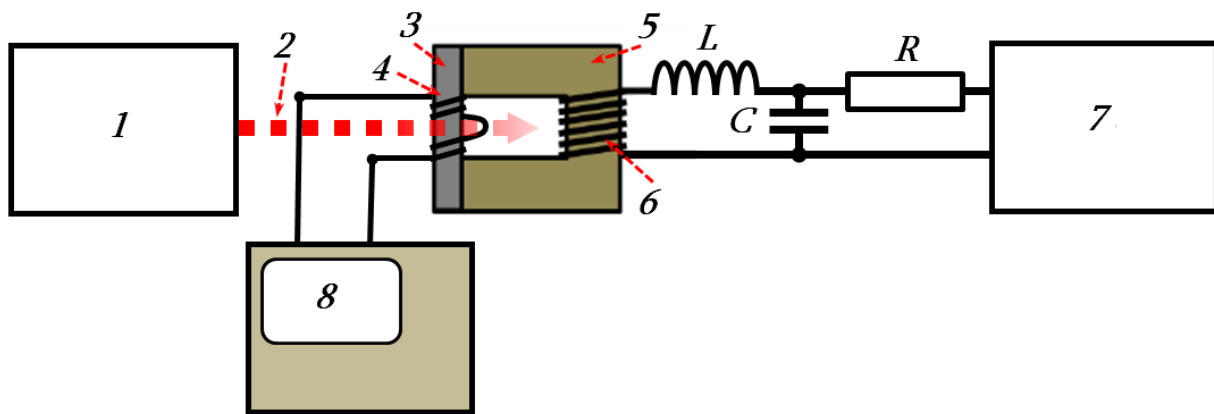
Fig. 1 The block scheme of experimental setup:

1 – Nd:YAG pulse laser, 2 – laser beam, 3 – YIG sample, 4 – registering coil, 5 – horseshoe ferrite, 6 – magnetizing coil, 7– regulated power supply, 8 – oscilloscope, L – decoupling inductor. R – ballast resistor, C – smoothing capacitance.

For decoupling of magnetizing coil 6 from the power supply 7 the voltage was applied to the coil through the RLC lowpass filter. Ballast resistor R (R=1kOm) at the same time provides the necessary magnitude of current through the magnetizing coil.

In our experiments for magnetizing of ferromagnetic sample the horseshoe-shaped ferrites with different configurations and dimensions were used. Dependence of magnetizations of YIG samples with two different ferrites on the voltage of power supply 6 applied to magnetizing coil through the RL circuit are shown in Fig. 2a and 2b. The magnitude of the output signals of corresponding ferromagnetic detectors depending on the voltage of power supply (see Fig. 1) are shown in Fig. 2 c and 2d. These experimental results are in a good agreement with the results of [2] in which a magnetic field was applied using an external electromagnet.

Particularly, the Fig. 2 shows, that when using the above method for the magnetization YIG sample, the amplitude of the detected signal reaches a maximum at the nonlinear region of the static magnetization curve. Reversing the direction of applied voltage to the magnetizing coils leads to the reversal of the sign of the detected signal.

Only one coil for the magnetization of the ferromagnetic sample and recording the detected signal can be used in the detector. However, in this case it is necessary to provide decoupling between the power source and the receiver of detected signal (Fig. 3).
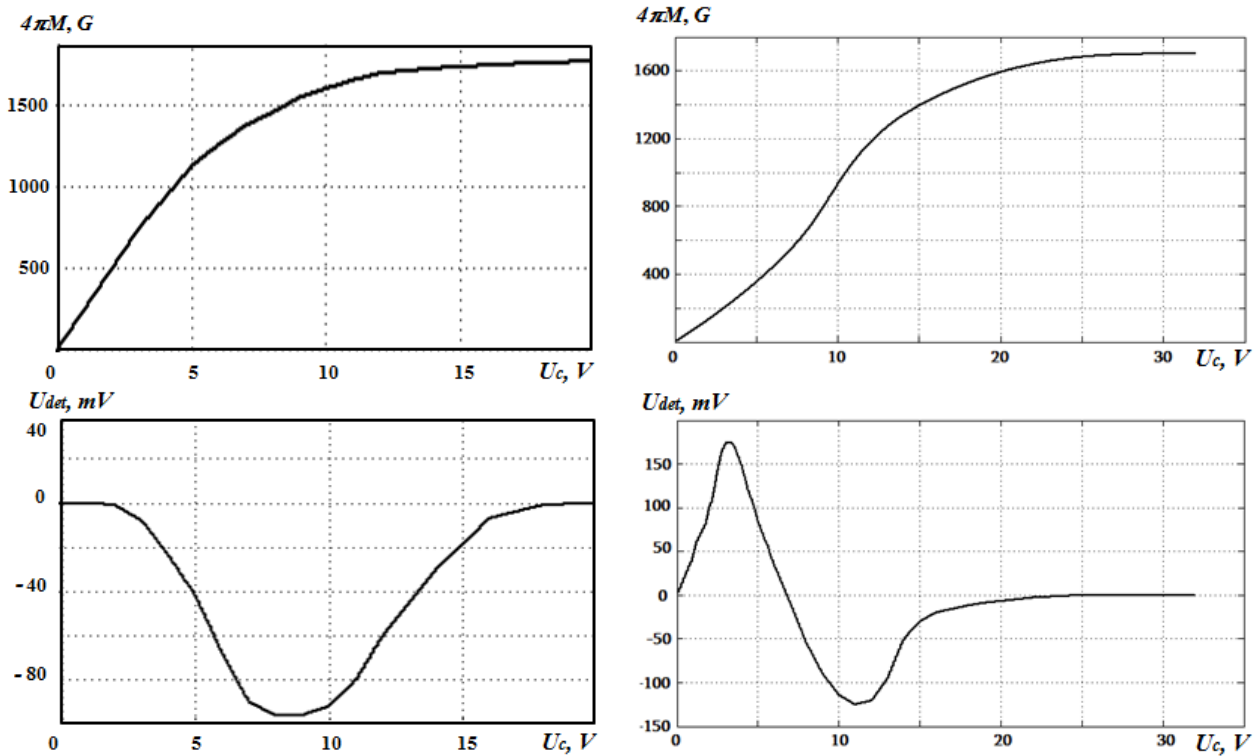
Fig. 2. Dependence of magnetization curves (a, b) and of the magnitudes of detected signals (b, c) on applied voltage to the magnetizing coils.
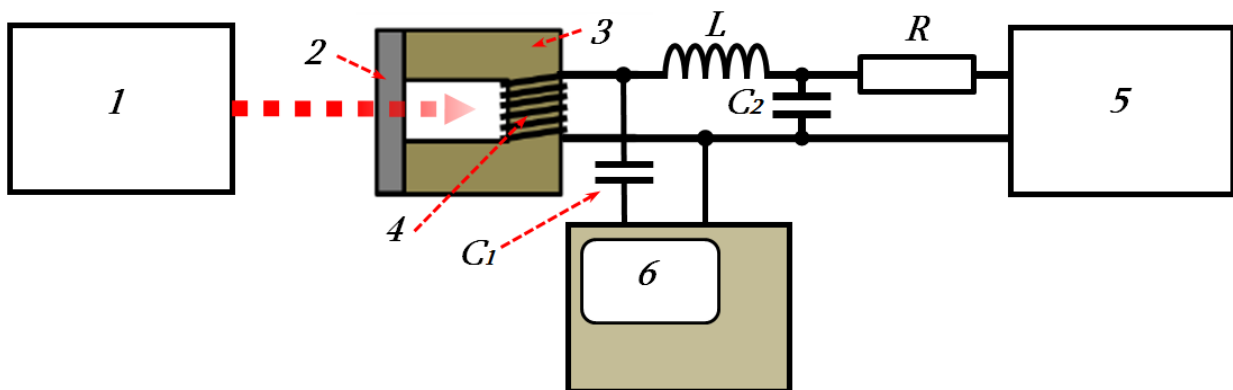
Fig. 3. The scheme of experimental setup with one inductive coil:

1 –laser, 2 – YIG sample, 3 – horseshoe ferrite, 4 – inductive coil, 5 – power source, 6 – oscilloscope, L – decoupling inductor, R – ballast resistor, C_1 – decoupling capacitance, C_2 – smoothing capacitance.

It should be noted that to the detection of short pulses should be used a high-frequency ferrite in the sensor.

III. CONCLUSION

In conclusion we mention that the results obtained can find wide practical application for the detection and conversion of frequencies of electromagnetic radiation for the optical recording, storage and processing of information, etc.

IV. REFERENCES

[1] B. Koopmans, van M. Kampen, J. T. Kohlheppand and W. J. M. de Jonge, "Ultrafast magneto - optics in nickel: magnetism or optics?", Phys. Rev. Lett., vol. 85, p.844, 2000.

[2] A. V. Kimel, A. Kirilyuk, F. Hansteen, R. V. Pisarev and Th. Rasing, "Nonthermal optical control of magnetism and ultrafast laser-induced spin dynamics in solids", J. Phys. Condens. Matter, 19: 043201 pp. 1-24, 2007.

[3] A. Kirilyuk, "From magneto-optics to ultrafast manipulation of magnetism", Journal of Science and Arts, vol. 3, p. 353, 2011.

[4] S. Wozniak, M. W. Evans and G. Wagniere, "Optically induced static magnetization near optical resonances in molecular systems", Mol. Phys. vol. 75, p. 81, 1992.

[5] A. B.-A. Baranga, R. Battesti, M. Fouche, C. Rizzo, G. L. J. A. Rikken, "Observation of the Inverse Cotton-Mouton Effect", <hal-00518059v2>, 2010.

[6] H. S. Hakobyan, A. H. Makaryan, V. M. Mekhitarian, V. R. Tadevosyan, "Detection of Laser Radiation in Optically Transparent Ferromagnetic", Proc. of International Conference on "Microwave and THz Technologies and Wireless Communications", Armenia-2012, pp. 52–60, 2013.

[7] R. M. Martirosian, A. H. Makaryan, V. M. Mekhitarian, V. R. Tadevosyan, "Optical Detection in a Ferromagnet", JETP Letters, vol. 99, No. 8, pp. 435-440, 2014.

[8] Р. М. Мартиросян, А. О. Макарян, В. М. Мыхитарян, В. Р. Татевосян, Ф. Назари, А. Г. Джулфаян, "Магнитно-нелинейные материалы для детектирования электромагнитного излучения", Физические основы приборостроения, т.5, no. 1, 18, сс.88-96, 2016.

Pre-Annealing Effects on a Pentacene Organic Thin Film Transistor With a Polymer Dielectric Interface

Arsen Babajanyan[1], Sul A Choi[2], Kyungchul Kim[2], Shant Arakelyan[2], Hanju Lee[2], Barry Friedman[3], Kiejin Lee[2,*]

[1] Department of Radiophysics, Yerevan State University, Yerevan 0025, Armenia
[2] Department of Physics and Basic Science Institute for Cell Damage Control, Sogang University, Seoul 121-742, Korea
[3] Department of Physics, Sam Houston State University, Huntsville, Texas 77341, USA
*Corresponding author E-mail: klee@sogang.ac.kr

A pentacene organic thin film transistor (OTFT) with polymethylmethacrylate (PMMA) gate dielectric layer was fabricated at 25 °C (RT), 90 °C, and 120 °C in situ substrate temperatures. In order to study the effect of pre-annealing treatment on the crystal structure, we observed the fabricated pentacene thin films by scanning electron microscope, atomic force microscope, and X-ray diffraction. The pentacene film remains in the bulk phase and the carrier's mobility decreases only with 120 °C substrate temperature compared with RT preparation. A pentacene OTFT with PMMA as a gate insulator layer exhibited enhanced electric characteristics, including hole mobility of 0.21 cm^2/Vs, current *on/off* ratio of order of 10^5, and a threshold voltage less than −4 V.

I. INTRODUCTION

Organic thin-film transistors (OTFT) have attracted much attention due to their attractive features such as low cost, low temperature processing, and mechanical flexibility [1,2]. Currently, because of these excellent properties there are many applications such as flexible organic light emitting diodes, radio frequency identification tags, smart cards, plastic logic circuits, etc. [3,4]. The three fundamental components of such devices are the contacts (source, drain, and gate), the semiconductor thin film, and the gate insulator layer. To improve the performance of organic transistors, the condition of the organic semiconductor/gate insulator layer interface is very important. Various materials with high dielectric constant have been investigated for gate insulator such as high-*k* inorganics, polymers, and self-assembled small molecules. Organic transistors with a polymer gate insulator layer exhibited OTFT performance comparable to inorganic dielectrics. Polymers such as poly(vinyl phenol), poly(styrene), poly(methyl methacrylate), and poly(vinyl alcohol) have been used as OTFT gate insulators [5,6].

Among the most popular organic semiconductors, pentacene is widely studied for p-channel organic transistors due both to its stability and its high field effect mobility [3]. Pentacene consists of a linear chain of five benzene rings. With X-ray diffraction techniques, the four different polymorphs can be classified according to their *d* (001) spacing perpendicular to the substrate surfaces: 14.1, 14.4, 15, and 15.4 Å. Two polymorphs of 14.4 and 15.4 Å have been found in the pentacene films grown on SiO$_2$ substrate; so called "thin film" and "bulk" phases, respectively [7-9]. The phase transition between the two polymorphs depends on the substrate deposition temperature and the film thickness. In organic semiconductors, molecular ordering has influence on the electrical performance of devices since charge transport is dominated by hopping [10,11]. Thus, the phase transition in pentacene induced by the post annealing process is correlates with the electric transport [12].

In this paper, we study the pre-annealing effect on the pentacene OTFT with a poly(methyl methacrylate) (PMMA) interface. First, we focus on the electrical characteristics of pentacene based OTFT using PMMA as the gate insulator layer. Second, we observe the morphology and crystallinity of pentacene thin films pre-annealed at various substrate temperatures by scanning electron microscope (SEM) and atomic force microscope (AFM).

II. EXPERIMENT

The pentacene OTFT was fabricated on highly doped p-type silicon substrates. PMMA (M_W = 996,000, obtained from Sigma-Aldrich) was dissolved in toluene with a concentration of 15 mg/ml and then spin-coated onto the highly doped p-type silicon substrate to form a 50 nm thin polymer layer. The PMMA layer was baked for 12 hours at the temperature of 80 °C in vacuum. Then the pentacene thin films were deposited on the PMMA/SiO$_2$ substrates at 25 °C (RT), 90 °C, and 120 °C by the thermal vacuum evaporation method. The resulting films were about 50 nm thick with deposition rate of approximately 0.1 Å/s and base pressure of about 5×10^{-6} Torr. After depositing the pentacene thin film, a 100 nm thick Au layer was deposited through a metal mask, using a thermal evaporator. The channel length and width of fabricated OTFT were 50

μm and 1.1 mm, respectively.

The electrical measurements of the device characteristics were performed using a Keithley 2400-SCS sourcemeter in the dark condition at RT. The structure, morphology, and crystallinity of pentacene thin films were investigated using SEM and AFM.

III. RESULTS AND DISCUSSION

Figures 1 show the surface morphology and topography of pentacene thin films grown on the SiO_2 layer and the PMMA/SiO_2 interface obtained by SEM and AFM, respectively. The grain size is larger for the pentacene thin film grown on the PMMA/SiO_2 interface. In addition, a small number of fiber-like domains were observed on the pentacene surface grown on PMMA/SiO_2 interface as shown in Fig. 1 (b) [13]. The grain size of pentacene grown on the SiO_2 layer was 1−1.5 μm while the grain size of pentacene grown on the PMMA/SiO_2 interface was 1−2.5 μm according to Fig. Fig. 1 (c), (d). The pentacene film grown on the PMMA/SiO_2 interface is well ordered and reveals larger dendritic grains compared to the pentacene film grown on the SiO_2 layer. Since transport properties is depend on the molecular ordering of the pentacene film at the grain boundary, the larger grain size and better ordering of pentacene grown on the PMMA/SiO_2 interface should improve the electrical properties of the pentacene OTFT [14].
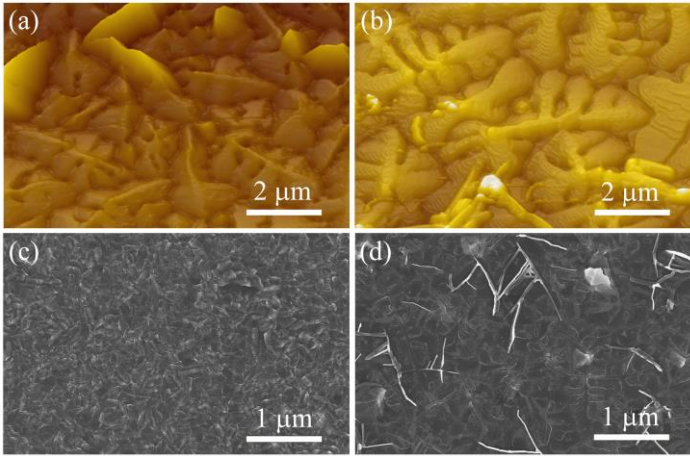
Fig. 1. (a), (b) SEM and (c), (d) AFM images of pentacene thin films grown (a), (c) on the SiO_2 and (b), (d) on the PMMA/SiO_2 substrate.
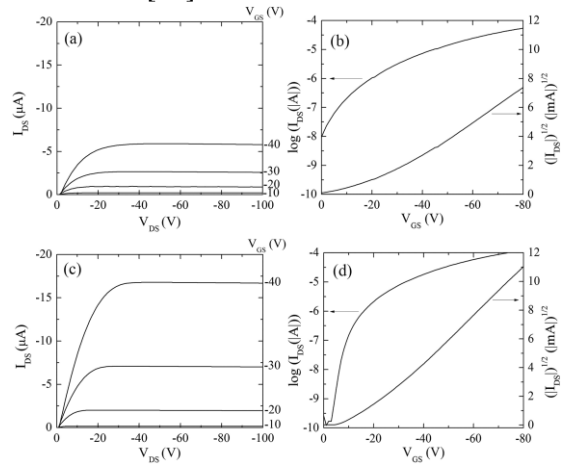
Fig. 2. *I−V* and transfer characteristics of the pentacene OTFT with (a), (b) the SiO_2 and (c), (d) the PMMA/SiO_2 as a gate insulator.

Fig. 2 compares the current-voltage (*I−V*) and transfer characteristics of the pentacene OTFT with (a), (b) the SiO_2 layer and (c), (d) the PMMA/SiO_2 interface as a gate insulator layer. The magnitude of the drain current (I_{DS}) for the pentacene OTFT with the PMMA/SiO_2 interface is evidently larger (about 3 times) than that for the pentacene OTFT with SiO_2 as an insulator layer at the same gate voltages V_{GS}. A hole mobility μ = 0.1 cm^2/Vs, a threshold voltage $V_T = -17$ V, and a current *on/off* ratio $\geq 10^3$ were obtained for the pentacene OTFT with SiO_2 as a gate insulator layer. A higher hole mobility $\mu = 0.2$ cm^2/Vs, a lower threshold voltage, $V_T = -12$ V, and a higher current *on/off* ratio $\geq 10^5$ were obtained for the pentacene OTFT with the PMMA/SiO_2 interface as a gate insulator. The additional PMMA layer enlarges the grain size of the pentacene thin film, decreases the threshold voltage, and increases mobility and current *on/off* ratio, thus improving the entire electric performance of the pentacene OTFT.

In order to study pre-annealing on the morphology of pentacene thin films, we investigated its effect by using SEM and AFM. Fig. 3 shows the SEM micrographs and AFM topography of pentacene thin films on the PMMA/SiO_2 substrate pre-annealed at different temperatures. At pre-annealing temperature of higher 120 °C, pentacene did not evaporate since the glass transition temperature (T_g) of PMMA is 90 °C and re-evaporation of pentacene has been observed for substrate temperature above 100 °C [20]. A large number of fiber-like domains were observed in pentacene layer (RT) as shown in Fig. 4 (a) [13]. The average grain size of the pentacene films and the number of fiber-like domains was decreased with increasing annealing temperature (Fig. 4 (b), (c)). The pentacene film has large dendritic grain structure with the grain size of 2−2.5 μm as shown in Fig. 3 (d). Spherical clusters with the grain size of 0.3−0.5 μm were observed. The grain size of pentacene film was decreased at the same pre-annealing temperature comparing (Fig. 3 (d)-(f)).
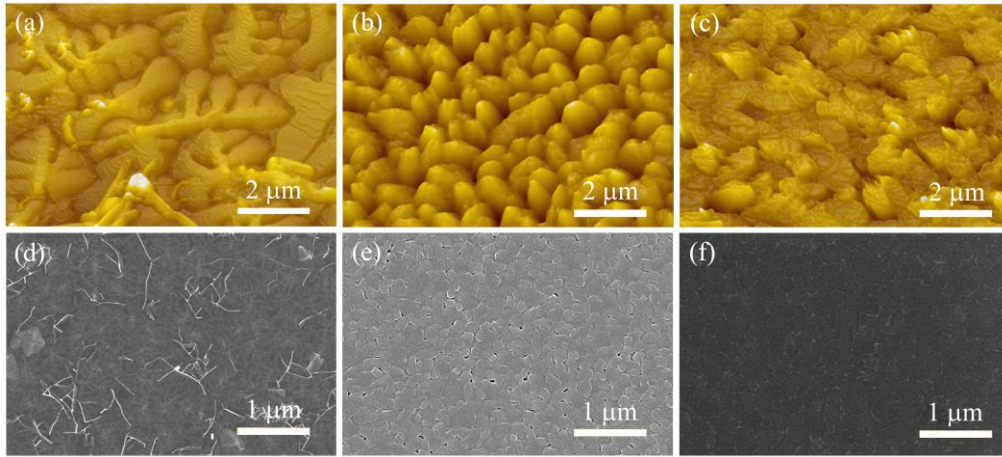
Fig. 3. (a), (b), (c) SEM and (d), (e), (f) AFM images of pentacene thin films pre-annealed at (a), (d) RT, (b), (e) 90 °C, and (c), (f) 120 °C grown on PMMA/SiO$_2$ substrate.

Fig. 4 shows the I–V and transfer characteristics of pentacene OTFTs with PMMA/SiO$_2$ as a gate insulator layer pre-annealed at (a), (d) RT, (b), (e) 90 °C, and (c), (f) 120 °C. As the substrate temperature increased to 90 °C, the drain current was gradually increased. The magnitude of the drain current I_{DS} and the mobility were decreased to a low value at the same annealing temperature as shown in Table. 1. The mobility was increased from $\mu = 0.1$ cm^2/Vs (SiO$_2$ as the gate insulator) to $\mu = 0.2$ cm^2/Vs (PMMA/SiO$_2$ as the gate insulator). The mobility of OTFT also increased due to the reduced grain boundary density as expected from the AFM images. All performance parameters of the fabricated OTFTs with PMMA/SiO$_2$ as a gate insulator are summarized in Tab. 1.
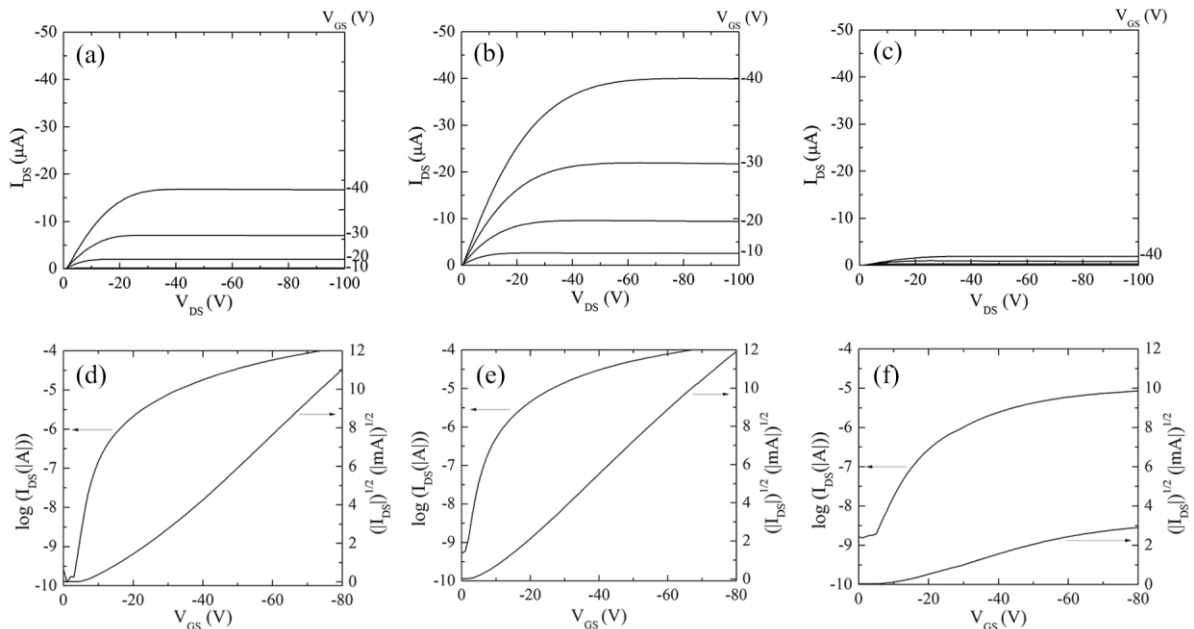
Fig. 4. (a), (b), (c) I–V and (d), (e), (f) transfer characteristics of pentacene OTFT with PMMA/SiO$_2$ as a gate insulator pre-annealed at (a), (d) RT, (b), (e) 90 °C, and (c), (f) 120 °C.

Various defects such as chemical impurities and dislocation may exist in the vacuum deposited films. D. Guo et al. reported that the number of defects such as dislocation and crystallite boundary inside the grains may be decreased and the degree of order and the grain size of the main charge transport layers near the interface may be increased, although annealing decreased the apparent grain size in the horizontal direction [15]. This occurs because of the high mobility and free energy of the defects, especially when a large number of defects and traps appear. The polymorph of the pentacene film deposited on the SiO$_2$ substrate transforms from the thin film phase to the bulk phase when the substrate temperature increased up to 120 °C.

Table 1. Summary of performance parameters of pentacene OTFT with PMMA/SiO$_2$ substrate as gate insulator.

Substrate pre-annealing temperature (^{o}C)	Mobility, μ_{sat} (cm^2/Vs)	Threshold voltage, V_T (V)	*On/off* ratio
25	0.2	−12	≥10^5
90	0.21	−4	≥10^5
120	0.016	−10	≥10^3

On the other hand, the X-ray diffraction spectra (data not shown here) for the pentacene evaporated on PMMA/SiO$_2$ substrate have four reflections (00*l*), indicating a thin film phase with the same interlayer spacing of 15.4 Å. The pentacene growth mode transition occurs due to the interfacial surface energy mismatches, related to the difference between the pentacene surface energy and the bulk energies of the two different phases [16,17]. Therefore, pentacene grains on PMMA/SiO$_2$ are highly interconnected with one another which can lead to more efficient charge transport than that on SiO$_2$.

IV. CONCLUSIONS

We fabricated pentacene-based OTFTs on PMMA as an insulator layer using different pre-annealing temperature conditions. Pentacene OTFT with PMMA as a gate insulator layer exhibit enhance electric properties; including hole mobility of 0.21 cm^2/Vs, current *on/off* ratio of 10^5 or larger, and the threshold voltage of less than −4 V. For pentacene thin films deposited on PMMA/SiO$_2$ substrate polymorphism not observed and there was no phase transformation which from the thin film phase to the bulk phase. The additional PMMA layer gives enhanced electric characteristics to pentacene OTFT related to device performance.

ACKNOWLEDGEMENTS

V. REFERENCES

[1] J. Veres, S. Ogier, G. Lloyd, Chem. Mater., vol. 16, pp. 4543-4555, 2004.
[2] G. Horowitz, Adv. Mater., vol. 10, pp. 365-377, 1998.
[3] C. D. Sheraw, L. Zhou, J. R. Huang, D. J. Gundlach, T. N. Jackson, M. G. Kane, I. Hill, Appl. Phys. Lett., vol. 80, pp. 1088-1090, 2002.
[4] C. D. Dimitrakopoulos, P. R. L. Malenfant, Adv. Mater., vol. 14, pp. 99-117, 2002.
[5] A. Faccheti, T. J. Marks, M. -H. Yoon, Adv. Mater., vol. 17, pp. 1705-1725, 2005.
[6] X. Peng, G. Horowitz, D. Fichou, F. Garnier, Appl. Phys. Lett., vol. 57, pp. 2013-2015, 1990.
[7] C. C. Mattheus, A. B. Dros, J. Baas, G. T. Oostergetel, A. Meetsma, J. L. de Boer, T. T. M. Palstra, Synth. Met., vol. 138, pp. 475-481, 2003.
[8] C. C. Mattheus, G. A. de Wijs, R. A. de Groot, T. T. M. Palstra, J. Am. Chem. Soc., vol. 125, pp. 6323-6330, 2003.
[9] C. D. Dimitrakopoulos, A. R. Brown, A. Pomp, J. Appl. Phys., vol. 80, pp. 2501-2508, 1996.
[10] D. J. Gundlach, T. N. Jackson, D. G. Schlom, S. F. Nelson, Appl. Phys. Lett., vol. 22, pp. 3302-3304, 1999.
[11] D. Guo, S. Ikeda, K.Saiki, Condens. Matter., vol. 22, pp. 262001 1-5, 2010.
[12] T. S. Ji, S.Y. Jung, V. K. Varaadan, Org. Electron., vol. 9, pp. 895-898, 2008.
[13] J. Yang, T. Q. Nguyen, Org. Electron., vol. 8, pp. 566-574, 2007.
[14] D. J. Gundlach, Y. Y. Lin, T. N. Jackson, S. F.Nelson, D. G. Schlom, IEEE Electron. Device Lett., vol. 18, pp. 87-89, 1997.
[15] D. Guo, S. Ikeda, K. Saiki, J. Appl. Phys., vol. 99, pp. 094502 1-7, 2006.
[16] L. F. Drummy, D. C. Martin, Adv. Mater., vol. 17, pp. 903-907, 2005.
[17] C. Kim, A. Facchetti, T. J. Marks, Adv. Mater., vol. 19, pp. 2561-2566, 2007.

1.6-Kilowatt GaN-Based L-Band Pallet Amplifier

Apet Barsegyan , Vinodh Thangam, and Daniel Koyama

Integra Technologies, Inc., 321 Coral Circle, El Segundo, CA 90245, USA

A GaN-based pallet amplifier optimized for avionics applications is presented. The pallet combines two Integra GaN HEMT transistors in parallel to produce 1.6 kilowatts output power, 15.5dB gain, and 55% efficiency operating at 100µS pulse duration and 2% duty cycle over the 1.03GHz to 1.09GHz band. For high power handling at the output, this pallet uses a Gysel RF combiner; the design and layout of the Gysel combiner have been modified to reduce its normally large size. At the input, the pallet achieves greater than 20dB input return loss using a conventional Wilkinson power divider.

I. INTRODUCTION

There is a growing demand for high power and high efficiency power amplifiers for avionics application. Gallium Nitride (GaN) High Electron Mobility (HEMT) technology offers higher power densities, higher voltage operation and excellent efficiency which makes it the perfect choice for high power avionics application. The higher power densities of the GaN HEMT translates to a small form factor and reduction in operational cost.

The design of a 1.60 KW GaN based L-Band pallet amplifier is discussed in this paper. The pallet amplifier operates over a bandwidth of 1.03 GHz to 1.09 GHz. The pallet amplifier supplies 1.6 kilowatts output power under 100µs pulse duration and 2% duty cycle. The pallet amplifier has a minimum power gain of 15.5 dB and 55% minimum efficiency.
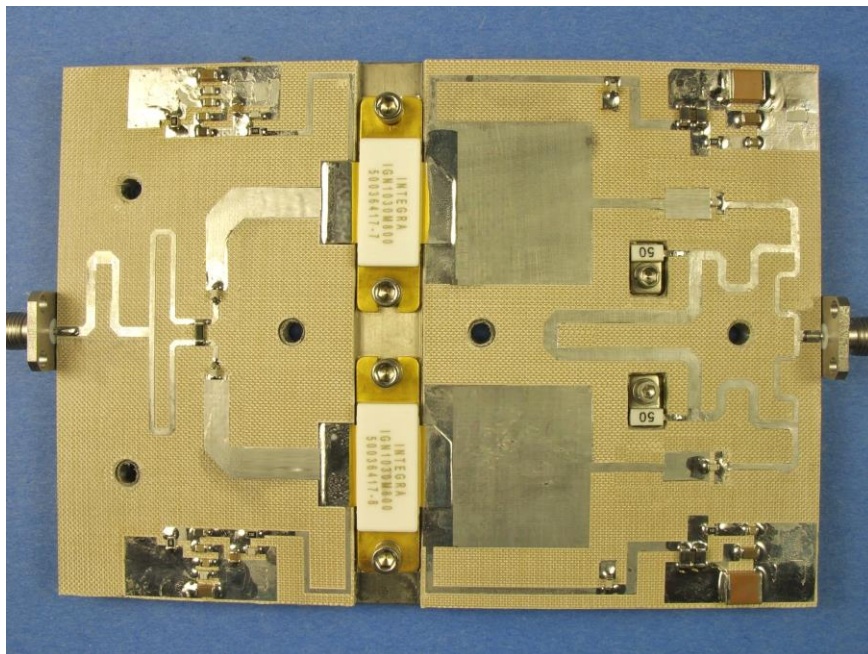
Fig. 1. 1.03-1.09 GHz, 800 Watt pallet photo. Dimensions: 86.3mm x 122.4mm

The pallet combines two 800 W Integra GaN transistors IGN1011M800. For high power handling at the output, this pallet uses a Gysel RF combiner; the design and layout of the Gysel combiner have been modified to reduce its normally large size. At the input, the pallet achieves greater than 20dB input return loss using a conventional Wilkinson power

II. PALLET AMPLIFIER DESIGN:

2.1. IGN1011M800 TRANSISTOR:
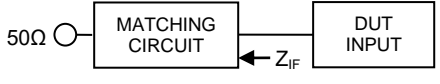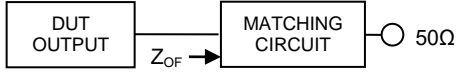
Transistor IGN1011M800 is an internally pre-matched, GaN HEMT. It is designed for L-band avionics applications operating over 1.03-1.09GHz instantaneous frequency band. Under 100us pulse width and 2% duty cycle conditions it supplies a minimum of 800 Watts of peak output power with 16dB of minimum gain. Transistor operates with 50V drain bias with 100mA bias current. It is specified for Class AB operation. Rated minimum drain efficiency is 55%, which is calculated as

$$N_d = P_{out} / (V_D \times I_{D\,pk})$$

Where N_d is drain efficiency, P_{out} is peak output power, V_D is drain bias voltage and $I_{D\,pk}$ is peak drain current.

Device input and output impedances are given in the table below:

Table 1. IGN1011M800 IMPEDANCE CHARACTERISTICS:

FREQUENCY (GHz)	$Z_{IF}(\Omega)$	$Z_{OF}(\Omega)$
1.030	4.4 – j 1.5	1.05 + j 0.25
1.090	4.6 – j 0.9	0.95 + j 0.30
Impedance Definition	50Ω — MATCHING CIRCUIT ← Z_{IF} — DUT INPUT	DUT OUTPUT — Z_{OF} → MATCHING CIRCUIT — 50Ω

2.2. Power Divider and Combiner:

A conventional Wilkinson power divider splits the input power equally between the transistors. The output power from the transistors are combined using a Gysel power combiner. The Gysel combiner has the advantage of higher power handling. The combiners have been designed and simulated individually. For each network, divider and combiner, isolation resistor was selected and evaluated. Both resistors were selected with sufficient power rating to handle the worst case scenario operation and provide safe operation in case one of the power transistors were to fail during filed operation.

Table 2 below summarizes the simulated S-parameters for both the power divider and combiner, including port to port isolation:

Table 2. S-Parameters for Wilkinson Divider and Gysel Combiner:

	F(GHz)	S21(dB)	S31(dB)	S11(dB)	S22(dB)	S33(dB)	S23(dB)
Wilkinson Divider	1.03	3.25	3.25	30.50	32.03	32.03	34.35
	1.09	3.26	3.26	26.42	25.53	25.53	29.80

	F(GHz)	S21(dB)	S31(dB)	S11(dB)	S22(dB)	S33(dB)	S23(dB)
Gysel Combiner	1.03	3.35	3.35	23.74	29.28	29.28	28.94
	1.09	3.35	3.35	32.04	39.91	39.91	29.43

2.2. 1600 Watt Pallet Amplifier:

The pallet amplifier combines two IGN1011M800 transistors in parallel to achieve 1600 Watt operating power across the 1.03-1.09GHz operating frequency range. Amplifier is specified with 50 Watt input drive level and minimum gain of 15 dB. Recorded worst case efficiency was 53%. Pulse droop, which was measured from 10us to 90us interval was -0.25dB recorded at 1.03GHz frequency. Recorded worst case Return Loss was 16.0dB across the band. Overall, amplifier demonstrates excellent stability against the load mismatch and it is rugged to 3:1 VSWR. Amplifier's power transfer curves, Pin-Pout characteristics, are given in the figure below.
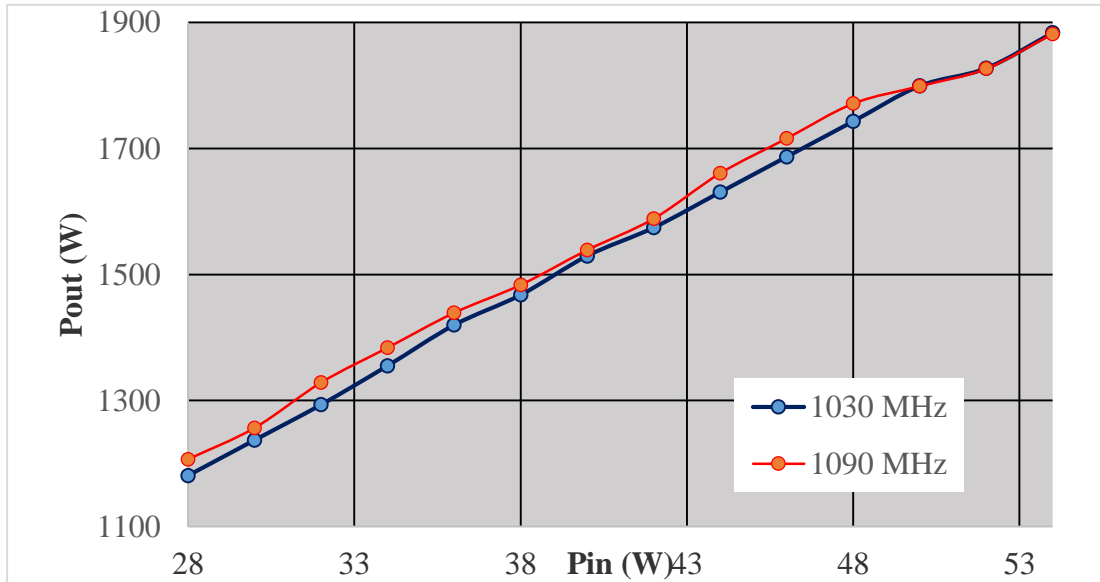
Fig. 1: Measured Power Output vs. Power Input Characteristics

It can be seen from Figure 1, at 50 Watt input drive level amplifier produces more than 1600 Watts of output power at 1.03 and 1.09GHz frequencies. The maximum power reaches to more than 1800 W when the drive level is increased further.
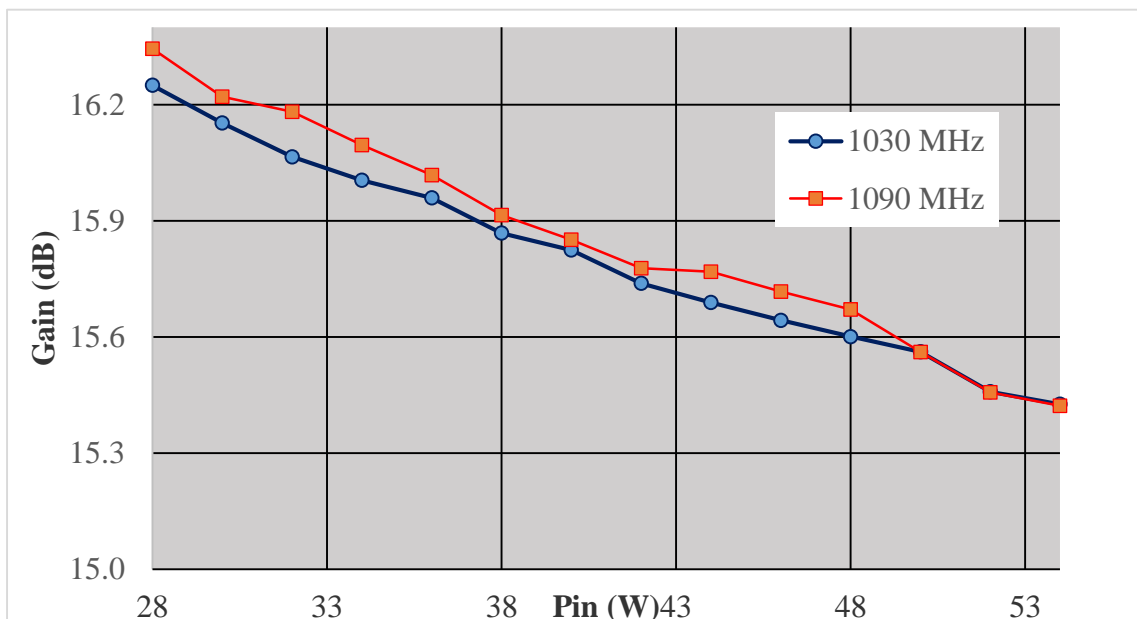
Fig. 2: Power Gain Vs Power Input

Figure 2, shows the plot of Power Gain and the Input power. The amplifier has slightly better gain at 1.09 GHz than at the 1.03 GHz. The amplifier is tuned to have a better gain at the higher frequency of operation.
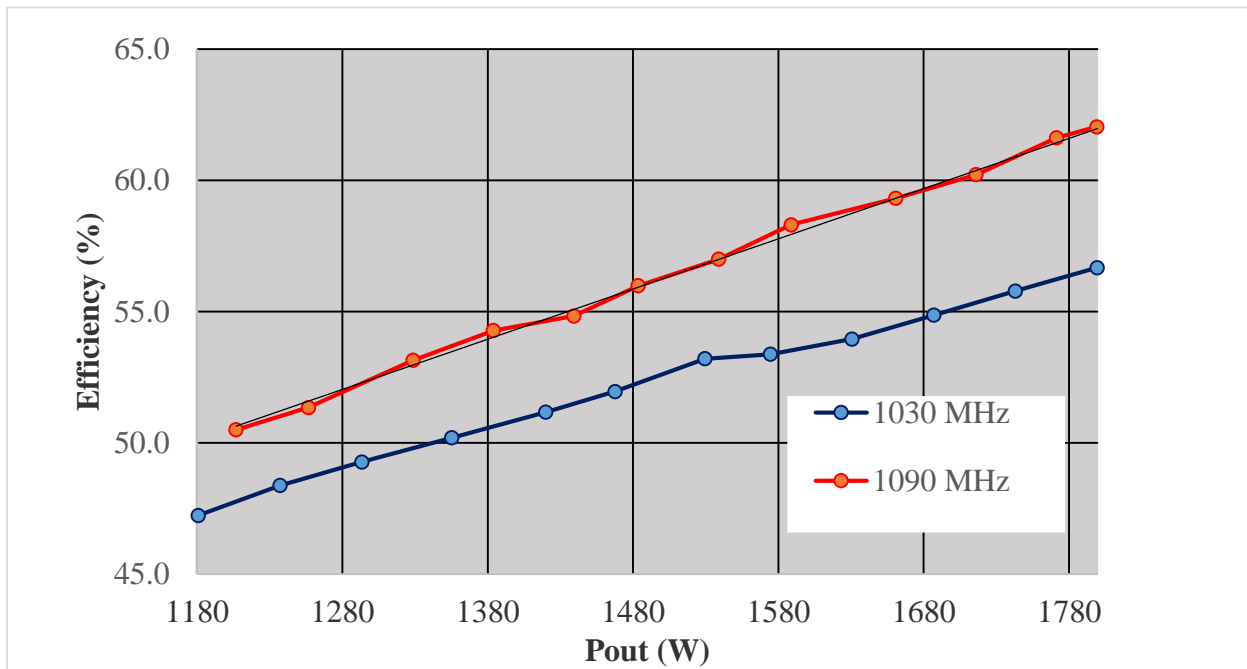
Fig. 3: Drain Efficiency Vs Power Output

Fig. 3 above shows the plot of amplifier drain efficiency versus output power. The minimum gain recorded with the input drive level of 50 W is 53% at 1.03 GHz. It is also clear that the efficiency of the amplifier improves at saturation power levels.

III. CONCLUSIONS

A 1600 watt L-band GaN based pallet amplifier was designed and implemented. A minimum of 1600 Watt operating power was obtained with 15dB power gain and 53% drain efficiency. Recorded worst case pulse droop was -0.25dB at 1.03GHz at power output level of 1827 Watt. At 1.03GHz and 1.09 GHz frequencies recorded drain efficiency was 54% and 59 %, respectively. This pallet amplifier can operate with medium pulse/duty cycle as well as short pulse/low duty cycle pulse conditions and demonstrates excellent pulse fidelity under both pulse conditions.

IV. REFERENCES

[1] Robert E. Collin, Foundations for Microwave Engineering, 2nd Edition, John Wiley & Sons
[2] Datasheet IGN1011M800 www.integratech.com
[3] Datasheet IGNP1011M1600 www.integratech.com

On Electron Holographic Phase Imaging of Threading Dislocations

L. B. Hovakimian

Institute of Radiophysics and Electronics of NAS RA, 0203 Ashtarak, Armenia

We study the phase shift of the electron holographic wave propagating in a transmission electron microscope through a thin semiconductor specimen containing a negatively charged threading dislocation line. The local retardation of the wave at and around the dislocation core is examined in cross-section imaging mode within the framework of Read's scenario of line charge screening. The properties of the resultant phase profile across the dislocation are discussed in terms of parameters related to the electro-chemical activity of the core. A novel method is proposed for retrieving from experimental phase images a quantitative measure of the Read barrier height. The capabilities of the method are explored by invoking the holography measurement results for a mixed type threading dislocation in *n*-doped GaN epitaxial layer.

I. INTRODUCTION

Electron holography (EH) in a field emission transmission electron microscope (TEM) is a coherent interferometric technique [1,2] that can be used for phase imaging of electrically active crystallographic defects with nanometer-scale resolution. Like its optical analogue, this technique is based on the interference of a reference wave with a scattered object wave and is directly sensitive to electromagnetic fields in solids. Several experimental groups have employed advanced EH instruments for extracting from interference-fringe patterns quantitative information on the electronic structure of threading dislocations (TDs) in wide bandgap materials, such as *n*-type GaN [3-7], ZnO [6-8], and 4H-SiC [9,10]. In this contribution, the objective is to derive a closed form expression for the phase shift of the EH wave passing through the repulsive barrier of a negatively charged TD. Our calculations are done in the cross-section geometry [6-10] on the basis of the Read model [6-14] for a screened line charge in an *n*-type material. Building on analytical results of this study, we propose a straightforward method for a quantitative assessment of the Read barrier height directly from the measured characteristics of EH phase shifts. In comparison to other quantification methods described in the literature [6-10], our alternative method has the virtue of simplicity. In particular, no necessity arises in introducing into analysis optimizing iterations and simulation fit parameters [6-8], or reconstructing [9,10] the variations in inner potential across TDs. An illustrative application of the method is presented below by relying on the experimentally detected features of the phase distribution across a mixed type TD in *n*-GaN epitaxial layer [7].

II. MODEL AND THEORY

Our treatment of the interaction of an incident EH wave with a thin TEM sample hosting an isolated, negatively charged TD starts off with the experimental cross-section geometry schematically shown in Fig. 1 of Ref. 7 (see, in addition, Fig. 1 of Ref. 10). In this geometry, the wave propagates in the *z*-coordinate direction and the sample with uniform thickness, *t*, is located in the region $-t/2 < z < t/2$. For symmetry reasons, the line of the straight TD coincides with the *y*-axis, so that $r = \sqrt{x^2 + z^2}$ gives the radial distance from the charged core. It is supposed [5-10] that the TD line charge is screened by a space-charge region of ionized donors, and that the radius, *R*, of the Read cylinder [6-14] satisfies the relation $2R < t$ [10]. Under kinematical conditions [1] the total phase shift, Φ_T, of the electron wave may be decomposed as [1, 6-10]

$$\Phi_T(x) = C_E \int_{-t/2}^{t/2} [V_B + V_D(r)]dz = \Phi_B + \Phi_D(x),\tag{1}$$

where the translational invariance along the *y*-direction is taken into account. In Eq. (1), the integration is performed along the electron optical path through the sample thickness, C_E is an interaction constant [1], V_B the mean inner potential (MIP) [1,15] corresponding to the index of refraction for electrons, the bulk phase shift due to host material is given by $\Phi_B = C_E V_B t$, and the slope of the defect-related phase shift, $\Phi_D(x)$, is determined by the position-dependent potential $V_D(r)$ of the TD.

If the structure of this $V_D(r)$ is described by means of the Read original expression [6-14], then the calculation of the line integral in (1) yields for $\Phi_D(x)$ the following result,

$$\frac{\Phi_D(x)}{\Phi_0} = \begin{cases} \dfrac{3|x|}{2R}\arccos\left(\dfrac{|x|}{R}\right) - \dfrac{(2R^2 + x^2)(R^2 - x^2)^{1/2}}{2R^3}, & |x| < R, \\ 0, & |x| > R, \end{cases} \tag{2}$$

in which

$$\Phi_0 = |\Phi_D(x=0)| = \frac{4}{3}\left(\frac{C_E}{e}\right)U_0 R, \tag{3}$$

e is the elementary charge, and U_0 the coulomb energy scale [3-14] defining the characteristic height of the Read potential barrier. Equation (2) tells us that in the vicinity of the TD core, where $V_D(r)$ is strong, the phase variation is governed by the asymptotic form

$$\frac{\Phi_D(x)}{\Phi_0} = -1 + 3\pi\frac{|x|}{R}, \qquad |x| \ll R. \tag{4}$$

In the opposite extreme, $\alpha(x) = (R-x)/R \ll 1$, the electron optical path appears near the boundary of the region where free electrons are depleted. Here the deflecting field of the TD is weak [11], and the absolute value of the phase (2) decays in accordance with the scaling relation

$$|\Phi_D(x)| \propto \Phi_0[\alpha(x)]^{5/2} \ll \Phi_0. \tag{5}$$

At $|x| > R$, the EH wave can feel only the MIP of the bulk material. Hence, on both sides away from the charge cylinder the total phase shift exhibits an *x*-independent behavior $[\Phi_T(x) = \Phi_B]$.

Figure 1 is a plot of $\Phi_D(x)/\Phi_0$ against x/R. It is immediately apparent from the graph that in Read's picture the effect of the TD on the retardation of the electron wave front can be characterized by two key parameters. Namely, the delay in the phase of electrons transmitted through the TD with respect to the phase of electrons transmitted through the surrounding bulk region is given by

$$\Phi_0 \propto \varepsilon^{-1}\frac{Q^{3/2}}{n^{1/2}}, \tag{6}$$

whereas the spatial extent of the phase profile is established by the diameter of the depletion cylinder [6-10],

$$D = 2R \propto \left(\frac{Q}{n}\right)^{1/2}. \tag{7}$$

Above, Q is the absolute magnitude of the charge per unit length [3-14] of the TD line, n the carrier concentration, and ε the dielectric constant of the host matrix. A pertinent observation is that $\Phi_D(x)$ exhibits in the limit $|x| \to 0$ a characteristic cusp. The presence of the cusp in the structure of the TD related phase shift was experimentally observed by Chung *et al* [10].

Let us also note that the functional form (2) leads to a remarkable electro-neutrality condition,

$$U_0 + \int_{-\infty}^{\infty} u_D(x)dx = 0 \tag{8}$$

$$u_D(x) = \frac{4}{\pi R^2} \frac{e}{C_E} \Phi_D(x)$$
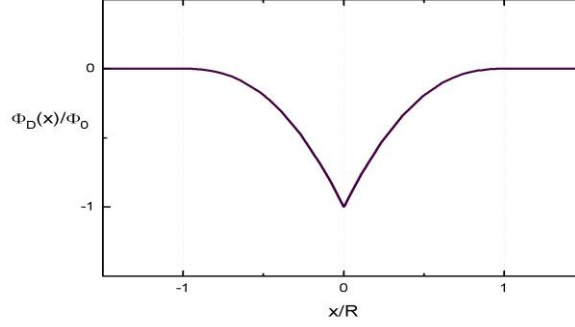
Fig. 1. The phase profile across the TD [Eq. (2)].

which rests upon the foundation stones of Read's shielding philosophy [11-13]. This condition demonstrates explicitly how the integral characteristics of holographic phase distributions become linked with the charge states [3-10] of TD cores.

III. RESULTS AND DISCUSSION

Having described in some detail the salient features of $\Phi_D(x)$, we return to Eq. (3) and rewrite it as

$$U_0 = \gamma_E \frac{\Phi_0}{R}, \tag{9}$$

where $\gamma_E = (4C_E / 3e)^{-1}$. Since the value of C_E is controlled [1] by the accelerating voltage of the TEM, the correlation form (9) makes it clear that a novel method can be suggested for the analysis and quantification of the Read barrier height on the basis of holographic phase images recorded in cross-section geometry. More precisely, Eq. (9) demonstrates that the extraction of the values of Φ_0 and R directly from measured phase profiles [6-10] turns out to be sufficient for determining the magnitude of U_0 without invoking more laborious procedures. As can also be noticed from Eqs. (6) and (7), the object (Φ_0 / R) shows no explicit dependence on such fit parameter [6-8] as n. Therefore a prior knowledge of the doping history of the sample [6-10] is not required if the formula (9) is used as a characterization tool. Armed with this information, we can now test the predictive power of (9) and its reliability by making a connection with the experimental facts.

Using a field emission TEM for which the interaction constant in Eq. (1) has the value

$$C_E = 7.29 \times 10^6 \frac{\text{rad}}{\text{V} \cdot \text{m}}, \tag{10}$$

Müller *et al* [6,7] were able to detect the holographic phase shift variation across a mixed type TD (with a Burgers vector of $1/3 < 11\bar{2}3 >$) embedded in a cross-section specimen prepared from *n*-doped GaN epitaxial layer with carrier concentration of $n \sim 2 \times 10^{19} \text{cm}^{-3}$. To improve the noise situation for a better signal-to-noise ratio, the phase profile perpendicular to the TD axis along the *x*-direction was obtained by averaging the line scans of the phase image along the *y*-direction. The observed delay in the phase at the TD region has been interpreted [6,7] as a direct and real space evidence for the space-charge phenomenon originating from a tightly bound negative charge at the core of an acceptor-like TD. Table I summarizes the data taken from a plot of measured phase distribution in Fig. 3 of Ref. 7. It is seen from the data that the interaction of the EH wave with the nanoscale space-charge cylinder leads to a substantial decrease in phase (about $\Phi_0 \cong 0.2 \text{ rad}$) at the TD core. With the experimental values of Φ_0 and R at hand, one may now arrive at a quantitative measure of Read's U_0 by utilizing Eqs. (9) and (10) and the calculated value of

$$\frac{\Phi_0}{R} \cong 8.7 \times 10^{-3} \frac{\text{rad}}{\text{nm}}. \tag{11}$$

Proceeding in this way, one comes to a conclusion that in super-wide-gap GaN ($E_g \sim 3.4$ eV) the Read barrier around a mixed type TD can be expected to be as high as $U_0^{(mix)} \cong 0.89$ eV .

TABLE I. Holography measurement results (Ref. 7).

Material	TD type	Φ_B (rad)	$[\Phi_B - \Phi_0]$ (rad)	R (nm)
n-doped GaN	Mixed	2.1	1.9	23

To check the accuracy of the quantification method outlined above, we turn our attention to the work of Cai and Ponce [5], where a holographic analysis has been performed under a somewhat different geometry to examine and compare the charge states in three different types of TDs (edge, screw, and mixed) in *n*-conducting GaN epilayers. The results from their investigation reveal that all TDs are in highly negatively charged states with associated positive space charge regions. At the same time, a large heterogeneity in the electro-chemical activity is observed among various TDs due to morphologically different cores. Figure 3b of Ref. 5 shows, in particular, that the measured barrier heights at the core regions of edge, screw and mixed TDs are around 0.5, 1.3 and 0.9 eV, respectively. On comparing this latter measured value with the above calculated value of $U_0^{(mix)}$, we may conclude, *a posteriori*, that for the mixed type TD in *n*-GaN the quantification method based on Eq. (9) works sufficiently accurately.

IV REFERENCES

[1]   L. Reimer and H. Kohl, Transmission Electron Microscopy: Physics of Image Formation. New York: Springer, 2008.

[2]   M. Linck, B. Freitag, S. Kujawa, M. Lehmann, and T. Niermann, "State of the art in atomic resolution off-axis electron holography", Ultramicroscopy, vol. 116, pp. 13-23, May 2012.

[3]   D. Cherns and C. Jiao, "Electron holography studies of the charge on dislocations in GaN", Phys. Rev. Lett., vol. 87, no. 20, p. 205504, Nov. 2001.

[4]   C. Jiao and D. Cherns, "Investigation of the charge on threading edge dislocations in GaN by electron holography", J. Electron Microsc., vol. 51, no. 2, pp.105-112, Feb. 2002.

[5]   J. Cai and F. A. Ponce, "Determination by electron holography of the electronic charge distribution at threading dislocations in epitaxial GaN", Phys. Stat. Sol. (a), vol. 192, no. 2, pp. 407-411, Apr. 2002.

[6]   E. Müller, D. Gerthsen, P. Brückner, F. Scholz, Th. Gruber, and A. Waag, "Probing the electrostatic potential of charged dislocations in *n*-GaN and *n*-ZnO epilayers by transmission electron holography", Phys. Rev. B, vol. 73, no. 24, p. 245316, June 2006.

[7]   E. Müller, D. Gerthsen, P. Brückner, F. Scholz, C. Kirchner, and A. Waag, "Electrical activity of dislocations in epitaxial ZnO- and GaN-layers analyzed by holography in a transmission electron microscope", Mater. Sci. Semicond. Process., vol. 9, no.1-3, pp.127-131, Feb.-June 2006.

[8]   E. Müller, D. Livinov, D. Gerthsen, C. Kirchner, A. Waag, N. Oleynik, A Dadgar, and A. Krost, "Properties of dislocations in epitaxial ZnO layers analyzed by transmission electron microscopy", in Zinc Oxide – A Material for Micro- and Optoelectronic Applications. Chapter 9. Springer, 2005.

[9]   S. Chung, M. R. McCartney, R. Berechman, Y. Picard, and M. Skowronski, "Holographic phase imaging of charged threading dislocations in 4H-SiC", Microsc. Microanal. vol. 16, no. S2, pp. 564-565, July 2010.

[10] S. Chung, R. A. Berechman, M. R. McCartney, and M. Skowronski, "Electronic structure analysis of threading screw dislocations in 4H-SiC using electron holography", J. Appl. Phys., vol. 109, no. 3, p. 034906, Feb. 2011.

[11] W. T. Read, Theory of dislocations in germanium, Philos. Mag., vol. 45, no. 367, pp. 775-796, 1954.

[12] H. F. Mataré, Defect Electronics in Semiconductors. New York: Wiley-Interscience, 1971.

[13] D. B. Holt and B. G. Yacobi, Extended Defects in Semiconductors: Electronic Properties, Device Effects and Structures. Cambridge: Cambridge University Press, 2007.

[14] T. Yokoyama, R. Takenaka, Y. Kamimura, K. Edagawa, and I. Yonenaga, "Direct observation of carrier depletion around a dislocation in GaP by scanning spreading resistance microscopy", Appl. Phys. Lett., vol. 95, no. 20, p. 202108, Nov. 2009.

[15] P. Kruse, A. Rosenauer, and D. Gerthsen, "Determination of the mean inner potential in III-V semiconductors by electron holography", Ultramicroscopy, vol. 96, no. 1, pp. 11-16, July 2003.

The Effect of Interface Traps on Electrical Characterization of Nanowires and Nanowire Junctionless FETs

A. Yesayan,[1] S. Petrosyan[1,2], F. Jazarri[3], J-M. Sallese[3]

[1]Institute of Radiophysics and Electronics, Alikhanian Brothers str. 1, 0203 Ashtarak, Armenia
[2]Russian-Armenian (Slavonic)University, H.Emin str.123, Yerevan 0051, Armenia.
[3]Swiss Federal Institute of Technologyin Lausanne, Lausanne 1015, Switzerland

In this paper we theoretically analyzed the effect of interface traps on Si nanowires (NW) and NW junctionless FET. We consider high density of interface traps (10^{12} cm^{-2}) and observe the conduction type switching due to surface traps by decreasing the NW radius when the NWs doping densities are less than 10^{18} cm^{-3}. However the impact of interface traps on NW electrical characteristics is apparent also at high doping densities which are usually utilized in NW junctionless FETs (JL FET). In this respect, we have included the effect of interface traps in analytical compact model previously derived for NWJL FET. Different trap energies and densities were considered. The proposed compact model reproduces correctly the results obtained from Sentaurus Synopsys 3D TCAD simulations.

I. INTRODUCTION

Interface traps have great influence on NWs electrical performance due to their high surface to volume ratio; a factor which is considered as a true advantage in respect to their applications [1-3].The balance between charges in the NW volume and charges trapped on the surface can deeply modify the electrostatics of the channel. Depending on the doping and trap densities, when nanometer scale structures are considered, deep depletion can take place even without any gate electrode. Modeling the influence of interface traps on device characteristics was already addressed in some papers [4-7]. In [4], an analytical model for the depletion induced by traps at the surface of a silicon nanowire was investigated. However, the authors assumed the full depletion of the channel and neglected the mobile charge density, where as these carriers are of prime importance for below threshold operation. Introduction of interface trapped charges in compact models have also been proposed in inversion mode MOSFETS [5-7]which is not appropriate for junctionless (JL) devices [8].

In this work, first we analyzed the conditions when the inversion charge raised due to surface traps practically can be neglected then we propose to include the effect of interface traps in the charge-based model developed for junctionless NW FETs [8]. In the first step, we will detail the process to account for traps in ungated nanowires. Next, the gate electrode will be introduced and an additional analysis of related traps features on $I-V$ characteristics will be analyzed. Different trap energies, densities as well as the exponential energy distribution of interface traps are considered. The analytical results are compared with Technology Computer Aided Design (TCAD) simulations.

II. THE INVERSION CHARGE RAISED DUE TO THE EFFECT OF SURFACE TRAPS

We assume an *n*-type semiconductor with a dopant density (N_D) and acceptor traps located at the semiconductor nanowire interface. Interface charge traps are amphoteric and whether they behave as donors or acceptors depends on the energy of the trap within the band-gap. Interface traps located above mid-gap behave as acceptor traps whereas those below mid-gape behave as donor traps [9-10].

We consider NWs with um lengths, so that only radial distribution of potential is important.

To describe the effect of surface traps on NW conductivity the Poisson equation should be solved considering both type of mobile charges: electrons and holes:

$$\frac{1}{r}\frac{\partial}{\partial r}\left(r\frac{\partial\varphi}{\partial r}\right) = -\frac{q}{\varepsilon_{sc}}(N_D^+ - n(r) + p(r)). \tag{1}$$

For the boundary conditions we consider the electric field in the center and on the surface:

$$\left.\frac{\partial\varphi}{\partial r}\right|_{r=0} = 0, \qquad\qquad \left.\frac{\partial\varphi}{\partial r}\right|_{r=R} = -q\,N_s f(E_t)/\varepsilon_{sc}, \tag{2), (3}$$

where N_s is the density of interface traps, $f(E_t)$ is the probability of occupation of interface traps at discrete energy level E_t. The occupation probability for acceptor type trap level within the band-gap of the semiconductor is determined as follows [9]:

$$f(E_t) = \frac{1}{1+\exp[\frac{E_t-E_F}{kT}]}, \tag{4}$$

where E_t is the trap energy, E_F is the semiconductor Fermi level and kT is the thermal energy. Here, we consider a degeneracy factor equal to 1. In this stage of development we consider discrete levels of trap energy. And include a general *"U"* shaped distribution afterwards.

The above described set of equations (1-4) have no analytical exact solution, instead numerical solution can provide the overall picture of surface traps effect. Below we present our calculations performed by Wolfram Mathematica.
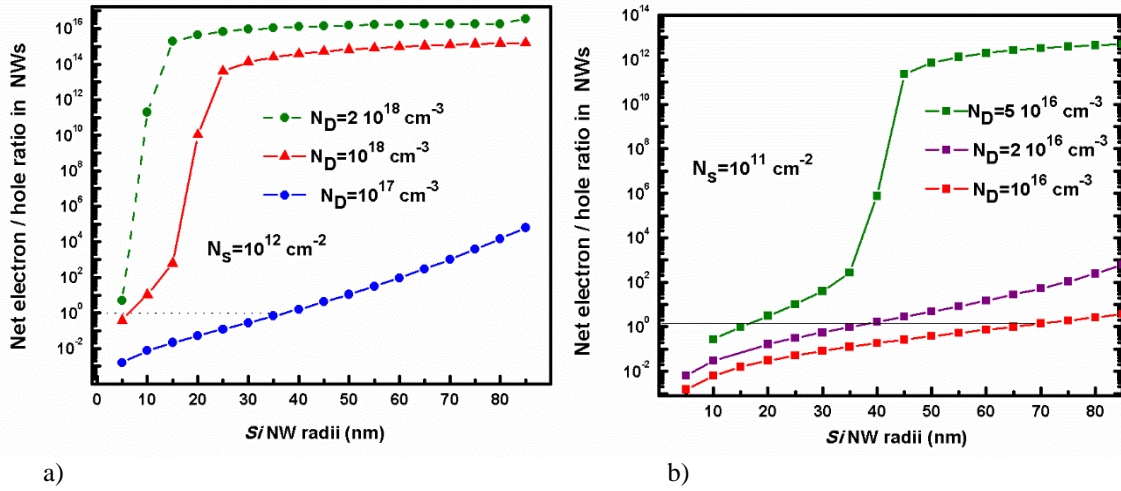
Fig. 1. Net electron-hole ratio in Si NW considering different doping densities and surface traps density: a) $N_s = 10^{12} cm^{-2}$, b) $N_s = 10^{11} cm^{-2}$.

From calculations illustrated in Fig. 1 is seen that at high density of surface traps ($N_s = 10^{12} cm^{-2}$) the inversion charge becomes essential with decreasing the NW radius only for NWs with doping densities less than $N_D = 10^{18} cm^{-3}$. Accordingly, for Si NWs with doping densities of order of $10^{18} cm^{-3}$ the inversion charge is not majority even at 5nm radius. Even considering low density of surface traps ($N_s = 10^{11} cm^{-2}$) the inversion charge becomes important when decreasing the NW radius only for lightly doped semiconductor NWs (see Fig. 2 (b) curves with $N_D = 2\,10^{16}$, $10^{16} (cm^{-3})$).

Thus we can conclude, that while considering highly doped semiconductor NW devices, such as junctionless FETs, the inversion charge raised due to the effect of surface traps can be neglected.

III. SURFACE STATES EFFECT ON NW JLFWET

We propose to generalize the charge-based model developed for junctionless NW FETs in [8,11] to include the effect of interface traps self-consistently. We still assume an *n*-type semiconductor. Therefore only interface traps located above mid-gap are of interest. Given the presence of active interface traps, an upward band bending takes place at the semiconductor surface.

According to (4) the interface trapped charge density satisfies:

$$Q_{SS}^- = -q \frac{N_s}{1+\exp\left(\frac{E_{t-i}}{kT}\right)\exp\left(-\frac{q\varphi_s}{kT}\right)} \quad . \tag{5}$$

Here, φ_s introduces the intrinsic Fermi level at the semiconductor surface (E_{is}) with respect to Fermi level, and E_{t-i}, the surface trap ionization energy with respect to the intrinsic Fermi level as well.

Next, we introduce the interface trapped charge density in the charge-based model developed in [8]. The solution developed therein can be summarized in two central relationships that link the surface potential (φ_s), the central potential (φ_0), and the surface electric field (E_s):

$$\varphi_s = \frac{qR^2}{4\,\varepsilon_{si}}\left(n_i \exp\left(\frac{\varphi_0 - V}{U_T}\right) - N_D\right) + \varphi_0, \tag{6}$$

$$E_s = \left[\frac{qn_iU_T}{\varepsilon_{si}}\left[\left(e^{\frac{\varphi_s - V}{U_T}} - e^{\frac{\varphi_0 - V}{U_T}}\right) - \frac{N_D}{n_i}\left(\frac{\varphi_s - \varphi_0}{U_T}\right)\right]\right]^{1/2}, \tag{7}$$

where R and ε_{si} are semiconductor NW radius and dielectric permittivity respectively, n_i is the intrinsic carrier concentration, $U_T = kT/q$. We consider source Fermi level as the reference level.

When the surface trap effect is included in the model the applied gate voltage at flat band conditions should compensate the band bending occurred as due to the metal-semiconductor work function difference but also due to the interface trapped charge thus we rewrite the eq. (10) in [8] as follows

$$Q_{sc} = -2C_{ox}\left(V_G^* + \frac{Q_{SS}^-}{C_{ox}} - \varphi_s\right). \tag{9}$$

Relations (6) to (9) can be implemented in any solver to get the gate and drain voltage dependences of the charge densities associated to the channel, to the gate and to the traps.

It is seen from (9) that we can introduce the interface trapped charge effect in charge based model [8] by adding $\delta = Q_{ss}^-/C_{ox}$ shift to the effective gate voltage and avoid further modifications of [8]. We propose at first calculate Q_{SS}^- for the given voltages (as we have described) and then add the shift δ to V_G^* in [8], also in drain current equations. This method which consists adding V_G^* shift helps not only to use the same analytical relationships, but also to perform all the calculations of charges and drain current explicitly as described in [11].

For clarity we remind here the drain current equation in depletion mode [11] and include the effect of traps:

$$I_{Dep}(V_G^* + \delta, V_D, V_S) = \frac{W}{L}\mu\left\{\left(\frac{1}{8C_{si}} - \frac{1}{4C_{ox}}\right)Q_{sc}^2 - \frac{Q_{sc}^3}{12Q_{fix}C_{si}} + +\left(\frac{Q_{fix}}{2C_{ox}} + 2U_T\right)Q_{sc} - U_TQ_{fix}\ln\left(1 + \frac{Q_{sc}}{Q_{fix}}\right)^2\right\}\Bigg|_{V_S}^{V_D} \tag{10}$$

where $Q_{sc}(V_G^* + \delta, V_D, V_S)$ is calculated either with analytical expression (19) in [8] or explicit expression (14) in [11].

Fig.2 displays the current density for NW FETs for a mid-gap traps density of 10^{12}cm^{-2} and setting the mobility to 1417cm^2/V·s (default value in TCAD Sentaurus software assuming constant mobility) versus the effective gate voltage at low ($V_D = 1$mV, $V_D = 0.1$V) and high ($V_D = 1$V) drain. It is worth to note that all the drain current and charge calculations from the model were done explicitly. In these calculations the interface traps at mid-gap are considered. The subthreshold slope degradation due to the presence of interface traps is illustrated in logarithmic scale on the left axis. To make more visible the effect of surface traps, the drain current is also obtained for zero density of interface traps at $V_D = 1$V and is depicted with black dashed-line. It is clear that the agreement between numerical simulations TCAD Sentaurus and the generalised explicit charge-based model validates a posteriori that the current model doesn't need to be modified.

In calculations of Fig.2 we have been considering discrete level for interface traps. However U-shaped distribution of interface states density in the band gap is the most common situation [12,13]. As we assume an n-type semiconductor, only interface traps located above mid-gap are of interest. Consequently an exponential distribution is a good approximation for U shape. Thus we assume exponential distribution for

the trap density with respect to the energy and replace N_s with $N_s^* = N_{sT} \int_0^{E_{sT}} \exp\left(-\frac{E_j - E_{sT}}{E_i}\right) dE_j$ and E_{t-i} with E_{sT}, where N_{sT} is the maximum value of interface state density, E_{sT} is the energy level of N_{sT}, and E_i is set to $0.035\ eV$ to be in consistent with default value in TCAD simulations.

Comparison of the analytical model and 3D TCAD simulations obtained for NW JL FET is shown in Fig.3. We note that the assumption of modeling an interface traps distribution with a single energy level and with tuned parameters (N_s^*, E_{sT}) fits quite well TCAD data, where the exponential energy distribution was implemented. To make more visible the impact of interface traps we have also plotted the drain current obtained at zero density of interface traps on the same graph.
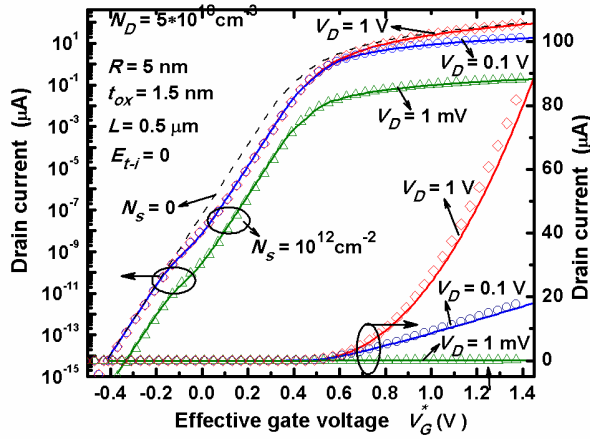

Fig.2. Drain current versus gate voltage in linear scale (right axis) and logarithmic scale (left axis) in a NW JL FET. The drain current at Ns=0 and V_D = 1V is depicted with black dashed line in logarithmic scale. Analytical model: lines. TCAD simulations: markers.
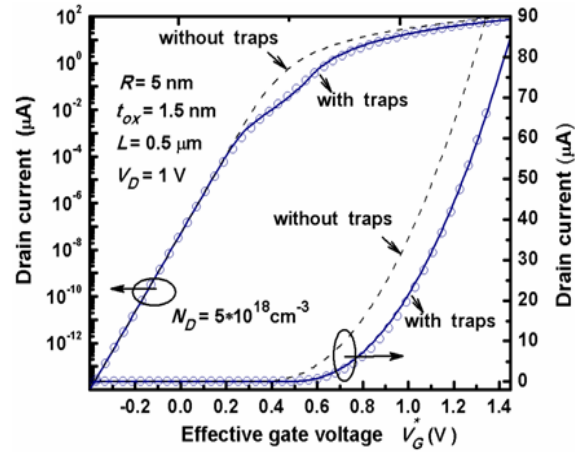
Fig.3. Drain current versus effective gate voltage in linear scale (right axis) and logarithmic scale (left axis) calculated at energy distribution of interface traps. The drain current calculated at Ns=0 is depicted with black dashed line. Markers; TCAD

IV. References

[1] Y. Cui, Q. Wei, H. Park, and Ch. M. Lieber, "Nanowire nanosensors for highly sensitive and selective detection of biological and chemical species," Science, vol. 293, no. 5533, pp. 1289-1292, Aug. 2001.

[2] F. Patolsky and Ch. M. Lieber, "Nanowire nanosensors," Materialstoday, vol. 8, no. 4, pp.20-28, April 2005.

[3] Ch. M. Lieber and Zh. L. Wang, "Functional Nanowires," MRS Bulletin, vol. 32, no. 2, pp. 99-108, Feb. 2007.

[4] A.C. E. Chia and R. LaPierre, "Analytical model of surface depletion in GaAs nanowires," J. App. Phys., vol. 112, no. 6, p. 063705, 2012.

[5] Z. Chen, X. Zhou, G. Zhu, and S. Lin, "Interface-trap modelling for silicon-nanowire MOSFETs,"in Reliability Physics Symposium (IRPS), May 2010, pp. 977-980.

[6] B. H. Hong, et al. "Subthreshold degradation of gate-all-around silicon nanowire field-effect transistors: effect of interface trap charge," IEEE Electron Device Letter, vol. 32, no. 9, p.1179, Sept. 2011.

[7] F. Najam, Sangsig Kim, and Yun Seop Yu, "Gate all around metal oxide field transistor: Surface potential calculation method including doping and interface trap charge and the effect of interface trap charge on subthreshold slope," J Semicond. Tech. Sci., vol. 13, no. 5, pp. d530-537, Oct. 2013.

[8] J.-M. Sallese, F. Jazaeri, L. Barbut, N. Chevillon, and C. Lallement, "A common core model for junctionless nanowires and symmetric double-gate FETs," IEEE Trans. Electron Devices, vol. 60, no.12, pp. 4277–4280, 2013.

[9] S. M. Sze, K. K. Ng, "Metal-Insulator-Semiconductor Capacitors," in .Physics of semiconductor devices, 3rd ed., J. Wiley & Sons, Inc., Hoboken: New Jersey, 2007, pp. 214-215.

[10] J. G. Simmons and G. W. Taylor, "Nonequilibrium steady-state statistics and associated effects for insulators and semiconductors containing an arbitrary distribution of Traps", Phys. Rev. B, vol. 4, no. 2, pp. 502-512, July 1971.

[11] A. Yesayan, F. Pregaldiny, and J.-M. Sallese, "Explicit drain current model of junctionless double-gate field-effect transistors," Solid State Electron, vol. 89, pp. 134-138, Nov. 2013.

[12] Z. Chen, B. B. Jie, and Ch-T. Sah, "Effects of energy distribution of interface traps on recombination dc current-voltage line shape," J. App. Phys., vol. 100, p. 114511, Dec. 2006,

[13] M. S. Kim, et al., "Distribution of interface states in MOS systems extracted by the subthreshold current in MOSFETs under optical illumination," J. Korean Phys. Society, vol. 43, no. 5, pp. 873-878, Nov. 2003.

Influence of Surface Recombination on the Efficiency of the Nanowire Solar Cells With Radial p-n Junction

S.G. Petrosyan [1,2], V.A. Khachatryan [2], A.E. Yesayan [1]

1_Institute of Radiophysics and Electronics, NAS RA, Alikhanyan Brs.1, Ashtarak 0203, Armenia._
2Russian-Armenian (Slavonic)University, H.Emin str.123, Yerevan 0051, Armenia.

Radial p–n junction solar cells have been theoretically predicted to have better efficiency than their planar counterparts due to decrease in the distance required to collect minority carriers compared to carrier diffusion length. This advantage is also significantly enhanced when the diffusion length is much smaller than the absorption length. We have developed an analytic model for the radial p-n-junction in a single nanowire (NW) core-shell structure. Here we present the NW efficiency dependence on the surface recombination rate for NWs with different radii. The considered radiation was taken as blackbody radiation at $5800°K$ temperature.
KEYWORDS: Silicon, nanowires, solar cell, p-n junction, surface recombination.

I.   INTRODUCTION

Recently interest in the use of solar energy has increased dramatically. To produce NW based solar cells new technologies and methods for the synthesis of NWs with different geometrical and physical parameters have been developed [1-6]. This new type of structures presents an important class of nanoscale building blocks with potential for exploring new device concepts, e.g., for photovoltaic applications or field-effect transistors. With the latest technologies, it becomes possible to realize solar cells based on NWs with radial p-n junctions [3-6]. This system has several advantages over conventional planar analogues, in particular associated with the fact that the collection and the generation of charge carriers takes place in mutually perpendicular directions. Thus, the studies of electrical and photovoltaic properties of semiconductor nanowires is important issue for the further development of solar cells.

Currently, the semiconductor nanowires are grown by different methods [7, 8]. The semiconductor nanowire radius may vary widely from tens of nanometers to micrometers. When the nanowires radius is in order of several nanometers, such radius is comparable with the de Broglie wavelength, and quantum effects are observable [9], which significantly changes the energy spectrum of the charge carriers. In nanowires with large radius the quantum effects are insignificant. In such structures, the radius of the nanowire becomes comparable with the other characteristic lengths of the electron gas (e.g. diffusion length). In this study we will consider silicon nanowires without quantum size effects and with absorption edge 1.08 microns covering partially the infrared portion of the solar spectrum.

II.   ANALYTICAL MODEL STRUCTURE

We consider the core/shell NW (see Fig. 1) with p-type core of (R_0) radius, n-type shell (R_{shell}) and the NW radius is (R).Due to the p-n junction formation in radial direction the space-charge layers are created on both sides of the core/shell interface and potential energy barrier is established. The electric field arises across the junction and the energy bands bent until the establishment of equilibrium state and the alignment of Fermi energy levels. We already have derived an analytic model for such radial p-n-junction in a nanowire core-shell structure [10].The NW is illuminated from the top by blackbody radiation at $5800°K$. Such topology is already constructed and characterised in the experimental work [5].The light is absorbed in quasi-neutral regions (both in n-type shell and p-type core) and in the space charge region. Generated in NW non-equilibrium carriers   are separated in the radial direction due to the p-n-junction electric field.   Only these separated non-equilibrium carriers participate in the formation of photocurrent.

Fig. 1.

To provide complete absorption of falling light NWs with lengths greater than the coefficient of total absorption   (α^{-1}) have to be considered. In this case it is possible to maximize the light absorption and charge carrier collection .
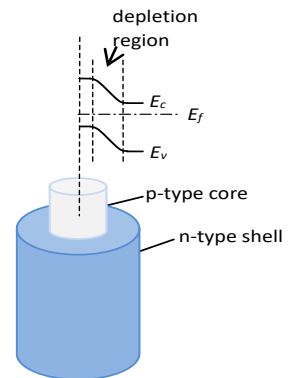
As we said we consider the Sun as a black body at temperature T_C. . The flow of thermal radiation depends on the temperature and the surface properties of the emitting body. For isotropic radiating surface the flow is determined by Planck's law [11]:

$$\Phi_0(\lambda, T) = \frac{a}{\lambda^5 (e^{\frac{b}{\lambda T}} - 1)}, \tag{1}$$

Where uses:

$a = 2\pi hc^2 = 3,7405 \cdot 10^{-16} \text{ W} \cdot \text{m}^2$

$b = \dfrac{hc}{k} = 1,4388 \cdot 10^{-2} m \cdot K,$

$h = 6.6252 \cdot 10^{-34} J \cdot \sec,$

$c = 2,9979 \cdot 10^8 \text{ m/sec},$

$k = 1.3806 \cdot 10^{-23} \text{ J}/K.$

$T_c = 5800^0 K$

Consequently, the total radiated photon flux from the unit surface at 1 s per unit wavelength is equal to:

$$N_{Ph_0} = \frac{\Phi_0(\lambda, T)}{\frac{hc}{\lambda}} = \frac{a'}{\lambda^4 (e^{\frac{b}{\lambda T_c}} - 1)}, \text{ where } a' = 2\pi c = 1,8827 \cdot 10^9 \text{ m/sec} \tag{2}$$

So the photon flux on the Earth in the unit surface at 1 sec in unit wavelength through the area perpendicular to the direction of propagation of light is equal to:

$$N'_{Ph_0} = \frac{a'(R_c/r)^2}{\lambda^4 (e^{\frac{b}{\lambda T_c}} - 1)}, \tag{3}$$

where $a'(R_c/r)^2 = 1,8827 \cdot 10^9 \text{ m/sec} \cdot \left(\dfrac{6.96 \cdot 10^8 \text{ m}}{1,5 \cdot 10^{11} \text{ m}}\right)^2 = 1.883 \cdot 10^9 \cdot 2.153 \cdot 10^{-6} \text{ m/sec} = 4.05 \cdot 10^4 \text{ m/sec}$

III. RESULTS AND DISCUSSIONS

Solving the drift-diffusion and current continuity equations in quasi-neutral regions by taking into account surface recombination and generation rates, we can find photocurrent in the described above system. The generation and recombination currents in depletion region have been included in the calculations as well.
The results of analytical calculations for the total photocurrent are illustrated in Fig. 2. As it was expected the photocurrent is higher at larger widths of quasi-neutral shell region and it strongly depends on surface recombination rate (Sp).For the wider shells the photocurrent saturates because the carriers collection area remains the same as the shell thickness becomes larger than diffusion length.
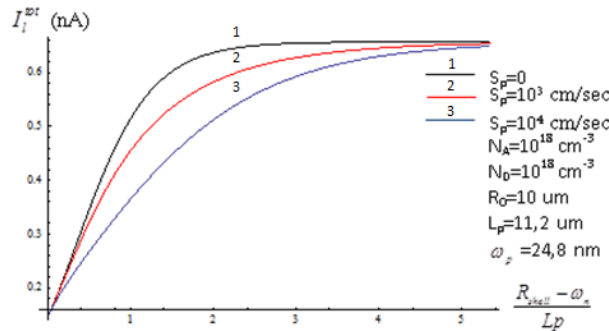

Fig.2. The dependence of total photocurrent I^{tot} on the ratio of quasi-neutral region width in n-shell over the hole-diffusion length (L_p) for different values of surface recombination rates (S_p).

78

The efficiency dependence on quasi-neutral shell region width and surface recombination rate is depicted in Fig. 3. As it is seen the efficiency falls for NWs with wider quasi-neutral shell region (see Fig. 3 a)). This is due to the situation of photocurrent and increase of whole incident on the cell radiation power with increase of the shell thickness. Meanwhile, as it was expected, as low is the surface recombination rate the higher is the efficiency.

In Fig. 3 b) is illustrated efficiency dependency on surface recombination rate for NW with shell radius 500nm.
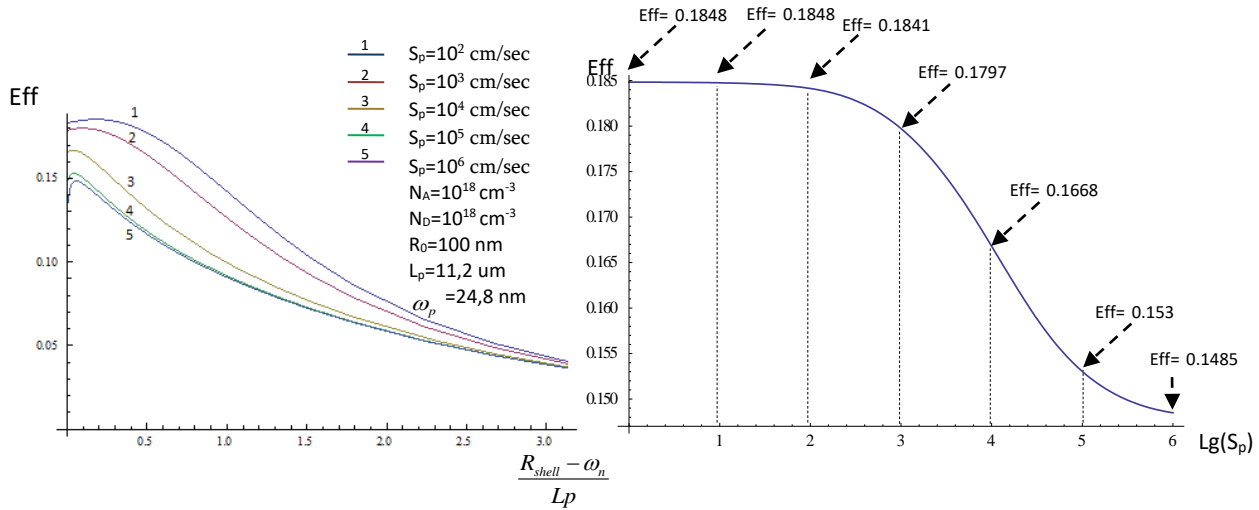
Fig.3. The dependence of a) efficiency on quasi-neutral shell region width at different values of surface recombination rates; b) max efficiency on variation of lg(S_p) for R_{shell}=500nm and R_0=10um.

IV. CONCLUSION

We have studied silicon single core/shell NW with radial p-n junction under the illumination. The theoretical analyze is have been performed for NWs with large range of shell radii. The geometrical dependencies of the main characteristics have been studied for the proposed NW structure. Further we present the main reasons of Voc decreasing in NW solar cells compared with planar ones. Optimization of nanowire geometry and proper choice of doping densities are mandatory to improve the cell efficiency. The developed model gives good understanding for designer to choose the optimal geometrical parameters for a single NW to get the satisfactory values of photocurrent, open-circuit voltage and cell efficiency.

V. REFERENCES

[1] E. C. Garnett, M. L. Brongersma, Yi Cui, M. D. McGehee , "Nanowire Solar Cells," Annu. Rev. Mater. Res., vol. 41, pp. 269-295, March 2011.
[2] C. Soci, A. Zhang, X.-Y. Bao, H. Kim, Y. Lo, D. Wang, "Nanowire photodetectors," J. Nanoscience and Nanotechnology, vol. 10, no. 3, pp. 1430-1449, Mar. 2010.
[3] B. M. Kayes, H. A. Atwater, N. S. Lewis, "Comparison of the device physics principles of planar and radial p-n-junction nanorod solar cells," J. Appl. Phys., vol. 97, no. 11, p. 114302, May 2005.
[4] E. C. Garnett, P. Yang, "Silicon nanowire radial p-n junction solar cells," J. Am. Chem. Soc., vol. 130, no. 29, pp. 9224-9225, Jul. 2008.
[5] P. Krogstrup, H. I. Jorgensen, M. Heiss, O. Demichel, J. V. Holm, M. Aagesen et al., "Single-nanowire solar cells beyond the Shockley–Queisser limit," Nature Photonics, vol.7, pp. 306-310, March 2013.
[6] J. A. Czaban, D. A. Thompson, and R. R. LaPierre, "GaAs core-shell nanowires for photovoltaic applications," Nano Lett., vol. 9(1), pp.148-154, 2009.
[7] Hong Jin Fan, Peter Werner, and Margit Zacharias "Semiconductor Nanowires: From Self-Organization to Patterned Growth", Small, vol. 2(6), pp.700-717, 2006.

[8] Huang Z, Fang H, Zhu J., "Fabrication of silicon nanowire arrays with controlled diameter, length, and density", Adv. Mater., vol. 19(5), pp. 744–748, 2007.

[9] E.Kazaryan, S.Petrosyan, "Physical fundamentals of semiconductor nanoelectronics", RAU, 2005.

[10] S.Petrosyan, A.Yesayan, S.Nersesyan, "Theory of NW radial p-n junction, World Academy of Scince, Engineering and Technology", vol.71, pp.1065, 2012.

[11] G.Pikus "Fundamentals of the theory of semiconductor devices", Science, 1965.

[12] http://www.ioffe.ru/SVA/NSM/Semicond/Si/index.html

[13] Green MA. "Solar Cells: Operating Principles, Technology and System Applications. Kensington, NSW", Aust.: Univ. New SouthWales, pp. 274-280, 1982.

Critical Radius of Full Depletion in Semiconductor Nanowires

S.G. Petrosyan [1,2], S.R. Nersesyan [1] and V.A. Khachatryan [2]

[1]*Institute of Radiophysics and Electronics, NAS RA, Alikhanyan Brs.1, Ashtarak 0203, Armenia.*
[2]*Russian-Armenian (Slavonic)University, H.Emin str.123, Yerevan 0051, Armenia.*

We have presented a simple analytical model for estimating critical radius of full depletion in semiconductor nanowires due to charge carrier trapping at surface states and radial band bending. The model describes the critical radius functional dependences on doping level, surface states parameters and appears as a very useful tool to understand transport properties of nanowires limited particularly by surface effects.

Keywords: semiconductor, nanowires, critical radius, full depletion.

I.   INTRODUCTION

Among other nanostructures, semiconductor nanowires (NWs) with a diameter typically of the order of 10 *nm* to 100 *nm* and aspect ratios as high as 10^2, even without quantum size effects, offer exciting possibilities as building blocks for different photovoltaic devices, in particular, for photosensitive elements in highly integrated optoelectronic devices [1] and for third generation of solar cells [2]. Nanowire based photo detectors can yield higher light sensitivity than their bulk or thin film counterparts due to the large surface-to volume ratio and small dimensions comparable to the carrier diffusion length [3,4].

Because of inherently large surface-to-volume ratio, NWs contain an extremely high density of surface states very often causing Fermi level pinning near the middle of the bandgap. Due to the exchange of electrons between the surface and volume and their trapping at surface states, NWs can exhibit a depletion space charge layer with an extension of the order of the NW diameter or even inversion effects [5], which can strongly influence the electric and photoelectric characteristics of NWs and NWs based devices. Control of the depletion layer thickness is important for the operation of NW devices as field-effect transistors [6], photoconductive optical detectors [8] and solar cells [9].

Later we will assume that the nanowire radius R is greater than de Broglie wave length, so we can neglect in our calculations quantum size effects.

II.   THE SIZE DEPENDENT SURFACE BAND BENDING AND CRITICAL RADIUS

We consider cylindrical NW with uniform donor type doping density N_D, and we consider that all dopants are ionized leading to a free carrier concentration of the same density. We assume acceptor-like recombination traps on the surface with the density N_S, capturing electrons from the volume and resulting in electric field in radial direction. For the simplicity we assume that only one type of acceptor-like states with ionization energy Eg exist on the surface. The negative charge of surface states gives rise to a positively charged depleted region, which is formed near the surface of the nanowire and has the width W. This causes surface band bending with the equilibrium potential barrier USO and, in general, results in an undeleted conducting neutral core of radius (R-W) within the nanowire.

There is a certain radius of NW, so called critical radius (RC), when the total NW is totally depleted from free charge carriers. We must note that such situation is possible if NS is enough large and all electrons from the volume of NW are not able to fill all surface states i. e

$$N_S > \frac{N_D R}{2}.$$

(1)

For thinner NWs the total charge per unit length of NW decreases, which causes the reduction of the surface potential barrier at equilibrium (Fig.1.c), and so the surface potential barrier becomes radius dependent for NW with R<RC.

To define the critical radius of NW the Poisson equation in cylindrical coordinates must be solved.

III. RESULTS AND DISCUSSION

We can examine the dependence of critical radius of semiconductor NW on doping level, surface states density and their ionization energy. Fig.1 shows the critical radius variation with surface state ionization energy for different values of doping level / Fig.1, curve 2,3/.
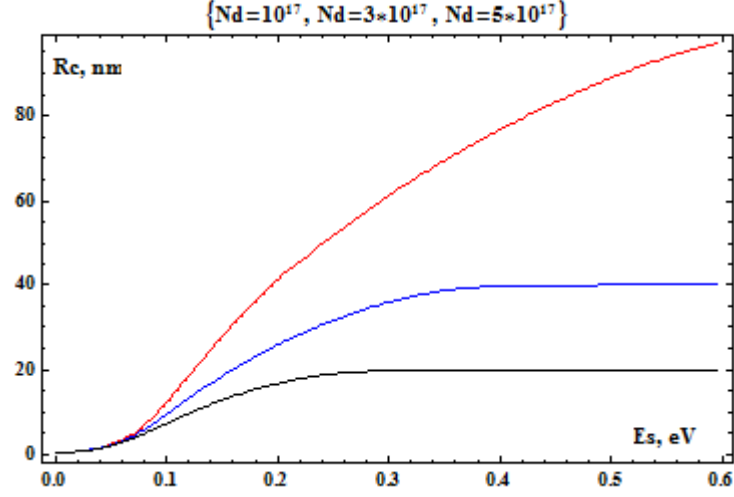
Fig.1. Critical radius dependence on ionization energy of surface states for Si-NW

$$(N_S = 5 \cdot 10^{11} cm^{-2}, N_D = 10^{17}, 3 \cdot 10^{17}, 5 \cdot 10^{17} cm^{-3}).$$
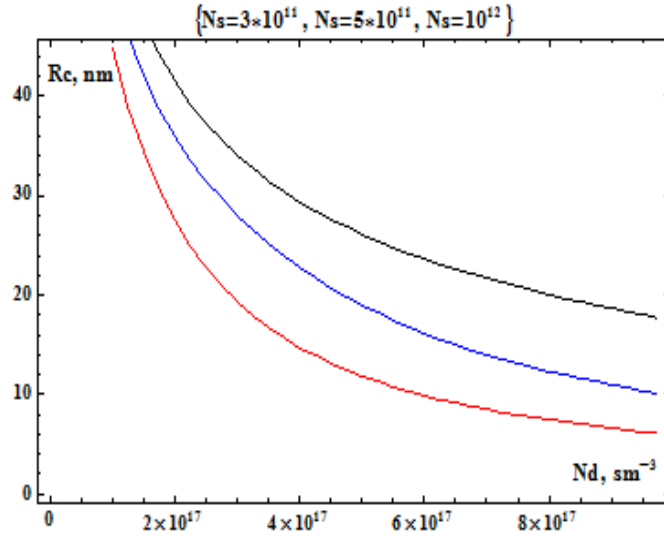
Fig.2. Critical radius dependence on doping level for Si-NW

$$(E_S = 0.25 eV, N_S = 3 \cdot 10^{11}, 5 \cdot 10^{11}, 10^{12} cm^{-2}).$$

Fig. 2 shows the variation of the critical radius versus doping level for different values of surface states concentrations ($N_S = 3 \cdot 10^{11}$, $5 \cdot 10^{11}$, 10^{12} cm^{-2}).

IV. CONCLUSIONS

Charge trapping by NW surface states can cause the formation of a depletion region near the surface of NWs limiting their electrical transport features, which is crucial function in most electronic devices. For small NW radii or doping level the number of free charges is insufficient to screen the electric field of charged surface states and NW can be nearly or fully depleted. Simple analytical approach has been proposed to estimate NW critical radius of such full depletion for the given surface states density, ionization energy and bulk doping level.

All above discussed depletion effects should be taken into account while designing particular devices containing NWs. One way to reduce the detrimental effects of surface states is to passivite the NW surface states by covering it with appropriate thin oxide or semiconductor film (core-shell heterostructures).

V. REFERENCES

[1] C. Soci, A. Zhang, X-Y.Bao, H. Kim et al.,J. Nanosci. Nanotechnol., vol. 10, no.1, 2010.

[2] V. Sivakov, G. Andra, A.Gawlik, A. Berger, et al., Nano Lett., vol. 9, no. 4, p.1549, 2009.

[3] G Mariani, R.B. Laghumavarapu, B. Tremolet de Villers, J. Shapiro, P. Senanyake, A. Lin, B.J. Schwartz, and D.L. Huffaker, Appl. Phys.Lett, vol.97, p. 013107, 2010.

[4] G Mariani, P.-S. Wong, A.M. Katzenmeyer, F. Leonard, J. Shapiri and D.L. Huffaker, Nano Lett., vol.11, p.2490, 2011.

[5] R-S.Chen, H.Y.Chen, C.Y.Lu et al., Appl. phys. Lett., vol. 91, p. 223106, 2007.

[6] H. Kind, H.Yan, B. Messe et al., Adv. Mater., vol.14, no. 2, p. 158, 2002.

[7] S.G. Petrosyan, S. Nersesyan, A. Yesayan. Armenian Journal of Physics, vol. 6, no. 2, p.72, 2013.

[8] R. Calarco, M. Marso, T. Richter, A.I. Aykanatet al, Nano Lett., vol.5, p.981, 2005.

[9] V. Schmidt, S. Senz, and U. Gosele, "Influence of the Si/Sio2 interface on the charge carrier density of Si nanowires", Appl. Phys. A:Mater. Sci.Process, vol. 86, pp.187-191, 2004.

[10] B. S. Simpkins, M.A. Mastro, C.R. Eddy, P.E. Pehrsson, "Surface depletion effects in semiconductor nanowires", J.Appl. Phys., vol.103, pp.104313-104313-6, 2008.

[11] A. C.E. Chia, R.R. LaPierre, "Analytical model of surface deplethion in GaAs nanowires", J.Appl. Phys, vol.112, pp. 063705-1-7, 2012.

Preparation Technology and Optical Properties of $CH_3NH_3PbI_{3-x}Cl_x$ Perovskite Thin Films

L. Matevosyan[1], A. Kechiantz[1], K. Avjyan[1], E. Zaretskaya[2], A. Ethiraj[3]

[1] *Institute of Radiophysics and Electronics, Alikhanian Brothers str. 1, 0203 Ashtarak, Armenia*
[2] *Scientific-Practical Materials Research Centre of the National Academy of Sciences of Belarus*
[3] *Center for Nanotechnology Research (CNR), VIT University, Vellore*

Optical properties of $CH_3NH_3PbI_{3-x}Cl_x$ thin films obtained by two-step vacuum deposition processing. Optical absorption edge (1.6 eV for as-deposited and annealed $CH_3NH_3PbI_{3-x}Cl_x$ film) has been estimated by using of absorption coefficient spectra curves. It is shown that the annealing of as-deposited $CH_3NH_3PbI_{3-x}Cl_x$ film leads to a sharp edge of the optical absorption and an increase of absorption coefficient in several times.

I. INTRODUCTION

In past five years have been seen hybrid organometallic perovskite solar cells performing promisingly on a low-cost avenue to the solar energy. Power conversion efficiency had been boosted up to 15% in 2013 [1]. Subsequently, the power conversion efficiency climbed to 19.3% by engineering the interface on a planar device [2]. This paper presents the results of optical investigations of $CH_3NH_3PbJ_{3-x}Cl_x$ mixed organometallic perovskite films prepared by thermal vacuum deposition or combining thermal vacuum deposition and vapor-processed technologies.

II. SAMPLE PREPARATION AND INVESTIGATION PROCEDURE

The chosen method of vacuum thermal evaporation, along with other thin-film technologies, is one of the most convenient way for preparation of perovskite thin films. For growth of mixed halide perovskite $CH_3NH_3PbJ_{3-x}Cl_x$ films inorganic lead iodide (PbJ_2) and organic methylammonium chloride CH_3NH_3Cl (MCl) precursors were used. Previously cleaned glass plates as a substrate and quartz crucibles for evaporation of precursor materials were used. As much as both materials well sublimated, the evaporator temperatures are adjusted below the melting temperatures of the selected materials, which allow us to make suitable control of the deposition process. Investigations has shown that the most good results are obtained in two-step process, when at firs were deposited PbJ_2 film followed by organic film evaporation. At the selected temperatures of the sources, good results are achieved when substrate exposure time for the organic source exceeding the exposure time of the inorganic source about twice. The typical corresponding times are 2-3 min and 4-6 min for film thickness approximately 500 nm. These $CH_3NH_3PbJ_{3-x}Cl_x$ films finally were annealed at 100 ^{0}C for 15-60 min. Color of resulting films changes from brown to dark brown and then to black depending on the composition. It was not possible to obtain the original films of a satisfactory quality when there is a reverse sequence of the evaporated materials and in co-evaporation mode also.

Optical properties of obtained films were investigated by independent measurements of transmittance (T) and reflectance (R) on spectrometer Filmetrics F20 (spectral range 400-1000 nm) at the normal incidence of light. Absorption coefficient (α) was calculated from measured data R and T by using of well known approximate relation in the interference free region: $T = (1 - R)^2 e^{-\alpha d} / (1 - R^2 e^{-2\alpha d})$ [3], where d is the film thickness calculated from reflectance spectra. In order to establish the nature of optical transitions, α was approximated with the empirical Urbach law $\alpha = \alpha_0 \exp(h\omega/E_u)$ (α_0 and E_u are the Urbach parameters) and power law $\alpha h\omega = B(h\omega - E_g)^m$.

III. RESULTS

Beforehand we say that an explicit dependence of the physical properties of obtained films on their thickness is not observed. Fig. 1. shows α spectra for 1- PbJ_2 precursor film, 2- as deposited $CH_3NH_3PbI_{3-x}Cl_x$ composite film, 3- annealed $CH_3NH_3PbI_{3-x}Cl_x$ composite film. It can be seen that the annealing of as

deposited $CH_3NH_3PbI_{3-x}Cl_x$ composite film leads to a sharp edge of the optical absorption and an increase of α in several times. Fig. 2 shows the dependencies of Lnα from photon energy for as-deposited (1) and annealed (2) $CH_3NH_3PbI_{3-x}Cl_x$ film. An exponential form of the fundamental absorption edge is observed in contrast to the PbJ_2 film.
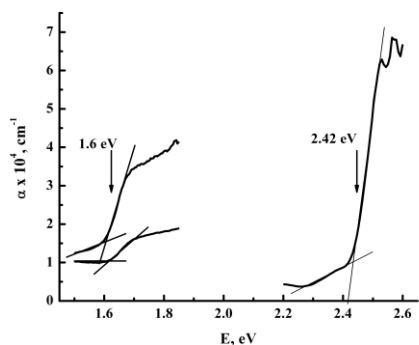
Fig.1
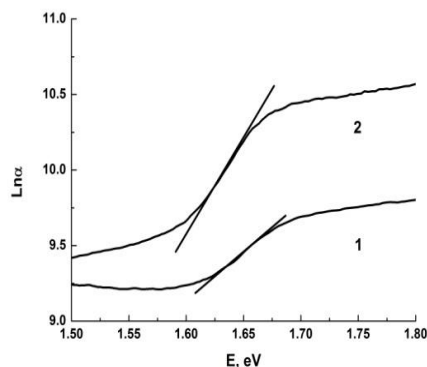
Fig.2

It is impossible to determine the type of optical transition (indirect or direct) (power low is not valid). Optical absorption edge (1.61 eV for as-deposited and annealed $CH_3NH_3PbI_{3-x}Cl_x$ film) has been estimated by using of α curves (Fig. 1). Similar optical properties have also been observed for the Tl_2S layered semiconductor crystals [4]. The value (2.43 eV) of lowest direct gap (X_1 to X_2 transition in Brillouin zone) in PbJ_2 film is satisfactory agreement with the bulk [5].

IV. CONCLUSION

Mixed organometallic $CH_3NH_3PbI_{3-x}Cl_x$ films were prepared by two-step vacuum deposition processing. It is shown that the annealing of as-deposited $CH_3NH_3PbI_{3-x}Cl_x$ composite film leads to a sharp edge of the optical absorption and an increase of α in several times.

V. REFERENCES

[1] M. Liu et al, "Efficient planar heterojunction perovskite solar cells by vapor deposition". Nature, vol. 501, 7467, p. 395, 2013.
[2] R.F. Service, "Perovskite solar cells keep on surging". Science, vol.344, no. 6183, p. 458, 2014.
[3] R. K. Willardson, A. C. Beer, "Semiconductors and Semimetals", New York, London, Academic Press, 1967.
[4] V. M. Belyukh et al, "Optical properties and band structure of layered Tl2S crystal", Solid State Physics, vol.55, no. 11, p. 2202- 2208, 2013 (in Russian).
[5] M. R. Torbs, "The optical properties and chemical decomposition of halids with layer structures", Phys. stat. sol. (b) vol. 49, p. 11, 1972.

Acknowledgements

The New Dual-Reflector Axisymmetric Antenna with Circular Generatrix The Main Reflector

N.R. Khachatryan, R.V. Ter-Antonyan

National Institute of Metrology, Komitas Ave., 49/3, 0015 Yerevan, Armenia

Dual-reflector axisymmetric antenna consisting of the main reflector with circular generatrix, displaced in relation to the axis of rotation, and subreflector with curvilinear generatrix, with sharpening on a symmetry axis directed towards a feed which phase centre is combined with focus of system is offered. The polar parametrical equations generatrix a subreflector and obvious expression for the transforming function which, by simple multiplication by the directional pattern of a feed, transfers the last to inphase amplitude distribution of a field in an antenna aperture are given. Are noted, without analyzing, two features of the antenna which are advantageously distinguishing its from know analog with parabolic generatrix the main reflector and elliptic generatrix a subreflector.

I.   BACKGROUND

In [1] the dual-reflector axisymmetric antenna with high frequency-independent matching with feed is offered. The last is reached by parallel shift parabolic generatrix the main reflecyot (MR) concerning a rotation axis. It the shift causes an inclination elliptic generatrix of a subreflector (SR) an emergence of the arc generatrix between a focal axis and rotation axis which at rotation gives rise to a SR with sharpening on a symmetry axis. The last directs the central ray of a feed to an external edge of the MR, and an extrem ray to an internal edge.Thereby the rays which are coming back to a feed are excluded.

The optical scheme of system is shown on Fig.1, which we borrowed from [2].

Fig.1 Path of the central and typical rays through system in the tranmit mode. AA, rotation axis, it is symmetry axis; 1, the MR with parabolic generatrix with focus in a point F_p; 2, a SR with elliptic generatrix with focuses in points O and F_p; O, focus of system; d, diameter of a SR, it is diameter of a focal ring, it is diameter "hole" in the MR.

The Russian developers of the antenna offered in [1] faced the fact that the antenna is unrealizable in the form of the traditional dual-reflector antenna with the shallow MR, with a feed located near top of the MR and a SR supported by a tripod. Exit was found in lengthening of a waveguide with a feedhorn end-to-end to a SR and a joint of the last in the iniform block. Fig.2 which we borrowed from [2]

illustrates told. Thougt the MR continued to remain rather deep, reconciled to it, absence in the antenna of the shading tripod consoled.
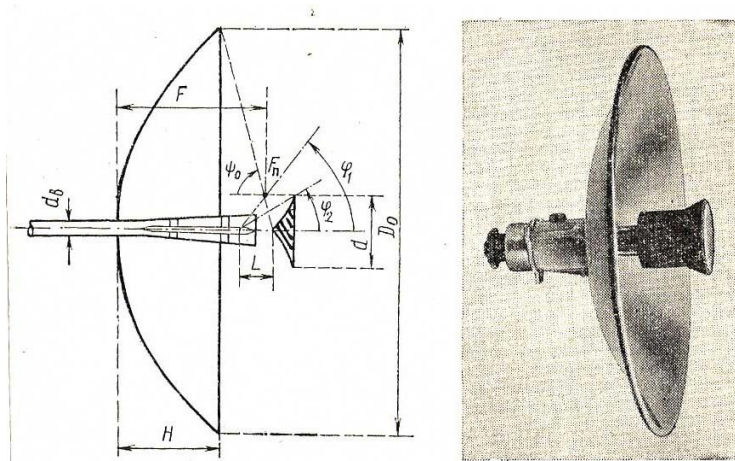
Fig. 2

Poe being, the concrete antenna with high matching with feedhorn, lost the know advantages of dual-reflector antennas. To is shortcomings existence a focal ring which complicated adjustment of the antenna increased.

Nevertheless, thanks to penetrative ability of developers the antenna, in due time, was introduced to radio relay lines of the Soviet Union [2], and now it is intrduced in telecommunication system of Moscow (Fig.3).

Fig.3

We claim that the SR with sharpening on a symmetry axis can quite be entered in traditional scheme dual-reflector antennas if as generatrix the MR to choose not parabolic, and circular generatrix. In this case the focal ring will disappear, and the axial size of a SR will poorly depend on location of focus of system on a symmetry axis as generatrix of a SR, providing focusing, will be a curve of the fourth order.
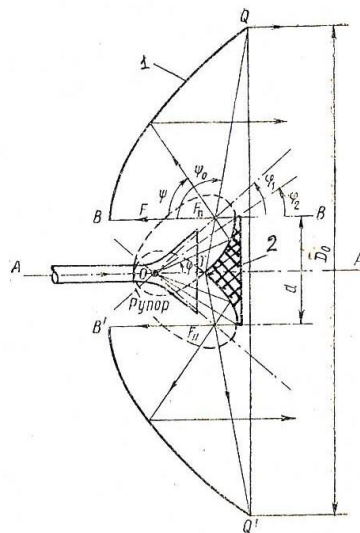
In Fig.4 the optical scheme of the antenna is shown.
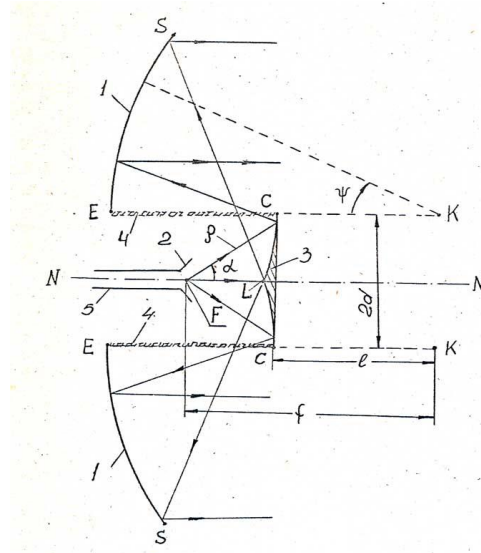
Fig,4 Path of the central and typical rays through system in the transmit mode. NN, rotation axis, it is symmetry axis; 1, the MR with circular generatrix ES with the center in a point K and with a radius of R; 2, feedhorn; F, focus of system; 3, a SR with generatrix LC; 2d, diameter of a SR, it is diameter "hole" in the MR; l ≤ 0.5R, controllable constant defining distance of the limiting point generatrix of a SR from a point K; f > l, controllable constant defining distance focus of system from a projection of a point K. on a rotation axis; ψ, central angle.

The mathematical ratios which are necessary for radio physical design of the antenna are given in the following section.

II. FOR DESIGNER

From geometrical optics with use of the designations Fig.4 it is possible to show that generatrix of a SR, providing focusing, it has to be described by the following polar parametrical equations:

$$\rho = 0.5\{M_1 + M_2^2/M_1\}, \tag{1}$$
$$\alpha = 2\arctg\{M_2/M_1\} - 2\psi, \tag{2}$$

where

$$M_1 = M - 2R\cos\psi + f\cos2\psi - d\sin2\psi, \tag{3}$$
$$M_2 = f\sin2\psi - R\sin\psi + d\cos2\psi, \tag{4}$$
$$M = 2R - 1 + \{(f-l)^2 + d^2\}^{1/2}. \tag{5}$$

We will note that the given equations come down to know [3] if to put d=0 and to change a sign of an angle α.

It is logical to take as given sizes diameter(2D) of the MR, diameter(2d) of a SR and value of the controllable constant l ≤ 0.5R which provides a form generatrix of a SR as on Fig.4. Then

$$\sin\psi_{max} = (D - d)/R, \tag{6}$$
$$\alpha_{max} = \alpha(\psi=0) = 2\arctg\{d/(M - 2R + f)\}, \tag{7}$$
$$s = R/\{2\cos\psi_{max}\} - d/\tg\psi_{max}, \tag{8}$$

where s, distance of the sharp end(L) of a SR from a projection of a point K on a rotation axis(Fig.4),

$$z = s - l, \tag{9}$$

where z, axial size of a SR,

$$f = s + \Delta \tag{10}$$

where Δ is chosen so that focus of system was located closer to the MR.

The equation $\alpha(\psi_{max}) = 0$, with use (2), can be given to look:

$$(d + R\sin\psi_{max})\cos\psi_{max} = \{2R - 1 + \{(f - l)^2 + d^2\}^{1/2} - f\}\sin\psi_{max} . \tag{11}$$

In the first order on d dependence from f in the right part (11) disappears and (11) becomes simpler:

$$(d + R\sin\psi_{max})\cos\psi_{max} = 2(R - 1) \}\sin\psi_{max} . \tag{12}$$

Substituting (6) in (12), we will receive the following formula for calculation of radius circular generatrix of theMR,

$$R = (D - d) / \{1 - 4(1 - z_0)^2(1 - l_0)^2\}^{1/2},$$

Where $z_0 = d/D$, $l_0 = l/R \le 0.5$.

From the energy conservation law in a beam tube it is possible to receive obvious expression for function which, by multiplication on the directive pattern of a feed, transforms the last to amplitude distribution of the field in an aperture of antenna:

$$q(\psi) = \{\{\alpha' \ \sin\alpha\} / \{(d_0 + \sin\psi)\cos\psi\}\}^{1/2} , \tag{13}$$

where the prim denotes the derivative of ψ.

Formulas [1] – [13] represent base for radio physical design of the antenna.

Trial calculations aperture efficiency are carred out for option $l/R = 0.49$, $f/R = 0.63$, $d/R = 0.05$, $\alpha_{max} = 19.7°$, $\psi_{max} = 23.7°$ with optimized the directive pattern of a feed and give the value exceeding 0.95.

III.   REFERENCES

1. I.L, Lee, "Improvements in or relating to Microwave Aerials", English patent No. 973583, Is published Oct. 1964.
2. G.Z. Ayzenberg, V.G, Yampolsky, O.N. Teryoshin, VHF antennas, Part 2. (SU), "Svyaz", M.,1977.
3. A.K. Head, "A new form for a giant radio telescope", Nature, vol.179, pp. 692-693, April 6, 1957.

Features of Radar Cross-section Determination Using Near-field Measurements

M. Ivanyan[1, 2], N. Khachatryan[1], E. Tagvoryan[1]

[1]*Institute of Metrology, Komitas Ave. 49/4, 0015 Yerevan, Armenia*
[2]*Synchrotron Research Institute (CANDLE), Acharyan Str. 31, 0040, Yerevan, Armenia;*
e-mail: mikayel.ivanyan@gmail.com

An updated algorithm for determine radar cross section (RCS) of object, based on near-field measurements, is presented. The algorithm has two components: the process of measurement and mathematical processing of the measured data. The illuminator and probe (electric or magnetic dipoles) are located on concentric scanning spheres (exterior and interior), covering the object. The measurements carried out for each fixed mutual arrangement of emitting and measuring probes, moving with a certain increments. Data processing carried out using the method of spherical harmonics and of the reciprocity principle. The problem is to exclude the direct fixation of the illuminator radiation by the measuring probe. The traditional way to eliminate this effect is to measure the electric and magnetic components of the scattering field of object for two orthogonal tangential orientations of the electric and magnetic dipole radiators. The presented generalized method allows excluding a direct effect of the radiator on the measuring probe by measuring only of the electrical components of the scattered field, and, in addition, to obtain the absolute value of RCS using relative measurements.

I. INTRODUCTION

Radar cross section (RCS) is a main characteristic of radar object. To remove the effect of the distance, the plane wave far-field scattering is considered. RCS is the ratio of the power density, scattered from the object $\left|\vec{E}^s\right|^2$ in a given direction to the power density of a plane wave incident on the object $\left|\vec{E}^i\right|^2$:
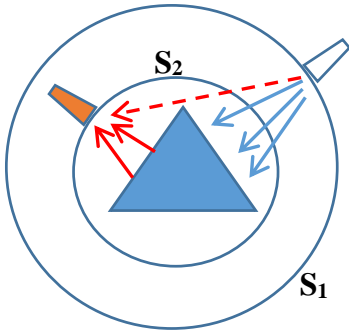
$$\sigma = \lim_{r\to\infty} 4\pi r^2 \left|\vec{E}^s\right|^2 / \left|\vec{E}^i\right|^2 \qquad (1)$$

Fig.1. Description of measurement scheme

RCS depends from the direction of incident plane wave, the observation direction and the polarization of incident plane wave as well. The full RCS distribution is represented as a two-positional diagram for each of two polarizations of incident planar wave. The far-field methods, currently used for RCS measuring, produced both in the open countryside, and in anechoic chambers [1]. Near-field measurement methods developed as well [2, 3]. In particular, in [2] two-dimensional algorithm of near field to far field converting was developed.

In works [4, 5] a three-dimensional method for determining RCS of objects by near-field measurements is proposed. Far-field characteristics of the scattered field are determined by exact mathematical processing of near-field measurements data. Briefly the method consists of the following (Fig.1). The object illuminated by emitter moving along the scanning surface S_1, which covers the object. The measuring probe is located on the second scanning surface S_2 which also covers the object, and covered by the first (emitter) surface. Measurements are performed across the probe scanning surface for each fixed position of the radiator. The case of two concentric spherical surfaces shown on Fig 1. In this case processing of measured data performed by the vector spherical harmonics method [6].

This paper contains an updated algorithm for the measured information processing. It allows, without changing the measurement circuit, to eliminate the mutual influence of the probes at each other, and, without using a reference object, to get the absolute value of RCS.

II. DATA PROCESSING ALGORITHM

In relation to the discussed problem, there are two possible ways to use the vector spherical harmonics

method: (a) measurements of the tangential component of the electric fields on the scanning surface for the two different orthogonal orientations of the radiator, placed in given point; (b) measurement of the tangential electric and magnetic components using electric and magnetic probes, for two orthogonal, tangential to scanning surface, orientations of the electric and magnetic kind of radiators (for example: for the point electric and magnetic dipoles).

The initial set of the measured electric and magnetic field components on the scanning surface S_2 may be symbolically represented as follows:

$$E'^{\vec{r}_1,\vec{\alpha}_1}_{\vec{r}_2,\vec{\alpha}_2}, H'^{\vec{r}_1,\vec{\alpha}_1}_{\vec{r}_2,\vec{\alpha}_2} \tag{2}$$

Here the superscripts indicate the location point $\vec{r}_1$ $(r_1, \theta_1, \varphi_1)$ and the polarization $\vec{\alpha}_1 = \vec{\theta}_1, \vec{\varphi}_1$ of the radiator. The subscript shows the location point of the probe $\vec{r}_2$ and the possible orientation of its polarization $\vec{\alpha}_2 = \{\vec{\theta}_2, \vec{\varphi}_2\}$. The prime indicates an availability of direct contribution from the radiator. Pure scattered fields are denoted as $E^{\vec{r}_1,\vec{\alpha}_1}_{\vec{r}_2,\vec{\alpha}_2}, H^{\vec{r}_1,\vec{\alpha}_1}_{\vec{r}_2,\vec{\alpha}_2}$ (unprimed).

In the cases of (a) and (b) the fields, reconstructed on the arbitrary observation point $\vec{r}$, based on the measured on the surface S_2 electrical [7] or electrical and magnetic [8] components, may be symbolically written with the help of conversion operators $\hat{E}_{E,H}, \hat{G}_{E,H}$ and $\hat{\hat{E}}_{E,H}, \hat{\hat{G}}_{E,H}$ respectively:

$$\{\dot{E},\dot{H}\}^{\vec{r}_1,\vec{\alpha}_1}_{\vec{r},\vec{\alpha}_2} = \frac{\hat{E}_{E,H}}{\hat{G}_{E,H}} \left(\left\{ E'^{\vec{r}_1,\vec{\alpha}_1}_{\vec{r}_2,\vec{\alpha}_2} \right\}, r \right), \frac{for\ r > r_2}{for\ r < r_2} \tag{3}$$

$$\{\dot{E},\dot{H}\}^{\vec{r}_1,\vec{\alpha}_1}_{\vec{r},\vec{\alpha}_2} = \frac{\hat{\hat{E}}_{E,H}}{\hat{\hat{G}}_{E,H}} \left(\left\{ E'^{\vec{r}_1,\vec{\alpha}_1}_{\vec{r}_2,\vec{\alpha}_2}, H'^{\vec{r}_1,\vec{\alpha}_1}_{\vec{r}_2,\vec{\alpha}_2} \right\}, r \right), \frac{for\ r > r_2}{for\ r < r_2} \tag{4}$$

The argument r in (3, 4) indicates the radius of the spherical surface of the restored field. Explicit expressions of the above operators, suitable for use in the context of this presentation, are given in [9, 10]. Schematic diagram of the synthesis of the far-field scattering from the far zone source is given on Figure 2.

Both of algorithms (3) and (4) can correctly restore the components of the radiation field at an arbitrary space point $\vec{r}$ for $r > r_2$ $(r < r_2)$ in absence of external (internal) radiation $\left(\{\dot{E},\dot{H}\}^{\vec{r}_1,\vec{\alpha}_1}_{\vec{r},\vec{\alpha}_2} = \{E,H\}^{\vec{r}_1,\vec{\alpha}_1}_{\vec{r},\vec{\alpha}_2} \right)$ [9-11]. The recovered components are identical for both of cases (3) and (4). In the presence of radiation source outside of scanning surface S_2, measured fields $E'^{\vec{r}_1,\vec{\alpha}}_{\vec{r}_2,\vec{\beta}}$, $H'^{\vec{r}_1,\vec{\alpha}_1}_{\vec{r}_2,\vec{\alpha}_2}$ contain, in addition to the scattered field $E^{\vec{r}_1,\vec{\alpha}}_{\vec{r}_2,\vec{\beta}}$, $H^{\vec{r},\vec{\alpha}_1}_{\vec{r}_2,\vec{\alpha}_2}$, the direct contribution of the illumination source. In general, when there is an external (internal) relative to the scanning sphere S_2 source of the radiation, the procedure of field restoration by the help of algorithm (3) in an arbitrary point in space $r > r_2$ $(r < r_2)$ distorts the true shape of the field $\left(\{\dot{E},\dot{H}\}^{\vec{r}_1,\vec{\alpha}_1}_{\vec{r},\vec{\alpha}_2} \neq \{E,H\}^{\vec{r}_1,\vec{\alpha}_1}_{\vec{r},\vec{\alpha}_2} \right)$ [9]. Correct account of external scattered radiation by the help of (3), as shown in [9, 10], is possible only if $r = r_2$, i.e. on the scanning surface itself:

$$\{\dot{E},\dot{H}\}^{\vec{r}_1,\vec{\alpha}_1}_{\vec{r}_2,\vec{\alpha}_2} = \frac{\hat{E}_{E,H}}{\hat{G}_{E,H}} \left(\left\{ E'^{\vec{r}_1,\vec{\alpha}_1}_{\vec{r}_2,\vec{\alpha}_2} \right\}, r_2 \right) = \{E', H'\}^{\vec{r}_1,\vec{\alpha}_1}_{\vec{r}_2,\vec{\alpha}_2} \tag{5}$$

Above distributions, obtained by algorithm (3) by using only measured near field tangential electrical components, are suitable for further reconstruction of the field, free from the source direct contribution, to the region out of the surface S_2 $(r > r_2)$ by using algorithm (4):

$$\{E,H\}^{\vec{r}_1,\vec{\alpha}_1}_{\vec{r},\vec{\alpha}_r} = \hat{\hat{E}}_{E,H} \left(\left\{ E'^{\vec{r}_1,\vec{\alpha}_1}_{\vec{r}_2\vec{\alpha}_2}, H'^{\vec{r}_1,\vec{\alpha}_1}_{\vec{r}_2,\vec{\alpha}_2} \right\}, r \right) \tag{7}$$

From the distribution (7) of the electromagnetic field, reconstructed in far-field region $(R \gg r_2)$, the complex angular diagram can be allocated:

$$\{E,H\}^{\vec{r}_1,\vec{\alpha}_1}_{\vec{R},\vec{\alpha}_R} = \widehat{\tilde{F}}_{E,H}\left(\left\{E'^{\vec{r}_1,\vec{\alpha}_1}_{\vec{r}_2,\vec{\alpha}_2}, H'^{\vec{r}_1,\vec{\alpha}_1}_{\vec{r}_2,\vec{\alpha}_2}\right\}, R\right)\frac{e^{ikR}}{R} \qquad (8)$$

For the reconstruction of the scattered field of object by imaginary source positioned in the far field, we use the principle of reciprocity [12]. The principle of reciprocity is valid for the whole system: object plus environment. For two elementary radiating electric dipoles with the unit dipole moments, this principle in our notations can be written as follows:

$$E'^{\vec{r}_1,\vec{\alpha}_1}_{\vec{R},\vec{\alpha}_R} = E'^{\vec{R},\vec{\alpha}_R}_{\vec{r}_1,\vec{\alpha}_1} \qquad (9)$$

One dipole (imaginary, radiating) is situated in the far zone at the point $\vec{R}\{R,\theta,\varphi\}$ (Fig.2). Its dipole moment $\vec{\alpha}_R$ is oriented along one of the angular unit vector of the spherical coordinate system: $\vec{\alpha}_R = \vec{\vartheta}$ or $\vec{\varphi}$. Another one coincides with the actual radiator, located on the corresponding scanning spherical surface S_1 at the point $\vec{r}_1\{r_1,\theta_1,\varphi_1\}$ with moment $\vec{\alpha}_1$ oriented along the angular unit vectors at this point: $\vec{\alpha}_1 = \vec{\vartheta}_1$ or $\vec{\varphi}_1$.

Thus, we have series of distributions of the tangential components $E'^{\vec{R},\vec{\alpha}_R}_{\vec{r}_1,\vec{\alpha}_1}$ ($\vec{\alpha}_1 = \vec{\theta}_1$ or $\vec{\varphi}_1$) of scattered electric field of object on the scanning surface S_1 ($\vec{r}_1 = \{r_1, \vartheta_1, \varphi_1\}$, $0 \le \vartheta_1 \le \pi$, $0 \le \varphi_1 \le 2\pi$) formed

Fig.2. Data processing algorithm

by the imaginary dipole illuminator, placed in the far zone on the arbitrary point on the sphere of radius $R \gg r_{1,2}$, ($0 \le \theta \le \pi$, $0 \le \varphi \le 2\pi$) with two orthogonal orientation of its dipole moment: $\vec{\alpha}_R = \vec{\theta}$ or $\vec{\alpha}_R = \vec{\varphi}$.

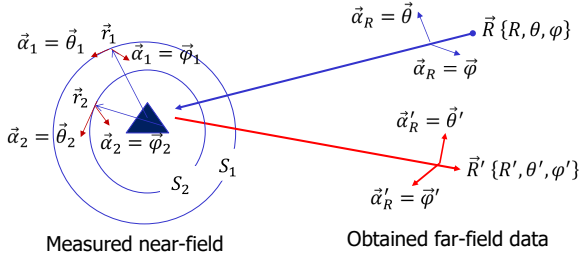Dipole radiator, located on the scanning sphere S_1, after application of the principle of reciprocity (9), converts to an imaginary measuring probe, which is experiencing the direct impact of imaginary emitter, placed in the far zone. True representation of external influences is achieved by using the algorithm (3):

$$\left\{\dot{E},\dot{H}\right\}^{\vec{r}_1,\vec{\alpha}_1}_{\vec{R},,\vec{\alpha}_R} = \widehat{E}_{E,H}\left(\left\{E'^{\vec{r}_1,\vec{\alpha}_1}_{\vec{R},\vec{\alpha}_R}\right\}, r_1\right) = \widehat{E}_{E,H}\left(\left\{E'^{\vec{R},\vec{\alpha}_R}_{\vec{r}_1,\vec{\alpha}_1}\right\}, r_1\right) = \{E',H'\}^{\vec{R},\vec{\alpha}_R}_{\vec{r}_1,\vec{\alpha}_1} \qquad (10)$$

The resulting information is sufficient to determine scattering field of object in the far zone, formed by a dipole, placed in the far zone, which is necessary for RCS determination:

$$\{E,H\}^{\vec{R},\vec{\alpha}_R}_{\vec{R}',\vec{\alpha}_{R'}} = \widehat{\tilde{E}}_{E,H}\left(\left\{E'^{\vec{R},\vec{\alpha}_R}_{\vec{r}_1,\vec{\alpha}_1}, H'^{\vec{R},\vec{\alpha}_R}_{\vec{r}_1,\vec{\alpha}_1}\right\}, R'\right) \qquad (11)$$

Sequential substitution in (11) operator expressions (8-10), we obtain an explicit expression, which is necessary for RCS determination:

$$\{E,H\}^{\vec{R},\vec{\alpha}_R}_{\vec{R}',\vec{\alpha}_{R'}} = \widehat{\tilde{E}}_{E,H}\left(\left\{\widehat{E}_{E,H}\left(\left\{\widehat{\tilde{E}}_{E,H}\left(\left\{\widehat{E}_{E,H}\left(\left\{E'^{\vec{r}_1,\vec{\alpha}_1}_{\vec{r}_2,\vec{\alpha}_2}\right\}, r_2\right)\right\}, R\right)\right\}, r_1\right)\right\}, R'\right) \qquad (12)$$

Hereinafter for brevity of writing, in the arguments of operators $\widehat{\tilde{E}}_{E,H}, \widehat{\tilde{G}}_{E,H}$ the magnetic fields components are omitted. Using the simplified form $\widehat{\tilde{F}}_{E,H}$ (8) of operator $\widehat{\tilde{E}}_{E,H}$ for the reconstruction of the far field, finally one can write ($R' = R$):

$$\{E,H\}^{\vec{R},\vec{\alpha}_R}_{\vec{R}',\vec{\alpha}_{R'}} = \widehat{\tilde{F}}_{E,H}\left(\left\{\widehat{E}_{E,H}\left(\left\{\widehat{\tilde{F}}_{E,H}\left(\left\{\widehat{E}_{E,H}\left(\left\{E'^{\vec{r}_1,\vec{\alpha}_1}_{\vec{r}_2,\vec{\alpha}_2}\right\}, r_2\right)\right\}, R\right)\right\}, r_1\right)\right\}, R\right)\frac{e^{ik(R+R')}}{k^2 R^2} \qquad (13)$$

To determine the RCS (1), as it was mentioned above, the power density of radiation (13) should be normalized to the value of a field power density of emission source, placed in far zone and determined in the

object area. The right combination of imaginary probe field with the field of object is achieved by applying the algorithm $\hat{G}_{E,H}$ (3) to its electrical field distribution (9) on the scanning sphere S_1 of the real illuminator:

$$\{\dot{E},\dot{H}\}_{\vec{r}_1,\vec{\alpha}_1}^{\vec{R},\vec{\alpha}_R} = \hat{G}_{E,H}\left(\left\{E'^{\vec{R},\vec{\alpha}_R}_{\vec{r}_1,\vec{\alpha}_1}\right\},r_1\right) = \hat{G}_{E,H}\left(\left\{E'^{\vec{r}_1,\vec{\alpha}_1}_{\vec{R},\vec{\alpha}_R}\right\},r_1\right) = \{E',H'\}'^{\vec{r}_1,\vec{\alpha}_1}_{\vec{R},\vec{\alpha}_R} \tag{14}$$

Subsequent use of the operator $\hat{\hat{G}}_{E,H}$ (4) determines the field components as the fictitious far-field source at the point, closed to origin in the absence of object:

$$\tilde{E}^{\vec{R},\vec{\alpha}_R}_{\vec{r}_0,\vec{\alpha}_0} = \hat{\hat{G}}_{E,H}\left(\left\{E'^{\vec{R},\vec{\alpha}_R}_{\vec{r}_1,\vec{\alpha}_1}, H'^{\vec{R},\vec{\alpha}_R}_{\vec{r}_1,\vec{\alpha}_1}\right\}, r_0 \to 0\right) \tag{15}$$

Finally, using (13-15), we obtain an expression for the two-positional diagram of RCS:

$$\sigma^{\vec{R},\vec{\alpha}_R}_{\vec{R}',\vec{\alpha}'_R} = \frac{4\pi}{k^2}\frac{\left|\hat{\hat{F}}_E\left(\left\{\hat{E}_{E,H}\left(\left\{\hat{\hat{F}}_{E,H}\left(\left\{\hat{E}_{E,H}\left(\left\{E'^{\vec{r}_1,\vec{\alpha}_1}_{\vec{r}_2,\vec{\alpha}_2}\right\},r_2\right)\right\},R\right)\right\},r_1\right)\right\},R\right)\right|^2}{\left|\hat{\hat{G}}_E\left(\left\{\hat{G}_{E,H}\left(\left\{\hat{\hat{F}}_{E,H}\left(\left\{\hat{E}_{E,H}\left(\left\{\tilde{E}'^{\vec{r}_1,\vec{\alpha}_1}_{\vec{r}_2,\vec{\alpha}_2}\right\},r_2\right)\right\},R\right)\right\},r_1\right)\right\},r_0\to0\right)\right|^2} \tag{16}$$

The updated algorithm (16) is based on the actual measured data: superposition of scattered field of the object and the field of emitter, which is acting direct on the probe. Required only tangential electric field components. Emitter and the measuring probe are placed in the neighborhood of object (Fig.1).

III. CONCLUSION

Updated algorithm does not increase of the required number of measurements: as before [4,5], the tangential to the scanning surface electric field components of the scattering object for two orthogonal orientations of the radiator (scanned as well) polarization to be measured. Scanning step of probes is determined by the working wavelength and the number of vector spherical harmonics, necessary for the correct reconstruction of the final result. Last depends on the degree of complexity of the object shape and the material from which it is made. The principle of reciprocity (9), used in the construction of the algorithm, is valid for an arbitrary inhomogeneous and anisotropic media [12]. Due to the updating, the processing of measured data becomes more complicated. The problem is solved with the help of the developed in [13] method of Fast Fourier Transform for the vector spherical harmonics. Generalization of the proposed method to the probes with arbitrary diagrams can be produced using a variety of techniques that take into account the distorting effect of the probe on the measured data values (see, for example, [14]).

IV. REFERENCES

[1] K. M. Passino, The RCS Handbook: Tools for Real Time Control Systems Software Development, John Wiley, NY, 2001.
[2] A. Broquetas, J. Palau, L. Jofre, A. Cardama, IEEE Trans AP vol.46, p.730, 1998.
[3] S. Sensani, R. Cioni, A. Guidoni, L. Fiori, A. Sarri, https://www.idscorporation.com/measurement/
[4] P.M. Herouni, M.I. Ivanian, DAN SSSR vol. 292, p. 849, 1987.
[5] M. Ivanyan, N. Khachatryan, E. Tagvoryan, IRPhE'2010 Conf. 2010, p.159.
[6] J.A.Stratton Electromagnetic Theory, McGraw-Hill, NY, 1941.
[7] A.C. Ludwig, IEEE Trans. on Antennas and Propagation, vol. 19, p.214, 1971.
[8] P.J. Wood, The Marconi Review, vol. 34, p.149, 1971.
[9] M. Ivanyan, N. Khachatryan, E. Tagvoryan, IRPhE'2014 Conf. 2014, p.102.
[10] M. Ivanyan, N. Khachatryan, E. Tagvoryan, Proc. of EAA 12, 2015, p.713.
[11] E.D. Gazazyan, M.I. Ivanyan, Izv. VUZ-ov, Radiofizika, vol. 30, 1987, p.1221.
[12] L.D. Landau, E.M. Lifshitz, Electrodynamics of Continuous Media, Course of Theoretical Physics, 8, Pergamon Press, Oxford, 1963.
[13] M. Ivanyan, N. Khachatryan, E. Tagvoryan, Proc. of EAA, vol.10, p.337, 2013.
[14] A.D. Yaghjian, IEEE Trans. on Antennas and Propagation, vol. 34, p.30, 1986.

Pedestrian Caused Doppler Signal Detection by Bispectrum Processing in Ku-Band Coherent CW Radar

A.A. Hakhoumian, T.V. Zakaryan, E.R. Sivolenko

Institute of Radiophysics and Electronics, National Academy of Sciences, Alikhanian 1, Ashtarak, 0203, Armenia

Receiving signals from moving objects, especially from pedestrian, are classified in special group. The pedestrian global motion consists of several micro-motions. In power spectrum the phase relations between micro-Doppler spectral components are lost. So to keep phase information inessential. Under those circumstances using in-phase (I) and quadrature (Q) components is sufficient for keeping phase information to retain useful maximal in bi-spectrum graph.

I. INTRODUCTION

As it is known, second order statistics, such as autocorrelation function and power spectrum provide only information amplitude information, but that information isn't enough for pedestrian detection. The reflected signal from narrative moving object with constant velocity estimation shows that in power spectrum there is only one useful frequency. That frequency is Doppler shift frequency. In case, then the object is moving with acceleration, there is spectrum correlation. The picks are appearing. It becomes more difficult to separate useful picks from noise. For example, separate useful picks, which are belong to moving pedestrian, from noise. So it is very important to estimate phase information. In this case it is very important to use more powerful tool such as higher order statistics [1-3].

The phase information can be provided by higher order statistics such as third-ordered autocorrelation function and third-ordered spectra known as bispectrum [4]. Using of higher order statistics gives opportunities to find not only amplitude information, but phase information in addition. We are using higher order statistics to disclose pedestrian micro-doppler signature. Pedestrian hands and legs are moving opposite sides. The speed of pedestrian hands and legs are allocated between null and double of pedestrian body moving speed. So we have mathematical pendulums with opposite phases but with the same frequencies. This means that we have Doppler shift to different sides [5, 6]. In general, they are micro-doppler shifts, because the pedestrian motion includes different body parts with different motion structure [7-10].

In this paper we have received IQ signal using ground surveillance radar. That signal was received from moving target [11, 12]. At first sight in power spectrum we have signal which gives full description of pedestrian. But deeply analysis using HOS gives great opportunity to find phase coupled components in spectrum.

II. METHOD DESCRIPTION

Received signal is including useful information. For disclosing that information it is necessary to find available length of reflected signal spectrum. The Discretization step number is $N = 4000$. Analyzing time will be $T_a = NT_d$, where T_a is analyzing time and $T_d = 0.0001 \, s$ is discretization time.

As it is mentioned above reflected signal from pedestrian is very difficult. It means we have signal which is including i frequencies, there $i = 1, 2, \ldots$. For signal $s(t) = \sum_{i=0}^{N} A\cos(2\pi f_i t)$ and its Fourier transform $S(f) = \sum_{n=1}^{N} s(t)\exp(j2\pi fnT_d)$ where $j = \sqrt{-1}$, the $R_x(n,1)$ triple autocorrelation function and $\dot{B}_x(p,q)$ bispectrum are functions of two variables. $R_x(n,1)$ triple autocorrelation function is set as

$$R_x(n,l) = \sum_{i=0}^{N-1} [x^{(m)}(i) - E][x^{(m)}(i+n) - E][x^{(m)}(i+l) - E]_\infty \qquad (1)$$

where $n = 0,\ldots,N-1$ and $l = 0,\ldots,N-1$ are the independent shift indices, $\langle \ldots \rangle_\infty$ denotes ensemble averaging for infinite realization number ; $E = \dfrac{1}{N}\sum_{i=0}^{N-1} x^{(m)}(i)_\infty$ is the mean value. $\dot{B}_x(p,q)$ bispectrum is complex-valued function of two independent frequencies p and q. It can be written as 2-D discrete Fourier transform of triple autocorrelation function:

$$\dot{B}_x(p,q) = \sum_{n=0}^{N-1}\sum_{l=0}^{N-1} R_x(n,l)\exp\left[-j2\pi(np+lq)\right] \qquad (2)$$

Namely, for two f_1 and f_2 independent frequencies equation (2) will be written as

$$B(f_1,f_2) = S(f_1)S(f_2)S^*(f_1+f_2) \qquad (3)$$

If $f_3 \neq f_1 + f_2$ or $\varphi_3 \neq \varphi_1 + \varphi_2$, $B(f_1,f_2) = 0$. So, reflected signal from contains coherent components and that components can be found using HOS, i.e. equation 3.

III.   MOVING OBJECT DETECTION.

Reflected signal from pedestrian consists of several micro-motions. They are micro-doppler shifts, because the pedestrian motion includes different body parts with different motion structure [6]. In power spectrum the phase relations between micro-doppler harmonics are lost. Therefore, it is impossible to recover phase coupled frequencies by energy spectrum estimation. So to keep phase information is essential. Under those circumstances using in-phase (I) and quadrature (Q) components is sufficient for keeping phase information to retain useful picks in bispectrum graph. Ground surveillance radar block-scheme is illustrated in Fig. 1.
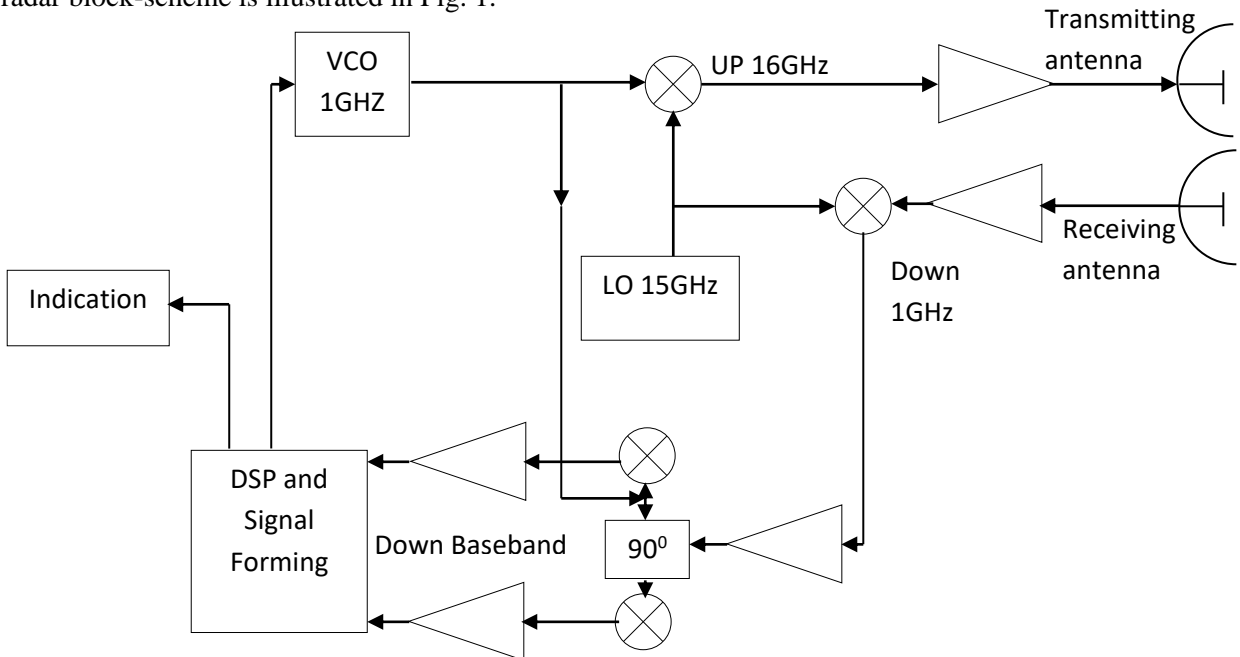

Fig. 1: Ku-band CW Radar simplified block-diagram.

Take in account that doppler frequency of pedestrian in Ku-band is lying on 10 Hz to 100 Hz due to phase features distortion phase noises have the highest importance. For this reason in ground surveillance radar system VCO and LO are chosen ultra-low phase noise. Although, LO has high linearity. There is need to estimate whole spectrum because pedestrian can move away and toward radar. In figure 2 are illustrated pedestrian moving away (a) and toward (b) the radar.

a)   b)
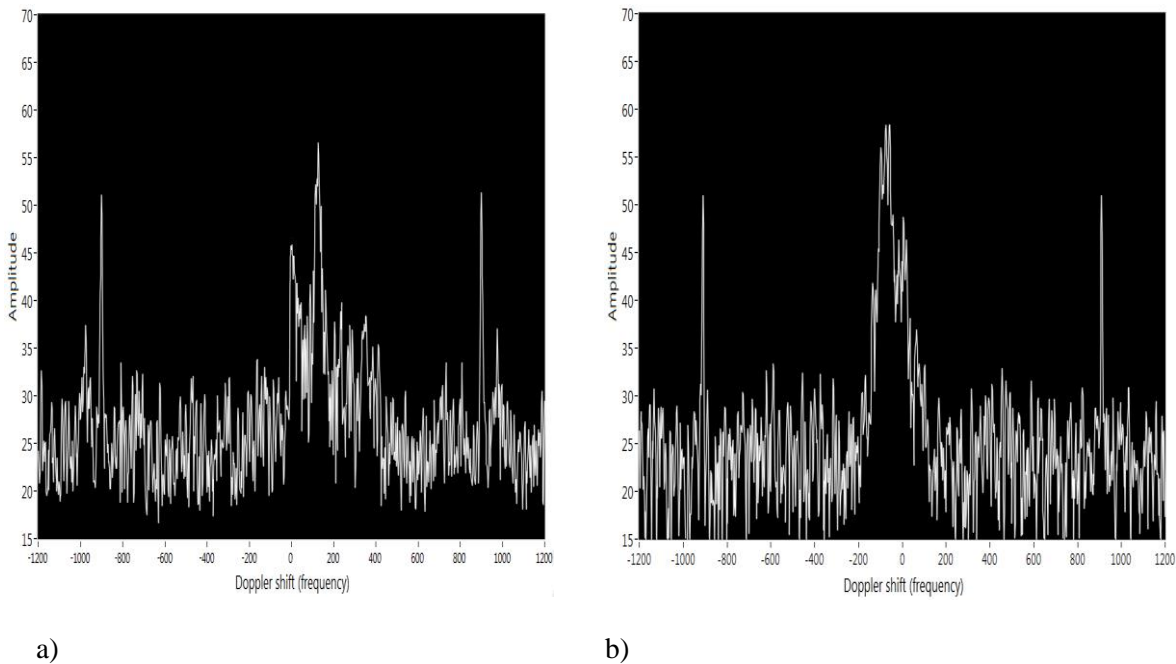
Fig. 2. The spectrum of moving pedestrian away (a) and toward (b) the radar.

As it is shown on figure 2 with coherent components, which we have received from moving object, we infuse two non-coherent components which picks are situated in $f = 900\,Hz$. Those non-coherent signals can be jammers, clutter, oscillator and etc. This was for show one of the main properties of bispectrum, i.e. phase coupling phenomenon [11]. In figure 3 are illustrated complex fast Fourier transform (FFT) and bispectrum estimation of received signal. There we have clutter and generated non-coherent signals.
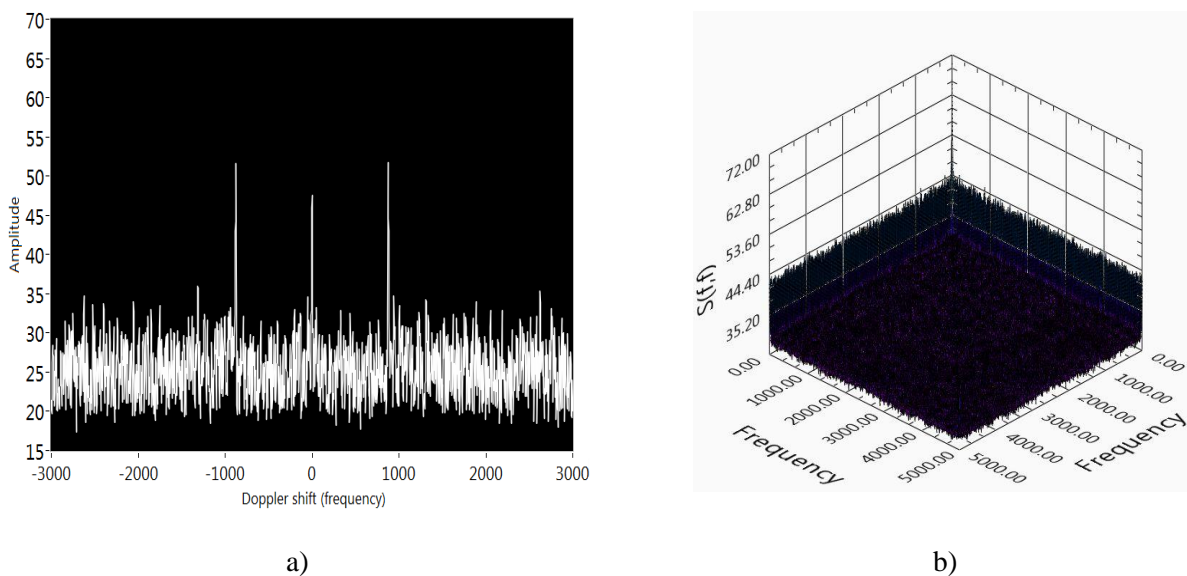

a)   b)

Fig. 3. Complex FFT (a) and bispectrum (b) of received signal.

As it is shown on figure 3 (a) from both sides on $f = 900\,Hz$ we have non-coherent signal. Signal to noise ratio is $SNR = 15\,dB$, But on figure 3 (b) we have not such kind of picks because they are non-coherent signals, henceforth they aren't phase coupled.

Ground surveillance radar emitted signal is reflected from all oscillating parts of moving object. The complex FFT and bispectrum estimation of moving object are shown on Fig. 4.
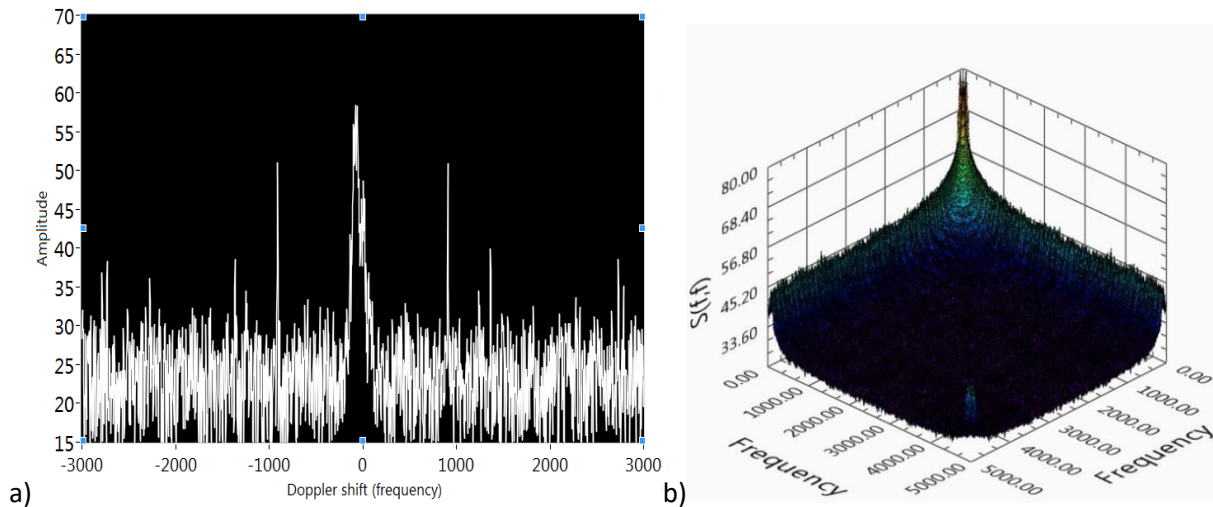
Fig. 4. The complex FFT (a) and bispectrum estimation (b) of moving object

As it is shown on figure 4 (b) non-coherent components on bispectrum graph are suppressed. There is only useful information, i.e. reflected signal from moving target with its own coherent components. At the same time signal to clutter ratio for complex FFT is $25\,dB$, meanwhile for bispectrum is $35\,dB$. Comparative analysis the results in fig 4 a) and b) allows to summarize that the benefits purchased by bispectrum-based approach is approximately $10\,dB$.

Fig. 5. Bispectrum XOY cross section

97

The most important property of bispectrum is disclosing of target motion structure. As it is shown on figure 5 the bright points are phase coupled components. They are $\left(60\,Hz, 60\,Hz\right), \left(110\,Hz, 30\,Hz\right), \left(30\,Hz, 110\,Hz\right), \left(80\,Hz, 70\,Hz\right)$ and $\left(70\,Hz, 80\,Hz\right)$. These components all belong to moving target.
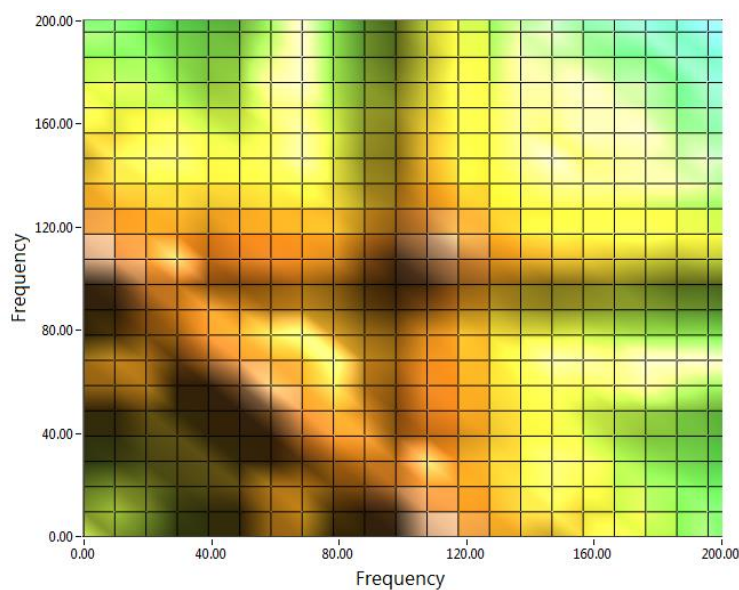
IV. CONCLUSIONS.

In this paper was shown one of the most important property of HOS i.e. phase-coupled frequencies finding. In particular, phase information finding using HOS has been examined. The most important points of HOS and bispectrum estimation are given and it has been shown that they can provide information which at second order statistics can't. Besides, the *SNR* of bispectrum better, than FFT. Finally, moving target identification method was presented. It gives opportunity to detect and find phase coupled components i.e. the coherent signals. The results are very promising.

V. REFERENCES.

[1] A. Totsky, I. Kurbatov, V. Lukin, A. Zelensky, "Use of 2-D filtering of bispectrum estimations for 1-D signal reconstruction in mixed noise environment", Proc. Second International Workshop on Spectral Methods and Multirate Signal Processing SMMSP'2002, Toulouse, France, 2002, pp. 171-178.

[2] A. Totsky, O. Krylov, I. Kurbatov, V. Lukin, J. Astola, and K. Egiazarian, "Statistical investigations of bispectral and image restoration for Gaussian and non-Gaussian noise environments", Proc. International TICSP, Workshop on Spectral Methods and Multirate Signal Processing SMMSP'2001, Croatia, pp. 231-241.

[3] Saeed V. Vaseghi "Advanced digital signal processing and noise reduction" second edition, UK by John Wiley & Sons, Ltd, 2000.

[4] A.V. Totsky, V.V. Lukin, A.A. Zelensky, J.T. Astola, K.O. Egiazarian, G.I. Khlopov, V.Ye. Morozov, I.V. Kurbatov, P.A. Molchanov, A.A. Roenko, D.V. Fevralev, "Bispectrum-based methods and algorithms for radar, telecommunication signal processing and digital image reconstruction" *TICSP series,* 2008, p 1-43.

[5] H. Avagyan, A. Hakhoumian, H. Hayrapetyan, N. Poghosyan, T. Zakaryan, "Novel Method of Cardiac Activity Extraction in L-Band Cw Radars." Armenian Journal of Physics, vol 2, pp. 92-96, 2013.

[6] H. Avagyan, A. Hakhoumian, H. Hayrapetyan, N. Poghosyan, T. Zakaryan, " Portable Non-Contact Microwave Doppler Radar For Respiration And Heartbeat Sensing." Armenian Journal of Physics, vol. 5, no. 1, pp. 8-14, 2012.

[7] Pavlo Molchanov "Radar Target Classification by Micro-Doppler Constributions" Tampere University of Technology, p 2-3 Tampere, 2014.

[8] В.И.Луценко, И.В. Луценко, Г.И. Хлопов "Спектральная модель обратного рассеяния радиоволн СВЧ - и КВЧ - диапазонов биологическими объектами ", "Электронные волны и электронные системы" т.12 стр.9-21, издательство «Радиотехника», 2007.

[9] A.A. Hakhoumian, E.R. Sivolenko "Pedestrian detection using higher order statistics (HOS) or polyspectral analyses", proceedings of the International Conference on "Microwave and THz Technologies and Applications", 2014 Aghveran, Armenia, pp. 68-71.

[10] A.Muzhikyan, A.Hakhoumian, S.Martirosyan, V.Nikoghosyan, N.Poghosyan, T.Poghosyan, K.Rustamyan, and T.Zakaryan, "Short-Range Ku-Band Hybrid-Mode CW-LFM Radar" Proc. of 11-th International Radar Symposium (IRS-2010), Vilnius, Lithuania, 16-18 June, 2010, pp.478-481.

[11] A.A. Hakhoumian, E.R. Sivolenko "Pedestrian Micro-Doppler Signature Disclosure as a Carrier Suppressed Amplitude Modulated Signal Detection" Armenian Journal of Physics, vol. 8, no 4, pp. 180-184, 2015.

[12] Wieslaw Kicinski, Arthut Szczepanski "Quadratic Phase Coupling Phenomenon and its Properties" Akademia Marynarki Wojennej, *Hydroacoustics* 7 pp. 97-106, 2004.

Collisional Buneman Instability in Current Carrying Plasma

E. Rostomyan

Institute of Radiophysics and Electronics,
Alikhanian Brothers str. 1, 0203 Ashtarak, Armenia

The stability of fully ionized plasma with relative electron-ion (*e-i*) motion is considered taking into account high level *e-i* collisions. The relative *e-i* drift speed is assumed to be much higher than the thermal spread of electrons, and in absence of collisions the system is subject to the low frequency and strongly growing Buneman instability. The transport equation with the Landau collision integral is solved taking into account the dependence of the collision frequency on the velocity of colliding particles. The effective frequency of *e-i* collisions is determined as a function of the system parameters. It is shown that with increase in the level of *e-i* collisions the Buneman instability gradually transforms to instability of dissipative type. The transition is traced in detail. The dependence of the growth rate on collision frequency is obtained.

I. Introduction

Plasma is rich in instabilities. Many of them are a result of the relative motion of the plasma components. These, instabilities are the most common in space and laboratory plasmas. A well-known example is the conventional beam-plasma instability. Another example is the Buneman instability [1], in which plasma electrons move with respect to ions. This instability plays an important role in many scenarios in space physics and geophysics. It was invoked to explain many phenomena in the Earth's ionosphere and in the solar chromosphere. A striking example of plasma with relative electron-ion (*e-i*) motion is the current-carrying plasma (CCP). The Buneman instability develops if the relative drift speed far exceeds the velocity of thermal spread $|\mathbf{u}| >> \upsilon_{\mathrm{Te}}$. This instability is low frequency and strongly growing (its growth rate is of order of the frequency). Physics of interaction of plasma components moving relatively to each other is essentially based on the concept of negative energy wave (NEW). This requires account of all factors which lead to NEW growth. Among them dissipation plays an important role. Dissipation leads to energy losses for the growth of NEW [2-3]. Influence of dissipation on the instabilities is very specific. Dissipation never suppresses the instabilities completely regardless on its level. High level dissipation transforms the streaming instability to instability of dissipative type [2-3]. Dissipative instabilities have a number of features: comparatively low growth rate, comparatively low level of excited oscillations, etc.

The main cause of energy dissipation in spatially unbound plasma is collisions. Collisions greatly influence on Buneman instability. If the plasma is fully ionized collisions are even more significant. This is due to the long distance character of interaction. Collisions cause energy dissipation with an array of ensuing effects: excitation of the NEW with further change of the physical character of the instability, etc. However, influence of collisions on Buneman instability has not been investigated yet. Due to the role of the Buneman instability in various plasma processes the necessity of the consideration is long overdue. The absence of investigations on a problem in spite of its importance may be explained by complexity of the problem only. The correct solution of the problem should be based on the solution of the transport equation with a

collisional term. In fully ionized plasma the term is nothing else but the Landau collision integral (LCI) [4]. This is very complex formation. It greatly complicates transport equation. Actually since 1936, when LCI was formulated there is very little literature on the solution of the transport equation with the LCI. Almost all successful attempts to accommodate the influence of the collisions on various processes in plasma are based on another model – on the model of Bhatnagar, Gross and Krook (BGK) [5]. In fully ionized plasma, where collisions are described by LCI the results of accounting for collisions are much less fortunate. It is known, that the collision frequency ν depends on the velocity υ as $\nu \approx \sigma \upsilon n \sim \upsilon^{-3}$ (n is density, σ-cross-section). LCI greatly complicates the transport equation and usually makes it intractable. The dependence of collision frequency on velocity, $\nu \sim \upsilon^{-3}$, complicates the procedure even more. Present paper aims at investigating of the influence of high-level e-i collisions on the Buneman instability. Investigation is carried out based on the solution of the transport equation with LCI.

II. STATEMENT OF THE PROBLEM. DISPERSION RELATION

For adequate investigation of the influence of electron-ion collisions on the Buneman instability consider fully ionized plasma, supporting a strong current. Electrons are drifting against ions in bulk. The relative drift speed far exceeds the velocity of electrons' thermal distribution, and the system undergoes instability of the Buneman type. Along with other aspects the collisions are a cause of energy dissipation with all consequent effects: excitation of the NEW, change of character of the instability etc. Stability of considered system with respect to potential oscillations is described by set of integro-differential equations: the transport equations for electron and ion distribution functions f_e and f_i coupled by according LCIs and Poisson equation.

$$\text{div}\mathbf{E} = 4\pi \left\{ e_i \int f_i d\mathbf{p} - e \int f_e d\mathbf{p} \right\}; \qquad \frac{\partial f_e}{\partial t} + \mathbf{v}\frac{\partial f_e}{\partial \mathbf{r}} + e\mathbf{E}\frac{\partial f_e}{\partial \mathbf{p}} = \mathrm{L}^{(ei)} \ ; \qquad \frac{\partial f_i}{\partial t} + \mathbf{v}\frac{\partial f_i}{\partial \mathbf{r}} + e_i\mathbf{E}\frac{\partial f_i}{\partial \mathbf{p}} = \mathrm{L}^{(ie)} \tag{1}$$

where $\mathbf{r}, \mathbf{p}$ and t are the coordinates, momentum and time, $\mathrm{L}^{(ei)}$ and $\mathrm{L}^{(ie)}$ are the LCIs for e-i and i-e collisions accordingly [6].

$$\mathrm{L}^{(ei)} = \frac{\partial}{\partial p_{e\alpha}} \int d\mathbf{p}_i Q_{\alpha\beta}^{(ei)} \left[f_i(\mathbf{p}_i)\frac{\partial f_e(\mathbf{p}_e)}{\partial p_{e\beta}} - f_e(\mathbf{p}_e)\frac{\partial f_i(\mathbf{p}_i)}{\partial p_{i\beta}} \right] \qquad\qquad Q_{\alpha\beta}^{(ei)} = \frac{2\pi(e_i e)^2}{|\mathbf{v}_e - \mathbf{v}_i|} L \left[\delta_{\alpha\beta} - \frac{(\upsilon_{e\alpha} - \upsilon_{i\alpha})(\upsilon_{e\beta} - \upsilon_{i\beta})}{|\mathbf{v}_e \text{-} \mathbf{v}_i|^2} \right] \tag{2}$$

$\mathrm{L}^{(ie)}$ and $Q_{\alpha\beta}^{(ie)}$ can be obtained from (2) by replacement $e \leftrightarrow i$. Other designations are following: $\mathbf{v}_{e,i}$ are electron and ion velocities, $\upsilon = |\mathbf{v}|$, $\alpha, \beta = x, y, z$, $\delta_{\alpha\beta} = 1$, if $\alpha = \beta$, and $\delta_{\alpha\beta} = 0$, if $\alpha \neq \beta$, L is the Coulomb logarithm. In (4) summation over repeated Greek indices is implied.

The set (1) is very complicate. Results may be obtained with significant simplifications only. We use condition of ions immobility i.e. $f_i \sim \delta(\mathbf{p}_i)$ and the linear approximation $f_e = f_e^{(0)} + f_e^{(1)}$ where $f_e^{(1)} = \mathbf{v} f_e^{(2)}(\mathbf{v})/|\mathbf{v}|$; $\left| f_e^{(1)} \right| << \left| f_e^{(0)} \right|$ All these lead to familiar form of transport equation

$$\frac{\partial f_e^{(1)}}{\partial t} + \mathbf{v}\frac{\partial f_e^{(1)}}{\partial \mathbf{r}} + e\mathbf{E}\frac{\partial f_e^{(0)}}{\partial \mathbf{p}} = -\nu(\upsilon)f_e^{(1)} \tag{3}$$

where the frequency of the collisions depends on velocity $\upsilon = |\mathbf{v}|$: $\nu(\upsilon) = C_\nu/\upsilon^3$; $C_\nu = 2\pi N_i (Ze^2)^2 L/m^2$

(N_i is ion density). We also assume that the basic state $f_e^{(0)}(\mathbf{v})$ is a stream of electrons with thermal spread

$$f_e^{(0)}(\mathbf{v}) = C_0 \exp\left(-\frac{(\mathbf{v}-\mathbf{u})^2}{2v_{Te}^2}\right); \qquad C_0 = \frac{N_e}{(2\pi)^{3/2} v_T^3} \tag{4}$$

(N_e is electron density, $v_{Te}^2 = T_e/m$, T_e and m are electron temperature and mass). Now we apply well-known procedure and carry out longitudinal permittivity $\varepsilon^{(l)}$ and dispersion relation (DR)

$$\varepsilon^{(l)}(\omega,\mathbf{k}) = 1 + \frac{4\pi e^2}{mk^2} I - \frac{\omega_{Li}^2}{\omega^2} = 0 \qquad\qquad I = \int \mathbf{k} \frac{\partial f_e^{(0)}(\mathbf{v})}{\partial \mathbf{v}} \frac{d\mathbf{v}}{\omega - \mathbf{k}\mathbf{v} + i\nu(\upsilon)} \tag{5}$$

At the first glance it may seem that the problem reduces to well known form and one can represent the results in terms of plasma dispersion function. However, this should not mislead. There are two important factors that abruptly change the situation and complicate present problem very much as compared to classical case. Firstly the well known procedure is based on the limit $\nu \to 0$, In the present case the rate of the collisions (as well as the dissipation) isn't small. In our statement it exceeds the frequency ω. Second factor is the dependence of the collision frequency on the integration variable.

III. INFLUENCE OF COLLISIONS. TRANSFORMATION TO DISSIPATIVE INSTABILITY

Now we try to obtain DR in a form, which allows analyzing the stability of the system. First we impart certain range of values to collision frequency $\nu = \nu(\upsilon)$ according to our aims. As we aim in investigating of the influence of e-i collisions on low frequency Buneman instability, in following consideration we assume $\nu(\upsilon) \gg \omega$, but, at the same time, ν remains smaller than the real part of the denominator of integrant. Keeping this in mind we merely single out real and imaginary parts

$$I = C_0(I_1 - iI_\nu); \qquad I_1 = -\frac{1}{v_{Te}^2} \int \frac{\mathbf{k}(\mathbf{v}-\mathbf{u})e^{-\frac{(\mathbf{v}-\mathbf{u})^2}{2v_{Te}^2}} d\mathbf{v}}{\omega - \mathbf{k}\mathbf{v}} \quad ; \quad I_\nu = -\frac{C_\nu}{v_{Te}^2} \int \frac{\mathbf{k}(\mathbf{v}-\mathbf{u})e^{-\frac{(\mathbf{v}-\mathbf{u})^2}{2v_{Te}^2}} d\mathbf{v}}{\upsilon^3(\omega - \mathbf{k}\mathbf{v})^2} \tag{6}$$

The integral I_1 actually represents the classical problem considered by Landau (including Landau damping), and it may be represented in terms of the plasma dispersion function F

$$I_1 = \frac{N_e}{v_{Te}^2}\left[1 + F\left(\frac{\omega - \mathbf{k}\mathbf{u}}{\sqrt{2}kv_{Te}}\right)\right] \qquad\qquad F(x) = \frac{x}{\sqrt{\pi}} P\int_{-\infty}^{\infty} \frac{e^{-z^2} dz}{z - x} + i\sqrt{\pi}xe^{-x^2} \tag{7}$$

(P denotes main part of integral). I_ν is responsible for collisional processes. There are two preferred directions in the I_ν: $\mathbf{u}$ and $\mathbf{k}$. We choose z axis along $\mathbf{k}$. Calculations lead to

$$I_\nu = \frac{C_\nu N_e}{v_T^3 u^3 b^3} \frac{1}{\sqrt{2}k} \qquad\qquad b = \frac{\omega - ku_z}{\sqrt{2}kv_T} \;\; ; \qquad \xi = \frac{u_z}{\sqrt{2}v_T} \gg 1$$

Substitutions into (5) gives DR in form

$$\varepsilon^{(l)} = 1 - \frac{\omega_{Le}^2}{(\mathbf{k}\mathbf{u})^2}\left\{1 + \frac{i\nu_{eff}}{\mathbf{k}\mathbf{u}} + 2\frac{\omega}{\mathbf{k}\mathbf{u}}\right\} - \frac{\omega_{Li}^2}{\omega^2} = 0 \; ; \qquad \text{where} \qquad \nu_{eff} = 8\sqrt{2}\pi \frac{N_i(Ze^2)^2 L}{u^3 m^2} \tag{8}$$

The expression (16) is derived by retaining first order terms (only) by parameters $\xi \gg 1$, $\omega/\mathbf{k}\mathbf{u} \ll 1$,

$\nu_{eff} / \mathbf{k}\mathbf{u} \ll 1$ and $\omega / \nu_{eff} \ll 1$. This corresponds to aims of our consideration. Also, the expression (16) is written to be similar to hydrodynamics (HD). Here it is to the point to note that despite the similarity, HD consideration of the problem from the beginning cannot lead to correct result. Some of the initial assumptions contradict each other. And, the most important, HD cannot give expression for the effective frequency of collisions. In HD collision frequency is introduced phenomenologically. Really, it should be borrowed from the kinetic theory. For given case kinetic consideration has led to expression for ν_{eff} in (8).

The DR (8) determines proper oscillations of a CCP with high level of *e-i* collisions and high relative *e-i* speed. The growth rate conventional Buneman instability attains its maximum δ_0 under the condition $\omega_{Le} = \mathbf{k}\mathbf{u}$. Collisions coming into interplay result in energy dissipation. With increase in level of the collisions, dissipation exhibits its properties more and more obviously. NEW of moving electrons grows. The Buneman instability gradually transforms to instability of dissipative type. To trace this transformation in details we introduce $\lambda_0 = \nu_{eff} / |\delta_0|$ and the DR (8) transforms to algebraic equation of third order

$$y^3 + i\lambda_0 y^2 / 2 - 1 = 0 \tag{9}$$

where $y = \omega / |\delta_0|$. Its roots are well-known [7]. Imaginary part of one of the roots actually presents growth rate for arbitrary value of the ratio $\lambda_0 = \nu_{eff} / \delta_0$. Here we are interested only in the behavior of the imaginary part depending on the value of the λ_0. It shows a decrease of the growth rate with increase in the level of dissipation as should be under transition to dissipative instability. In limit $\nu_{eff} \gg \omega$ one can easily obtain growth rate of developing instability

$$\delta_{\nu} = \omega_{Le}^{3/2} \sqrt{\frac{m}{2M\nu_{eff}}} = \delta_0 \sqrt{\frac{2\delta_0}{\nu_{eff}}} \ll \delta_0 \tag{10}$$

The instability in this limit is of dissipative type. This may be justified by smallness of the growth rate (10) and by its dependence on ν_{eff} as $\delta_{\nu} \sim 1/\sqrt{\nu_{eff}}$, which is conventional for dissipative instabilities.

IV. References

[1] O. Buneman, "Dissipation of currents in ionized media," Phys.Rev.Let, vol.1, p.8, 1958; Phys Rev vol.115, p.503, 1959.
[2] E.V. Rostomyan, EPL, vol.77, p.45001, 2007. Rostomyan E.V. Phys Lett A, vol.373, p.2581, 2009.
[3] E.V. Rostomyan, IEEE Trans. Plasma Sci, vol.31, p.1278, 2003; J Plasma Phys vol.78, no. 5, p.531, 2012.
[4] L.D. Landau, Sov Phys, JETP, vol.7, p.203, 1936.
[5] P.L.Bhatnagar, E.P.Gross and M. Krook, Phys Rev, vol.94, p.511, 1954.
[6] E.M. Lifshits, L.P. Pitaevskii, Physical Kinetics Pergamon Press, 1981.
[7] A.Korn, M.Korn, Mathematical Handbook. McGraw-Hill book Comp, 1968.

A Radio Frequency Spiral Scanning Deflector for keV Electrons

S. Zhamkochyan[1], R. Ajvazyan[1], J. Annand[2], H. Elbakyan[1], L. Gevorgian[1], A. Margaryan[1]

[1]*A.I. Alikhanyan National Science Laboratory, Alikhanyan Brothers Str. 2, Yerevan, Armenia*
[2]*School of Physics & Astronomy, University of Glasgow, G128QQ Scotland, UK*

A new sensitive deflector to perform spiral sweeps of keV electrons by means of radio frequency (RF), fields in a frequency range of 500-1000 MHz is described. By converting the time dependence of incident electrons to a hit position dependence on a spiral, this device forms a basis for THz bandwidth timing processor over an interval extended beyond the RF period. Potentially it has a number of applications in fixed-frequency cathode-ray-tube based instruments such as RF Streak Cameras or the RF photomultiplier tubes. Both techniques can provide 1 ps resolution, and the capability to digitize light signals up to 100 ns duration. Potentially they have applications in many different fields of science and technology. The results of current theoretical and experimental studies are presented.

I. INTRODUCTION

It is well known that timing systems based on radio frequency (RF) fields can provide picosecond temporal precision. The basic principle of RF timing is conversion of information in time domain to a spatial domain by means of a high frequency deflector. The information carriers are photo- or secondary electrons, which are accelerated (usually to a few keV), deflected by the RF field, and then detected on a screen or position sensitive detector. The initial time information is mapped on to a special distribution, i.e. a position of an electron on a screen corresponds to its arrival time. Two factors, "physical" and "technical", determine the time resolution of a circular scanning tube [1, 2]. Physical is largely determined by the velocity distribution of the photoelectrons produced at the cathode and can be calculated from $\Delta t_p = [2.34 \times 10^{-8} (\Delta \varepsilon)^{1/2}]/E$, where $\Delta \varepsilon$ is the energy dispersion of the photoelectrons at the cathode and E is the accelerating electric field after the cathode. If $\Delta \varepsilon = 0.3\,\text{eV}$ and $E = 10^4$ V/cm, $\Delta t \approx 1$ ps. Technical is determined, for an isochronous tube, by the RF deflector and electron detection system and is given by $\Delta t = \Delta d / v$, where Δd is a convolution of the size of the electron beam spot and the position resolution of the electron detector and $v = 2\pi R / T$ is the scanning speed. R is the radius of the scanning circle and T is the period of the RF field. With $\Delta d = 0.01\,\text{cm}$, $R = 2\,\text{cm}$ and $T = 10^{-9}\,\text{s}$ (RF frequency is 1000 MHz), we have $\Delta t_d = 1\,\text{ps}$. The "technical" time resolution and dynamic range (time interval) of such a RF timing processor is determined by scanning speed, i.e. by the period T of the applied RF field. The "technical" time resolution is improved when the RF frequency is increased, while the dynamic range is decreased.

Our eventual goal is to produce a timing processor which has 1 ps timing resolution, 1 THz bandwidth, 1 Tbit/s sampling rate and virtually unlimited dynamic range. With this in mind we have developed a spiral scanning RF timing technique suitable for a Streak Camera or the RF PMT. This is based on a sensitive and compact circular sweep deflection system for keV electrons, capable of operating in the 500– 1000 MHz frequency range [3]. This helical shape deflector was developed for RF Photomultiplier Tube (RFPMT) applications [4, 5] and its ability to operate with low applied RF power is crucial in ensuring that induced pickup on the front-end components of the RFPMT is kept to low levels.

Here we describe a dual helical deflection system to produce spiral rather than circular scanning pattern. Current results of theoretical and experimental studies are presented.

II. RF TIMING AND CIRCULAR SCANNING

The operational principles of the RF timing technique exemplified by an RF PMT with point size photocathode are shown in Fig. 1. The primary photon pulse hits the photocathode (1) and produces photo-electrons (PE). The time structure of the produced PE bunch is identical to that of the light pulse. These electrons are accelerated by a voltage V applied between the photocathode and an electron transparent

electrode (2). The electrostatic lens (3) then focuses the electrons onto the screen (7) at the far end of the tube, were the electron detector is placed. Along the way the electrons pass through the circular sweep RF deflection system, consisting of electrodes (4) and RF tuning system (6), which operates at 500-1000 MHz frequencies. They are deflected to form a circle on the screen. The sensitivity of this new RF deflector, where the electrodes have a helical geometry (Fig. 2)   is about 1 mm/V or 0.1 $rad/W^{1/2}$ and is an order of magnitude higher than the sensitivities of the RF deflectors used previously (see [3] for details).The time structure of the input photon signal is transformed into a spatial PE image (5) and recorded. In this way the timing error sources are minimized, because PEs are timed before any further signal amplification and processing.
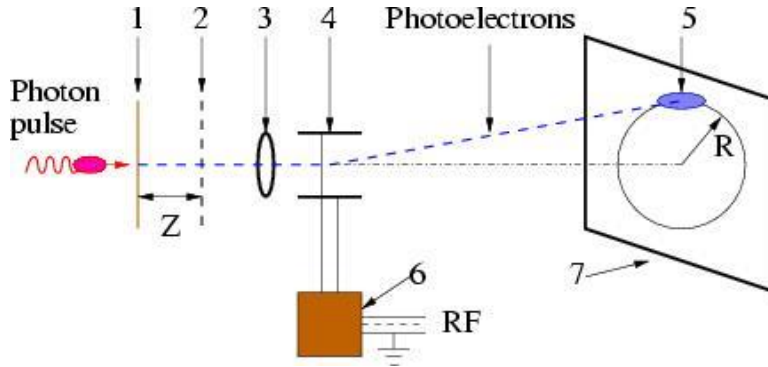

Fig. 1: The schematic layout of the RFPMT with point-size photocathode. 1- photo-cathode, 2- electron transparent electrode, 3- electrostatic lens, 4- RF deflector, 5- image of photo electrons, 6- RF tuning system, 7- SE detector.
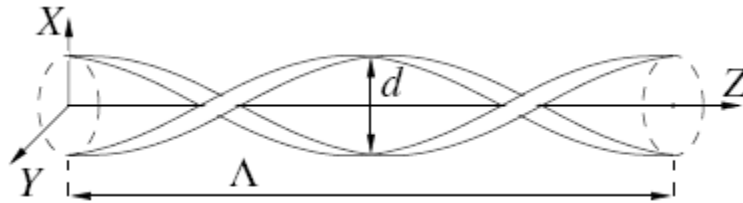

Fig. 2: Schematic of the helical RF deflector.

III. SPIRAL SCANNING WITH TWO RF DEFLECTORS

Combining two harmonic signals with close ω_1 , ω_2 frequencies will result in an amplitude beating effect. For instance, with equal amplitude sine waves we have:

$$A\cos\omega_1 t + A\cos\omega_2 t = 2A\cos\frac{\omega_1 - \omega_2}{2}t\cos\frac{\omega_1 + \omega_2}{2}t$$

The beat frequency is given by the difference of the two frequencies $\omega_{beat} = |\omega_1 - \omega_2|$. Operating two RF deflectors, RFD1 or RFD2 individually the trajectories of scanned electrons will follow circumferences with radii R_1 and R_2. Operating the RFD1 and RFD2 deflectors simultaneously results in spiral scanning with a frequency $\omega_{beat} = |\omega_1 - \omega_2|$, and maximum and minimum radii $R_1 + R_2$, $|R_1 - R_2|$ (Fig.3). The "Beat" in superposed response modulates the radius of the scanned circle and dramatically increases the scanning period (e.g. if $\omega_2 = 1.1\omega_1$, $T = 1/(T_2 - T_1) = 10T_1$).
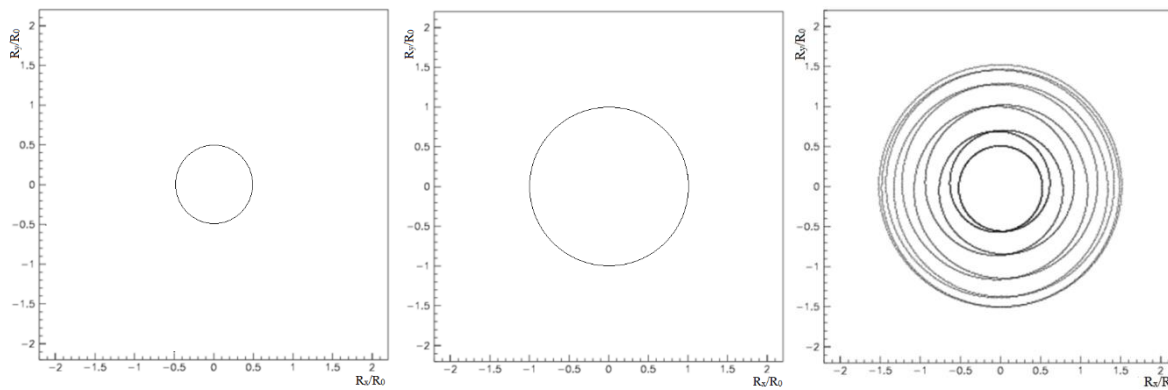
Fig. 3: Example of spiral scanning; left two images correspond to RFD1 and RFD2 operating separately, right image corresponds to their simultaneous operation.

A dual helical deflection system, consisting of two aligned helical deflectors (Fig. 4), was used for producing a spiral scanning pattern.
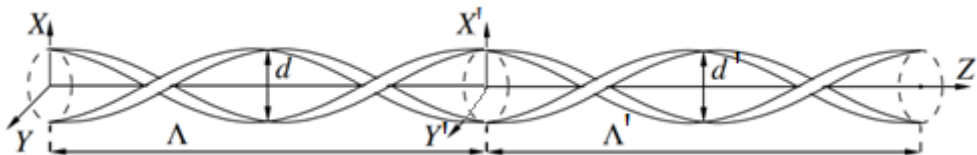

Fig. 4: A schematic of spiral scanning RF deflector

For experimental investigations an evacuated test tube with thermionic cathode was used (Fig. 5). The cathode (1) emits electrons, which are accelerated by a voltage applied between the cathode and an electron transparent electrode (2). An electrostatic lens (3) then focuses the accelerated electrons on to the phosphor screen (6) at the far end of the tube. The electrons are deflected by the RF system, consisting of electrodes (4), (5) RF sources and tuning circuit.
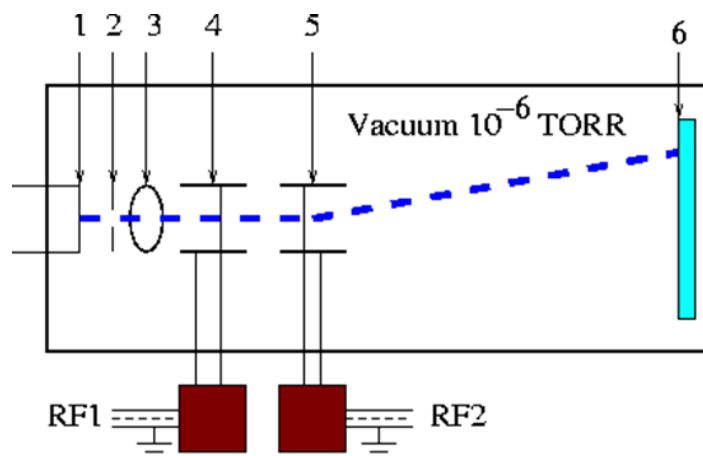

Fig. 5: A schematic representation of the experimental setup: 1- thermionic cathode, 2-accelerating electrode, 3-electrostatic lens, 4,5- RFD1and RFD2 deflectors, 6- phosphor screen.

The parameters of the deflectors of RFD1 and RFD2 were tuned to operate at frequencies $\omega_1 = 500$ MHz and $\omega_2 = 550$ MHz and produce circles with radii R_1 and $R_2 = 2R_1$ when operating individually (Fig 6^{a,b}). The image of the deflected 2.5 keV continuous electron beam at the phosphor screen, with both deflectors operating simultaneously, appears to be an approximately a uniform distribution between radii $R_1 + R_2$ and $|R_1 - R_2|$ (Fig. 6^c). This is due to summing of a huge number of periods of the formed spiral. It

should be noted that in these studies, two independent oscillators were used, i.e. two RF signals were not phase locked, and also that the resolution of the phosphor screen was not optimum.
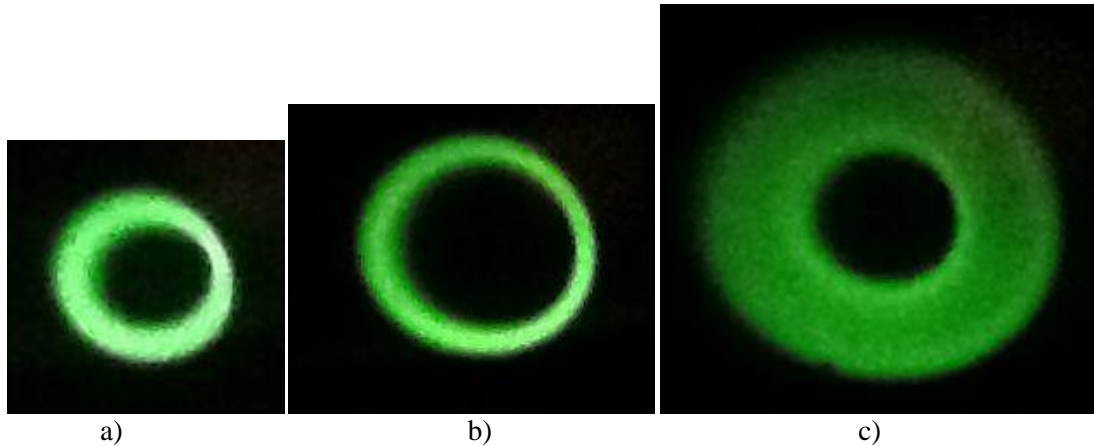

Fig. 6: Images of the deflected 2.5 keV continuous electron beam at the phosphor screen. The parameters of the deflectors of RFD1 and RFD2 are tuned to operate at frequencies (a) $\omega_1 = 500$ MHz and (b) $\omega_2 = 550$ MHz and produce circles with radii R_1 and $R_2 = 2R_1$ when operating individually, (c) image of the deflected 2.5 keV continuous electron beam at the phosphor screen, when both deflectors are operating simultaneously.

IV. SUMMARY

A dual helical RF deflection system to produce a spiral scanning pattern of keV energy electrons is described. The time structure of an optical signal is scanned on to a spiral spatial structure which will pottentially provide time measurement with ps resolution over intervals up to a few hundred ns. This will essentially increase the range of applications of streak cameras and related devices. A major advantage of the helical electrodes is that the system can be optimized to the velocity of the transiting electrons, so that loss of deflection sensitivity due to transit time effects is avoided. Fine tuning of the effective capacitance of the system results in the deflection electrodes forming a resonant circuit, with a quality factor Q in excess of 100. On resonance, the sensitivity of the deflection system is about 1mm/V or 0.1rad/W$^{1/2}$ and around 1W (into 50 Ω) of RF power is sufficient to scan 2.5 keV electrons circularly at a radius of 2 cm radius. This makes the deflector suitable for high rate and high resolution timing devices such as the RFPMT [4, 5], where development continues. Preliminary experimental studies of a dual helical deflection system to produce spiral scanning were encouraging and development continues. Future developments include a dual helical deflection system employing two phase locked RF frequencies and the use high resolution pixel detectors to replace the phosphor screen.

ACKNOWLEDGEMENTS

V. REFERENCES

[1] E. K. Zavoiski and S. D. Fanchenko, "Image converter high-speed photography with 10^{-9}-10^{-14} time resolution", Appl. Optics, vol 4, no.9, pp. 1155-1167, 1965.

[2] R. Kalibjian, et al., "A circular streak camera tube", Rev. Sci. Instrum., vol 45, no.6, pp. 776-778, July 1974.

[3] L. Gevorgian et al., "A radio frequency helical deflector for keV electrons", Nucl. Instr. and Meth. A, vol 785, pp. 175-179, 2015.

[4] A. Margaryan et al., "Radiofrequency Picosecond Phototube" Nucl. Instr. and Meth. A, vol 566, pp. 321-326, 2006.

[5] A.Margaryan et al.,"Radio Frequency Phototube", United States Patent, Patent No. US 8,138,450 B, Date of Patent: March 20, 2012.

On Radio Physical Design of The Dual-Reflector Radio Telescope with a Fixed Main Spherical Reflector and a Movable Subreflector Type Gregory

R. V. Ter-Antonyan

National Institute of Metrology, Komitas Ave., 49/3, 0015 Yerevan, Armenia

It is revealed, earlier unnoticed, relationship between the radius of a spherical reflector, diameter of a movable aperture of the radio telescope and location of focus of system on an axis of symmetry which limit generatrix a movable subreflector type Gregory and excludes possibility of deep subreflector with a feed located inside. The simple ratio connecting the key controlled constants of optical scheme, thereby, providing to the designer a freedom of choice of an order of radio physical design of the radio telescope is received.

I. BACKGROUND

In [1] for effective reception of the important hydrogen line (1,420MHz) it is offered to construct rather cheap dual-reflector radio telescope(RT) with the main reflector in the form a giant fixed hemispherical reflector and a small movable barrel-shaped axisymmetric subreflector(SR), which axis passes through the center of a hemisphere.

Signal in the form of rays parallel to on axis of symmetry of SR, being reflected from a circular segment of a hemisphere, below called by a reception aperture, goes to the reflecting surface of a SR and being rereflected it is focused. At the same time rays going from a reception aperture to SR cross an axis of the last in different points.

To accept a signal from other direction it is necessary to turn a SR with receiving device around the centre of a hemisphere.

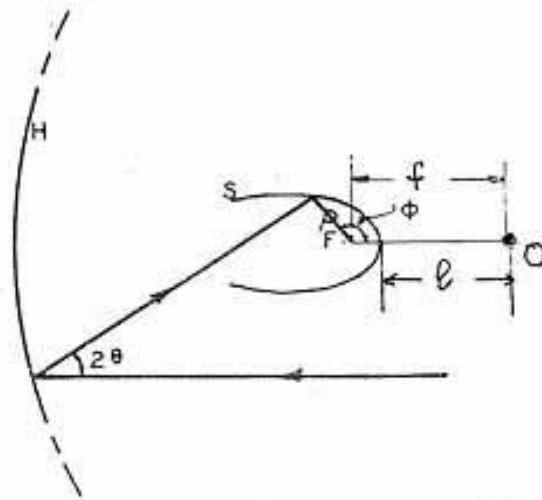The optical scheme of RT is shown on Fig.1 which we borrowed from [1].

Fig.1. Path of a typical ray through system. F, focus; H, hemispherical reflector; O, centre of hemisphere; S, subreflector; f and l, distances, repectively, focus of system and top of a SR from the center of a hemisphere, normalized on the radius of curvature of the last; θ, central angle.

We will explain that the barrel-shaped form of a SR is caused by the specifics generatrix SR it as a curve of the fourth order which as approaching caustic of hemisphere inclines to an axis of symmetry of a SR. Thus increase in diameter of a reception aperture is reached at reduction diameter of a SR.

Doesn`t disturb the author [1] that when lengthening generatrix SR up to caustic of hemisphere focus of system appears deeply in a SR.

In [1] it is noted that both the hemisphere, and SR can be made of screen with size mesh of one inch.

In [2] it is offered to construct the giant dual-reflector RT wich could work effectively up to 40 GHz according to the scheme [1]. As such RT could look it is shown on Fig.2.
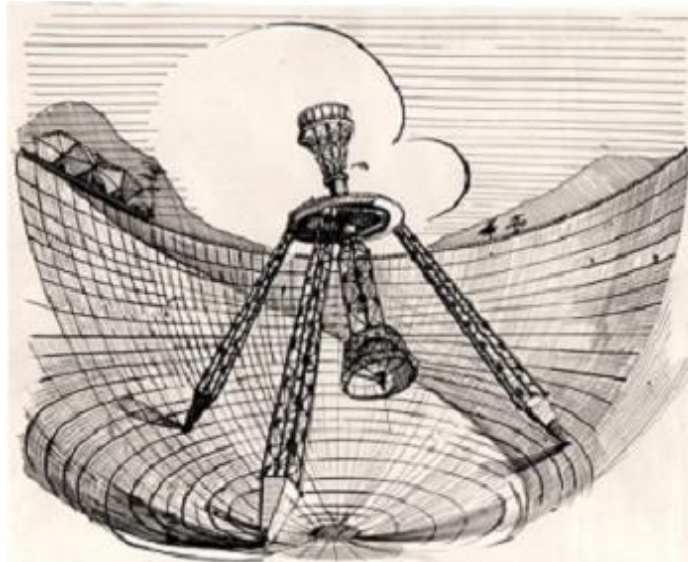

Fig..2

The order of radio physical design of the RT offered by the autor [2], with the chosen diametr of a reception aperture, leaves the radius of curvature of a hemisphere the free size which should be chosen proceeding from common sense.

On Fig.3 which we borrowed from [2] clearly it is visible what in process of lenghthening generatrix SR point of intersection of the ray going from a reception aperture with a axis of symmetry SR, moves towards focus of system, coincides with it and continues to move towards a hemisphere.
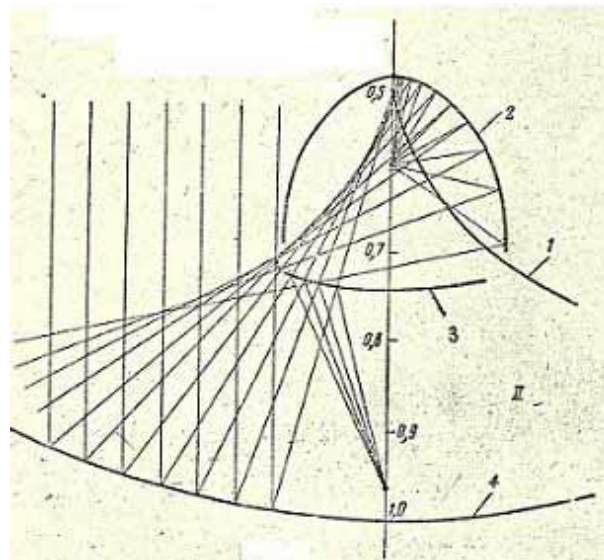

Fig,3. 1, cautic of hemisphere; 2, barrel-shaped SR; 4, hemispherical reflector, reception aperture.

The fact that both authors don`t notice that the real reception devise installed on an axis of symmetry of a SR, the not reception part will intercept rays going from a reception aperture is represented surprising.

Thus when lengthening generetrix of a SR to caustic of a hemisphere there is an effect of annular shading of a reception aperture that is inadmissible.

Therefore, the designer has to cut off generatrix of a SR ray passing through focus of system and proceed from the arising obvious connection, $f=1/(2\cos\theta_{max})$, where $2\theta_{max}$ – angular size of a reception aperture.

The arisen connection excludes a barrel-shaped form of a SR, removes focus of system of limits of a SR, does radius of curvature of a hemisphere by dependent size and dictates new approach to radio physical design of the RT stated below.

II. FOR THE DESIGNER

To difference from [2], we prefer to write down the equations of generatrix of SR, providing focusing, in a polar parametrical form which is compositionally very tempting and stimulates search of the opportunities which are contained in the equations.

The equations are written down in the designations Fig.1 added with our designations is

$$\rho = \{M_1 + (M_2)^2/M_1\}, \tag{1}$$
$$\phi = 2\theta - 2\text{arctg} \{M_2/M_1\}, \tag{2}$$

where

$$M_1 = M - 2\cos\theta + f\cos2\theta, \tag{3}$$
$$M_2 = f\sin2\theta - \sin\theta, \tag{4}$$
$$M = 2-2l + f. \tag{5}$$

We will emphasize that M_1, M_2 and M are geometrically interpreted.

For the ray passing through focus, $\phi_{max} = 2\theta_{max}$. From (2) that it is possible if $M_2=0$, that is

$$f = 1/(2\cos\theta_{max}), \tag{6}$$

where

$$\cos\theta_{max} = \{1 - (D/(2R))^2\}^{1/2}, \tag{7}$$

R, radius of curvature of a hemisphere, D, diameter of a reception aperture.

At design of the RT the central shading of a reception aperture which we will include in consideration by means of equality (7) is important.

$$\rho (\theta_{max}) \sin(2\theta_{max}) = d/(2R), \tag{8}$$

where d, diameter of a SR.

Substituting in the left part (8) expression for $\rho (\theta_{max})$ from (1), we will receive connection necessary to the designer,

$$(2-2l - \cos\theta_{max}) \cos\theta_{max} = d/D. \tag{9}$$

Connection (9) provides to the designer freedom of choice of an order of radio physical design of the RT.

We will emphasize that at our approach to radio physical design of the RT there is free a choise of value of the controllable constant l defining position of top of a SR. At approach of the last to top of caustic of a hemisphere diameter of the SR intercepting the rays going from a reception aperture is minimized at the same time, antenna characteristics of the RT significantly worsen. The numerical calculations connected with the compromise choise of value l the designer can find in [3].

III. EXAMPLE

In [4], in the section "Spherical reflectors", by consideration of the RT [1], autors recommend to take the radius of curvature of a hemisphere equal to diameter of a reception aperture. For this option, having put $l = 0,49$, we will receive: $\theta_{max} = 30°$(recpectively, apex angle of cone of the review of the sky is equal to120°), $f = 1/\sqrt{3} = 0,577\ldots$, $d/D = 0,13$.

We recommend to remove slightly focus of system from on extreme ray (θ_{max}) and in numerical value f to keep two decimal signs. Specifically, instead of $f = 0,577\ldots$ to take $f = 0.58$.

IV. REFERENCES

1. A.K.. Head, "A new form for a giant radio telescope", Nature, vol.179, pp.692-693, April 6, 1957.
2. P.M. Geruni, "Design problems of spherical dual-reflector antennas", Radio Engng. Electron. Phys., vol.9, pp.1-8, 1964.
3. C.J.E. Phillips, P.J.B. Clarricoats, "Optimum design of a Gregorian-corrected spherical-reflector antenna", Proc. IEE, vol.117, pp.718-733, no.4, 1970.
4. W.N. Christiansen, J.A. Högbom, Radiotelescopes. Cambridge Universiti Press, L., 1985.

Change of Flux Density Characteristic of the Radio Source Cassiopeia A for the Period 2008-2015 Years

G.S. Avetisyan

Institute of Radiophysics and Electronics, Alikhanian Brothers str. 1, 0203 Ashtarak, Armenia

Current research is based on results of regular radio-astronomical observations (2008-2015 years) which was done on Saravandsky scientific experimental site IRPHE the National Academy of Sciences of the Republic of Armenia. In this work, nature of average annual change of intensity of a radio emission and also veracity (authenticity) of frequency of change of a stream of a radio source of Cassiopeia A are discussed. It is shown that in the mentioned period intensity of a radio emission of Cassiopeia A decreased approximately with an average annual speed of 0,6%, and from results of average annual values of the period 2008-2015 years a curve was constructed with low 2.7 -3 years period of change.

I. INTRODUCTION

In work [1] we provided the general data on temporary change of radiation intensity of Cassiopeia A, identified with the remains supernew constellations Cassiopeia. It has been shown that intensity of its radiation on wavelength λ=4,2м during half a century has decreased more than by one and a half times with an average annual speed about 0,5% . It was noted that this decrease is not strictly monotonous, and has variable nature, and according to some authors, even periodic character.

Decrease of a radio emission stream of supernew source is well known phenomenon . It has been theoretically predicted [2] and confirmed by many observations. Temporary irregular fluctuations of a stream of its radio emission too are quite explainable and as was mentioned in [1] can be result of the complex processes leaking in supernew sources. There are not sufficient information for confident confirmation or denial any explanation for periodicity change of radio source intensity of Cassiopeia A's radiation. However, we can give some theoretical assumptions, that periodicity are connected with rotation of the individual active areas in supernew sources, reorientation of the magnetic fields, pulsations, etc.

The full data collection of observation was made by authors of work [3], on the basis analysis of which, they came to conclusion about existence of a periodic component in a variation of a radio emission of Cassiopeia A. However, these data, which was received from results of other authors' experiments, are non-uniform, methods of observation information registration are different, and the most important, observation were not held sufficiently regular time.

The purpose of the real work is supplement to article [1] and to investigate temporary periodic component in change of a radio emission of a source of Cassiopeia A. During last decades, systematic observations of the sky were done using radio interferometer of Byurakan situated in polygon of the IRPhE NAS. The purpose of observation sky, which contain radio sources Lebed-A and Cassiopeia A, is establishment of physical connection between the ionospheric and seismic phenomena during the periods of an earthquake.

In the late nineties of the last century, the program of these observation was organized in order to the obtained suitable data for immediate use in the field of astrophysics, in particular, for the solution of the task defined above, without prejudice to the program of seismic supervision. During observation, the antenna of a radio interferometer were directed to chosen area and fixed in a such way, that radio sources of Cygnus A and Cassiopeia A culminate equally distant from the axis of the maximum in their diagrams when passing through a local meridian. Such statement of experiment allowed considerably simplify observation, to increase informational content and stability of the obtained data without influence on quality of the solution of problems, especially astrophysical problems. The solution is based on data of the relative measurements, and sources of radiation culminated near the Zenith, passing through rather wide diagram of antennas in the plane of declension of sources. During 2007-2014 years almost daily observations were made of the area of a sky, which was chosen according from the above-stated conditions. During this period, from observed data were collected about 856 records, which were the best from the point of view of their minimum distortion hindrances.
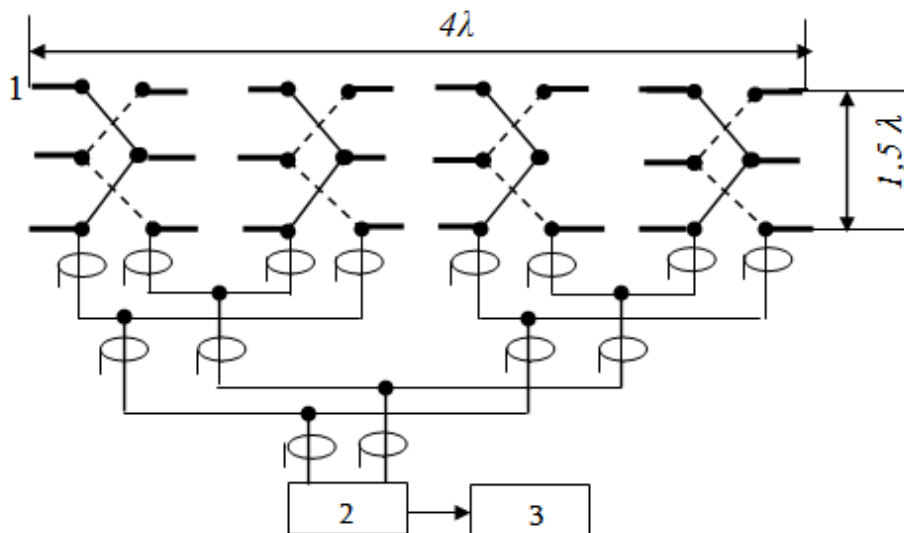

Fig. 1. Block diagram of the radio telescope 1 - the antenna, 2 - the symmetrizing knot, 3 – the radiometer

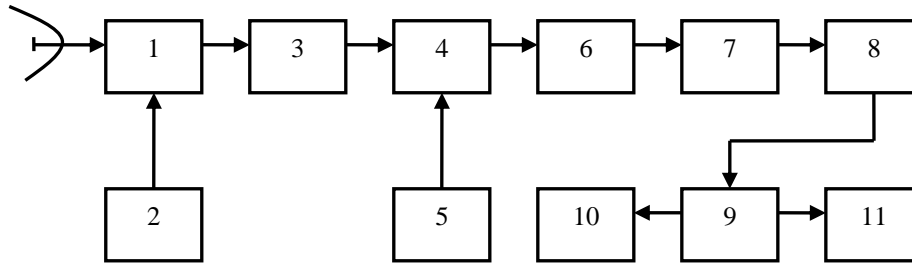| [1] **Parameter**	[2] A_{eff}	[3] φ_3 dB	[4] Θ_3 dB	[5] f_0	[6] Δf	[7] K_{yc}	[8] $F_{ш}$
[9] **Value**	[10] 50 m^2	[11] 40º	[12] 15º	[13] 72MGz	[14] 400KGz	[15] 70 dB	[16] ≥ 2.5

Antenna parameters

Fig. 2. Block diagram of the radiometer
1 - antenna switch, 2 - noise generator, 3 –low-noise amplifier, 4- mixer, 5- a heterodyne, 6- amplifier of intermediate frequency, 7- detector, 8 - DC amplifier, 9- storage device, 10- computer, 11- recorder

III.   RESULTS

Based on these records, the attitude of σ=Тк/Тл was determined, where Тк and Тл are the registered antenna temperatures of radiation sources of Cassiopeia A and Swan A. Table 1 shows the the average annual values of σ calculations.

Detailed analysis of data of the table and their comparison with results of the previous periods of observations, which in our opinion are sufficiently homogeneous and continuous for a long period of time. This shows temporal periodicity in variability of radiation of Cassiopeia A , and random deviations, which can be connected to the processes going on in a source and conditions of distribution of radio waves in interstellar and near-earth environments.

Year	2007	2008	2009	2010	2011	2012	2013	2014
$\sigma_г$	1,028	1,008	0,975	1,01	0,985	0,965	0,98	0,93

**Average annual (σг) values of the relation of streams
of a radio emission of Kassiopea-A/Lebed-A for the period 2007-2014 years**

On graphics of average annual values of the period 2007-20014 years (Fig. 1), it is shown the curve with weak, near 2,7-3 years the period of changes σ (heavy line), however its amplitude is less than values of average monthly vibrations σ (on the last this periodicity is not observed). It should be noted, that if the given curve considered as a part of the expected periodic curve, then the measuring data obtained by us in the period of 2001-2006 is converging.
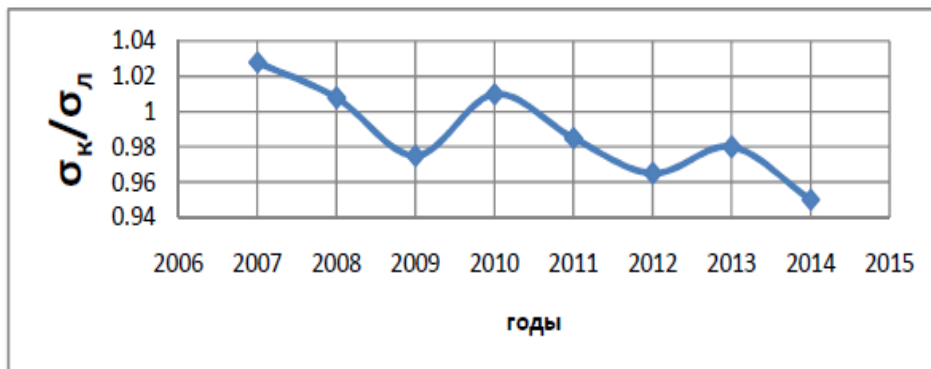
Variation of average annual value of the relation of streams of a radio emission

Errors of measurements at all series of observations were practically the same (Δσ≤0,025), because for these periods wavelength, tools, admission methods and registration of radiation have not changed, therefore their contribution to results of the analysis of these observations would not have essential value.

IV.   REFERENCES

[1] R. M. Martirosyan, A.G. Ghulyan, V. A. Sanamyan, G. A. Pirumyan, "The remark concerning periodicity of a variations of intensity a radiation source Cassiopeia A," Astrophysics, vol. 50, no.2, p. 253-257, 2007.

[2] I. S. Shklovsky, Astron. Zh. vol.37, p. 256, 1960.

[3] A. N. Barabanov, V. P. Ivanov, K. S. Stankevich, S. P. Stolyarov, Astron. Zh. vol. 63, p. 296, 1986.

Conical Bessel Beam Radial Line Slot Antenna

O.Mahmoodian, A.Hakhoumian, N.Poghosyan and V.Mekhitarian

Institute of Radiophysics and Electronics, Alikhanian Brothers str . 1.0203 Ashtarak, Armenia

The conical beam planer ring-slot antenna on radial transmission line has been designed and investigated. Resonance conditions for shorted and open end radial line have been evaluated. Using of resonance-type radial line for feeding the ring-slot antenna increases the antenna emission efficiency. The radius of ring slot is chosen from the maximum condition of first kind Bessel function $J_1(kr)$. The directivity pattern has been measured for emission to free space, after diffraction on metallic disk, and after transmission through dielectric thick layer.

I. INTRODUCTION

Bessel beams are the solution to Helmholtz equations. They appear to propagate without diffraction and thus they have potential to replace Gaussian beams in a number of applications such as optics and microwave [6].A good example in the field of microwave is conical scanning which is an earlier application of radar system to improve the accuracy of antenna to point the moving targets. Bessel beam is a field of electromagnetic or acoustic while its amplitude is described by a Bessel function of first kind. Bessel beam radial line slot Antenna consists of a disk of metal as a resonator which is placed either above or separated from another such disk as a ground-plane by a dielectric material. The upper disk is excited by attaching an RF power source between the circumferences of the inside radius of the probe feed. There is a non conductive concentric slot around the center of antenna, which its radius is calculated by the first kind of Bessel function $J_1(kr)$.Resonance type Radial line is composed of a parallel conductive metal and its counterpart, either another plate or ground-plane, will generate transverse Electro Magnetic (TEM) waves.E_z has no variation in Z direction and corresponds to the total voltage $E_z d$. The component $H\varphi$ corresponds to the total radial current $2\pi r H\varphi$, outward in one plate and inward in other plate, giving rise to a total characteristic impedance[2]:

$$Z_{total}=d(E_Z / H\varphi)/ 2\pi r \qquad (1)$$

Where E_z and $H\varphi$ are electric and magnetic fields respectively and d is dielectric material.
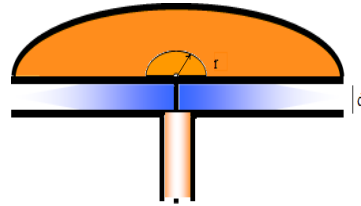

Fig. 1: schematic view of radial Bessel beam antenna

Let's consider the waves that propagate in radial direction between two perfect conductive planes like waveguide that is called radial transmission line. Among any types of electromagnetic waves that can propagate

in such medium (line), we consider only such, waves which satisfied the following condition and it depends only on the radius r.

$$\frac{1}{r}\frac{\partial}{\partial r}(r\frac{\partial \psi}{\partial r})+k^2\psi=0 \tag{1}$$

So in this case $k_c^2=k^2-k_c^2=k^2$ and resulting

$$\psi=A_1H_0^{(1)}(kr)+A_2H_0^{(2)}(kr). \tag{2}$$

The first term of (2) defines a traveling wave Propagating to the transmission line axis (converging waves), and the second diverging from the axis of the traveling wave. Electric and magnetic fields of this wave can be described by:
$$E_z= BH_0^{(2)}(kr)$$

$$H\varphi=iZ_0^{-1}BH_1^{(2)}(kr) \tag{3}$$

where $B=K^2A_2$, and H_0 and H_1 are the Hankel functions and $K=2\pi/\lambda$.

The characteristic impedance of radial transmission line is:

$$Z_{oi} = \eta\ G_o(kr)/G_1(kr)= d\eta/2\pi r\ .\ H_0^{(2)}(kr)/-iH_1^{(2)}(kr) =\frac{d\eta}{2\pi r}\ [\ J_0^2(kr)+ N_0^2(Kr)\ ]^{1/2}\ e^{i\theta(kr)}/\ [\ J_1^2(kr)+ N_1^2(Kr)\ ]^{1/2}\ e^{i\psi(kr)} \tag{4}$$

Where η is intrinsic impedance of free space $\approx 377\ \Omega$. G_o and G_1 are related to the Hankel function[2,7].

II. INPUT IMPEDANCE AND RESONANCE CONDITION

The input impedance of lossless line with length *l* and loaded z_l is:

$$Z_i = Z_0[\ (Z_L \cos(\ \theta_i - \psi_L) + j\ Z_{oL}\ \sin(\theta_i - \theta_l))]/\ (Z_{oL} \cos\ (\psi_i - \theta_L) + j\ Z_L \sin\ (\psi_i - \psi_L))]. \tag{5}$$

This is similar to the standard uniform transmission line equation except for the complex phase angles.
The G_o and G_1 functions and the complex phase angles θ and ψ are now are mentioned:

$$G_o(kr)=[\ J_0^2(kr)+ N_0^2(Kr)\ ]^{1/2} \tag{6}$$

$$G_1(kr\ )=[\ J_1^2(kr)+ N_1^2(Kr)\ ]^{1/2} \tag{7}$$

$$\theta\ (kr)= arc\ tang[-\ N_0(Kr)/J_0(kr)] \tag{8}$$

$$\psi\ (kr)= arc\ tang\ [-J_1(kr_l)/N_1(kr_l)] \tag{9}$$

Where J_x is the real term and N_x is the complex term of the Hankel function H_x. In the case of short-circuit when the $Z_l=0$,formula (5) reduces to:

$$Z_i= jZ_o\ [\sin(\theta_i - \theta_l)\ /\ \cos\ (\psi_i - \theta_L)] \tag{10}$$

In order to have resonance the input impedance should be zero. In the case of short circuit formula (10) the numerator is zero when $\sin(\theta_i - \theta_l)=0$ if $(\theta_i - \theta_l)=n\pi$ n=1,2,3,……….r is so smaller than λ and goes to zero. In formula (7), for r=0, $N_0(Kr_i)= \infty$ and arc tang of ∞ equal to $\pi/2$ and we have $(\theta_i - \theta_l)=(\pi/2- \theta_l)= \pi$ and $\theta_l= \pi/2$. By putting these values in formula (10) we see that for the case of short-circuit condition Z_i is equal zero means we have resonance. And for the special case where $Z_L = \infty$ (open-circuit), the radial transmission line equation (5) reduces to:

$$Z_i =-JZ_0\ [\cos(\ \theta_i - \psi_L)\ /\ \sin\ (\psi_i - \psi_l)] \tag{11}$$

About open-circuit condition we do something same as short one. Input impedance should be zero as follow: $\cos(\ \theta_i - \psi_L)=0$ And $(\ \theta_i - \psi_L)=(2n\pm1)\ \pi/2$ where n=0,1,2,....We know that $\theta_i= \pi/2$ and according formula

number(9) we have $\psi_L=\pm n$ л .In formula (9)-$J_1(kr_l)/N_1(kr_l)$ should be equal to zero if $J_1(kr_l)=0$ and resonance condition will be happened when kr $=(3.83,7.01,10.17,13.3,..)$.

III. ANTENNA RESONANCE RADIUS VALUE

In this part we are going to find the value of the radial radius for short and open conditions to calculate the resonance radius of antenna. In the case of short circuit we know that $(\theta_i - \theta_l)=n$л and arc tang $N_0(kr_l)/J_0(kr_l)$ = л/2 thus $J_0(kr_l)$ = when, Kr$=(2.4,5.35,8,65,11.7,\ldots)$.

For open condition $\psi_L=\pm n$л and $J_1(kr_l)/-N_1(kr_l)=0$ and $J_1(kr_l)=0$ when kr$=(3.83,7.01,10.17,13.3,..)$.

By values of kr for both open and short circuit we will find the value of the resonance radius of antenna.

IV. ANTENNA EMISSION AND SLOT RADIUS

Antenna emission is happened from the slots when $H\varphi$ has the maximum value.

Radial wave in radial transmission line is limited to a perfectly conducting cylindrical surface r=a.

then for magnetic and electric fields we can write:

$$E_Z= D[J_0 (kr) N_0 (ka)- J0_0(ka) N_0 (kr)]. \tag{12}$$

$$H_\theta=iZ_0^{-1} D[J_1 (kr) N_0 (ka)- J_0(ka) N_1 (kr)]. \tag{13}$$

In this study we are going to design and test short ended antenna and as mentioned before $J_0(kr)=0$,and therefore the right part of formula (13) is zero and $N_0(ka)$ is constant value. Now H_ϕ is maximum if $J_1(kr)=$maximum, it means $kr=(1.83,5.35,8,56,\ldots)$.the radius of each slot on antenna can be calculated easily by putting values of kr.
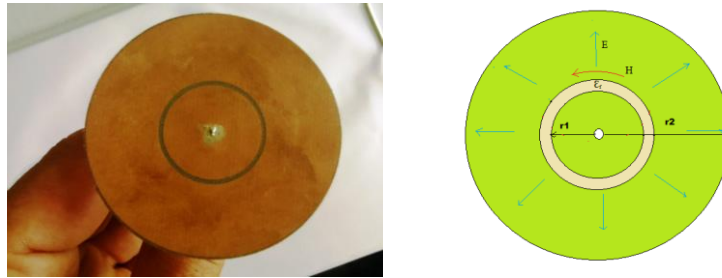

Fig. 2: Conical Bessel beam radial line slot Antenna

V. RESULTS

In this section the directivity pattern of antenna for emission to free space, after diffraction on metallic disk, and after transmission through dielectric thick layer is measured and plotted. At first step antenna is tested without using dielectric or metallic disk in front of it. The directivity of antenna is presented in Figure 1(a). In second step a metallic disk with dimension of r=27 mm and distance 22.7 mm is located in front antenna 1 (b).At last we placed a dielectric disk ($\varepsilon_r=6$) in front of antenna. Distance between antenna and dielectric disk is about 35 mm .thickness and diameter of dielectric are 12mm and 60 mm respectively.1(c).
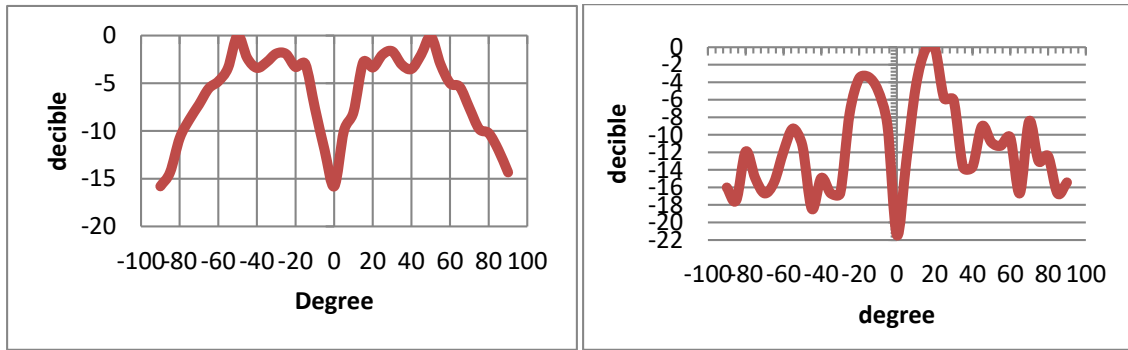
(a)

(b)
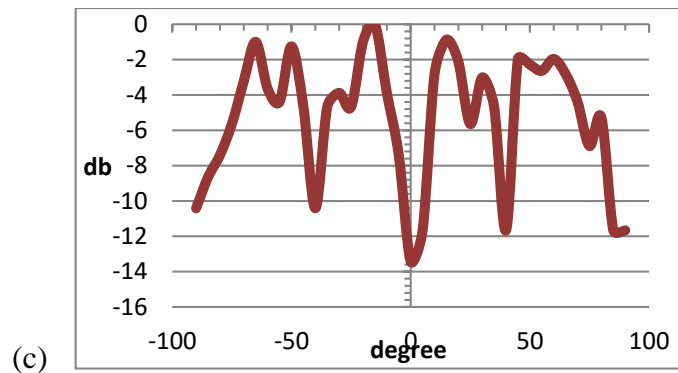
(c)

Fig. 3.(a) directivity of antenna,(b)directivity of antenna with a metallic ring located in front of antenna with 2.27 .(c) directivity, when a dielectric $\varepsilon_r=6$ is placed with distance about 30 mm in front of antenna
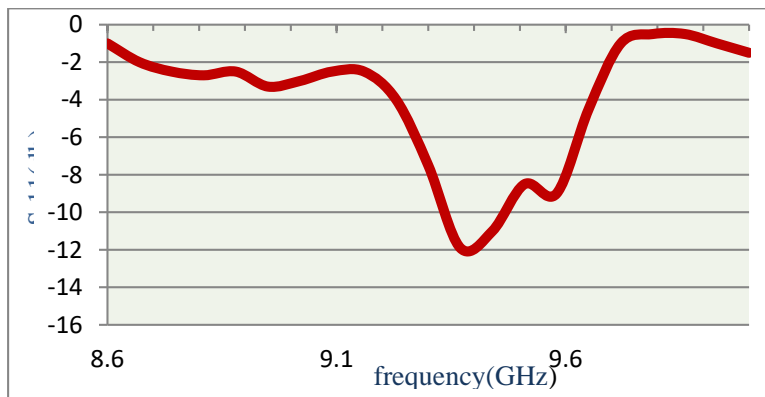

Fig. 4: short-circuited Antenna resonance and reflection coefficient

$F_{1=}8.6Ghz$, $f_2 =10Ghz$ $F_c=9.45$ Ghz $S_{11}= -12$ db
$\Delta f=9.6-9.3=300$ Mhz   bandwidth=.031   vswr=1.13:1

VI. CONCLUSION

Radial ring structure is promised to electro dynamic structure in order to forming conical Bessel beam. Using the external diameter of radial line antenna satisfied resonance condition and provide high efficiency and wider band width .Radiation pattern of radial line ring slot antenna can be controlled by additional metallic disk or dielectric upper straight.

VII.   References

[1] S. Ramo, J.R. Whinnery and Th. Van Duzer, Fields and Waves in Communications and Electronics. 3rd ed., Wiley 1993, QC665.E4R36.

[2] Ralph Holland, Radial Transmission Lines, VK1BRH, 2002.

[3] Maurice C. Hately GM3HAT and Ted Hart W5QJR, The Cross-Field-Antenna Part *I* antenna X, September 1998.

[4] Constantine A. Balanis, Antenna theory analysis and design, 3rd ed., John Wiley & Sons, 2005.

[5] Qiwen Zhen, Vectorial Optical Fields: Fundamentals and Applications., World Scientific, 2013.

[6] M. A. Salem, Kamel A. H., N. Edip. "Microwave Bessel beams generation using guided modes," IEEE Transac. on Antennas and Propagation, vol. 59, no.6, pp. 2241-2247, 2011.

[7] А. Д. Григорьев, Электродинамика и микроволновая техника. Москва, "Высшая школа", 1990.